Elucidating the Impact of Mutant Huntingtin Aggregates on Neuronal Dysfunction in *Drosophila Melanogaster*

Inaugural-Dissertation
to obtain the academic degree
Doctor rerum naturalium (Dr. rer. nat.)

Submitted to the Department of Biology, Chemistry, Pharmacy
of Freie Universität Berlin

by

Megan Bonsor

Berlin, 2024

Period of studies: 01/09/2019 – 29/02/2024

Supervisor: Prof. Dr. Erich Wanker

Institute: Max Delbrück Center for Molecular Medicine in the Helmholtz-Association.

Herewith I certify that I have prepared and written my thesis independently and that I have not used any sources and aids other than those indicated by me.

1st reviewer: Prof. Dr. Erich Wanker
2nd reviewer: Prof. Dr. Stephan Sigrist

Date of defence:

2nd October 2024

Dedicated to Dan and Eva

Summary

Huntingtin (HTT) is a highly conserved and ubiquitously expressed, multi-functional protein. Mutations within exon 1 of the Huntingtin gene (*HTT*) are translated into a pathogenic expansion (>36 glutamines) of the polyglutamine (polyQ) tract, giving rise to an aggressive neurodegenerative disease: Huntington's disease (HD). Aggregates are well established as a key hallmark which are linked to the pathogenesis of HD. A small, truncated mutant fragment of HTT (mHTTex1), has been identified as a component of neuronal aggregates in HD patient brains, and its presence recapitulates HD-like symptoms in model systems. However, the molecular mechanisms dictating mHTTex1 aggregation and toxicity remain elusive.

To this end, a novel *Drosophila Melanogaster* (*D. melanogaster*) model was developed to investigate mHTTex1 aggregates. Transgenic fly strains were generated that pan-neuronally co-express HTTex1 mNeongreen (HTTex1-mNG) and HTTex1 mScarlet-I (HTTex1-mSc-I) fusion proteins with 17, 52, or 75 glutamine repeats (HTTex1Q17-mNG/-mSc-I, HTTex1Q52-mNG/-mSc-I, and HTTex1Q75-mNG/-mSc-I) which enabled detection of mHTTex1 aggregation *in situ* by measuring Forster Resonance Energy Transfer (FRET). Through the neuronal expression of this FRET-based HTTex1 aggregation biosensor, the localisation of HTTex1 within the fly brain was tracked. Co-expression of pathogenic mHTTex1 fusion proteins (HTTex1Q52-mNG/-mSc-I and HTTex1Q75-mNG/-mSc-I) resulted in the formation of SDS stable mHTTex1 aggregates , which correlated with reduced lifespan and mobility in flies. A novel FRET-based fluorescence-activated cell sorting method (FACS) was established which enabled quantitative readout of mHTTex1 aggregates within live cells derived from fly brains.

To interrogate the impact of mHTTex1 aggregates on the proteome, label free quantitative proteomics (LC-MS) analysis of both immunoprecipitated (IP) mHTTex1 aggregates from fly head lysates and whole fly brain samples was performed. Immunoprecipitates and whole brain lysates from flies expressing mHTTex1 with both pathogenic and non-pathogenic polyQ tracts were compared. The results obtained revealed that mHTTex1 aggregates significantly associate with proteins involved in intercellular transport and lead to a global increase of proteins associated with the endomembrane system. The findings of this work establish mHTTex1 aggregates as profound disrupters of the neuronal proteome. RNAi knockdown of the key upregulated protein sff resulted in significant toxicity, highlighting a potential protective role increased sff protein levels may play against HTTex1-induced toxicity.

Contents

1. Introduction

Since the beginning of humanity, we have strived to understand the minds and bodies we inhabit. From the earliest human remains exhibiting evidence of brain surgery [1,2], to the first scientific writings detailing the medical observation of brain injuries [3] , it is clear early humans innately understood the importance of the brain. As civilisation advanced**,** the brain was established as the origin point where “all senses are connected” [4] via nerve cells, dendrites, and axons, each with a specialised function [5,6]. Later, this nervous system was found to consist of a basic cellular unit: neurons [7,8]. Today, we understand the human brain to be a “scaled -up primate brain” consisting of 86 billion interconnected neurons [9,10]. These neurons electrochemically transmit sensory information from our environment to the brain, orchestrating both our conscious and subconscious responses to external stimuli. The intricate quantity and biological makeup of these neurons is responsible for the vast spectrum of human cognitive, behavioural, and emotional responses [10–12]. As neurons underpin every aspect of human behaviour, any disruptions in neuronal function can result in profound and detrimental consequences.

One such consequence of neuronal dysfunction is neurodegenerative disease. Neurodegenerative diseases such as Alzheimer’s, Parkinson’s, and Huntington’s disease (HD) are typified by the loss of neuronal density and function. Specifically, the progressive degeneration of selectively vulnerable neuronal populations causes an array of distinct cognitive and motor impairments, ultimately culminating in premature mortality [13,14]. In the absence of a cure, individuals with neurodegenerative diseases require high quality palliative and therapeutic care throughout their lifetime, posing a significant challenge to healthcare systems worldwide [15]. Therefore, the impact of neurodegenerative diseases extends beyond the individual, affecting families and communities, creating a ripple effect that reverberates throughout society [16,17]. Despite centuries of research into the brain and its diseases, we still lack fundamental understanding of the key pathogenic mechanisms underlying neurodegenerative diseases. By concentrating research efforts on uncovering the fundamental pathogenic principles of a single neurodegenerative disease, like HD, we can potentially extend the applicability of these discoveries to other neurodegenerative conditions.

1.1. Huntington’s disease (HD)

HD, formerly known as Huntington’s chorea, is a rare neurodegenerative disease that intersect the fields of genetics, neuroscience, and sociology. Caused by a dominantly inherited mutation in the Huntingtin gene (*HTT*), HD manifests in adulthood as a progressive decline in cognitive, behavioural, and motor function [18–20]. The impact of HD spreads far beyond its genetic and clinical aspects. Due to the monogenetic and hereditable nature of HD, it is pervasive through small, isolated communities devastating generations of individuals [21,22]. Furthermore, individuals with HD, both past and present, have faced social stigma, discrimination, and inequality [23,24]. This work begins by establishing a multidimensional view of HD, exploring its historical roots, genetic etiology, epidemiological patterns, and clinical features. In doing so, this chapter aims to lay a comprehensive foundation for understanding the cause and impact of HD.

1.1.1. History

Historically, disease symptoms have often been mistakenly attributed to religious or spiritual origins. HD, characterised by the hallmark symptom of chorea, epitomises this misconception. The term 'chorea' finds its etymological roots in the ancient Greek word for dance, owing to the abrupt, uncontrollable muscle movements that create an illusion of rhythmic, involuntary dancing [25]. References to chorea-like symptoms can be traced back to as far as the Middle Ages, where they were described as 'Dancing mania' or the 'St. Vitus Dance' [26]. In historical accounts, groups of individuals are described as “suddenly seized with this disease... proceeded dancing and jumping along the road” [27] with some “continuing to suffer all their lives from a trembling of their limbs” [27]. These individuals often found themselves isolated from their communities [25] and subjected to religious rituals in attempts to expel perceived evil spirits [26]. Consequently, people afflicted with chorea were marginalised, and comprehensive medical knowledge about HD remained elusive until the industrial age.

It was not until 1872, when George Huntington published 'On Chorea' [28], that a comprehensive medical description of "hereditary chorea" was first established. Building on the observations of his father and grandfather, Huntington wrote of a rare disease which "attended generally by all the symptoms of common chorea, only in an aggravated degree, hardly ever manifesting itself until adult or middle life, and often occupying years in its development, until the hapless sufferer is but a quivering wreck of his former self" [28]. Unbeknownst to himself, Huntington had provided the most complete clinical description of the disease that would forever become synonymous with his name. Huntington's work, fuelled by the rediscovery of Mendelian inheritance and the momentum of the eugenics movement, generated significant interest and fear regarding the hereditary nature of HD.

By the early 1900's HD was established as an autosomal dominant inherited disease [29], prompting reputable scientists to advocate for the compulsory sterilisation of HD patients [30,31]. Studies tracing HD-affected families ancestry reinforced archaic notions reminiscent of those held in the Middle Ages. Ancestors of HD patients were falsely portrayed as witches [32] and "liable to bear the marks of a grossly psychopathic taint" [33]. Although proven to be scientifically inaccurate [34], these studies laid the foundation for atrocious eugenics campaigns against HD patients that lasted well into 20th century [35]. Such persecution compelled families to conceal their disease history out of fear. Thereby making scientific research into the genetic causes of HD near impossible.

The discovery of the genetic locus responsible for HD in 1983 followed a decade-long investigation into an isolated Venezuelan population residing near Lake Maracaibo [21]. This breakthrough, occurring more than 900 years after the initial mention of dancing mania, dispelled centuries of misinformation about the cause of HD, affirming its purely genetic nature.

1.1.2. Aetiology and epidemiology

After the identification of the HD locus, subsequent early investigations revealed interesting patterns in the age of disease onset, particularly in the context of familial inheritance [36]. HD patients were found to exhibit a phenomenon known as genetic anticipation, where disease onset occurred earlier with each successive generation. Notably, this phenomenon appeared more pronounced when HD was inherited from the paternal line [37,38]. However, the underlying mechanism responsible for the clinical anticipation and manifestation of HD were not clarified until a decade later.

The pivotal breakthrough in our understanding of the genetic basis of HD occurred in 1993 when researchers discovered the Interesting Transcript 15 (IT15) gene on chromosome 4 at site 4p16.3 [39]. Within exon 1 of the IT15 gene, now recognised as the Huntingtin gene (*HTT*), researchers uncovered a polymorphic trinucleotide repeat consisting of cytosine, adenine, and guanine (CAG) [39]. While control individuals exhibited CAG repeats ranging from 11 to 34, a survey of 75 HD families revealed repeat lengths between 42 and 66 [39]. Subsequent studies advanced this classification: fewer than 27 repeats as the normal range, 27-35 as intermediate, 36-39 as reduced penetrance, and over 40 as full penetrance [40]. Interestingly, due the inherent instability of repeat nucleotide sequences, there have also been cases reported of sporadic HD [41–43]

From the discovery of the *HTT* gene, it was clear that the length of the CAG repeats inversely correlated with age of HD onset [39,44–46]. Individuals harbouring longer CAG repeats experienced greater repeat instability during spermiogenesis, contributing to more pronounced anticipation in cases of paternal HD transmission and a higher risk of juvenile HD [47]. However, individuals with the same CAG length are unlikely to present symptoms of HD at the exact same age [48] with CAG repeat length only accounting for up to 70% of the variability in the age of HD onset [49]. Variation in HD presentation is also affected by differences in somatic expansion; where CAG repeats further expand in the brain cells of patients, result in the intracellular repeat lengths far greater than that observed in the blood [50–52]. Additionally, inherited single nucleotide polymorphisms (SNPs) in key disease modifying genes [48,53] have been shown to affect HD onset and symptoms. Further variability in HD presentation may be conveyed through difference in epigenetics influenced by environment, diet, and lifestyle [54].

Consequently, there is a notable divergence in the prevalence of HD across various geographical regions. Globally, the prevalence of HD increased from 2.71 individuals per 100,000 in 2012 to 4.88 per 100,000 in 2022 [55]. However, this increase is not uniform across all continents and populations. A comprehensive meta- analysis conducted between 2011 and 2022, spanning 21 countries and involving 27 studies, revealed a varying distribution of HD prevalence [55]. When examined by continent, South America exhibited the highest prevalence of HD at 11.42 individuals per 100,000, followed by North America at 8.87 per 100,000, Europe at 6.37 per 100,000, Asia at 2.39 per 100,000, and Africa at 0.25 per 100,000. Notably, isolated regions worldwide, such as Northern Scotland, are geographical hotspots for HD. Despite overall population decline, population clusters in Northern Scotland collectively exhibit the highest recorded HD prevalence rates globally, with 23.3 per 100,000 individuals carrying the pathogenic HD mutation [56]. Such isolated areas have historical ties to discrete populations dating back thousands of years, leading to reduced genetic variation due to the founder effect [57]. Therefore, the modern-day population in these regions exhibits a heightened incidence of rare genetic conditions like HD when compared to the general population.

The global increase in HD prevalence is unlikely due to an increase in actual HD cases. Instead, this phenomenon may be attributed to several influencing factors. First, advancements in diagnostic testing have enabled accurate identification of *HTT* mutations and measurements of CAG repeat lengths, thus leading to more HD cases being clinically identified [58]. Second, improvements in both mental and physical healthcare have led to an overall increase in population longevity [59]. This extension of healthy lifespan means more individuals reach the age at which HD symptoms typically manifest, further contributing to the observed rise in prevalence. Additionally, heightened awareness of hereditary diseases, including HD, and progress in disease-modifying trials [60] have encouraged individuals to seek diagnosis in the hope of participating in clinical trials aimed at finding a cure [61]. This increased willingness to come forward for diagnosis has, in turn, led to a more accurate reflection of HD prevalence rates. Conversely, the low prevalence of HD in Africa and Asia may not accurately represent the actual number of individuals with the pathogenic HD mutation in these regions. In many African and Asian countries, limitations in access to healthcare, scientific education about HD, and clinical diagnostic testing make it challenging to identify early signs of HD [62,63]. Consequently, cases often go unnoticed or undiagnosed, contributing to the under-representation of HD in these areas.

1.1.3. Clinical symptoms

HD is clinically characterised by a complex combination of behavioural, cognitive, and motor disturbances. These clinical manifestations are underpinned by widespread neuropathological changes [18].

The onset of HD typically occurs between the ages of 30 and 50 (***Figure 1***), with an average disease duration of 17 to 20 years [64]. However, the earliest signs of HD are often subtle behavioural symptoms that appear decades before motor symptoms become evident [65,66]. Initially, individuals may exhibit mild behavioural changes such as irritability, anxiety, and, in some cases, obsessive-compulsive tendencies [67]. These behaviour changes can be accompanied by psychosis [68] and sleep disorders [69,70] which collectively impact day-to-day life. Additionally, HD patients commonly experience apathy, manifesting as decreased activity, self-care, and a lack of initiative [71] which worsens with disease progression [72]. Comorbid with apathy is the most common and serious psychopathological feature of HD: Depression [73]. A higher percentage of pre-HD diagnosis individuals have major depression than control populations [65,74]. The rate of depression increases with proximity to motor symptom onset [75] and persists throughout their lifetime. Sadly, suicidal ideation in individuals pre-HD diagnosis and stage 2 of the disease, when independence diminishes, is approximately 2.5 times that of control individuals [76]. As a result, 1 in 10 individuals attempt suicide post HD diagnosis [60] making HD patients more likely than any other neurodegenerative disease patients to attempt or die by suicide [77,78].

Early behavioural symptoms are often compounded by a decline in cognitive functions. Cognitive functions such as implicit memory, attention, episodic learning, and emotional recognition begin declining early in HD progression [79–82]. One of the first indicators of HD is slower cognitive processing whereby the completion of ordinary tasks, requiring fast thinking and motor skills, becomes effortful [83]. Individuals with HD have difficulty estimating time which becomes apparent as early as 15 years before motor diagnosis [84]. Once punctual individuals begin to exhibit frequent lateness and underestimating the time required to complete tasks. As HD progresses, the collective decline in cognitive abilities causes difficulties in communication. Individuals with HD struggle to comprehend conversations and respond in a timely manner with clear speech, which directly impacts their social relationships. In later stages of HD, the progressive decline in cognitive functioning is diagnosed as dementia [85], whereby HD patients lose the ability to perform daily duties required for independent living.

The manifestation of motor symptoms further reduces the independence of HD patients (***Figure 1)***. Motor disturbances manifest later in disease progression, and are often the most apparent clinical feature in HD. The hallmark feature of HD is the initial presence of hyperkinetic choreiform movements which are involuntary and irregular [64]. Initially small muscle twitches present in distal muscles such as fingers, toes, and facial muscles. Gradually, the muscle twitches develop into larger choreiform movements which impede the individual's ability to walk [86]. As HD progresses, hypokinetic symptoms such as hypokinesia and bradykinesia dominate causing movement to slow and range of motion to become restricted [87]. Additionally, slow dystonia movements cause patients to exhibit an abnormal posture caused by the increase muscle tone [88]. Problems with swallowing, also known as dysphagia, impact the ability of patients to eat and drink resulting in dramatic weight loss, which is accentuated by cachexia, a loss of skeletal muscle mass due to metabolic dysregulation [89–92]. Motor dysfunction progressively worsens to the point of immobility, resulting in advanced stage HD patients becoming bed-bound and requiring full time care either from a professional or family member [93]. Ultimately, dysphagia and cachexia complications, alongside suicide, are the most common causes of mortality in HD patients [94,95].

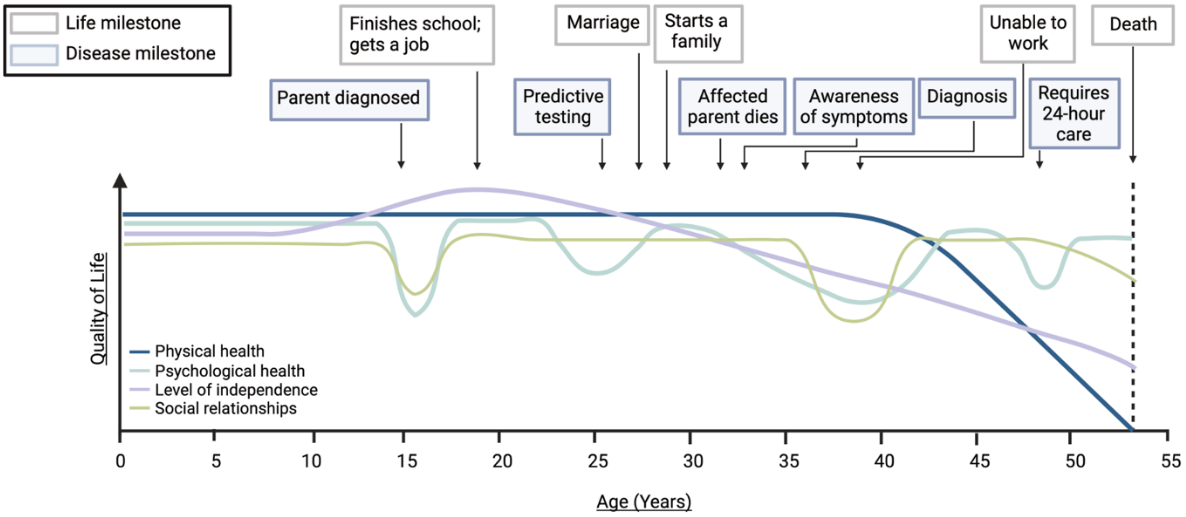

Figure 1. Timeline of the life and disease milestones of a HD patient

A schematic showing the hypothetical impact of both life and disease milestones on the physical health (blue), psychological health (light blue), level of independence (purple) and social relationships (green) of a HD patient. The impact of HD on the overall quality of life of an individual begins long before symptom onset and is considerably influenced by the wider effects of being a member of a HD family. (Adapted from[19] *and created using Biorender).*

However, when discussing HD symptoms, it is vital to remember HD patients are not only individuals with a medical condition but also members of families and communities. The hereditary nature of HD means many HD individuals have been caregivers to affected family members, bearing witness to the symptomatic decline of loved ones (***Figure 1***) [96,97]. This first-hand experience makes the HD-affected individual acutely aware of their own fate, which inevitably places pressure on themselves, their wider family system and social circle. The onset of behavioural and cognitive symptoms also hinders the HD individuals' ability to maintain relationships and employment, leading to disrupted family functioning [98] and social withdrawal [99]. As the disease advances into motor disturbances, independence is relinquished and with it a sense of self [96].

In conclusion, HD is characterised by a complex interplay of symptoms, gradually progressing from subtle behavioural changes to cognitive decline and severe motor disturbances. In recognising the profound impact of these symptoms on individuals and their families, it becomes clear that the symptoms extend far beyond medical terminology. These symptoms are life-altering changes endured by HD sufferers. Therefore, it is crucial to humanise the experience of HD, acknowledging not just the clinical symptoms but the personal, emotional, and social dimensions these symptoms affect.

1.1.4. Neuropathology

Multisystem neuropathological changes in HD patients underscore all clinically observed symptoms. The most prominent area of neurodegeneration is the striatum, located within the basal ganglia (***Figure 2A***).

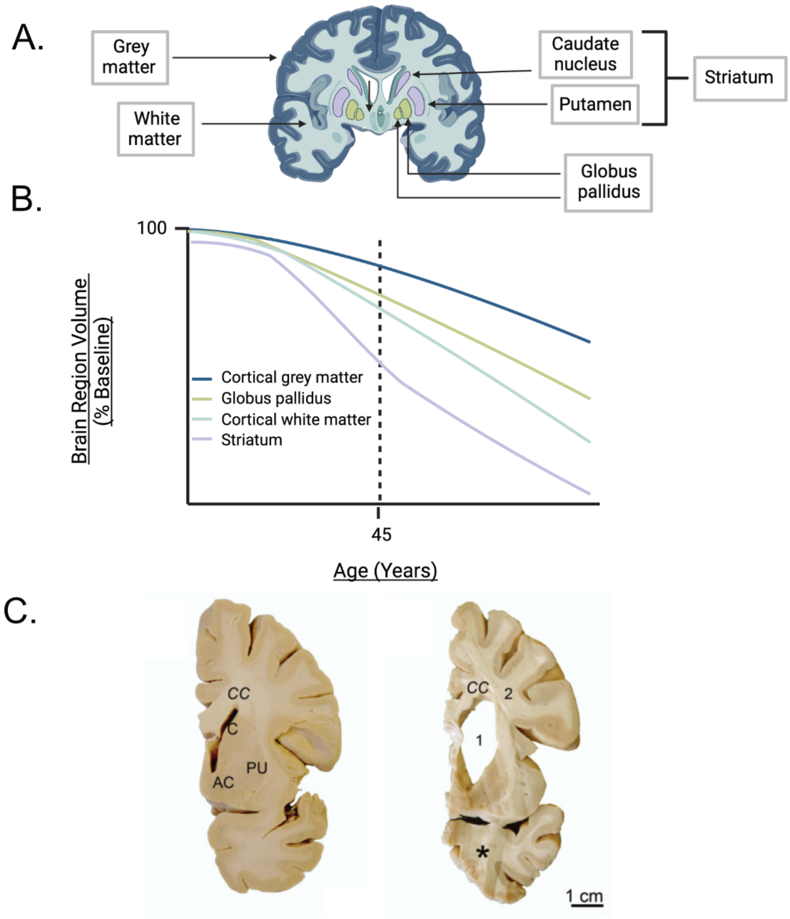

Figure 2. Neuropathological changes in the HD brain

A) *A cartoon of a coronal section of the human brain with key areas affected in HD labelled. (Created using Biorender).* ***B)*** *Hypothetical and conceptual model of the trends in volumetric MRI measures of HD. This qualitative representation was based on the observations detailed in observational studies*[100,101]*where the striatum undergoes the most rapid volume loss (Adapted from*[102,103]*, created using Biorender).* ***C)*** *Coronal sections of post-mortem HD brains: The left section was obtained from a control individual where the corpus* *callosum (CC), nucleus accumbens (AC), caudate nucleus (C) and putamen (PU) are indicated. The right section was obtained from a HD patient which displays widening of the lateral ventricle (1), reduction of the cerebral white matter (2) and striatal atrophy (C and PU). (Abbreviations: AC, accumbens nucleus; C, caudate nucleus; CC, corpus callosum; PU, putamen; 1, widened lateral ventricle; 2, reduced cerebral white matter). (Adapted from*[104] *and in part created using Biorender).*

The striatum consists of the caudate nucleus, putamen and the globus pallidus which collectively control decision making, voluntary motor control, emotion, and habit formation [105] (***Figure 2A***). 95% of the total neuronal population within the striatum is made up of GABAergic medium spiny projection neurons (MSNs) and 5% interneurons [104]. MSNs are classified either as indirect MSNs (iMSNs) which express D2 dopamine receptors or direct MSNs (dMSNs) which express D1 dopamine receptors. The different classes of MSNs have divergent roles within the striatum; dMSNs excite while iMSNs inhibit their respective connected structures in the basal ganglia [106]. Degeneration of the iMSNs occurs first in HD, which prevents motor inhibition, giving rise to the hyperkinetic movement symptoms observed in early-stage HD patients. Eventually, progressive degeneration of dMSNs prevents motor release and therefore manifests as hypokinetic motor symptoms which present later in HD [107]. Reduction in striatal volume is detectable more than 20 years before symptomatic HD diagnosis [103] and is accompanied by thinning of the cortical grey matter and reduction in cerebral white matter volume early in HD progression [108–111] (***Figure 2B***). Later enlargement of the lateral ventricles occurs alongside neuronal loss in most other brain structures including but not limited to: the cerebral cortex, total white matter, cerebrum, and cerebellum [112–114] (***Figure 2C***).

1.1.5. Treatment

Presently, there is no causative treatment or cure for HD. Therefore, current treatment plans for HD patients are based around a multidisciplinary symptom management. It is crucial to emphasise that there is no one-size-fits-all treatment for HD. Since each patient presents a unique combination of symptoms, treatment plans must be tailored to each individual’s needs.

Medications primarily target the management of chorea, one of the most common symptoms of HD. Tetrabenazine (TBZ), the first drug approved for chorea specifically associated with HD, acts by reversibly inhibiting the human vesicular monoamine transporter 2 (VMAT2), thereby depleting monoamines from nerve terminals [115,116]. While the precise mechanism by which TBZ mitigates chorea remains a subject of ongoing research, it remains the most widely prescribed treatment for HD. Olanzapine (OZ), traditionally prescribed as an antipsychotic for schizophrenia, is another commonly used medication for HD [117]. Interestingly, OZ has demonstrated the ability to stabilise the progression of motor symptoms in HD, in addition to addressing behavioural symptoms of HD [118,119]. Furthermore, selective serotonin reuptake inhibitors (SSRIs) are frequently prescribed, given that approximately 40% of HD patients experience HD-associated depression [60]. Managing HD pharmacologically is not without its challenges. Achieving a balance is crucial; treatment should alleviate primary symptoms without exacerbating comorbid ones. For instance, while TBZ effectively manages chorea, improving mobility and enhancing the patient's quality of life, it may worsen depression or suicidality in patients who have both chorea and these comorbid conditions. In this case, a less effective chorea treatment may be chosen to prevent accelerated deterioration of the patient's quality of life from exacerbated depression [60,120]

Deterioration of HD patient's quality of life is further mitigated through non-pharmaceutical interventions. Physiotherapists and occupational therapists play a significant role in helping patients maintain mobility and comfort in daily life [121,122]. Language and speech therapists assist those who experience speech difficulties, enabling continued communication with friends and family [123]. Additionally, dieticians and psychologists contribute to the physical and mental well-being of patients [124,125]. While treatment plans for HD patients are effective, they require taking multiple mediations and intensive therapy session throughout the lifetime of the patient. Therefore, a therapeutic approach aimed at directly treating the cause of HD rather than long term symptom management would be extremely beneficial to patients.

To this end, current research is focused on lowering the levels of the huntingtin protein (HTT) by suppressing *HTT* gene expression. One approach is through anti-sense oligonucleotides (ASOs), small single-stranded DNA molecules that bind to RNA, which promote degradation and consequently lower protein expression [126]. While targeting of the mutant huntingtin gene (*mHTT*) is theoretically possible due to the CAG repat expansion, many other genes within the body also carry CAG repeats [127]. Therefore, the risk for off-target effects of *mHTT*-targeting ASOs is high. Hence current ASOs focus either on non-selectively lowering the levels both wild type HTT (wtHTT) and mHTT protein or targeting specific single nucleotide polymorphisms (SNPs) present in HD populations. Presently, four ASO therapies for HD have been assessed in clinical trials: Tominersen, WVE-120101, WVE-120102 and WVE-003 [126,128–130].

The non-selective HTT lowering ASO Tominersen lowers both mHTT and wtHTT huntingtin levels. In 2021, Tominersen phase 3 clinical trials were halted due to safety concerns [126]. Now, a new phase 2 clinical trial called GENERATION HD2 is underway to evaluate if lower doses in early manifest HD patients will make Tominersen a viable treatment option for HD [126]. Unlike Tominersen, WVE-120101 and WVE-120102 target mHTT through CAG repeat length-associated SNPs rs362307 (SNP1) and rs362331 (SNP2) respectively. These SNPs are present in 40% of European HD patients [130,129]. Both allele specific ASOs underwent Phase I/Ia clinical trials, named PRECISION-HD1 and PRECISION-HD2. However, due to the lack of significant mHTT lowering when compared to placebos, both trials were halted [126]. In 2023, another SNP targeting ASO WVE-003 is currently in a phase1b/2a clinical trial called SELECT-HD where it will be tested on early manifest HD patients. After showing successful mHTT lowering in HD mice, WVE-003 is a promising therapeutic candidate [126].

In summary, HD still lacks a cure, and current treatment primarily focuses on symptom management. Recent scientific developments in HD ASO treatment have provided hope for a more targeted treatment of HD. However, while current ASO therapies have garnered much attention, careful consideration must be taken with regards to lowering HTT levels, as this may have adverse consequences.

1.2. Huntingtin protein (HTT)

Up to this juncture, we have established that rare inherited CAG repeat mutations in the *HTT* gene cause a cascade of behavioural, cognitive, and motor symptoms underpinned by specific patterns of neurodegeneration observed in HD patients. Current research efforts are centred on reducing HTT protein levels through *HTT* gene-targeting therapies. However, one *HTT* gene gives rise to multiple transcripts and protein isoforms.

The *HTT* gene comprises 67 exons and encodes a 3144 amino acid (aa) protein [131]. The *HTT* gene undergoes canonical transcription, resulting in two major full-length transcripts: a 'short' 10.3kb mRNA and a 'long' 13.7kb mRNA, depending on alternative polyadenylation of the 3' untranslated region (UTR) [132,133]. These two *HTT* isoforms exhibit distinct tissue expression patterns, with the long isoform being enriched in the brain, while the short isoform predominates in dividing cells [133]. In addition, alternative splicing of the canonical *HTT* transcript, driven by the length of CAG repeats, gives rise to a truncated HTT exon 1 transcript (*HTT1a*) [131,134,135–137].

Both the translation of truncated transcripts and the proteolytic cleavage of the full-length HTT protein leads to the formation of multiple polyglutamine (polyQ)-expanded N-terminal protein fragments, with the smallest being the HTT exon 1 protein (HTTex1) [135,136,138]. These HTTex1 protein fragments have been identified in post-mortem HD brains, where they exhibit significant pathogenicity and often aggregate within nuclear inclusions [139].

Despite extensive research efforts, the complete structure and precise function of HTT remains elusive. In the following section, we provide a comprehensive review of the current knowledge concerning the structure and function of the HTT protein and its truncated HTTex1 fragment, before proceeding to discuss aggregation and its implications for the pathogenesis of HD.

1.2.1. Huntingtin (HTT) Structure

Full-length wild type HTT (wtHTT) is a substantial 348-kDa protein, ubiquitously expressed throughout life, with particularly elevated levels in the central nervous system (CNS) [134,140]. Interestingly, homologues of HTT have been discovered in species ranging from invertebrates such as sea urchins to humans. Thus, highlighting HTT as a highly conserved and important protein [140].

To date approximately 75% of the 3144 aa HTT protein, in complex with its interaction partner 40-kDa HTT-associated protein (HAP40), has been structurally resolved up to 2.6Å resolution using cryo-electron microscopy (cryoEM) (***Figure 3***) [141,142]. These structures reveal that HTT can be divided into three distinct domains: the amino-terminal N-HEAT domain (aa 91-1684), the central bridge domain (aa 1685-2091), and the carboxy-terminal C HEAT domain (aa 2098–3104) [141,142] (***Figure 3A***). The remaining 25% of the HTT-HAP40 complex represents highly flexible regions that remain unresolved by cryoEM. These regions encompass the N-terminal HTTex1 domain (aa 1-90) and an N-terminal intrinsically disordered region (IDR) (aa 407-665) [141] (***Figure 3A***).

The N-terminus of the HTT protein corresponds to exon 1 of the *HTT* gene, and accounts for approximately 2% of the whole protein [141]. The N-terminus consists of an initial 17 amino acids (N17) followed by a stretch of pure glutamine repeats (polyQ tract) and ending in a proline-rich domain (PRD). Although high-resolution cryo-EM has not fully resolved the N-terminal domain, lower-resolution techniques like mass spectrometry (MS) and small-angle X-ray scattering (SAXS) have shed light on its structure [142] (***Figure 3B and 3C***).

The N17 domain is predicted to form an amphipathic helix (AH) which is crucial for interaction with lipid membranes [143–146] and may function as a nuclear export signal (NES) [147]. Following the N17 is the polyQ tract, a highly flexible region which can adopt various conformations including random-coil [148–150], beta sheet [151,152], or alpha helical structures [153–155]. The disease-causing CAG repeat expansion in the *HTT* gene is translated to an expansion of the polyQ tract. Therefore, the length of the polyQ domain is dependent on the number of glutamines [142]. Studies using the HTT-HAP40 complex found HTT polyQ expansion induces structural changes within the N-terminus of HTT, causing the N-terminal domain to occupy a larger volume of conformational space when compared to controls [141] (***Figure 3B***).

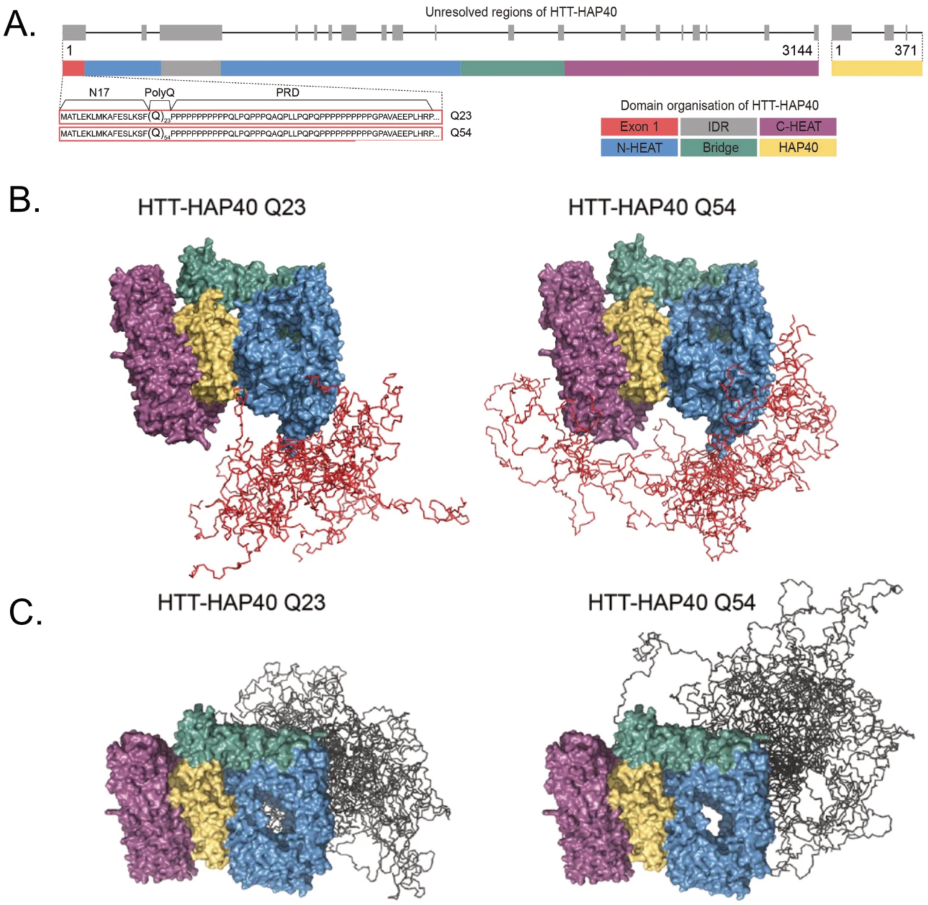

Figure 3. The domain organisation and structure of HTT

A) *Domain organisation of HTT mapped to a schematic sequence with Exon 1 (red), N-HEAT (blue), Bridge (green), C-HEAT (purple) and IDR (grey) depicted. The unresolved regions of HTT-HAP40 mapped to the HTT sequence are depicted in grey. Within Exon 1 a polyQ expansion of 23 or 54 Q repeats was used (Adapted from* [142]*).* ***B)*** *Integrated model of the structure of full-length HTT-HAP40 using cryo-EM, SAXS and cross-linking mass spectrometry data (N-HEAT, blue; bridge, green; c-HEAT, purple; HAP40, yellow).The simulated structure of Exon 1 (red ribbon) is illustrated in both Q23 and Q54 HTT* ***C)*** *The same structure depicted in* ***B****, with the simulated structure of the IDR (grey ribbon) in both Q24 and Q54 HTT. The IDR is spatially constrained by the conformational space occupied by exon 1. (Adapted from* [142]*).*

Thus, the polyQ tract is currently hypothesised to function as flexible sensor, interacting with other regions of HTT and its binding partners [141,156,157]. After the polyQ tract is the PRD, which consist of two stretches of pure proline repeats separated by a proline, lysine and glutamine alternating region that forms a rigid left-handed type II polyproline helix [158–160]. The PRD is known to interact with tryptophan (WW) and Src homology 3 (SH3) domain proteins [161–163]. The role of the PRD is multifaceted, with current hypotheses suggesting the PRD plays a key role in stabilising the polyQ tract and mediating HTT protein-protein interactions (PPIs) [160]**.**

The main body of HTT (aa 91-3144) consists of several HEAT repeats, named after the four proteins in which a tandem array of repeats was initially detected: **H**untingtin, **E**longation factor 3, protein phosphatase 2**A**, **T**OR1 [164] (***Figure 4***). The first N-HEAT domain (aa 91-1684) comprises 21 HEAT repeats, collectively forming an α-solenoid structure [142]. Positioned between N-HEAT repeats 6 and 7 is the IDR (aa 407-665) [142], an unresolved disordered region extending outward from the N-HEAT domain which is subject to post-translational modifications (PTMs). The IDR is influenced by the conformational space occupied by the expanded N-terminal domain (aa 1-90), potentially affecting its accessibility to key HTT PPIs [142] (***Figure 3C***). The C-HEAT (aa 2092-3137) comprises 12 HEAT repeats, forming an alpha-helix-containing elliptical ring structure [141,142]. Within the C-HEAT lies a highly conserved nuclear export signal (NES) motif (aa 2397-2406) [165], which may dictate the cellular localisation and subsequent function of HTT. The N-HEAT and C-HEAT domains are connected by the BRIDGE domain (aa 1685-2091), formed by 6 tandem α-helical repeats. The flexible BRIDGE domain and additional loop interactions loosely connect the N-HEAT and C-HEAT domains, conferring substantial structural flexibility to HTT. Consequently, in the absence of HAP40, HTT can adopt up to 100 structurally distinguishable conformations [166] through intramolecular domain interactions [141]. This structural flexibility of HTT governs not only the intramolecular binding between HTT domains [167] but also influences the function of HTT through intermolecular interactions.

1.2.2. HTT function

Decades of research have focused on the consequences of HTT dysfunction, yet surprisingly research has failed to draw a conclusive stance on HTT's native function. Knockout of HTT in mice results in embryonic lethality and disrupts neuronal development in the central nervous system (CNS) [168–170] , underscoring the importance of wtHTT during development. Yet the precise mechanisms underlying the vital neuroprotective role of HTT remains uncertain. To address this, researchers have assembled an ever-growing catalogue of HTT modifications and intermolecular interactors, which provide valuable clues about HTT's function.

HTT undergoes various post-translational modifications (PTMs), including proteolysis and the addition of small proteins or functional groups to specific residues. Proteases, recognizing PEST sites rich in proline (**P**), glutamic acid (**E**), or aspartic acid (D), serine (**S**), and threonine (**T**), cleave HTT, potentially altering its function by generating smaller HTT fragments[171] (***Figure 4***). In HD, increased proteolysis leads to higher levels of toxic N-terminal protein fragments [172,173]. Additionally, HTT undergoes phosphorylation, SUMOylation, ubiquitination, acetylation, and palmitoylation [174]. These modifications, depending on specific residues, regulate HTT transport, degradation, PPIs, and self-assembly [175–179]. Collectively, PTMs play a pivotal role in determining HTT's sub-cellular localisation and protein interactions [174].

An array of structural conformations and PMTs enable HTT to associate with over 2971 proteins [180]**.** Given this extensive network of PPIs and its conserved neuroprotective role, HTT is hypothesised to function as a scaffold for assembling multiple protein complexes that regulate various cellular processes, including protein degradation, vesicle transport, gene expression, and cell survival [181–185].

One important cellular process regulated by HTT is autophagy, the major pathway responsible for degrading dysfunctional organelles and proteins. Autophagy is particularly critical in terminally differentiated cells such as neurons, to ensure long-term proteostasis maintenance [186]. HTT directly interacts with cargo receptor p62 [182] enhancing its affinity for both ubiquitinated proteins and autophagosome receptor LC3. Furthermore, HTT competes with the HEAT domain protein mTOR [187] for ULK1 binding [182]. The HTT/ULK1 complex formation blocks mTOR-mediated repression of ULK1 kinase activity, thereby promoting autophagosome formation [187–190]. Additionally, HTT enhances retrograde motility of autophagosomes, facilitating their transport toward the soma by directly interacting with the retrograde motor dynein [191] and acting as a scaffold for forming a microtubule motor complex with HAP1, dynactin, and kinesin-1 [192,193]. This active role in autophagosome formation and transport underscores HTT's role in regulating the autophagic degradation of dysfunctional neuronal proteins.

Beyond autophagy, HTT also plays a crucial role in intracellular vesicle trafficking along neuronal microtubules. HTT facilitates the transport of various vesicle cargoes, including clathrin-coated vesicles [194], synaptic vesicles [195–197], lysosomes, and endosomes [198]. Particularly noteworthy is HTT's role in enhancing the transport of brain-derived neurotrophic factor (BDNF), a critical factor for protecting striatal neurons [199]. Additionally, HTT regulates vesicle traffic velocity by interacting with glyceraldehyde 3-phosphate dehydrogenase (GAPDH), which provides local energy for fast axonal transport [200]. The direction of vesicle transport is influenced by PTMs of HTT, specifically phosphorylation at serine 421 (S421) by kinases Akt/PKB and SGK, dictating whether cargo is transported anterogradely or retrogradely.

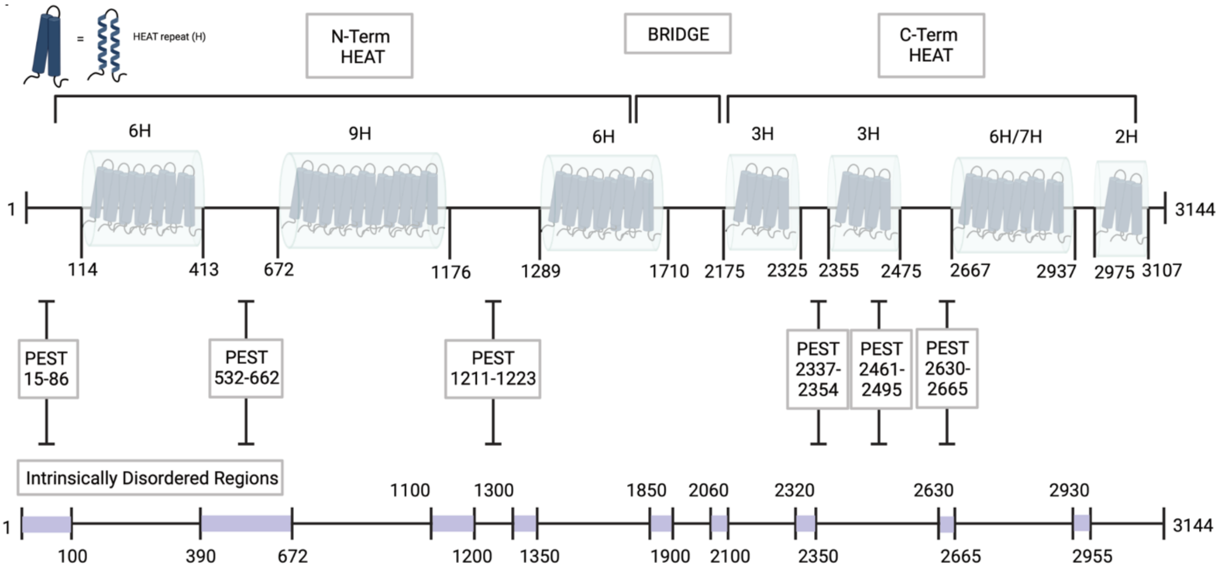

Figure 4. Schematic of the HEAT repeats, PEST, and disordered regions of HTT

The heat repeats (H) consist of two helixes which are the basic unit of the larger N-Term Heat and C-terminal HEAT domains. Between the domains there are PEST sites which are prone to proteolysis. HTT contains many disordered regions (purple) throughout the HTT protein which have yet to be structurally resolved. (Adapted from [134]).

HTT's involvement in gene expression and transcription is another facet of its function. The polyQ domain found in HTT is also present in other transcription factors (TFs), suggesting a role as a transcriptional regulating domain [201]. HTT interacts with key transcription factors such as cAMP-response element (CREB)-binding protein (CBP) [202], nuclear factor-kB (NF-kB) [203], and neuron-specific TF NeuroD [200]. HTT also modulates transcriptional activation and repression through binding corepressors, including nuclear co-repressor (NCOR) [204] and transcriptional corepressor C-terminal-binding protein (CtBP) [205], as well as co-activators like the Gln-Ala repeat transcriptional activator CA150 [205] and TAFII130 [206]. Of particular significance is HTT's sequestration of repressor element-1 transcription factor/neuron restrictive silencer factor (REST/NRSF) [207], promoting the transcription of brain-derived neurotrophic factor (BDNF) crucial for neuronal development and maintenance.

Furthermore, HTT exhibits pro-survival properties. Early experiments in cells and cultured neurons showed HTT expression prevents stress-induced cell death [208,209]. Further *in vivo* work showed lowering of HTT induced cell death, while overexpression protected neurons from excitotoxicity and injury [209–211], supporting HTT’s pro-survival properties. Research has shown HTT promotes cell survival, in part, through blocking the activation of caspase-3 and 9, therefore inhibiting apoptosis [208].

While it has become commonplace for publications to reiterate that “HTT function remains unclear”, the evidence reviewed above unmistakably portrays HTT as a multifaceted hub that orchestrates crucial pathways vital for neuronal development and survival. Significantly, HTT's reach extends beyond neurons, with recent studies implicating its role in macrophage function [212]. This revelation prompts intriguing questions about how HTT's predominant role in the central nervous system intersects with the immune system—a topic ripe for further investigation. The future holds promise with advancements in higher-resolution structural determination of HTT [142], both with and without HAP40, as well as the development of new PPI methods capable of detecting low-affinity interactions [213–215]. These innovations offer the potential for a deeper insight into HTT's structure and interaction partners. Thus, may develop our understanding of HTT as a neuroprotective protein.

1.2.3. HTT fragments- Huntingtin exon 1 (HTTex1)

In HD patients and model organisms, there exists a variety of truncated forms of the HTT protein, which differ in size and toxicity. These truncations can occur at both the N-terminal and C-terminal ends of the full-length HTT protein [216]. Among these N-terminal HTT fragments, comprising the N17 and polyQ domains alongside other variable domains, have been extensively studied (***Figure 5***). These fragments are primarily generated through two main mechanisms: proteolytic cleavage and alternative splicing.

Proteolytic cleavage of full-length HTT has been observed through the action of caspases 3, 1, 6, and 2 at specific amino acid sites, and this process is dependent on the length of the polyQ tract [217–220]. Additionally, calpain cleavage has been identified at four distinct sites within the N-terminus of HTT (aa 437, 465/469, 536/540, and between aa 63-111), with its efficiency also being influenced by the polyQ length [221,222]. Research has also established aspartic endopeptidases can produce additional N-terminal HTT fragments [223]. Recently, fourteen different isoforms of N-terminal fragments were identified, ranging from 250 kDa to 50 kDa, in HTT knock-in mouse models, with the smallest being HTTex1 [173]. HTTex1, comprising of the N17 and polyQ domains, is notably absent in WT controls [173]. Any cleavage generating N-terminal fragments also generates corresponding C-terminal fragments, although research on the latter remains limited [181,203,224]. Current evidence suggests that C-terminal fragments impair activity of the microtubule-associated protein dynamin 1, potentially affecting vesicle trafficking and leading to cell death [224].

Alternative splicing represents another mechanism for HTT fragment generation. In the presence of CAG repeat mutations, one of two cryptic polyadenylation signals, located within intron 1 of the *HTT* transcript at positions 2710 and 7327 base pairs (bp), becomes activated. This leads to incomplete splicing of the *HTT* transcript between exon 1 and exon 2, resulting in the production of a small *HTT1a* polyadenylated mRNA that includes exon 1 and the 5' part of intron 1 [135,136]. The extent of alternative splicing is correlated with the length of the CAG repeat, with longer repeats producing more *HTT1a* transcripts [136]. This dependence on CAG repeat length has led to the hypothesis that aberrant splicing may be influenced by the sequestration of spliceosome components at the CAG repeat tract or dysregulation of splicing factor gene expression [225–228]. Recent findings indicate that *HTT1a* transcripts, along with the full-length *HTT* transcript, accumulates in nuclear RNA clusters [137].

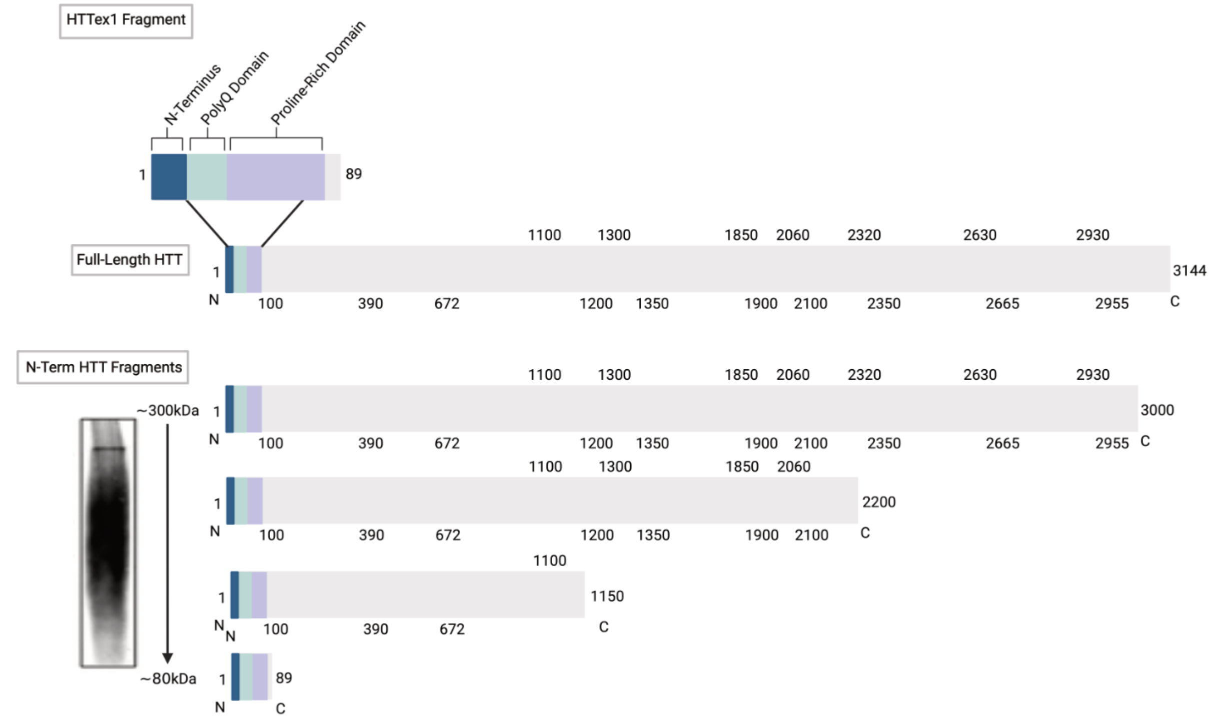

Figure 5. Schematic of HTTex1 and other N-terminal protein fragments of HTT

The HTTex1 fragment is the smallest N terminal fragment of HTT and consists of the initial 17 N terminal amino acids (dark blue), the polyQ domain (light blue) and the proline rich domain (purple). The range of HTT N terminal fragments can present as a smear of potentially soluble or oligomerised HTT protein fragments when separated on 8 % polyacrylamide gels and immunodetection by the 1C2 antibody [229] *(Created using Biorender).*

These clusters are hypothesised to either promote aberrant splicing or acting as a protective mechanism to sequester *HTT1a* transcripts and prevent their translation into HTTex1 protein [137]. It is worth noting that, apart from HTTex1, little is known about the role of alternative splicing in generating other HTT fragments.

Both C-terminal and N-terminal HTT fragments, along with N-terminal mRNAs, have been detected in the brains of HD patients, HD model organisms, and patient-derived cells [135,138,172,223,230]. Early evidence suggested that small N-terminal HTT fragments are present at higher levels in the striatum, the region most sensitive to neurodegeneration in HD (***see section 1.1.4***) [172]. Accumulating evidence now indicates that the smallest N-terminal protein fragment, HTTex1, plays a significant role in driving toxicity in HD [136,139,231].

A comparison of seven commonly studied N-terminal HTT fragments revealed that polyQ-expanded mHTTex1 (Q120) is the most toxic, leading to reduced survival, impaired motor function, and increased neurodegeneration at any level of expression [232]. In contrast, HTTex1 with a non-pathogenic polyQ expansion (25Q) has no toxic effect [232]. Furthermore, the R6/2 mouse model expressing the human HTTex1 transgene exhibits the earliest onset and fastest disease progression among HD mouse models [231]. Therefore, supporting the notion of mHTTex1 being the primary toxic HTT protein fragment. Aside from its toxicity, mHTTex1 is also unique among HTT fragments due to its abnormal migration in SDS gels; it migrates slower than larger HTT fragments and at an incorrect molecular weight [232]. This suggests that mHTTex1 forms a distinct SDS-resistant structural conformation, even in its soluble state. Notably, lower levels of soluble mHTTex1 lead to the formation of insoluble structures that are retained in the pockets of SDS gels [232].

These findings underscore mHTTex1 as a uniquely toxic HTT fragment with abnormal biophysical properties compared to other N-terminal HTT fragments. These distinct biophysical properties drastically impact protein folding and drive the formation of cytoplasmic and nuclear aggregates [233,234].

1.3. HTTex1 aggregation- oligomers, fibrils, and inclusion bodies

Neuronal aggregation is a hallmark feature of HD [139,235] and the presence of aggregates correlates with polyQ length and stage of HD [139,236,237]. Post-mortem analysis of HD patient brains found mHTTex1 as well as other N terminal mHTT fragments to be enriched in inclusions [138,139]. Here we outline how mHTTex1 aggregates are formed, their structure, and what distinct species of aggregates exist ranging from oligomers, fibrils, and inclusion bodies (IBs).

1.3.1. Aggregation kinetics

The formation of aggregates is extremely complex, and highly debated. Currently, mHTTex1 aggregation is hypothesised to follow a nucleation-dependant process [144,238] which kinetically proceeds via a lag phase, a primary nucleation event, a growth phase, and a plateau (***Figure 6A***). Each phase is characterised by specific mHTTex1 structural intermediates (***Figure 6B***).

The lag phase is characterised by slow conformational changes which are initiated at the monomeric mHTTex1 level (***Figure 6A and 6B***). As previously mentioned, the mHTTex1 monomer contains the intrinsically disordered polyQ domain which lacks a defined structure (***see sections 1.2.1 and 1.2.3***). As such, in a soluble state the polyQ domain is inclined to adopt a more thermodynamically stable conformation. Solid state NMR studies have highlighted that the expanded polyQ domain of the mHTTex1 monomer intramolecularly collapses, adopting a more stable β-hairpin structure [239,240] (***Figure 6B***). This β-hairpin consists of two anti-parallel polyQ β- strands of the same molecule, which form intramolecular hydrogen bonds and are connected by a β-turn consisting of several glutamine residues [239,240]. Within the lag phase, mHTTex1 monomers reversibly self-associate and interconvert between various oligomeric states such as dimers, trimers, and tetramers (***Figure 6B***) [241].

During the lag phase, the rate limiting step is the formation of an initial “nucleus” which initiates aggregation (***Figure 6A and 6B***). The nucleus is thought to be a low abundance mHTTex1 oligomer, the formation of which is termed the primary nucleation event. The primary nucleation event is initiated by spontaneous oligomerisation of mHTTex1 monomers and is both polyQ length and protein concentration dependant [238]. Subsequently, multiple β-hairpins from different mHTTex1 monomers stack together using inter- and intramolecular interactions to form a more stable β-sheet, flanked by the PRD and N17 domains [242]. Within the β-sheet, β-hairpins stack together at angles ranging from 0° to ±11° creating a tilted β-sheet conformation unique to mHTTex1 [242]. The formation of the β-hairpin structure, and the subsequent formation of a β-sheet is hypothesised to be the critical initiation step of aggregation [144,243,244]. Furthermore, both the PRD and N17 domains have been shown to exert different effects on the β-sheet formation. The N17 domain has been hypothesised to initiate mHTTex1 aggregation by mediating interaction with other N17 domains of mHTTex1 monomers, increasing the local concentration of polyQ and therefore promoting β-sheet formation [144]. In contrast, the PRD has been shown to supress mHTTex1 aggregation, by possibly stabilising the helical conformation of the expanded polyQ domain [245].

The growth phase proceeds quickly whereby long planar β-sheets recruit more β-hairpin-containing mHTTex1 monomers to their exposed terminal β-strands, thereby increasing in length (***Figure 6A and 6B***). Additionally, a maximum of nine β-sheets laterally associate via interdigitating hydrogen bonds between the glutamine side chains to form filaments [246]. The tight β-sheet core is further stabilised by intra- and inter-sheet side chain and backbone hydrogen bonds [239,246]. Expansion of the polyQ domain increases the surface area of the β-sheet core, thus promoting stronger lateral bonds between sheets and higher order bundling to form amyloid fibrils [242,246–248]. Amyloid fibrils have a distinct cross- β structure, formed by β-sheets running parallel to the fibril axis and β- strands running perpendicular to the fibril axis. The mHTTex1 amyloid fibrils form a “bottle brush” like structure, with the polyQ domain forming a β-sheet core region which is surrounded by the protruding bristle-like PRDs [249,250]. Elongation and branching of these fibrils also occurs through secondary nucleation. Secondary nucleation is driven by preformed aggregation intermediates, also known as “seeds”. These seeds can break off from existing fibrils and either template new fibril formation or instigate branching of existing fibrils – overall speeding up the aggregation process and resulting in the formation of large complex fibril bundles [246,251,252].

Finally, a plateau phase is detectable in *in vitro* models of mHTTex1 aggregation. Within an *in vitro* system there is a limited amount of mHTTex1 monomers, which are depleted by incorporation into higher order fibrils. Thereby resulting in no available monomers to potentiate further aggregation. A similar phenomenon may occur *in vivo*, whereby the mHTTex1 amyloid fibrils act as thermodynamic sinks, depleting available monomers which are being constantly produced by the protein synthesis machinery of the cell. Interestingly, depletion of soluble mHTTex1 in *in vivo* HD models correlates with the increase of large SDS stable HTTex1 structures [173,232].

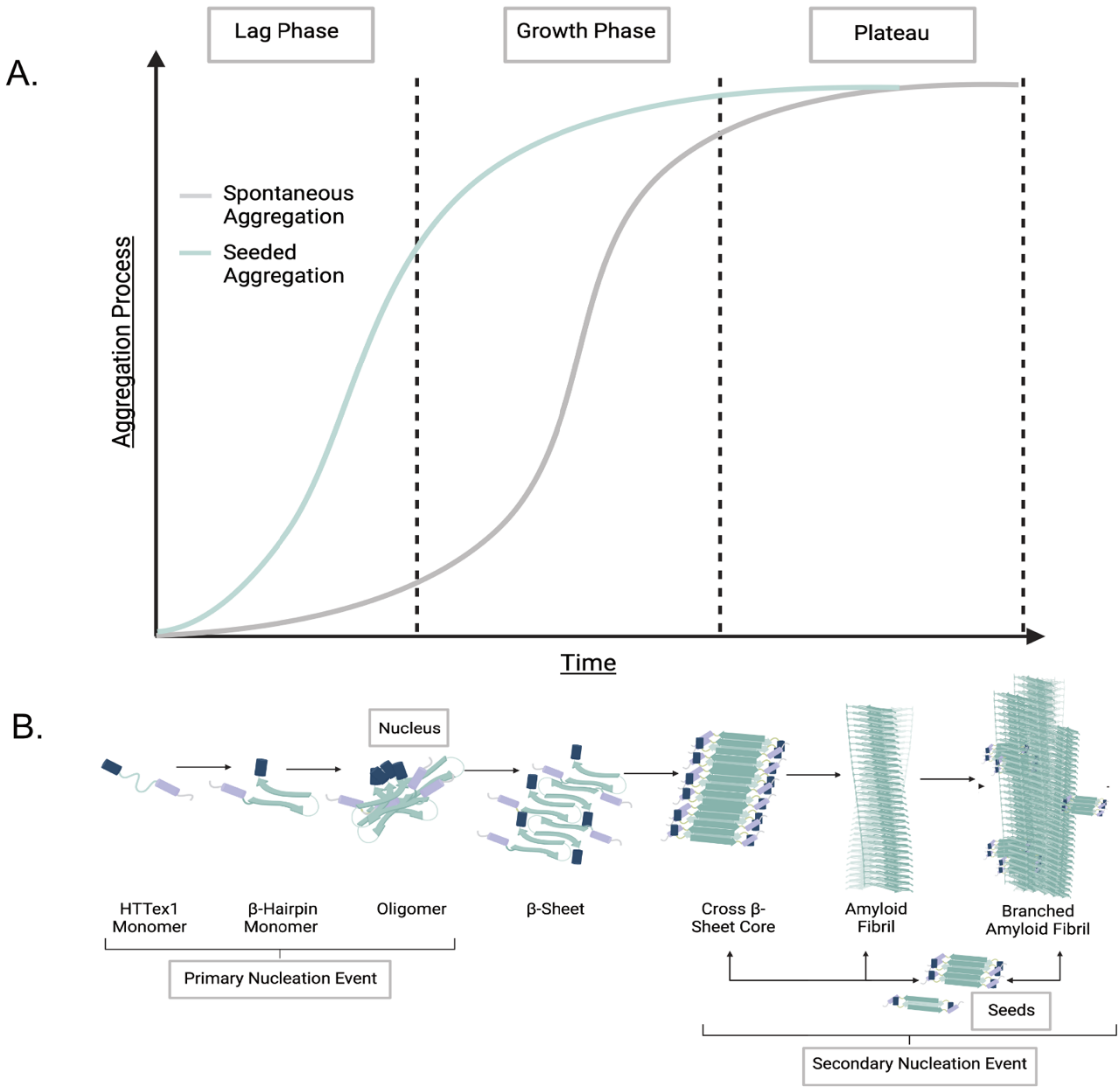

Figure 6. The aggregation kinetics of HTTex1

A) *Schematic of the sigmoidal aggregation kinetics curve of HTTex1, illustrating spontaneous aggregation with lag, growth, and plateau phases. Seeded aggregation, initiated by small aggregated HTTex1 forms (seeds), accelerates aggregation kinetics by templating the formation of an ordered aggregate structure.* ***B)*** *Illustration of theoretical HTTex1 protein structures during corresponding aggregation phases: Soluble HTTex1 monomers undergo slow conformational changes, forming β-hairpin structures that self-associate into oligomers, marking the primary nucleation event. Multiple oligomers with β-hairpin structures form a stable β-sheet, and interactions between β-sheets create the cross- β core of an amyloid fibril. Maturing fibrils can laterally associate to form branched structures. HTTex1 seeds template fibril elongation and further aggregation through secondary nucleation. Inspired by* [144,253,254] *and Anne Ast's Doctoral Thesis, 2018, unpublished. Created using Biorender.*

1.3.2. Defining aggregates and aggregate species

As mentioned above, mHTTex1 aggregation proceeds through a series of distinct intermediate structures: monomers, small oligomers (dimers, trimers, and tetramers), β-sheet containing filaments and amyloid fibrils. Crucially, the term "aggregate" is broad and often used ambiguously in the literature, leading to confusion. To provide clarity, in this work an aggregate is defined, at minimum, as the self-assembly of two or more monomers of the same protein into a supra-molecular structure. Consequently, aggregates can range from dimers to small pre-fibrillar oligomers and large branched amyloid fibrils. In addition to these aggregate species, that are generally formed of many monomers of the same protein like HTTex1, IBs have been observed in HD patient brains and model systems that contain a large number of different mostly insoluble proteins [255] (***Figure 7***). Each of these mHTTex1 aggregate species exhibit distinct properties, existing in varying degrees of solubility, size, and stability within either the cytoplasm or nucleus of cells [256,257].

Non-pathogenic HTTex1 primarily exists in a monomeric state, whereas pathogenic polyQ expansions result in the absence of detectable mHTTex1 monomers. Instead, the expanded mHTTex1 self assembles into oligomers consisting of dimers, trimers, or tetramers [258] (***Figure 7***). The formation of these small soluble oligomers is more prevalent with HTTex1 proteins that contain very short, non-pathogenic polyQ lengths (<Q8), whereas longer polyQ lengths lead to faster oligomerisation and subsequent fibril nucleation [259]. Soluble mHTTex1 oligomers are hypothesised to exist *in vivo* in oligomeric pools, the size of which inversely correlates with the formation of insoluble aggregates in HD mice [260]. Larger sedimentable oligomers, which can be detected by HTT antibodies, exhibit morphological heterogeneity, with *in vivo* oligomers having spherical or annular morphologies [261,262]. These larger oligomers can resist SDS treatment, appearing as a smear on SDS-PAGE gels above the expected monomeric size [263]. Importantly, the presence of insoluble oligomers precedes the detection of IBs and the onset of HD symptoms in various HD models [260,264,265]. Thus, it is reasonable to assume the existence of a rapidly interconverting, heterogeneous population of soluble, sedimentable pre-fibrillar oligomers and fibrillar structures within HD cells. The conversion from a pre-fibrillar oligomeric state to an insoluble fibrillar state can be considered the rate-limiting step in mHTTex1 aggregation reactions, with oligomers serving

as precursors to amyloid fibrils and IBs in cells [262,266]. It is essential to recognise that oligomers are ephemeral in nature: they are rapidly formed and then transition into higher-order structures, making a thorough analysis of their properties challenging [262].

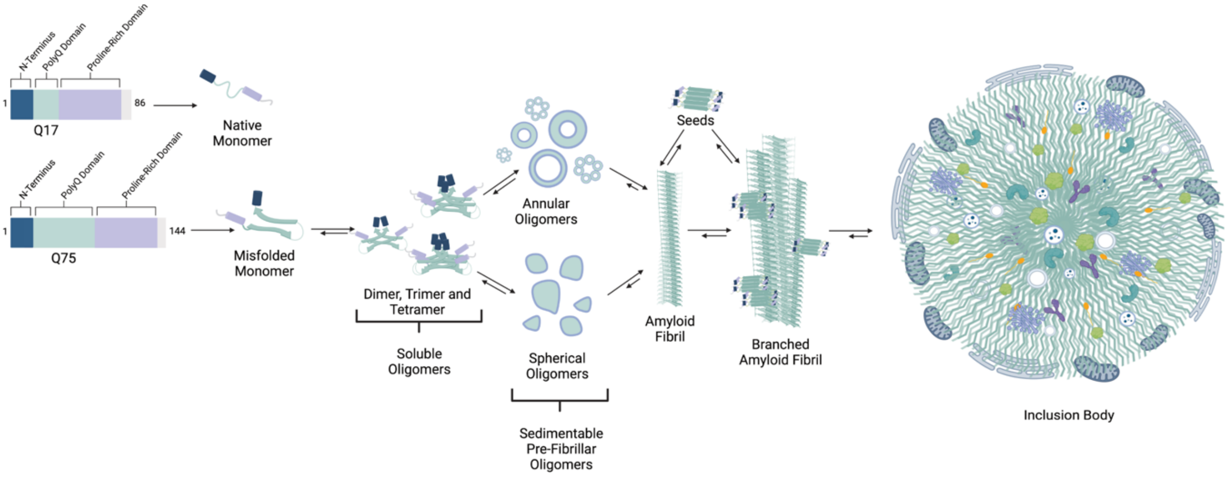

Figure 7. Pathogenic HTTex1 adopts multiple aggregation intermediates

Non-pathogenic expansion (Q17) results in a stable native monomer, while pathogenic polyQ expansion (Q75) produces a low-abundance misfolded monomer. Misfolded monomers preferentially co-aggregate to form small soluble oligomers (dimers, trimers, and tetramers). Soluble oligomers self-associate, accumulating into larger, sedimentable, and non-sedimentable pre-fibrillar and fibrillar oligomers with diverse morphologies. A structural transition to an ordered β sheet conformation promotes amyloid fibril formation. Oligomers can directly accumulate on the fibril, causing branching and elongation. Seeds also bind to monomers , driving a self-propagating aggregation mechanism. Amyloid fibrils co-aggregate with other species and cellular components to form large inclusion bodies. At any moment, various HTTex1 aggregate species with distinct structures, sizes, and stabilities coexist within the cell. The interconversion between aggregate species becomes less energetically favourable with increasing aggregate size and stability (arrows). (Adapted in part from [262]and created using Biorender).

Like oligomers, mHTTex1 fibrils also exhibit heterogeneity, allowing mHTTex1 aggregation to manifest in various fibril types. This heterogeneity arises from the tilted stacking orientations within the fibril core, a unique feature of mHTTex1 fibrils when compared to other amyloid fibrils [242]. Furthermore, fibrils can laterally associate with monomers causing secondary nucleation and branching, resulting in polymorphic fibril species (**Figure 7**). *In vitro* studies initially revealed that temperature directly influences the structure and subsequent toxicity of mHTTex1 fibrils [267,268]. Fibrils grown at 4 °C (T-fibrils) displayed a nonbundled structure with higher flexibility in the PRD, while fibrils grown at 37°C (N-fibrils) exhibited a thicker, bundled structure with a less flexible PRD. The dissociation of T- and N-fibrils gave rise to smaller protofibrils (P-fibrils), which were shown to act as seeds, initiating monomeric mHTTex1 aggregation. Importantly, all three fibril subtypes were found to be interconvertible [269]. Small seeding-competent fibril structures resembling P-fibrils have been identified *in vivo* in HD mouse and *Drosophila Melanogaster (D. melanogaster)* models, preceding the onset of HD symptoms [253,270,271]. Similar seeding-competent structures have also been found in HD patient brains, with seeding activity positively correlating with disease progression[253,272].

In the nucleus and cytoplasm, large mHTTex1 fibrils can co-aggregate to form distinct types of IBs (***Figure 7***). Cytoplasmic IBs have a skeletal structure consisting of a dense fibrillar core, resistant to protease and detergent treatment [273,274]. This core is believed to form through a polyQ-dependent liquid-to-solid phase transition, driven by interactions between the polyQ and PRD regions of mHTTex1, increasing the local concentration of mHTTex1 to the critical level required for phase separation [275]. Lipids, intracellular vesicles, and other mHTTex1 aggregate species become entrapped within and around the IB core [266,276,277]. Additionally, cytoplasmic IBs sequester transcriptional regulators, molecular chaperones, components of the unfolded protein response (UPS) and autophagolysosomal pathways [278,279]. An outer shell of mHTTex1 fibrils surrounds the core and associates with critical cellular components such as mitochondria and the endoplasmic reticulum network (ER) [276,280–282]. In contrast, nuclear IBs exhibit a different morphology characterised by a fibril- dense round shape with an absence of membranes, organelles, or vesicles inside or at the periphery [276]. Cells with nuclear inclusions display altered nuclear ultrastructure, including changes in nuclear condensation, membrane structure, and pore density [276,283]. IBs, predominantly composed of mHTTex1, have been identified in the cortex and striatum of post-mortem brains from HD patients, as well as in animal and cell models [135,138,282]. Typically, IBs are detected before the onset of clinical symptoms in HD [237] and increase in density in a polyQ-dependent manner [284]. Patients with juvenile-onset HD tend to have more nuclear IBs, while adult-onset HD patients typically exhibit cytoplasmic IBs [237,284,285], suggesting that IB localisation may impact HD pathogenesis. However, the formation of IBs does not consistently correlate with HD symptoms and proteotoxicity [253,286]. Consequently, mHTTex1 IBs appear to play contradictory roles within the cell.

It is important to remember the cell is not a closed system. Multiple polymorphic types of oligomers and fibrils can co-exist within the same crowded environment [257]. These diverse aggregate species interact and co -aggregate forming larger IB assemblies which associate with an array of proteins in difference cellular compartments and neuronal subtypes. As a result, dissecting the precise role of each aggregate species in HD pathology is challenging. Therefore, the collective pathogenic impact of aggregates needs to be further clarified in depth.

1.4. Molecular pathogenesis of HD

Although research on HD has been ongoing for centuries, the true pathogenic mechanism underlying HD remains inconclusive. As described previously, HD is caused by a CAG repeat expansion in the HTT gene, which is translated into a polyQ expansion of the HTT protein (***see sections 1.1.2 and 1.2.1***). Current research proposes two contrasting perspectives on the pathogenesis of HD: one highlighting a toxic gain-of-function due to the polyQ expansion in the HTT protein or CAG expansion in the HTT transcript, and the other suggesting a loss-of-function effect resulting from altered wtHTT function.

The prevailing theory attributes HD pathogenesis to a toxic gain-of-function, initiated by expansion of the polyQ domain. It is important to note that HD is one of nine inherited neurodegenerative diseases stemming from polyQ expansions [287]. These include six spinocerebellar Ataxias (SCAs) (SCA1, SCA2, SCA3/Machado-Joseph disease, SCA6, SCA7, and SCA17), spinal and bulbar muscle atrophy (SBMA), and dentatorubral-pallidoluysian atrophy (DRLPA). Despite the polyQ expansion occurring in functionally distinct proteins, these nine polyQ diseases share many features. These include genetic inheritance, adult-onset disease manifestation, primary central nervous system degeneration, and the presence of mutant polyQ-containing protein aggregates [288,289]. Strikingly, a common thread among all polyQ diseases is the direct correlation between the length of CAG repeats and the age of disease onset [288,289]. Longer CAG repeats lead to earlier disease onset, strongly implicating CAG repeat expansion and subsequent polyQ expansion as the driver of a toxic gain-of-function mechanism.

Contrary to the gain-of-function theory, there is a body of evidence suggesting a significant contribution of wtHTT loss-of-function to HD pathogenesis. Previous studies involving HTT knockdowns and knockouts have emphasised the essential role of wtHTT in normal cellular function. For instance, HTT knockdown in mice results in embryonic lethality [168–170]. Additionally, wtHTT plays a pivotal role in mediating interactions with a diverse array of proteins and functions as a structural scaffold for the assembly of multiple protein complexes involved in crucial cellular processes [181–185]. As such, a loss of normal wtHTT function may also significantly contribute to the pathogenesis of HD.

The impact of CAG repeat expansion on HD pathogenesis is undoubtedly complex. CAG repeat expansion results in the production of the truncated HTT1a transcript, which translate to into a monomeric mHTTex1 protein [135,136]. Additionally, polyQ- dependant cleavage of full length HTT can also form other small protein fragments [173] (***see section 1.2.3***). These fragments can form oligomers, fibrils and eventually co-aggregate along with organelles, vesicles, and other subcellular structures into large IBs (***see section 1.3.2***) [256,257]. Thus, CAG repeat expansion results in the formation of different types of potentially pathogenic molecules: RNA transcripts, soluble HTT proteins, and aggregates [135,136]. Therefore, to unravel how CAG repeat expansion leads to the vast neurodegeneration observed in HD patients, we must first address how each form of HTT may contribute to HD pathogenesis.

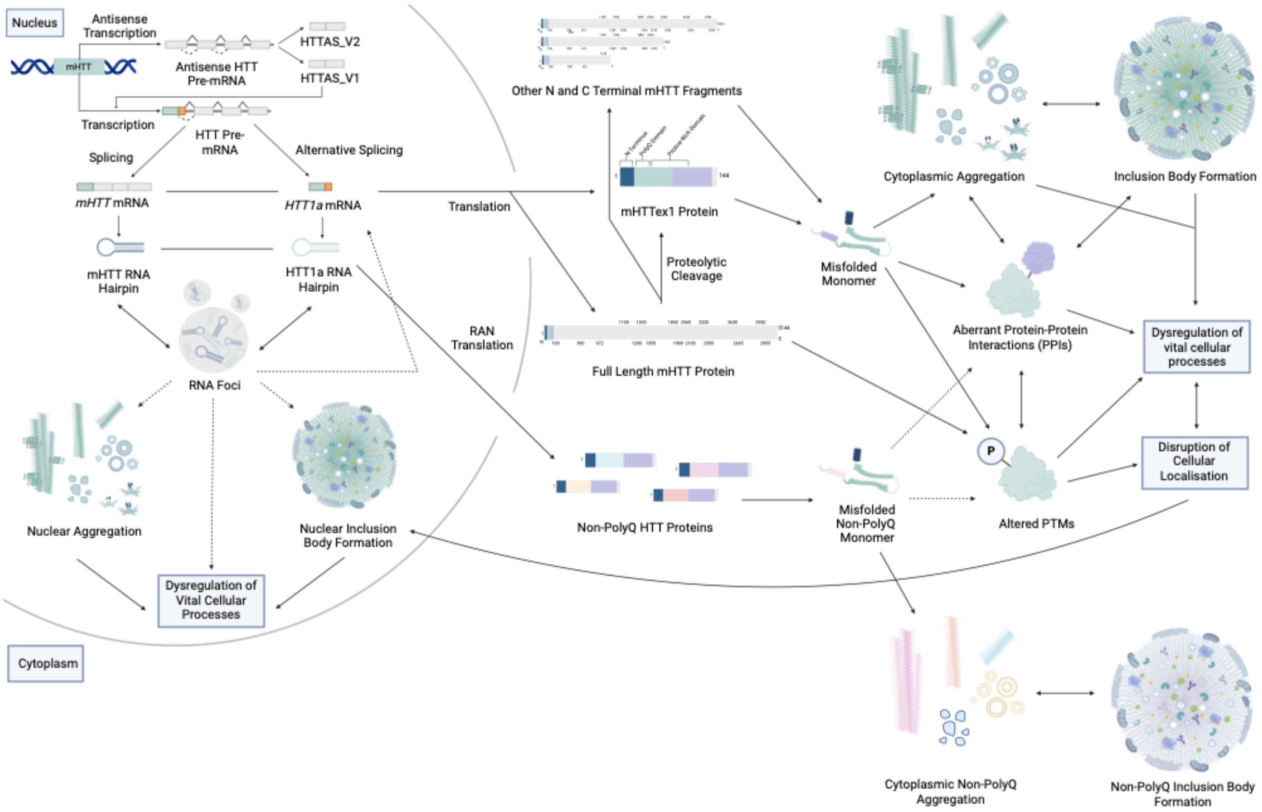

Figure 8. Mechanisms of molecular pathogenesis in HD

A schematic depicting the evidenced (solid arrow line) and hypothesised (dotted arrow line) RNA, protein, and aggregate-mediated mechanism of toxicity in HD. In the nucleus, CAG repeat expansion of the HTT gene (mHTT) can promote anti-sense transcription which generates non-coding RNAs (HTTAS_V1 and HTTAS_V2), inhibiting HTT expression. Canonical transcription produces HTT pre-mRNA, spliced into mHTT mRNA or HTT1a mRNA. Both transcripts form hairpin RNA structures, accumulating in nuclear RNA foci, hypothesised to promote nuclear aggregation and inclusion body formation, disrupting cellular processes. RNAi foci may serve as hubs for alternative splicing which may potentiate the formation of HTT1a transcripts. Both mHTT and HTT1a transcripts are translated into their respective proteins. In the cytoplasm, full-length mHTT protein undergoes proteolytic cleavage, generating N-terminal HTT and other fragments. Full-length mHTT with a polyQ tract can undergo altered post-translational modifications, disrupting cellular localization and function. mHTTex1 protein forms misfolded monomers, co-aggregating into higher order aggregates and inclusion bodies. These aggregates undergo altered post-translational modifications, interacting or sequestering proteins and organelles, disrupting cellular function. RAN translation produces non-polyQ HTT proteins (polyAla, polySer, polyLeu, polyCys), contributing to HD pathology through misfolding and co-aggregation (inspired by[19,216] *and created using Biorender).*

1.4.1. RNA-mediated toxicity

To understand the role of RNA-mediated toxicity in HD, we can draw valuable insights from other CAG repeat disorders. A prime example is spinocerebellar ataxia type 12 (SCA12), an inherited neurodegenerative disease caused by CAG repeat expansion in the 5' untranslated region (UTR) of the protein phosphatase 2A gene (PPP2R2B) [290]. Unlike polyQ diseases, this CAG expansion leads to the transcription of a CAG-containing mRNA but does not result in the translation of a polyQ-expanded protein. Nevertheless, patients with SCA12 exhibit neuronal atrophy and motor symptoms [291]. Expanding upon this, studies involving transgenic model organisms expressing transcripts with extended CAG repeats in the 3' UTR show the development of pathogenic features even in the absence of detectable polyQ-expanded proteins [292,293]. Collectively, these results indicate that CAG expansion in RNA alone is sufficient to induce toxicity.

One proposed explanation for this RNA-mediated toxicity lies in the alteration of RNA structure induced by CAG repeats (***Figure 8***). This leads to abnormal folding of the mutated RNA into a hairpin motif, facilitated by hydrogen bonds between G- and C- bases on opposing strands. Consequently, both the stability and accessibility of RNA are affected in a CAG repeat-dependent manner [225,294,295]. Such RNA hairpin structures are observed in *mHTT* transcripts and accumulate in nuclear RNA foci through aberrant RNA-protein interactions [295]. These *mHTT* RNA foci are known to sequester muscleblind 1 (MBNL1), a crucial regulator of alternative splicing, resulting in mRNA splicing dysregulation [295]. Importantly, as mentioned earlier, evidence from HD mice shows that RNA foci consist of both alternatively spliced *HTT1a* RNA and full-length *HTT* RNA [137] (***see section 1.2.3***). Therefore, RNA foci could potentially act as hubs for alternative splicing, promoting the formation of *HTT1a* transcripts that, in turn, translate into the highly toxic HTTex1 protein [137]. Conversely, it is worth noting that RNA foci might also serve as a protective mechanism by sequestering *HTT1a* transcripts, preventing the expression of the toxic HTTex1 protein [137].

In addition to polyQ-encoding *HTT* mRNA, other forms of HTT associated RNAs exist within the cell due to antisense transcription (***Figure 8***). In HD, an antisense *HTT* transcript is generated which can be alternatively spliced into two short non-coding RNAs (*HTTAS_v1* and *HTTAS_v2*) [296,297]. Overexpression of the *HTTAS_v1* transcript has been shown to inhibit HTT expression, and CAG repeat expansion reduces *HTTAS_v1* expression, consequently increasing HTT levels [296]. These findings collectively provide compelling evidence that HD could indeed originate from the toxic gain-of-function of the CAG repeat length at the RNA level.

1.4.2. Soluble protein mediated toxicity

Earlier, we established HTT as an essential protein which is extensively modified and scaffolds key protein assemblies to conduct vital cellular functions (***see section 1.2.2***). Therefore, any alterations in HTT interaction, localisation or structure will impact HTT function, contributing to cellular toxicity and disease. At the soluble protein level, polyQ expansion leads to 1) aberrant PPIs, 2) alterations in post-translational modifications, and 3) the generation of smaller HTT fragments. These effects are intricately interconnected, with changes in one process directly impacting the others, collectively contributing to the cellular dysfunction underlying HD (***Figure 8***).

Aberrant interactors are proteins which interact with mHTT and not wtHTT (***Figure 8***). Structurally polyQ expansion inherently promotes aberrant PPIs, as it elongates the intrinsically disordered polyQ domain of HTT. This in turn encourages the interaction of mHTT with other IDR- containing proteins [298,299]. Specifically, expansion of the polyQ domain has been shown to induce mHTT interaction with proteins involved in mitochondrial function and RNA processing, processes known to be affected in HD [298,300]. Additional to promoting aberrant PPIs, the expanded polyQ domain has been shown to also abnormally stabilise wtHTT interactions [301,302]. One example is polyQ expanded HTT interacts with its binding partner huntingtin-associated protein 1 (HAP1) stronger than wtHTT [301], which dysregulates downstream autophagy and receptor trafficking critical for neuronal function[303]. Therefore, the polyQ dependant gain of aberrant interactions and modulation of wtHTT interactions could be a key instigator of HD.

One mechanism by which the polyQ domain modulates mHTT interactions is through the alteration of PTMs (***Figure 8***). The polyQ domain resides within the PEST 1 domain [174], which is a key site for PTMs (***see section 1.2.2***). In mice expressing mHTT, an increase in PEST 1 phosphorylation (at serine 1181 and 1201) and a decrease in acetylation (at lysine 919, 1204 and 1246) was observed, which directly impacted mHTT subcellular localisation when compared to WT mice [304]. Furthermore, expansions of the polyQ domain have been shown to directly reduce HTT's interaction with the huntingtin interacting protein 14 (HIP14), reducing HIP14-mediated mHTT palmitoylation and increasing neurotoxicity [305]. Thus, directly linking alterations in PPIs with changes in PTMs and subsequent HD pathogenesis.

Proteolytic cleavage is another key PTM of HTT, which produces N terminal HTT fragments that have been consistently detected in human HD brains and HD mouse models [172,173,306] (***Figure 8***). These N terminal fragments have been shown to be sufficient to induce neurotoxicity [231] and inhibition of HTT cleavage drastically reduces the toxicity of mHTT [307–309]. Therefore, the increase of proteolytic cleavage in HD and the association of N terminal fragments with increased toxicity strongly implicates the generation of small HTT fragments as a key event in HD. Collectively, the gain of aberrant PPIs or modulation of wtHTT interactions effects a broad range of downstream cellular processes which can lead to the neuronal dysfunction observed in HD. Additionally, polyQ driven alterations in PTMs can produce small, toxic mHTT fragments and alter the localisation of mHTT. At the protein level the toxic gain-of-function of the polyQ tract is a key instigator of cellular dysfunction, considerably driving molecular pathogenesis in HD.

The complexity of HD pathology is further compounded by antisense repeat associated non-ATG (RAN) translation proteins (***Figure 8***). RAN translation, a mechanism initiated by secondary RNA structures, can produce proteins without the need for an AUG start codon on the mRNA [310]. This can shift the reading frame at CAG repeats, resulting in translation of polyalanine (polyAla), polyserine (polySer), polyleucine (polyLeu), and polycystine (polyCys) tracts [311]. The production of RAN translation proteins is CAG length dependant, with longer CAG repeats promoting the formation of RAN translation proteins [311,312]. In HD, RAN translation products have been detected in the brains of patients, aggregating in the most affected regions, such as the caudate and putamen [311]. Contradicting research has both implicated [311] and refuted [313] RAN translation products as contributors to HD pathology. Future efforts focusing on the precise physiological levels of RAN translation proteins, and their corresponding effects on molecular mechanisms will be key to understanding the broader impact of RAN translation in HD.

In summary, CAG repeat expansion and the accompanying polyQ expansion induce changes at both the RNA and soluble protein levels. These changes in *mHTT* RNA structure coupled with alterations in mHTT PTMs, PPIs and size directly impact mHTT function. While a definitive single molecular mechanism that serves as the primary driver of HD remains elusive, it is evident that the pathology of HD is a complex process. Mitochondrial function, transcription, intracellular trafficking, and proteostasis are all significantly impaired in the disease [303,314]. These interconnected pathways collectively contribute to the cellular dysfunction observed in HD. However, whether HD pathogenesis is primarily driven at the RNA or protein level remains to be conclusively determined.

1.4.3. The role of aggregates – protective or toxic?

Aggregates have long been regarded as a hallmark feature of HD (***see section 1.3***), yet the debate over their role in inducing toxicity remains complex and contentious. This debate extends not only within the HD research community but also resonates in the broader context of neurodegenerative diseases. The core of this debate hinges on the subjective definition of what qualifies as an aggregate. Earlier, aggregates were defined as the self-assembly of two or more monomers of the same protein into a supra-molecular structure. (***see section 1.3.2***). Consequently, our definition encompasses a wide spectrum of molecules, ranging from dimers to small pre-fibrillar oligomers and extensive branched amyloid fibrils.

In dissecting the toxicity of aggregates, it is essential to distinguish aggregates from IBs. Although mHTT IBs have a fibrillar aggregate core, they associate with other proteins to form large visible puncta within the cell (***see section 1.3.2***). Early research into HD identified IBs within the nucleus, cytoplasm, and neuronal processes of HD patient neurons [255]. IBs were found to precede the onset of HD symptoms and neuronal atrophy [315], and were thought to be the predominant form of misfolded mHTT. Additionally, the incidence of IBs increased proportionally with CAG repeat length [236]. Thus, leading to the traditional view that these large structures must cause HD. Subsequent research reinforced this hypothesis, revealing that IBs sequester crucial proteins such as molecular chaperones, ubiquitin proteasome proteins, transcription factors, and RNA binding proteins [316], leading to a widespread loss of cellular function. Moreover, IBs were found to disrupt the nuclear, ER, Golgi and mitochondrial membranes [276,317,318]. Thereby, impacting organelle organisation and downstream processes such as transcription, proteostasis, vesicular trafficking and metabolism [317,319].

Paradoxically, IBs have been more frequently observed in the cerebral cortex than the striatum, where severe atrophy is observed in advanced HD patients[237,320]. When identified in the striatum, IBs have been found in interneurons instead of the more atrophy– prone medium spiny neurons [321]. The presence of IBs in neurons that are relatively spared from neurodegeneration contradicts the notion that IBs are the cause of HD, instead suggesting they may confer a protective effect [322]. In support of this concept, studies using neuronal HD models have highlighted that neurons can die without the detection of IBs. Instead, IB formation appears to enhance neuronal survival by reducing the availability of soluble mHTT within the neuron [323]. Furthermore, highly pathogenic N-terminal HTT protein fragments have been identified as a key component of the IBs found in HD patient brains [135,138,324], indicating IBs may reduce the available mHTT fragments within the neuron as a protective response [323,325]. Additional research indicated that presence of IBs does not always correlate with HD pathogenesis [237,325,326], strongly suggesting that IBs are not the main toxic species in HD[320,327]. Thus, it becomes evident that the role of IBs in HD is nuanced. Initially serving as a protective buffer for toxic mHTTex1 aggregates, IBs later develop into structures that sequester various proteins and organelles, leading to the disruption of essential cellular processes.

Crucially, disruptions in cellular processes occur prior to the observable formation of IBs. Research findings indicate that alterations in transcription factor pathways [328,329] and impediments in neuronal processes such as axonal transport [330,331] precede IB formation.

Thus, indicating that before visible IBs form, smaller mHTT aggregate species already instigate detrimental cellular effects. Building upon this, analysis of the structure of IBs further reveals the presence of vesicles, organelles, and lipids sequestered within the fibrillar IB core [276]. This suggests that smaller mHTT aggregate species sequester key cellular components prior to IB development. Consequently, the origin point of HD pathogenesis may be traced back to the beginning of IB formation, possibly at the aggregate level.

As outlined previously, mHTT aggregation is a multi-step process populated by intermediate species: misfolded monomers, oligomers, and fibrils (***see sections 1.3.1 and 1.3.2***). While it is apparent mHTT aggregates exert a toxic effect in various model systems [231,] the extent to which each aggregate species individually contributes to HD pathogenesis remains unclear. Recent evidence has pointed to small, seeding-competent mHTT structures as robust markers of HD phenotypes, which exhibit a stronger correlation with HD pathogenesis than IBs [257]. Furthermore, research utilising yeast models has emphasised mHTT oligomers as potent templates for aggregation, which are required for toxicity [332]. This toxic role of oligomers is further supported by the observation that cells harbouring mHTT oligomers experience faster cell death compared to those with IBs or monomers [264]. With increasing size and stability, the toxic effect of mHTT aggregates decreases, suggesting that smaller aggregate species are the main driver of toxicity in HD [333,334,419]. Nevertheless, elucidating the specific structural characteristics of these small oligomeric intermediates responsible for HD toxicity remains challenging due to current scientific limitations [257,335]. It is also plausible that a single, specific species is not the primary driver of HD. Rather, an abnormal mHTT fold, mediated by the expanded polyQ domain, may act as a "toxic surface" inherently attracting other molecules [320]. In doing so, this toxic surface could catalyse further aggregation and perpetuate toxicity through interactions with an increasing array of proteins and organelles within the cell.

In conclusion, revisiting the question—Are aggregates toxic? Based on the evidence reviewed, it is clear that aggregates inherently possess toxicity (***Figure 8***). However, discerning the specific species responsible for the highest toxicity remains a challenge, primarily due to experimental limitations in identifying and distinguishing various oligomers and small pre-fibrillar aggregates. Furthermore, the question of whether aggregate-mediated toxicity is the primary driver of HD remains unanswered. The potential influence of RNA and perturbations in soluble protein dynamics cannot be entirely dismissed (***see sections 1.4.1 and 1.4.2***) (***Figure 8***). Thus, additional research on the role of aggregates in HD should prioritise the establishment of *in vivo* models, allowing for the monitoring of mHTT aggregation within its native context and elucidating its relationship with RNA and monomeric protein changes.

2. Aims

In HD, neuronal mHTTex1 aggregates are a consistent and defining pathological feature. However, the precise relationship between mHTTex1 aggregation and the development of HD pathology remains incompletely understood. Emerging evidence also suggests that RNA and monomeric protein alterations play pivotal roles in driving toxicity in HD. To gain a comprehensive understanding of the causal mechanisms underpinning HD pathology, it is imperative to explore the influence of aggregates on RNA and protein dynamics in an *in vivo* context.

Therefore, the primary aim of this research project was to establish a novel *D. melanogaster* model to explore the impact of mHTTex1 aggregates on the proteomic, cellular, and phenotypic *in vivo* landscape. To achieve this, a construct was designed which enables the co-expression of HTTex1 mNeongreen (HTTex1-mNG) and HTTex1 mScarlet-I (HTTex1-mSc-I) fusion proteins independently within the same model system, with the goal of leveraging Förster resonance energy transfer (FRET) to determine whether mHTTex1 aggregates can be visualised within *D. melanogaster* neurons. Moreover, this work aimed to uncover whether FRET can be used as a selection marker for live cells containing HTTex1-mNG/-mSc-I aggregates and whether the presence of such aggregates relates to any phenotypic effects in the model.

The second aim of this project was to employ the newly developed *in vivo D. melanogaster* model to investigate how aggregates impact RNA and protein mechanisms within the cell. To achieve this aim, both isolated mHTTex1 aggregates and whole brain samples were analysed using mass spectrometry (MS). Thus, enabling the profiling of proteins that are associated with aggregates and the identification of global proteome dysregulation in fly model brains.

Finally, the third aim was to functionally interrogate the role dysregulated proteins may play in HD, using RNA interference (RNAi) knockdown experiments conducted *in vivo*. The effects of RNAi knockdown were assessed through a combination of phenotypic and biochemical assays, to provide insights into the impact of proteins dysregulated in the presence of mHTTex1 aggregates on HD phenotypes. By addressing these aims, potential mechanisms underlying toxicity in HD are intended to be uncovered, thereby enhancing our understanding of the role mHTTex1 aggregation plays in HD pathology.

3. Results

3.1. FRET as a technique to study mHTTex1 aggregation *in vitro* and *in vivo*

The mHTTex1 protein is known to form aggregates, and such aggregates are a pathological hallmark of HD (***see section 1.3***). Understanding the role of mHTTex1 aggregates in HD necessitates a comprehensive examination of their neuronal distribution, associated proteins, and broader proteomic consequences. Therefore, investigation of mHTTex1 aggregation requires a method that provides a clear, easily detectable readout and is compatible with both *in vitro* and *in vivo* systems.

While previous studies have used mHTTex1 fused to single fluorophores to visualise mHTTex1 aggregation [276,336,337], this approach has presented limitations. A single fluorophore can generate a fluorescent signal for both soluble and aggregated mHTTex1. Hence, relying on a single fluorescence signal alone does not enable accurate differentiation between these two protein states. Therefore, studies must turn to techniques such as fluorescence recovery after photo-bleaching (FRAP), electron microscopy (EM) or co-localisation analysis to infer mHTTex1 aggregation. A way to combat the restrictions of single fluorophore mHTTex1 aggregate detection is to employ Förster resonance energy transfer (FRET), a technique relying on the distance-dependent transfer of energy between two fluorophores with overlapping emission and excitation spectra [338] (***Figure 9A***). When proteins tagged with FRET compatible fluorophores are soluble, the fluorescence of both the donor and acceptor molecules can be measured, with minimal background FRET. However, when such proteins co-aggregate, the donor and acceptor fluorophores come into proximity. Subsequent excitation of the donor fluorophore causes energy to be transferred to the acceptor fluorophore via intermolecular long-range dipole-dipole coupling. Therefore, resulting in FRET which can be measured as a quenching of the donor fluorescence and an increase in the acceptor fluorescence [338,339] (***Figure 9B***).

To provide an alternative method to monitor mHTTex1 aggregation free from the aforementioned limitations, the first aim of this work was to create a FRET-based HTTex1 aggregation biosensor which would be compatible with both *in vitro* and *in vivo* model systems (***Figure 9C***).

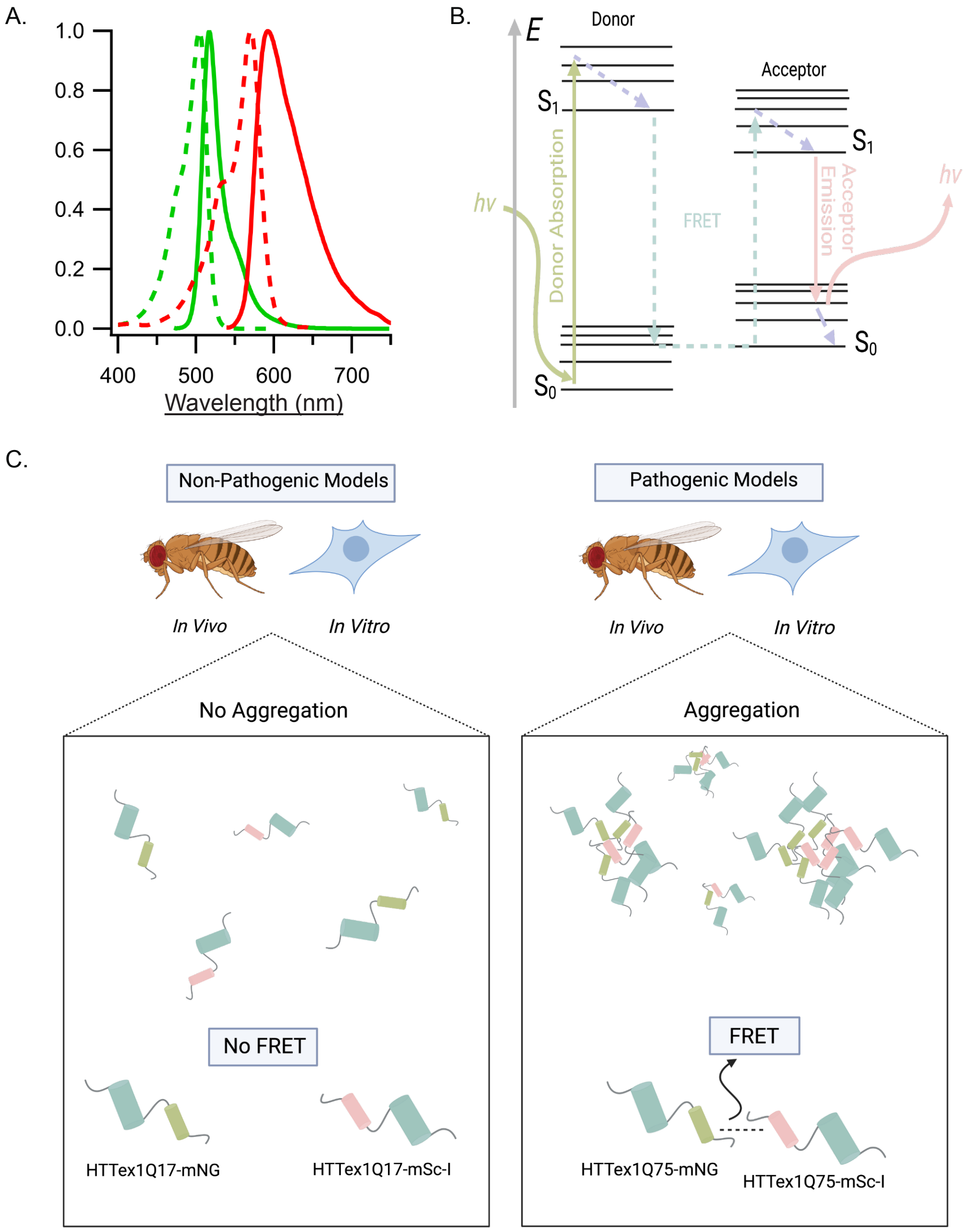

Figure 9. FRET principles and using FRET to model mHTTex1 aggregation

A) *A schematic showing the absorbance (dashed lines) and emission spectra (solid lines) of mNG (green) and mSc-I (red)* [340] ***B)*** *A Jablonski diagram showing how FRET occurs between two fluorophores. Absorption of a photon by the donor fluorophore (mNG) causes an electron to be excited from ground state (S_0) to a higher energetic state (S_1). This excited state is unstable, and the electron relaxes back to ground state. The energy released from the relaxation of the donor fluorophore electron is transferred via FRET, causing excitation of an* *electron of the acceptor fluorophore (mSc-I). When the acceptor electron relaxes back to ground state, this causes the emission of acceptor fluorescence rather than the donor fluorescence. Adapted from* [341] *and created using Biorender.* ***C)*** *A schematic showing how FRET can be used to model mHTTex1 aggregation both in vitro and in vivo. Upon co-expression of non-pathogenic HTTex1Q17-mNG and HTTex1Q17-mSc-I fusion proteins, FRET does not occur as the fusion proteins have a very low propensity to aggregate. Whereas co-expression of pathogenic HTTex1Q75-mNG and HTTex1Q75-mSc-I fusion proteins would result in aggregation which brings both the donor and acceptor fluorophores into close proximity, therefore enabling FRET. Created using Biorender.*

3.2. An *in vitro* mHTTex1 FRET-based aggregation sensor model

3.2.1. Designing a novel mHTTex1 FRET- based aggregation sensor with mNeongreen (mNG) and mScarlet-I (mSc-I) HTTex1 fusion proteins

The first step in creating an *in vivo* and *in vitro* compatible FRET-based HTTex1 aggregation biosensor was to create a custom plasmid to facilitate the co-expression of two copies of HTTex1 proteins either fused the next generation fluorophores mNeongreen (mNG) or mScarlet-I (mSc-I) within the same model system (***Figure 10A***).

Each plasmid consisted of one copy of HTTex1 coding sequence with either 17, 52 or 75 glutamines (HTTex1Q17, HTTex1Q52 and HTTex1Q75) fused C-terminally to a mNG coding sequence followed by a C-myc sequence, to enable the expression of HTTex1-mNG FRET donor fusion proteins with a C-myc epitope tag. The C-myc epitope tag was incorporated as a control tag which could be used for detection of the HTTex1-mNG fusion proteins, in the event detection of the mNG protein was not possible. A second copy of the HTTex1Q17, HTTex1Q52 and HTTex1Q75 coding sequences was subsequently cloned into the corresponding HTTex1-mNG plasmids. These coding sequences were fused C-terminally to a mSc-I coding sequence followed by a V5 sequence, to facilitate the expression of HTTex1-mSc-I FRET acceptor fusion proteins with a V5 epitope tag. Like the inclusion of the C-myc tag for the HTTex1-mNG fusion proteins, the V5 tag was included to act as a control method of detecting the HTTex1-mSc-I fusion proteins. Thus, the resulting HTTex1-mNG/-mSc-I plasmids were designed to enable the independent co-expression of both HTTex1-mNG and HTTex1-mSc-I fusion proteins from the same construct (pUAST-HTTex1Q17-mNG/-mSc-I, pUAST-HTTex1Q52-mNG/-mSc-I and pUAST-HTTex1Q75-mNG/-mSc-I) (***Figure 10A***).

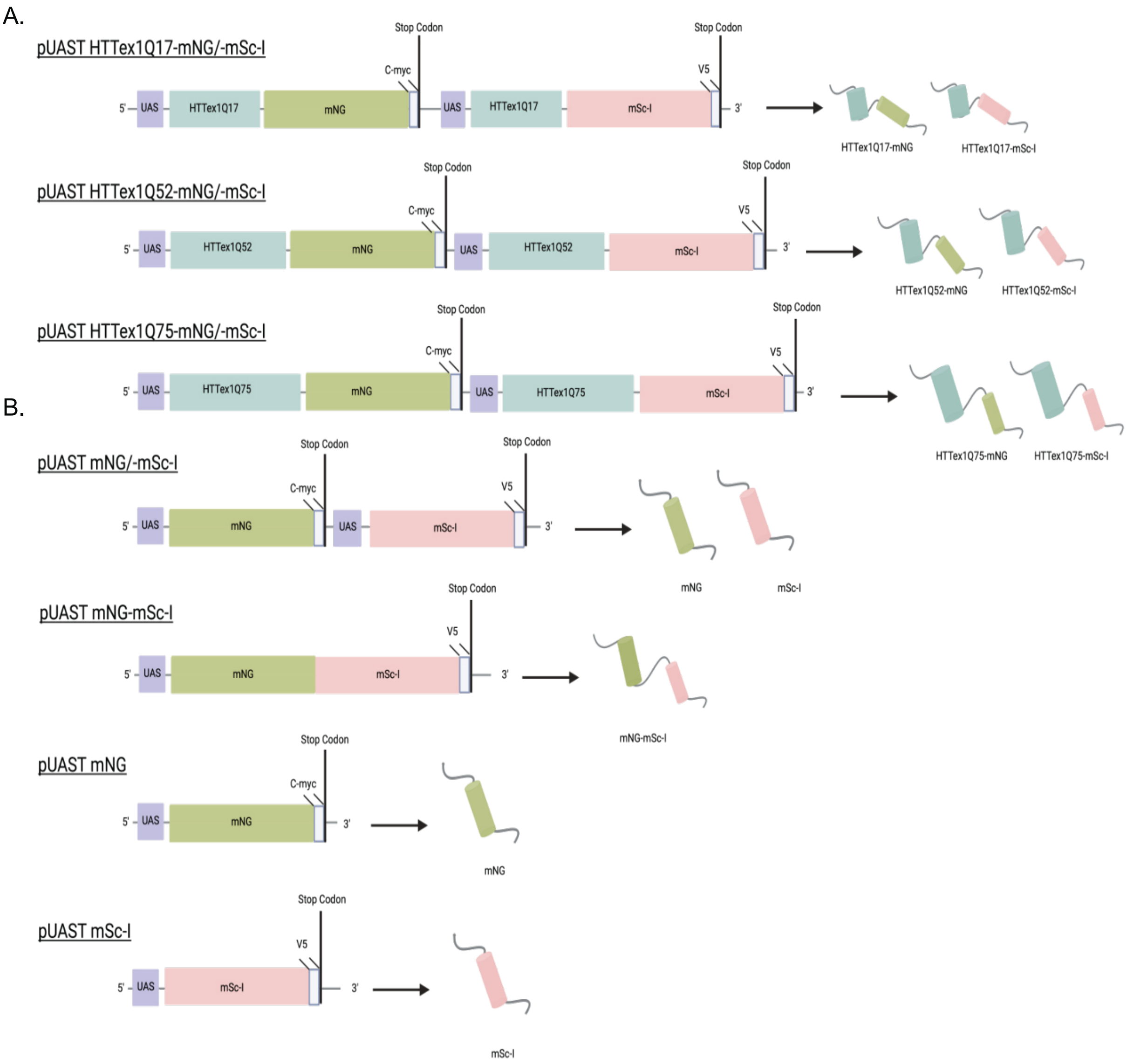

Figure 10. The design of the FRET-based HTTex1 aggregation biosensor constructs

A) *Schematic of the HTTex1Q17-mNG/-mSc-I, HTTex1Q52-mNG/-mSc-I and HTTex1Q75-mNG/-mSc-I constructs and their respective proteins.* ***B)*** *Schematic of the mNG-mSc-I (FRET positive), mNG/-mSc-I (FRET negative), mNG and mSc-I constructs and their respective proteins. Created in Biorender.*

For FRET measurement, it was essential to have single fluorophore controls as well as FRET positive and FRET negative controls to allow accurate detection of FRET generated from HTTex1 fusion protein co-aggregation. Therefore, plasmids were created which would enable the expression of both mNG and mSc-I proteins individually (pUAST-mNG and pUAST-mSc-I), independently from the same plasmid (pUAST-mNG/-mSc-I) and as fusion protein (pUAST-mNG-mSc-I). These plasmids served as single fluorophore, FRET negative and FRET positive controls respectively (***Figure 10B***). All final plasmids (***Supplementary Table 1***) were subject to analytical digestion and sanger sequencing to confirm their sequence identity (***Supplementary Figure 1E and 1H***).

3.2.2. Pathogenic HTTex1-mNG/-mSc-I fusion proteins co-aggregate and cause FRET *in vitro*

Previous work using mHTTex1 protein fragments conjugated to FRET compatible fluorophores has shown FRET to be a reliable measure of amyloidogenic mHTTex1 aggregate formation [257]. Hence, it was hypothesised that co-aggregation of pathogenically expanded mHTTex1-mNG and mHTTex1-mSc-I fusion proteins (HTTex1Q52-mNG/-mSc-I and HTTex1Q75-mNG/-mSc-I) would bring the mNG and mSc-I fluorophores into proximity, which should generate a FRET signal corresponding to mHTTex1 aggregate formation (***Figure 9C***). To assess whether the co-expression of HTTex1-mNG/-mSc-I fusion proteins indeed resulted in a detectable FRET signal upon HTTex1-mNG/-mSc-I co-aggregation, a HEK293 cell model was first employed.

To induce the co-expression of the HTTex1-mNG/-mSc-I fusion proteins from their respective pUAST vectors (***Figure 10A and Supplementary Table 1***), the yeast transcription activator protein GAL-4 must be expressed from the pCMV-GAL4 vector and bind to the UAS sequences upstream of the transgene [342].Therefore, HEK 293 cells were co-transfected with pUAST-HTTex1-mNG/-mSc-I vectors and a titration of pCMV-GAL4, to determine the optimal amount of pCMV-GAL4 necessary for HTTex1-mNG/-mSc-I fusion protein co-expression. Subsequent western blot (WB) analysis was performed using the anti-HTT antibody MAB5492 (***Figure 11A***), anti-C-myc antibody to detect HTTex1-mNG (***Supplementary Figure 2B***) and anti-mCherry to detect HTTex1-mSc-I (***Supplementary Figure 2A***). Distinct bands were observed slightly above the expected molecular weight for HTTex1Q17-mNG/mSc-I, HTTex1Q52-mNG/-mSc-I and HTTex1Q75-mNG/-mSc-I across all blots (expected molecular weight: ~45kDa, ~49kDa and ~51kDa, observed molecular weight: ~48kDa, ~50kDa and ~60kDa respectively). This discrepancy in observed versus predicted molecular weight of HTTex1 has been previously identified and is due to the polyQ repeat domain decreasing protein mobility therefore causing slower migration through SDS-PAGE gels [343].

Furthermore, the immunodetection of the corresponding protein bands using both the anti-C-myc and anti-mCherry antibodies confirmed the independent co-expression of both HTTex1-mNG and HTTex1-mSc-I fusion proteins in transfected cells (***Supplementary Figure 2A and 2B***). Upon closer analysis, a decrease in band size with increasing polyQ length was observed, which indicated a higher abundance of HTTex1Q17-mNG/-mSc-I fusion protein in comparison to HTTex1Q52-mNG/-mSc-I or HTTex1Q75-mNG/-mSc-I fusion proteins. Such bands were absent in the 0µg pCMV-GAL4 and mNG-mSc-I co-expressing control samples, which validated the observed bands were due to HTTex1-mNG/-mSc-I fusion proteins only (***Figure 11A***).

The mHTTex1 protein has been shown to form aggregates in both *in vivo* and *in vitro* models of HD [343]. However, there is evidence that the presence of fluorescent tags may alter mHTTex1 aggregation [276]. Therefore, after WB confirmation of soluble HTTex1-mNG/-mSc-I fusion protein co-expression it was vital to investigate whether these fusion proteins were able to aggregate *in vitro*. To this end, cell lysates were analysed using a denaturing filter retardation assay (dFRA). This technique involves applying heat and SDS-denatured lysate onto a cellulose acetate membrane. After vacuum filtration, the soluble denatured protein passes through the membrane pores, but the large SDS-stable structures are retained on the membrane and can be identified using immunodetection. Therefore, the dFRA enables specific detection of large, SDS-stable mHTTex1 aggregates [344]. Cells co-expressing HTTex1Q75-mNG/-mSc-I fusion proteins were found to harbour large, SDS-stable mHTTex1 structures which were not present in HTTex1Q17-mNG/-mSc-I co-expressing cells (***Figure 11B***). To investigate the morphology of these mHTTex1-mNG-/mSc-I aggregates, cells were analysed using confocal microscopy. Cells co-expressing HTTex1Q52-mNG/-mSc-I and HTTex1Q75-mNG/-mSc-I fusion proteins exhibited large puncta. In contrast, such puncta were absent in HTTex1Q17-mNG/-mSc-I co-expressing cells, therefore suggesting these structures may be co-aggregated mHTTex1-mNG/-mSc-I fusion proteins (***Figure 11C***).

To qualitatively determine whether the co-aggregation of mHTTex1-mNG/-mSc-I fusion proteins resulted in FRET, transfected HEK293 cells were assessed using confocal microscopy (***Supplementary Figure 3A***). To detect FRET, samples were excited with a laser corresponding to the mNG excitation wavelength (490nm) and emission was detected in range corresponding to mSc-I emission (580-630nm), thereby enabling qualitative detection of FRET positive structures. The large puncta observed in HTTex1Q52-mNG/-mSc-l and HTTex1Q75-mNG/-mSc-l co-expressing cells were strongly FRET positive, which suggests the puncta were the result of HTTex1-mNG/-mSc-I fusion protein co-aggregation.

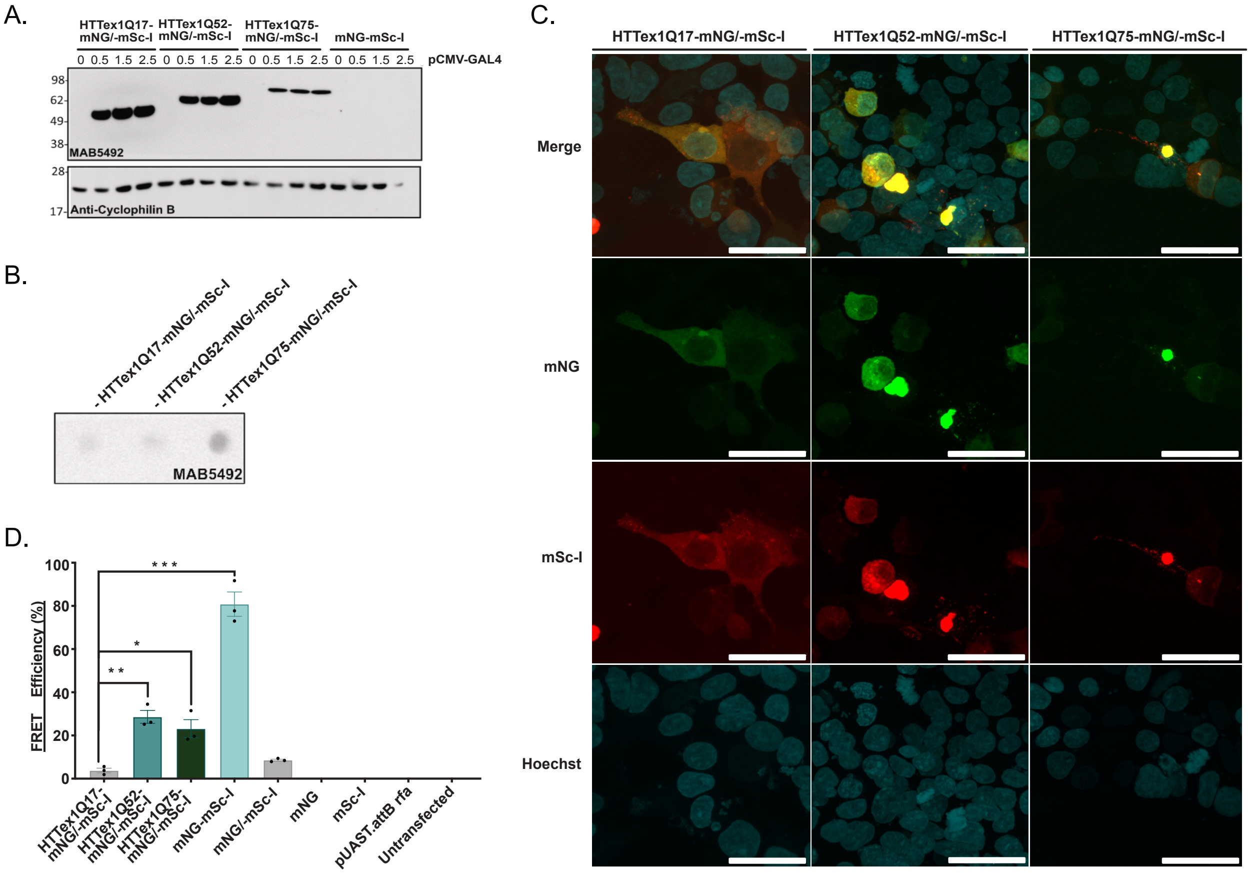

Figure 11. HTTex1-mNG/-mSc-I fusion proteins aggregate generate FRET in vitro

A) *WB analysis of the HTTex1-mNG/-mSc-I fusion protein in HEK293 cell lysates derived from cells co-transfected with 0, 0.5, 1.5 and 2.5 µg of pCMV-GAL4 plasmid and 1.5µg of pUAST-HTTex1-mNG/-mSc-I plasmids. Anti-HTT a.a 1-10 (MAB5492) antibody and Anti-cyclophilin B were used for immunodetection.* ***B)*** *dFRA analysis of SDS-stable HTT structures in cell lysates. 80 µg protein loaded per dot. Anti-HTT a.a 1-10 (MAB5492) antibody used for immunodetection.* ***C)*** *Confocal images of HEK293 cells co-transfected with 7.5 µg pCMV-GAL4 and 4.5µg respective pUAST-HTTex1-mNG/-mSc-I plasmids. Scale bar=25 µm.* ***D)*** *FRET efficiency of pUAST-HTTex1-mNG/-mSc-I transfected HEK293 cells. Each dot represents a separate biological replicate (3 per group). Statistical significance assessed by unpaired T-test. (**= P<0.01, ***=P<0.001). Error bars= SEM*

In contrast, a diffuse weaker FRET signal distributed throughout the cytoplasm was present in HTTex1Q17-mNG/-mSc-I and mNG/-mSc-I co-producing cells. Thus, supporting the hypothesis HTTex1 fusion proteins with non-pathogenic polyQ tracts have a low aggregation propensity. As a control, cells expressing the mNG-mSc-I FRET positive control fusion protein were analysed and showed a uniformly distributed FRET signal (***Supplementary Figure 3A***). Therefore, collectively these results indicated the observed puncta were the result of mHTTex1-mNG/-mSc-I fusion protein co-aggregation.

Previous work has shown mHTTex1 aggregates possess an amyloid-like structure [238]. Therefore, to investigate whether the observed puncta were in fact co-aggregated HTTex1-mNG/-mSc-I fusion proteins, transfected HEK293 cells were stained with Amytracker 480; a fluorescent tracer molecule which emits light in the blue spectra range (excitation maximum = 420nm, emission maximum = 480nm) when bound to amyloid fibrils, protofibrils and protein aggregates [345,346] (***Supplementary Figure 2D***). The puncta in cells co-expressing HTTex1Q52-mNG/-mSc-I and HTTex1Q75-mNG/-mSc-I fusion proteins were positive for Amytracker 480 signal (***Supplementary Figure 2C***). Therefore, confirming the observed puncta were amyloid-like structures, consistent with previous descriptions of mHTTex1 aggregates.

Finally, to assess whether the co-aggregation of mHTTex1-mNG/-mSc-I fusion proteins into amyloid-like aggregates resulted in quantitative FRET, the FRET efficiency of transfected HEK293 cells was calculated using plate reader-based sensitised emission measurements (***Figure 11D***). As a FRET positive control, cells expressing the mNG-mSc-I fusion protein were analysed which exhibited a high mean FRET efficiency (80.8%), indicating that the mNG-mSc-I fusion is a bright and well performing FRET donor/acceptor pair. For the FRET negative controls, cells co-expressing mNG and mSc-I (mNG/-mSc-I), as well as those independently expressing the single fluorophores mNG or mSc-I were analysed. These displayed low mean FRET efficiencies (8.6%, -110.7% and -0.1% respectively), suggesting little background FRET from either fluorophore. As a background control, untransfected cells and cells transfected with the empty pUAST-attB-rFA plasmid were also analysed, which likewise showed low mean FRET efficiencies (-113.2% and -42.5% respectively). Overall, it was confirmed by these control experiments that FRET detection required mNG and mSc-I co-expression and for both fluorophores to be in proximity.

Importantly, both HTTex1Q52-mNG/-mSc-I and HTTex1Q75-mNG/-mSc-I co-expressing cells exhibited a significant increase in mean FRET efficiency (28.6% and 23.1% respectively) when compared to that of HTTex1Q17-mNG/-mSc-I co-expressing cells (3.8%), confirming FRET measurements can be used to infer the co-aggregation of pathogenically expanded HTTex1Q52-mNG/-mSc-I and HTTex1Q75-mNG/-mSc-I fusion proteins. Thus, supporting the functionality of the FRET-based HTTex1 aggregation biosensor for *in vitro.*

3.2.3. Development of a FRET-based fluorescence-activated cell sorting (FACS) method for isolation of HTTex1-aggregate containing cells

After confirming pathogenically expanded mHTTex1-mNG/-mSc-I fusion proteins co-aggregated and form FRET positive puncta, it was clear FRET signals can be used to visualise mHTTex1-mNG/-mSc-I co-aggregates. Expanding on these results, it was postulated that FRET may also be used as a selection marker for the enrichment of cells containing HTTex1-mNG/-mSc-I co-aggregates. To investigate this hypothesis, transfected HEK293 cells were taken forward for fluorescence activated cell sorting (FACS). To enable detection of FRET in cells, a previously published sequential FRET FACS gating strategy was optimised for use with mNG and mSc-I fluorophores [347].

FACS is a flow cytometry base method, in which single cells are separated from a homogenous sample solution into fluid droplets which pass through a laser beam. Depending on the characteristics of the cell i.e. size, granularity and fluorescence, the laser beam light is scattered in a forward or sideward direction (FSC/SSC) [348]. This pattern of scattering can be used to selectively sort and enrich for specific cellular populations.
Cells were first analysed using FSC/SSC, using these gates debris and doublet cells were excluded, therefore only single cells were taken forward for subsequent analysis (***Figure 12A***). To establish the gates corresponding to mNG and mSc-I fluorescence, cells expressing the either mNG or mSc-I fluorophores individually were analysed. A gate was drawn to include mNG events along the X axis and mSc-I events along the Y axis. Using this gating, double positive cells expressing both mNG and mSc-I were detected as events which resided between the X and Y axis (***Figure 12B***). Interestingly, cells co-expressing the non-aggregating HTTex1Q17-mNG/-mSc-I fusion proteins had a larger percentage population

(30.4%) of double positive cells than cells co-expressing the aggregation prone HTTex1Q52-mNG/-mSc-I (24.6%) and HTTex1Q75-mNG/-mSc-I (18.4%) (***Figure 12E***). Therefore, this FACS data further supported the notion that there was a higher abundance of HTTex1Q17-mNG/-mSc-I fusion protein than HTTex1Q52-mNG/-mSc-I and HTTex1Q75-mNG/-mSc-I fusion proteins in co-transfected cells.

Next, to determine what proportion of the double positive cell population were also FRET positive, double positive cells co-expressing mNG and mSc-I individually (mNG/-mSc-I) and as a fusion protein (mNG-mSc-I) were analysed using FRET and mNG fluorescence (***Figure 12C***). The FRET positive mNG-mSc-I control cell population displayed a distinct upward shift in the Y axis in comparison to the FRET negative mNG/-mSc-I control, indicating a higher FRET fluorescence. FRET gates were subsequently drawn based on these FRET positive control events. Upon analysis of HTTex1-mNG/-mSc-I transfected cells, cells co-expressing HTTex1Q52-mNG/-mSc-I or HTTex1Q75-mNG/-mSc-I formed a new sub-population within the FRET gates, which was absent in cells co-expressing HTTex1Q17-mNG/-mSc-I (***Figure 12C***). This sub-population exhibited a higher FRET fluorescence than mNG donor fluorescence, which was comparable to that of the mNG-mSc-I FRET positive control, and therefore were classified as FRET positive.

Subsequent quantification of the FRET-FACS data confirmed cells expressing the mNG-mSc-I fusion exhibited a high mean percentage of FRET positive cells (40.5%). Whereas untransfected cells, as well as cells co-expressing mNG/-mSc-I, mNG and mSc-I had a low mean percentage of FRET positive cells (0%, 1.1%, 0% and 0% respectively), therefore validating that the FRET-FACS approach enabled detection of FRET within cells (***Figure 12F***). Moreover, cells co-expressing HTTex1Q75-mNG/-mSc-I displayed a statistically significant increase in the mean percentage of FRET positive cells (7.035%) when compared to the HTTex1Q17-mNG/-mSc-I co-expressing control (0.845%) (***Figure 12F***). Likewise, HTTex1Q52-mNG/-mSc-I co-expressing cells displayed an increase in the mean percentage of FRET positive cells (2.223%) when compared to HTTex1Q17-mNG/-mSc-I co-expressing control cells (0.845%), however this increase was not found to be statically significant (***Figure 12F***). Regardless, these data pointed toward a polyQ-dependant increase of FRET, which suggested FRET increased relative to the aggregation propensity of the corresponding mHTTex1-mNG/-mSc-I fusion proteins. Indeed, when these FRET positive cells were sorted and imaged using confocal microscopy, large intracellular puncta were present only in cells co-expressing the more aggregation-prone HTTex1Q52-mNG/-mSc-I or HTTex1Q75-mNG/-mSc-I fusion proteins (***Supplementary Figure 3B***), indicating the detected FRET was due to aggregation.

To confirm if FRET was an accurate measure of cells containing mHTTex1-mNG/-mSc-I aggregates, FRET positive cells were further analysed using pulse shape analysis (PuLSA). PuLSA is based on the principle that fluorescent mHTTex1 aggregates display higher pulse heights and narrower pulse widths of fluorescence when analysed using FACS [349,350]. Hence, it was hypothesised that if FRET is indeed an indicator of mHTTex1-mNG/-mSc-I aggregation, it should be possible to similarly use the pulse height and width measurements of FRET fluorescence (FRET-PuLSA) to detect cells containing co-aggregated mHTTex1-mNG/-mSc-I fusion proteins.

FRET- PuLSA analysis of cells co-expressing pathogenic HTTex1-mNG/-mSc-I fusion proteins (HTTe1Q52-mNG/-mSc-I and HTTex1Q75-mNG/-mSc-I) revealed the presence of a new sub population to the left of the main events peak (***Figure 12D***). The cells within this sub-population displayed a higher FRET pulse height and narrower FRET pulse width, therefore were gated as PuLSA positive. Upon quantification, cells co-expressing HTTex1Q75-mNG/-mSc-I exhibited the highest mean percentage of FRET-PuLSA positive cells (5.85%) (***Figure 12G***) followed by HTTex1Q52-mNG/-mSc-I co-expressing cells (1.395%). In contrast, a negligible FRET-PuLSA positive cell population was observed in HTTex1Q17-mNG/-mSc-I, mNG-mSc-I and mNG/-mSc-I co-expressing control cells (0.61%, 1.035% and 0.535% respectively) (***Figure 12G***). Thus, indicating that FRET-PuLSA measurements, like the FRET FACS measurements (***Figure 12F***), followed a polyQ dependant trend whereby the percentage of FRET-PuLSA positive cells increased relative to the aggregation propensity of the HTTex1-mNG/-mSc-I fusion protein.

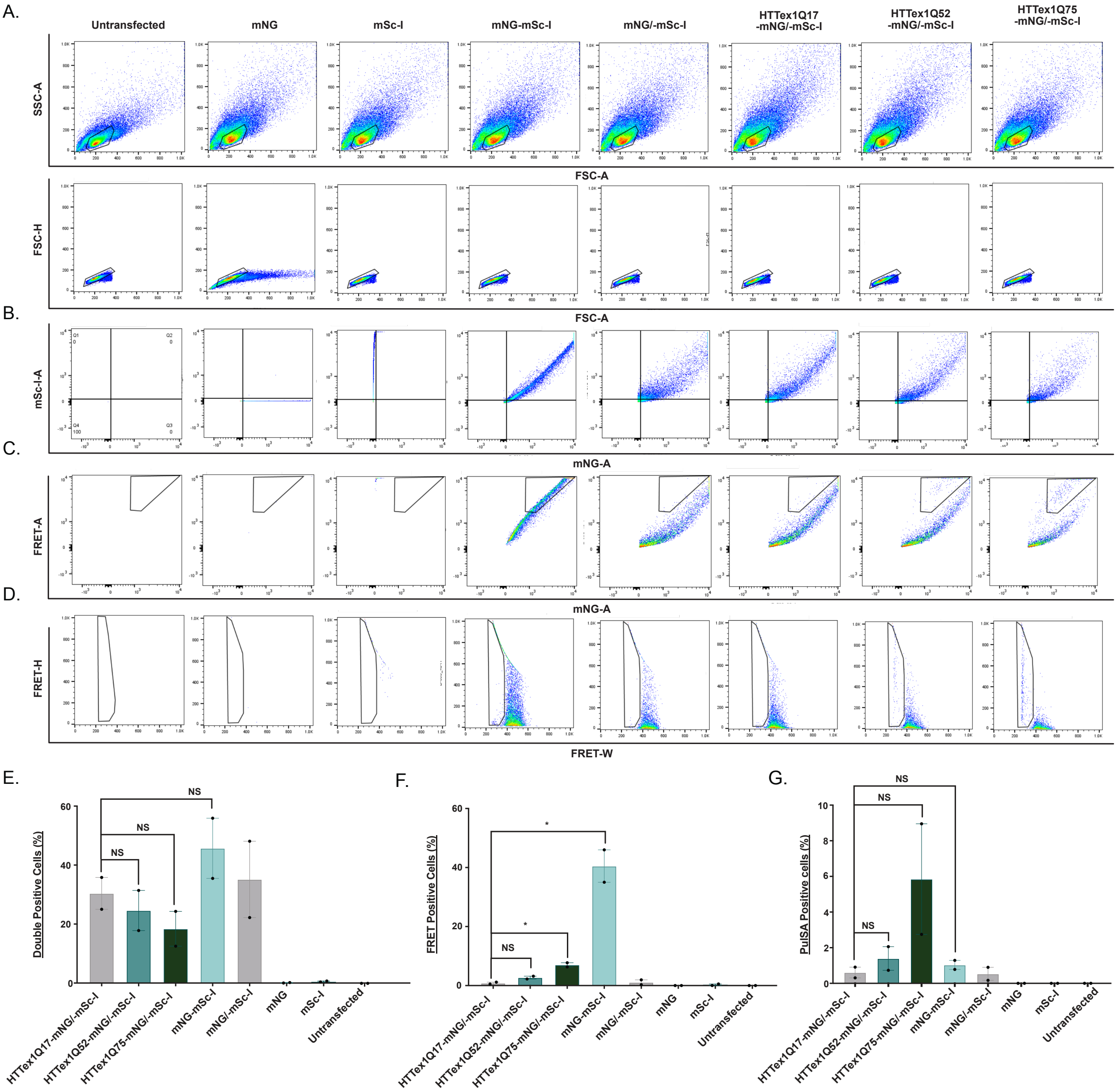

Figure 12. FACS detection of FRET positive mHTTex1 aggregates in HEK293 cells

*FACS cytograms showing**: A)** Debris exclusion (side scatter area (SSC-A) vs forward scatter area (FSC-A) and doublet exclusion (forward scatter height (FSC-H) vs FSC-A). **B)** Double positive gating (mSc-I pulse area (mSc-I A) vs mNG pulse area (mNG-A)), **C)** FRET donor-corrected gating (FRET pulse area (FRET A) vs mNG pulse area (mNG-A)) and **D)** FRET PuLSA gating (FRET-A vs FRET-W). Arbitrary units (a.u.) of exactly 50,000 cells (n=50,000) plotted. Plots depicting: **E)** percentage double positive, **F)** percentage FRET positive, and **G)** percentage FRET PuLSA positive HEK 293 cells from total cell population measured by FACS. Each dot represents a separate biological replicate (2 per group). Statistical significance assessed by unpaired T-test (NS=P>0.05, *=P<0.05). Error bars=SEM.*

Collectively, the detection of FRET using FACS, combined with confocal microscopy and PulSA measurements, strongly indicate that FRET measurements can be used both to specifically detect mHTTex1 aggregation *in vitro* and as a selection marker for cells containing HTTex1 aggregates.

3.3. Establishing an *in vivo* FRET-based aggregation sensor model

3.3.1 Creating transgenic *D. melanogaster* models of mHTTex1 co-aggregation

The results obtained from the HEK293 cells experiments showed pathogenically expanded mHTTex1-mNG/-mSc-I fusion proteins (HTTex1Q52-mNG/-mSc-I and HTTex1Q75-mNG/-mSc-I) can co-aggregate, and this co-aggregation can be detected using FRET. However, this model was limited to detecting mHTTex1-mNG/-mSc-I co-aggregation in an *in vitro* context, and therefore lacked insight into the potentially neurotoxic effects exerted by mHTTex1 aggregates. Therefore, to investigate the relationship between mHTTex1-mNG/-mSc-I co-aggregates and neuronal dysfunction in HD, it was imperative to create a model system which combined the FRET based detection of mHTTex1-mNG/-mSc-I co-aggregation and provided a phenotypic readout of toxicity. To this end, transgenic *D. melanogaster* strains co-expressing HTTex1-mNG/-mSc-I fusion proteins were generated.

To generate such transgenic fly strains, *D. melanogaster* embryos were co-injected with pUAST HTTex1-mNG/-mSc-I, mNG-mSc-I, mNG/-mSc-I, mNG, mSc-I (***Supplementary Table 1***) plasmid DNAs and a site-specific bacteriophage integrase (phiC31). At the time of injection, the embryos exist as one multinucleated cell (syncytium) into which both the plasmid DNA and phiC31 integrase are co-injected at the posterior end. Following subsequent budding and cellularisation, germline precursor cells (pole cells) form at the posterior inject site and accept the injected DNA (***Figure 13A***). The injected embryos harboured a bacteriophage attachment site (attP) at position 68E on chromosome 3 (genotype: yw; M{3xP3-RFP.attP'}ZH-68E). Consequently, within the pole cells the phiC31 integrase mediates B/P recombination between the attB sites within the pUAST plasmids and the complementary 68E chromosome 3 attP docking site. Through this site-specific germ line integration of the transgenic DNA, chromosomal position effects are avoided and as such generated transgenic fly strains can be directly compared. The injected embryo then develops into an adult transgenic fly containing germline integration of corresponding transgenes. Subsequent mating of the transgenic flies with *white* negative (*white*-) flies results in progeny which contain the transgene in all cells. Successful transformant progeny were selected based on the *mini-white* genetic marker, which results in an easily discernible orange eye colour (***Figure 13A***). Transformants were then mated with the balancer strain (CyO/Sp;TM6/MKRS) to create stable transgenic fly lines (CyO/+:TM6/Transgene). In total, 7 new transgenic fly lines were generated: HTTex1Q17-mNG/-mSc-I, HTTex1Q52-mNG/-mSc-I, HTTex1Q75-mNG/-mSc-I, mNG-mSc-I, mNG/-mSc-I, mNG and mSc-I (***Supplementary Table 2***).

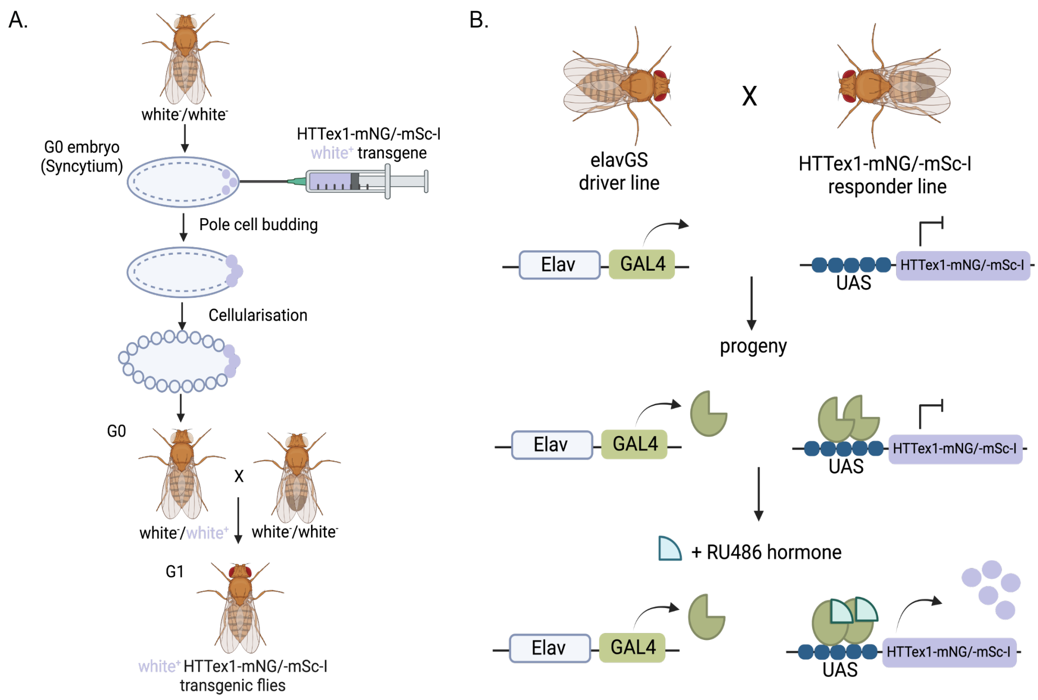

Figure 13. Generating transgenic HTTex1-mNG/-mSc-I flies

A) *Schematic depicting the injection of plasmid DNA into the fly embryo (G0 embryo also known as the syncytium). Adapted from* [351] ***B)*** *Schematic of the elavGS hormone (RU486) inducible system. Adapted from* [352]. *Created using Biorender.*

To confirm the transgenic identity of the 7 newly generated fly strains (***Supplementary Table 2***), genomic DNA was extracted and used as the template for PCR amplification. PCR products of the expected sizes were amplified and visualised via agarose gel electrophoresis (***Supplementary Figure 4A and Supplementary Table 3***). Subsequent sanger sequencing of the PCR amplified fragments confirmed the correct transgenic identity of the newly generated flies.

3.3.2. Temporally controlled co-expression of pathogenic mHTTex1-mNG/mSc-I fusion proteins results in SDS- stable aggregates and neuronal puncta

In generating the transgenic flies, the aim was to create a model system to investigate the phenotypic effects of mHTTex1-mNG/-mSc-I fusion protein co-aggregation, and thus provide insight into the wider effects mHTTex1 aggregates may play in the neurological toxicity observed in HD. The first step in addressing this aim was to drive the independent co-expression of both HTTex1-mNG and HTTex1-mSc-I fusion proteins within the neurons of the transgenic flies.

To achieve this, the GAL4/UAS elavGS inducible system [342] was initially used. As outlined previously (***see section 3.2.1***), the GAL4 protein is a transcriptional activator originally derived from yeast, which binds to UAS sequences and initiates transgene expression [342]. In the elavGS system, the GAL4 DNA binding domain is combined with a steroid hormone receptor transcriptional activation domain. Only when bound to the hormone RU-486 is GAL-4 able to bind the UAS sequence and induce transgene expression [353] (***Figure 13B***). The expression of the hormone inducible GAL4 protein in the elavGS system is under the control of the tissue specific embryonic lethal abnormal vision (elav) promotor. Elav is a vital protein which is pan-neuronally expressed, regulating axon guidance, synapse formation and photoreceptor development in flies [354]. Therefore, when GAL4 is under the control of the elav promoter, it is only expressed in post mitotic neurons, neural progenitor cells and glial cells[354]. To use the elavGS system to control gene expression in flies, two fly strains are required. The first is termed the driver strain, which expresses the hormone-inducible GAL4 pan-neuronally. The second is the responder strain, which contains the transgene under the control of the UAS sequence. In the responder flies, there is no transgene expression, as there is no GAL4 present. When the driver and responder strain are crossed, the resulting progeny both express the hormone inducible GAL4 protein and contain the transgene under the control of the UAS. Upon feeding the progeny with hormone (RU486) infused food, the GAL4 will bind the UAS sequence and drive transgene expression in the neurons of the flies (***Figure 13B***).

Using this system, the responder strains, containing the HTTex1-mNG/-mSc-I, mNG-mSc-I, mNG/-mSc-I, mNG and mSc-I transgenes were mated with the elavGS driver strain. The resulting progeny will herby referred to as elavGS;HTTex1-mNG/-mSc-I, elavGS;mNG-mSc-I, elavGS;mNG/-mSc-I, elavGS-mNG, elavGS-mSc-I. Using the female progeny, three RU486 hormone dosing conditions were applied to assess whether the developmental timing of mHTTex1-mNG/-mSc-I co-expression in neurons influenced the flies. In the first condition, flies were aged for three days and then placed on hormone-infused food for six days, before being placed back onto non-hormone food for the remainder of the experiment, thereby enabling short-term HTTex1-mNG/-mSc-I co-expression (6d-ON/OFF). In the second condition, from the first day post-occlusion flies were placed on hormone-infused food and were maintained on hormone food thought the duration of the experiment which enabled constitutive co-expression of HTTex1-mNG/-mSc-I (ON). In the third condition, flies were never placed onto hormone food and therefore should not co-express HTTex1-mNG/-mSc-I (OFF) (***Figure 14A***).

To analyse whether the elavGS driver tightly controlled HTTex1-mNG/-mSc-I fusion protein co-expression in fly neurons, crude head lysates from ON and OFF flies were analysed by WB. As a negative control, head lysates from driver flies which were treated with hormone (elavGS ON) were analysed using MAB5492, anti-C-myc and anti-mCherry antibodies for immunodetection. Only background, non-specific bands were visible in the subsequent blots, thus validating the specificity of the selected antibodies for HTTex1, mNG and mSc-I proteins respectively. It must be noted however the elavGS OFF control exhibited unequal protein amounts (***Figures 14B, 14C and 14D respectively***), possibly due to the dark red colour of the fly eyes, which may interfere with the colorimetric bicinchoninic acid assay (BCA) assay used to assess protein amount in fly head lysates. As a HTTex1-mNG/-mSc-I negative and C-myc negative control, head lysates from elavGS;mNG-mSc-I ON flies were analysed which showed a band at the predicted size (~60kDa) when probed with the anti-mCherry antibody only, further validating the specificity of the antibodies.

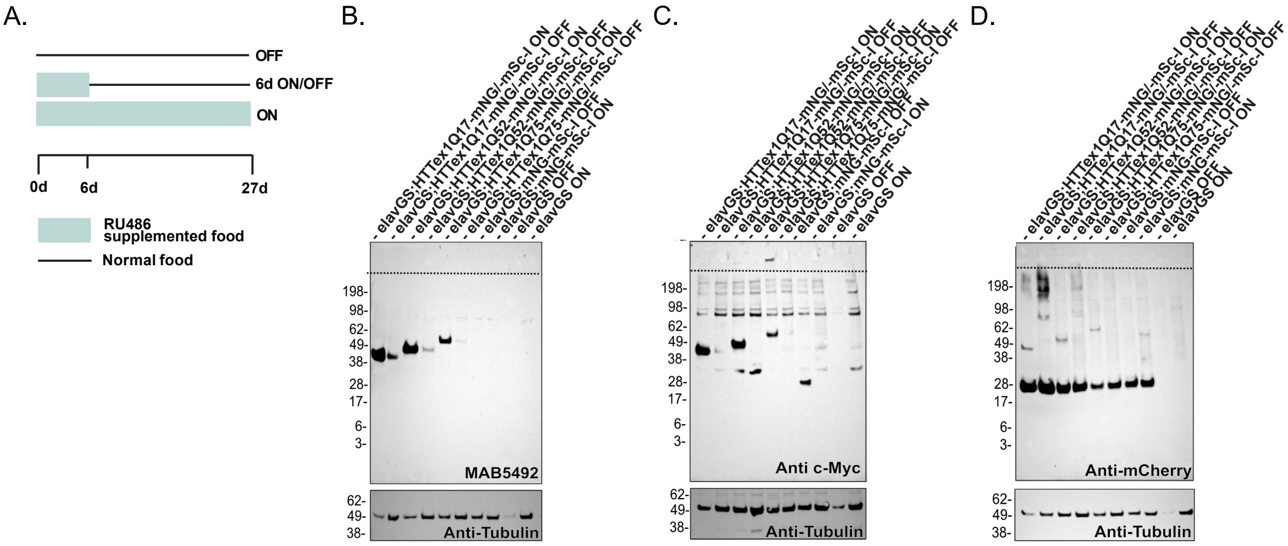

Figure 14. SDS- stable aggregates are formed upon constitutive HTTex1Q75-mNG/-mSc-I co-expression

A) *Schematic of treatment conditions of fly strains with RU486 to temporally control transgene expression. Created using Biorender. WB analysis of the HTTex1-mNG/-mSc-I fusion proteins in head lysate derived from 27-day old flies using* ***B)*** *anti-HTT a.a 1-10 (MAB5492),* ***C)*** *anti c-Myc (to detect HTTex1-mNG-c-myc) and* ***D)*** *Anti-mCherry (to detect HTTex1-mSc-I-V5) antibodies. Gel pockets shown above the dotted line. An anti-tubulin antibody was used as a loading control for immunodetection. 20 µg protein loaded per lane.*

Using MAB5492, anti-C-myc and anti-mCherry antibodies for immuno-detection (***Figures 14B, 14C and 14D respectively***), bands were visible in elavGS;HTTex1-mNG/-mSc-I ON samples corresponding to soluble HTTex1Q17-mNG/-mSc-I, HTTex1Q52-mNG/-mSc-I and HTTex1Q75-mNG/-mSc-I fusion protein expression (~48kDa, ~50kDa and ~60kDa respectively). As was previously found in the HEK293 cell model WB data (***Figure 11A***), the observed bands displayed a higher molecular weight than expected due to the polyQ repeat domain which decreases soluble HTTex1 protein mobility during SDS-PAGE [343]. Surprisingly, when probing with the MAB5492 antibody, bands were also observed in all elavGS;HTTex1-mNG/-mSc-I OFF samples which indicates the expression of HTTex1-mNG/-mSc-I fusion proteins in the absence of GAL4-induced protein expression (***Figure 14B***). Previous work has found similar results with some GAL4-UAS systems exhibiting “leaky expression”, where low-level transcription and translation occur even in the absence of GAL4 expression [355–357]. Interestingly, in elavGS;HTTex1Q75-mNG/-mSc-I ON samples there was a signal visible in the gel pockets when probed with anti-C-myc antibody (***Figure 14C***). This was accompanied with a visible decrease in the soluble HTTex1Q75-mNG/-mSc-I band intensity when compared to elavGS;HTTex1Q17-mNG/-mSc-I ON and elavGS;HTTex1Q52-mNG/-mSc-I ON samples. Protein retention within the gel pocket is characteristic of mHTTex1 aggregates [270], which are resistant to SDS therefore remain too large to pass though the pores of the gel during electrophoresis. Thus, these findings demonstrated that the constitutive expression of HTTex1Q75-mNG/-mSc-I fusion proteins, which resulted in co-aggregation in the HEK293 *in vitro* cell model (***see section 3.2.2***), also may lead to the formation of SDS-stable aggregates *in vivo*.

Subsequent confocal microscopy analysis of 6d ON/OFF, ON and OFF elavGS;HTTex1-mNG/-mSc-I fly brains was performed to investigate whether the SDS-stable mHTTex1-mNG/-mSc-I aggregates could be visualised *in vivo* (***Figure 15A,15B and 15C***). In the brains of all elavGS;HTTex1-mNG/-mSc-I OFF flies there was a noticeable background fluorescence (***Figures 15A, 15B and 15C***). Thus, providing further support to the WB data findings that the elavGS system does not tightly control HTTex1-mNG/-mSc-I fusion protein expression. Interestingly, across all conditions all samples displayed a striking red fluorescence within the optical neurons which was absent in the elavGS controls (***Figure 15A, 15B, 15C and Supplementary Figure 4B***). To eliminate the possibility that this fluorescence was due to mSc-I expression, brains from transgenic flies which express mHTTex1 without a fluorescent tag were also imaged (***Supplementary Figure 4C***). Both elav;HTTex1Q17-V5 and elav;HTTex1Q75-V5 flies expressed HTTex1 without a florescent tag, yet still exhibited the same red fluorescence in the optical neurons. Thus, indicating the observed fluorescence to be a characteristic feature of transgenic fly lines in the lab. Deeper analysis of the genotype of the transgenic flies revealed all were generated from phiC31 integration of transgenes into the yw; M{3xP3-RFP.attP'}ZH-68E strain. This strain contains a red fluorescent protein (RFP) marker controlled by a 3xP3 promoter flanked by LoxP sites, which results in RFP expression in the eyes and ocelli (simple eyes). Therefore, due to retention of the 3xP3-RFP marker, RFP is expressed in all the transgenic strains and was subsequently identified as a distinct band running at ~27kDa on anti-mCherry immunodetected blot (**Figure 14D**). To circumvent this expression of RFP in the eyes, subsequent imaging focused only on the mid-brain of the flies.

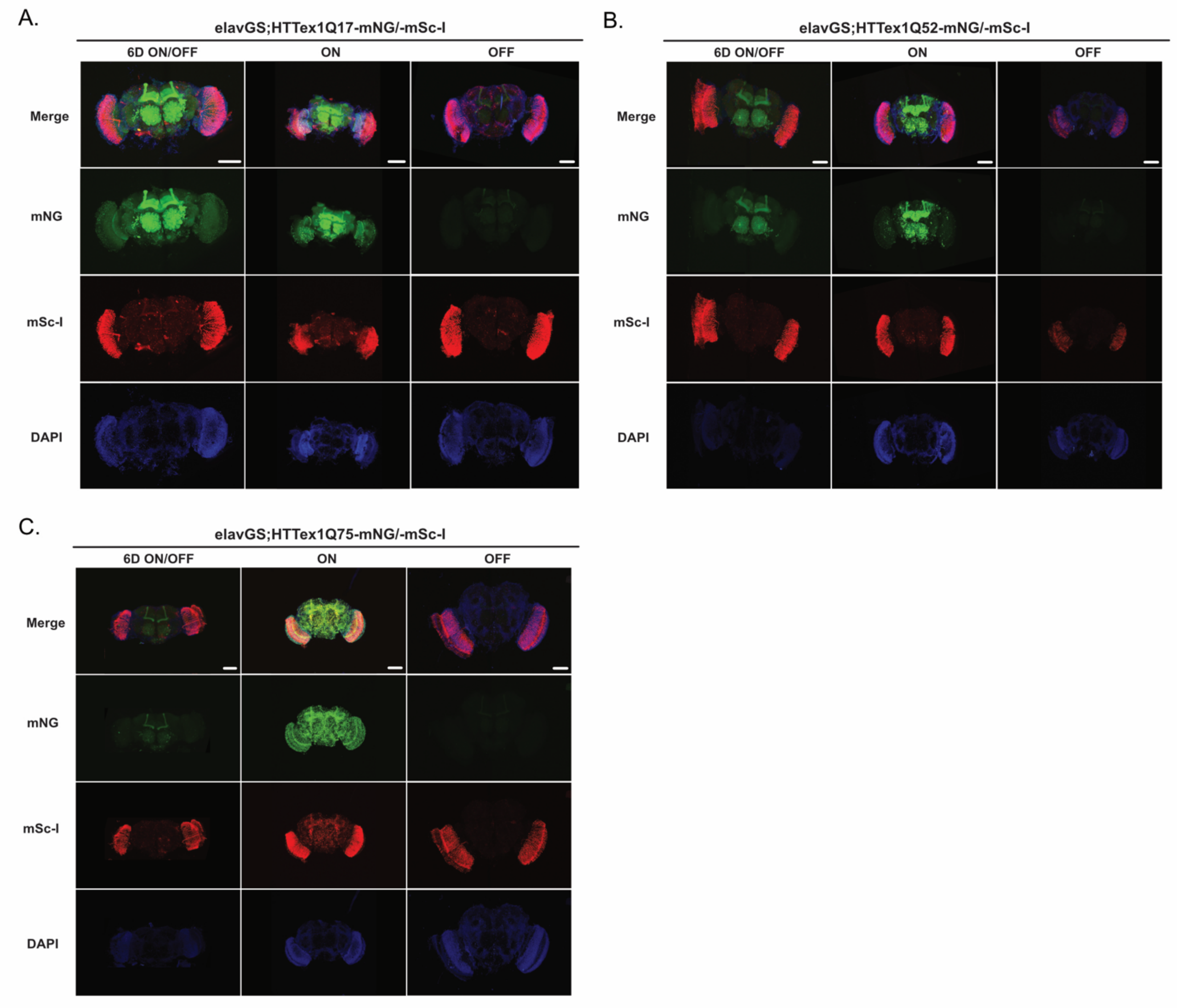

Figure 15. Pathogenic mHTTex1-mNG/-mSc-I fusion proteins form neuronal puncta in vivo using temporally controlled elavGS expression system

A), B) *and* ***C)*** *Confocal images of transgenic elavGS;HTTex1-mNG/-mSc-I brains derived from 27-day old flies. Scale bar= 100 µm.*

In the mid-brain of elavGS;HTTex1Q52-mNG/-mSc-I and elavGS;HTTex1Q75-mNG/-mSc-I flies, noticeable fluorescent puncta were observed (***Figure 15B and 15C***). These puncta were most apparent in elavGS;HTTex1Q75-mNG/-mSc-I ON samples, with fewer observed in elavGS;HTTex1Q52-mNG/-mSc-I ON and none present in elavGS;HTTex1Q17-mNG/-mSc-I ON samples. Similarly, a small number of puncta were observed in the mid-brain of elavGS;HTTex1Q75-mNG/-mSc-I and elavGS;HTTex1Q52-mNG/-mSc-I 6d ON/OFF flies.

Whereas the puncta were completely absent in elavGS;mNG/mSc-I and elavGS:mNG-mSc-I fly brains (***Supplementary Figure 4B***).

When considered together with the WB data (***Figure 14***), the identification of puncta in fly brains expressing pathogenic mHTTex1-mNG/-mSc-I fusion proteins implies that co-expression of these fusion proteins results in the formation of aggregates *in vivo* in a polyQ-dependent manner. Furthermore, short-term expression of pathogenic mHTTex1-mNG/-mSc-I fusion proteins was sufficient to produce fluorescent aggregates in the brains of transgenic flies, while constitutive co-expression predictably led to more mHTTex1-mNG/-mSc-I aggregates.

3.3.3. Temporally controlled co-expression of pathogenic mHTTex1-mNG/-mSc-I fusion proteins reduces lifespan and motility of HD transgenic flies

As previously mentioned, research has linked the presence of mHTTex1 aggregates with the symptom onset and progression of HD [358,359] (***see section 1.4.3***). Hence, following the observation that pathogenic mHTTex1-mNG/-mSc-I fusion proteins (HTTex1Q52-mNG/-mSc-I and HTTex1Q75-mNG/-mSc-I) co-aggregate *in vivo* in the FRET HD fly model, it was examined whether the formation of such aggregates in fly neurons was associated with any behavioural phenotypes.

First, it was assessed whether the developmental timing of HTTex1-mNG/-mSc-I expression influences the survival of transgenic elavGS;HTTex1-mNG/-mSc-I fly strains. Survival was measured by the counting of dead flies until the last fly in the experiment died. Based on the survival curves (***Figure 16A***), the median lifespan was calculated (***Figure 16B***), which represents the time point at which half the population died. A negligible difference in the median lifespan of flies upon short term, constitutive or non- induced HTTex1Q17-mNG/-mSc-I co-expression (elavGS;HTTex1Q17-mNG/-mSc-I 6d ON/OFF ~100 days, elavGS;HTTex1Q17-mNG/-mSc-I ON ~100 days, elavGS;HTTex1Q17-mNG/-mSc-I OFF flies ~96 days respectively) was observed (***Figure 16B***). Thus, indicating pan-neuronal long or short-term co-expression of HTTex1Q17-mNG/-mSc-I does not reduce survival of flies.

Similarly, both short term and non-induced co-expression of HTTex1Q52-mNG/-mSc-I and HTTex1Q75-mNG/-mSc-I resulted in comparable median lifespans (elavGS;HTTex1Q52-mNG/-mSc-I 6d ON/OFF ~100 days, elavGS;HTTex1Q52-mNG/-mSc-I OFF flies ~94 days, elavGS;HTTex1Q75-mNG/-mSc-I 6d ON/OFF ~96 days and elavGS;HTTex1Q75-mNG/-mSc-I OFF ~97 days) (***Figure 16B***).

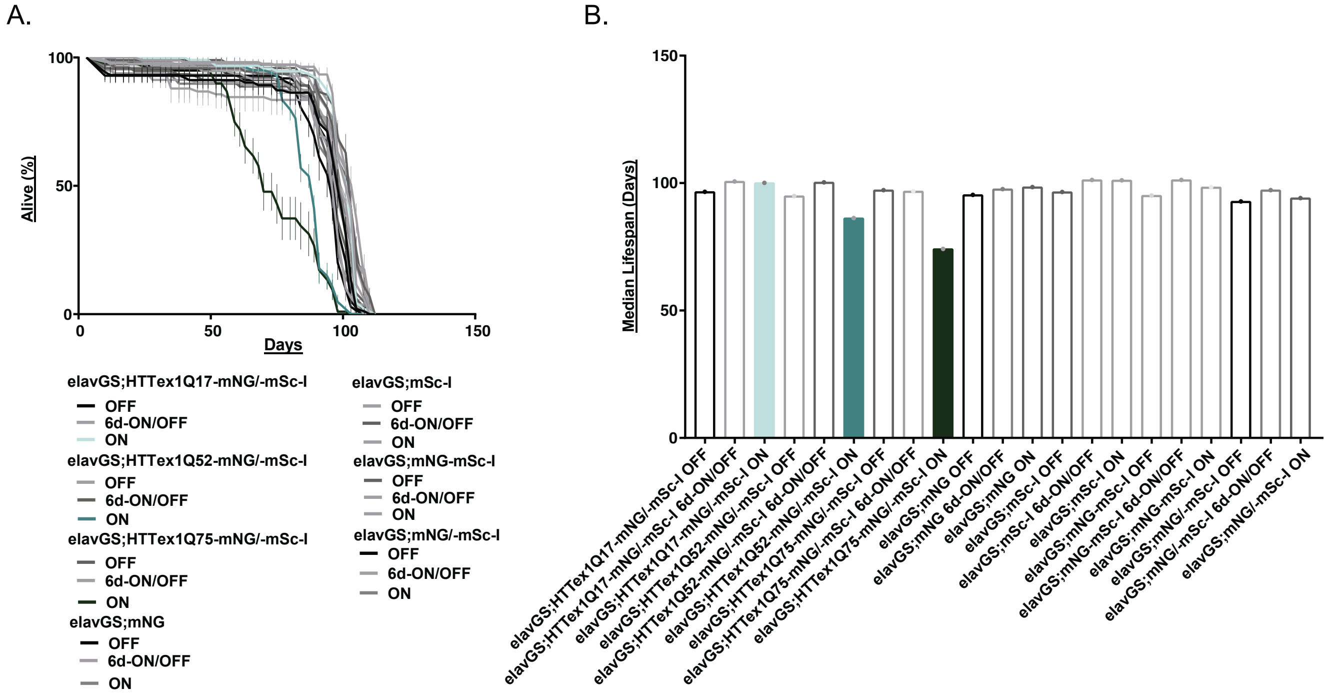

Figure 16. Pathogenic mHTTex1-mNG/-mSc-I fusion proteins reduce survival only when constitutively co-expressed using the elavGS system

A) *Lifespan plotted as percentage of alive flies from 1 biological replicate per strain (N≈100 flies per biological replicate).* ***B)*** *Median lifespan calculated using IC50 values from lifespan curve depicted in A). Each dot represents 1 biological replicate.*

Therefore, indicating that the small amount of aggregates present in both these strains (***Figure 15B and 15C***) were not sufficient to alter survival. In comparison, constitutive co-expression of HTTex1Q52-mNG/-mSc-I resulted in a slight reduction of median lifespan (elavGS;HTTex1Q52-mNG/-mSc-I ON ~86 days), whereas co-expression of HTTex1Q75-mNG/-mSc-I resulted in a more pronounced reduction in median lifespan (elavGS;HTTex1Q75-mNG/-mSc-I ON ~74 days) (***Figure 16B***). Interestingly, this observed polyQ-dependant decrease in survival complimented the observation that constitutive expression of

HTTex1Q75-mNG/-mSc-I resulted in more aggregates than constitutive expression of HTTex1Q52-mNG/-mSc-I (***Figure 15B and 15C***). Thus, supporting the hypothesis that mHTTex1 aggregates may play a neurotoxic role in HD [139,257,173,]. Jointly, these data suggest that only long-term co-expression of HTTex1Q52-mNG/-mSc-I and HTTex1Q75-mNG/-mSc-I negatively affects survival. Therefore, implying only the presence of considerable amounts of HTTex1-mNG/-mSc-I aggregates conveys a pathogenic effect *in vivo*.

To ensure the observed changes in survival were solely due to HTTex1-mNG/-mSc-I expression, the survival of flies expressing mNG and mSc-I proteins individually (mNG and mSc-I), in combination (mNG/-mSc-I) or as a fusion (mNG-mSc-I) was measured (***Figure 16A and 16B***). Short-term, constitutive and non-induced expression of mNG, mSc-I, mNG/-mSc-I and mNG-mSc-I proteins resulted in similar median lifespans of the corresponding flies (***Figure 16B***). Therefore, evidencing that the pan-neuronal expression of fluorescent proteins alone conveys no toxic effect on survival. Hence, the observed differences in survival of elavGS;HTTex1Q52-mNG/-mSc-I ON and elavGS;HTTex1Q75-mNG/-mSc-I ON flies was the result of constitutive co-expression of the corresponding mHTTex1 protein fragments.

3.3.4. Constitutive co-expression of HTTex1-mNG/mSc-I fusion transcripts *in vivo*

After phenotypic assessment of HTTex1-mNG/-mSc-I transgenic flies, only constitutive co-expression of HTTex1Q52-mNG/-mSc-I and HTTex1Q75-mNG/-mSc-I fusion proteins resulted in a mild reduction in lifespan when compared to controls. However, previous work has shown that constitutive expression of untagged pathogenically expanded mHTTex1 results in a drastic reduction in median lifespan to approximately 33 days [257]. Therefore, it was hypothesised the modest effect of pathogenic mHTTex1-mNG/-mSc-I fusion protein co-expression on lifespan may be the result of either: 1) the elavGS driver not efficiently driving transgene expression or 2) the fusion proteins themselves were not sufficiently toxic. Therefore, to first rule out the elavGS driver's potential inefficiency in driving transgene expression, an alternative gene expression system was implemented.

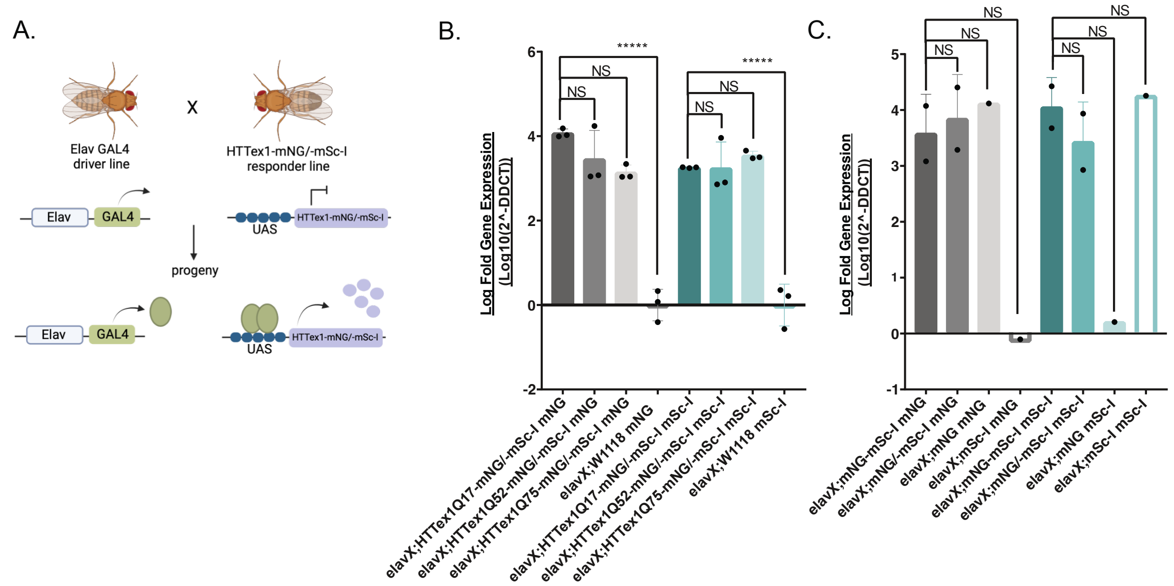

Figure 17. Constitutive elavX mediated co-expression of HTTex1-mNG/-mSc-I

A) *Schematic of the elavX system. Adapted from* [352]*. Created in Biorender.* ***B)*** *RNA prepared from the heads of 27-day old flies from the indicated strains was analysed by qPCR to obtain Ct values for HTTex1-mNG (grey bars) and HTTex1-mSc-I (blue bars) transcript expression using mNG and mSc-I specific primers, respectively. Log fold gene expression calculated using the 2–ΔΔCt method* [360]*, normalised to elavX;W1118 and tubulin (aTub848). Each dot represents 1 biological replicate (3 analysed per sample). Statistical significance assessed by ordinary one-way ANOVA multi-comparisons (NS=P>0.05, *****=P<0.0001****).*** *Error bars= standard deviation.* ***C)*** *qPCR analysis performed with the same conditions as described for B) to detect mNG tagged (grey bars) and mSc-I tagged (blue bars) transcripts in control flies using mNG and mSc-I specific primers, respectively. Each dot represents 1 biological replicate (2 analysed per sample, with the exception of elavX;mNG and elavX;mSc-I where 1 was analysed). Statistical significance assessed by ordinary one-way ANOVA multi-comparisons (NS=P>0.05****).*** *Error bars= Standard deviation*

To this end, the GAL4/UAS elavX system was employed. This system uses the GAL4/UAS method of transgene expression as outlined previously (***see sections 3.2.1 and 3.3.1***). Like the elavGS system, the elavX system consists of a driver strain which expresses GAL4 under the control of the pan-neuronal elav promoter. However, unlike the elavGS system, the GAL4 protein does not require the administration of hormone to bind the UAS sequence. Instead, upon crossing of the elavX driver strain with the HTTex1-mNG/-mSc-I responder strain, the resulting progeny express a constitutively active GAL4 which drives constant pan-neuronal expression of the transgene throughout the lifetime of the fly (***Figure 17A***). Hence, if in fact the HTTex1Q52-mNG/-mSc-I and HTTex1Q75-mNG/-mSc-I fusion proteins were significantly toxic, constitutive co-expression of these fusion proteins from the embryonic stage would result in more drastic phenotypic disturbances in adult flies.

After the HTTex1-mNG/-mSc-I responder strains were mated with the elavX driver strain, it was imperative to assess whether the HTTex1-mNG and HTTex1-mSc-I transgenes were independently co-expressed within the elavX;HTTex1-mNG/-mSc-I progeny. As a negative control, the *white* negative background strain W1118 was mated with the elavX driver. HTTex1-mNG/-mSc-I transcript levels present in 27-day old adult fly heads were quantified using qPCR (***Figure 17B and 17C***). To calculate fold gene expression, the 2−ΔΔCt method [360] was employed, where the obtained cycle threshold (Ct) values were normalised to the internal control tubulin (aTub84b) and elavX;W1118 flies. The resulting fold changes were log transformed for statistical analysis. First, to validate the qPCR primer specificity, flies which expressed the GAL4 protein, but contain no transgene (elavX;W1118) as well as flies with either mNG or mSc-I transgenes (elavX;mNG and elavX;mSc-I respectively) were analysed.

No mNG or mSc-I transcripts were detected in the elavX;W1118 flies (***Figure 17B***) and expression of only mNG or mSc-I transcripts was detected in the respective elavX;mNG and elavX;mSc-I flies (***Figure 17C***) . Thereby, confirming the specificity of the designed qPCR primers and the lack of sequence overlap between the mNG and mSc-I transcripts. In flies containing the mNG and mSc-I transgenes either independently (elavX;mNG/-mSc-I) or as a gene fusion (elavX;mNG-mSc-I), both mNG and mSc-I transcripts were present (***Figure 17C***). Similarly, in HTTex1-mNG/-mSc-I transgenic flies (elavX;HTTex1Q17-mNG/-mSc-I, elavX;HTTex1Q52-mNG/-mSc-I and elavX;HTTex1Q75-mNG/-mSc-I), the presence of both mNG and mSc-I HTTex1Q17, HTTex1Q52 and HTTex1Q75 fusion transcripts was detected (***Figure 17B***). This confirmed the ability of the elavX driver to independently drive co-expression of the two separate UAS controlled HTTex1-mNG/-mSc-I transgenes within the same fly strain. Further statistical analysis was performed, which highlighted no significant difference between the expression of mNG or mSc-I HTTex1Q17, HTTex1Q52 and HTTex1Q75 fusion transcripts (***Figure 17B***). Therefore, it can be assumed both mNG and mSc-I transcripts were expressed at similar levels with the heads of the transgenic fly strains, regardless of which UAS sequence the transgene expression was controlled by.

3.3.5. Constitutive co-expression of pathogenic mHTTex1-mNG/-mSc-I fusion proteins results in the formation of large SDS-stable aggregates

After confirming the independent co- expression of HTTex1-mNG/-mSc-I fusion transcripts in the elavX;HTTex1-mNG/-mSc-I transgenic fly strains, it was important to assess whether the corresponding HTTex1-mNG and HTTex1-mSc-I fusion proteins are co-produced in fly heads.

To this end, fly head lysates from 27-day old flies were analysed by WB using the anti-HTT antibody MAB5492, anti-C-myc and anti-mCherry antibodies for immunodetection (***Figure 18A, 18B and 18C***). Bands slightly above the estimated size, as was observed previously (***see sections 3.2.2 and 3.3.2***), were identified corresponding to the respective HTTex1-mNG/-mSc-I fusion proteins (HTTex1Q17-mNG/-mSc-I= ~48kDa, HTTex1Q52-mNG/-mSc-I= ~50kDa and HTTex1Q75-mNG/-mSc-I= ~60kDa). In contrast, no such bands were observed in the elavX;W1118 control. Hence confirming the independent co-expression of both HTTex1-mNG and HTTex1-mSc-I fusion proteins within the neurons of the transgenic flies. It must be noted, in the anti-mCherry blots a distinct band can be seen for all elavX;HTTex1-mNG/-mSc-I samples at approximately 28kDa which is absent in the elavX;W1118 controls, due to the previously described expression of RFP in all transgenic strains (***see section 3.3.2***). Interestingly, as was observed using the HEK293 cell model (***see section 3.2.2***), a decrease in band size with increasing polyQ length was observed, which indicated a higher abundance of HTTex1Q17-mNG/-mSc-I than of HTTex1Q52-mNG/-mSc-I or HTTex1Q75-mNG/-mSc-I fusion proteins. Additional exposure of the anti-C-myc and MAB5492 blots revealed the decrease in soluble HTTex1Q75-mNG/-mSc-I fusion protein band intensity was accompanied by an increase in insoluble signal in the gel pockets. As protein retention within the gel pocket is characteristic of mHTTex1 aggregates [270], these results indicated the presence of SDS-stable HTTex1Q75-mNG/-mSc-I aggregates in the fly heads.

To confirm the presence of large SDS-stable mHTTex1-mNG/-mSc-I aggregates, head lysates from 27-day old flies were further analysed by dFRA using both the MAB5492 antibody and PHP2 antibodies for immunodetection (***Figure 18D and 18E***). The PHP2 antibody binds to the proline-rich domain of HTTex1, which has been shown to be exposed in mHTTex1 fibrils

[361]. Since mHTTex1 aggregates contain many exposed epitopes, PHP2 can be considered as an antibody that preferentially detects mHTTex1 aggregates [270].

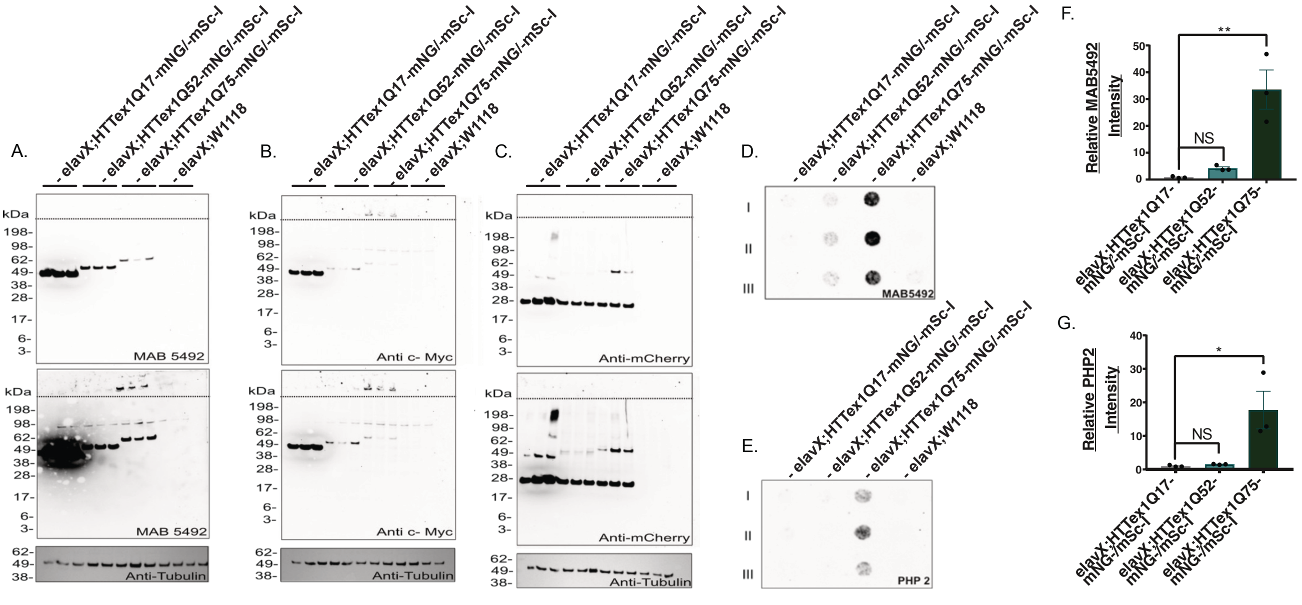

Figure 18. Constitutive co-expression of pathogenic mHTTex1 mNG/-mSc-I fusion proteins in fly neurons results in the formation of large, SDS-stable aggregates

WB analysis of the HTTex1-mNG/-mSc-I fusion proteins in 27-day old fly head lysates in 3 biological replicates (1 per lane). ***A)*** *Anti-HTT a.a 1-10 (MAB5492)* ***B)*** *anti-C-myc and* ***C)*** *anti-mCherry antibodies used for immunodetection. Membranes were exposed for 20 seconds (top blot) and 5 minutes (bottom blot). Gel pockets shown above the dotted line. Anti-tubulin antibody used for immunodetection as a loading control**.** 20 µg lysate loaded per lane.* ***D)*** *Anti-HTT a.a 1-10 (MAB5492) and* ***E)*** *PHP2 dFRA analysis of fly head lysates from 3 biological replicates of 27-day old flies (indicated by I, II and II). 70 µg protein loaded per dot. (performed by Frederick Wieshmann).* ***F)*** *Quantification of relative MAB5492 intensities and* ***G)*** *PHP2 intensities from dFRA blots. Each dot represents a biological replicate (N=3), the average of 2 technical replicate measurements per each biological replicate was plotted. Statistical significance assessed by ordinary one-way ANOVA multi-comparisons (NS= P>0.05, *=P<0.05). Error bars= SEM.*

First using the MAB5492 antibody, a small amount of SDS-stable aggregates in elavX;HTTex1Q52-mNG/-mSc-I flies was observed, with a higher amount detected in elavX;HTTex1Q75-mNG/-mSc-I flies (***Figure 18D***). As expected, no aggregated HTTex1-mNG/-mSc-I structures were detected in elavX;HTTex1Q17-mNG/-mSc-I and elavX;W1118 flies. Using the PHP2 antibody, SDS-stable aggregates were found to be present in elavX;HTTex1Q75-mNG/-mSc-I flies (***Figure 18E***). However, in contrast to the MAB5492 dFRA, no such structures were detected in elavX;HTTex1Q52-mNG/-mSc-I. The inability of the PHP2 antibody to detect HTTex1Q52-mNG/-mSc-I aggregates may be due to structural differences between HTTex1Q52-mNG/-mSc-I and HTTex1Q75-mNG/-mSc-I aggregates, which may result in differential accessibility of the PHP2 antibody epitope. Alternatively, this may be due an overall lower abundance of mHTTex1 aggregates being present in the brains of elavX;HTTex1Q52-mNG/-mSc-I flies in comparison to that of elavX;HTTex1Q75-mNG/-mSc-I flies.

When quantifying the dFRA signals in both MAB5492 and PHP2 immunoblots, a significant increase in SDS-stable aggregates was observed in samples from HTTex1Q75-mNG/-mSc-I co-expressing flies when compared to the HTTex1Q17-mNG/-mSc-I co-expressing control flies (***Figure 18F and 18G***). Therefore, these results clearly indicate constitutive neuronal expression results in a significantly higher abundance of SDS-stable HTTex1Q75-mNG/-mSc-I aggregates than SDS-stable HTTex1Q52-mNG/-mSc-I aggregates in the heads of HD transgenic flies.

3.3.6. Co-production of mHTTex1-mNG/-mSc-I fusion proteins results in the formation of fibrillar and amorphous aggregates in fly neurons

The results so far have revealed abundant SDS-stable aggregates in elavX;HTTex1Q75-mNG/-mSc-I fly heads, while elavX;HTTex1Q52-mNG/-mSc-I samples exhibited fewer aggregates (***see section 3.3.5***). Previous research has established that aggregate conformation and sub-cellular localisation may impact toxicity [269]. Therefore, to gain a deeper understanding of the structure of HTTex1Q52-mNG/-mSc-I and HTTex1Q75-mNG/-mSc-I aggregates and potentially infer their respective toxicity *in vivo*, fly head lysates and fly brains were examined using electron microscopy (EM).

First, to assess the structure of mHTTex1-mNG/-mSc-I aggregates, fly head lysates were analysed using immunoelectron microscopy (iEM). EM grids coated with fly head lysate from 27-day old flies were incubated with the anti-HTTex1 antibody PHP2, which was subsequently detected by an anti-mouse gold-labelled secondary antibody. As gold is an electron dense element, it increases electron scatter which when observed using iEM results in high-contrast dark spots. These dark spots, observed through iEM, would indicate where the PHP2 antibody has bound and therefore show what structures may be mHTTex1-mNG/-mSc-I aggregates. In both elavX;HTTex1Q75-mNG/-mSc-I and elavX;HTTex1Q52-mNG/-mSc-I samples branched aggregates were observed which co-localised with gold particles (red arrows) (***Figure 19A***). The elavX;HTTex1Q52-mNG/-mSc-I samples harboured smaller structures which had a lower number of co-localised gold particles, in comparison to elavX;HTTex1Q75-mNG/-mSc-I samples which had larger structures with more dense gold particle decoration. In contrast, gold particles were found to be rarely co-localised with elavX;HTTex1Q17-mNG/-mSc-I structures (***Figure 19A***). The structures present in elavX;HTTex1Q75-mNG/-mSc-I and elavX;HTTex1Q52-mNG/-mSc-I samples resembled those identified in previous studies of elavX;HTTex1Q97 fly head lysates (Leonard Roth, Master's Thesis, 2022, unpublished) and published data [269,362]. This demonstrates that the branched morphology of the observed mHTTex1-mNG/-mSc-I aggregates is not an artifact of fluorophore conjugation to the mHTTex1 protein fragments.

Upon quantification, the mean percentage of gold bound to these structures (greater than 1 per aggregate) of the total gold detected on the grids was calculated (***Figure 19B***). The percentage was found to be highest in elavX;HTTex1Q75-mNG/-mSc-I samples (34.8%) with less in elavX;HTTex1Q52-mNG/-mSc-I samples (27.4%) (***Figure 19B***), indicating these samples had a higher incidence of structures highly decorated with gold. In contrast, a comparatively low mean percentage of gold was bound to structures in elavX;W1118 and elavX;HTTex1Q17-mNG/-mSc-I samples (10.4% and 10.5% respectively) (***Figure 19B***). Although this difference in gold decoration was not found to be significant, the higher levels of gold decoration found in pathogenic HTTex1-mNG/-mSc-I samples indicates the detected structures are HTTex1-mNG/-mSc-I aggregates. Therefore, when taken together these data provide compelling evidence that the mHTTex1-mNG/-mSc-I fusion proteins form branched, fibrillar-like structures in the brains of the transgenic flies.

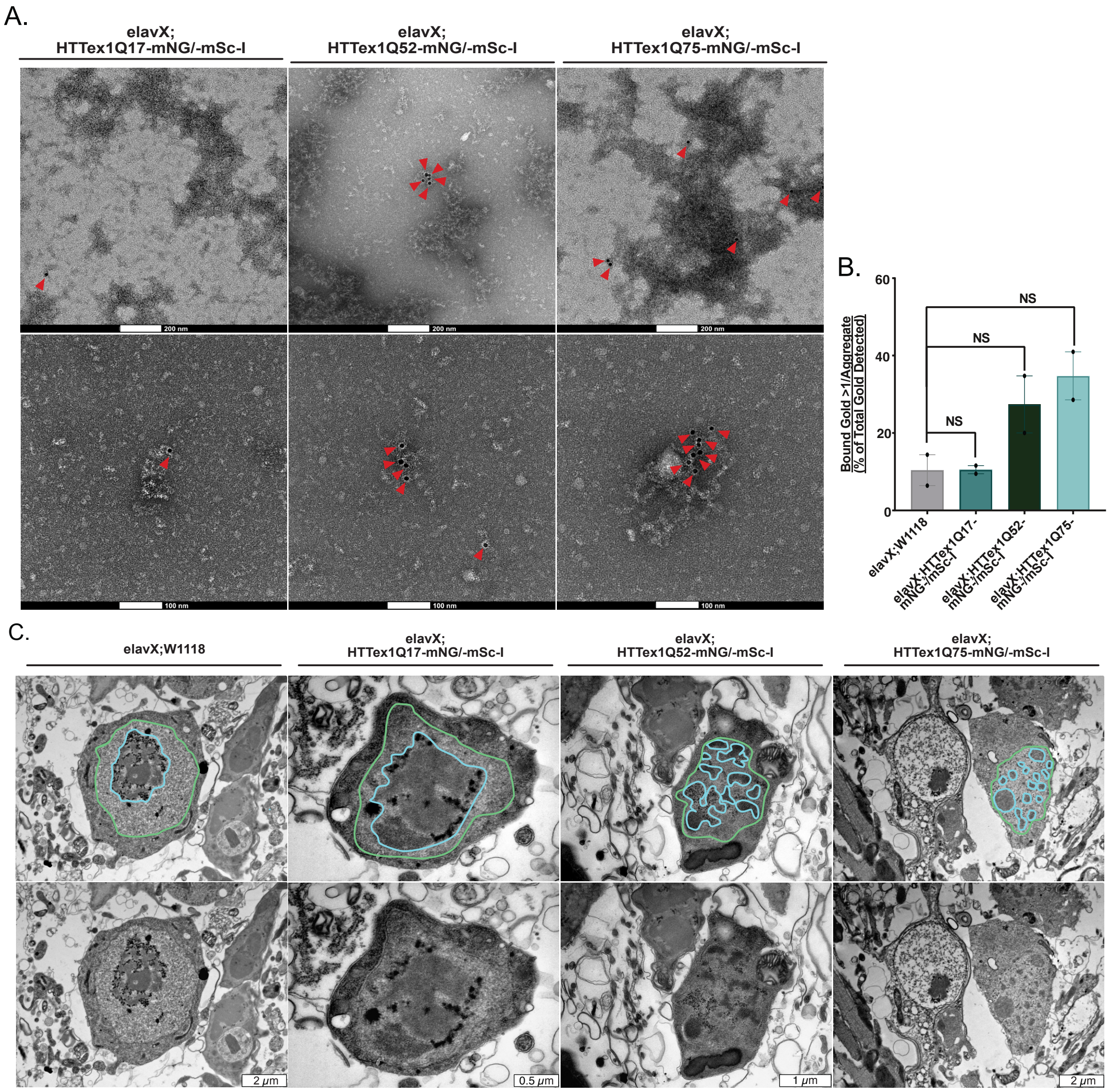

Figure 19. HTTex1-mNG/-mSc-I fusion proteins form fibrillar structures and disrupt organisation of the nucleus in fly neurons

A) *iEM images of fly head lysate immunodetected with PHP2 (anti-HTT antibody) primary antibody and anti-mouse gold labelled secondary antibody (black dots). Gold particle labelling indicated with red arrows. 0.1µg protein added to each grid. Upper panel: Scale bar= 200 nm. Lower panel: Scale bar= 100 nm.* ***B)*** *Quantification of the incidence of more than one gold particle bound to an aggregate structure, as a percentage of the total gold detected per grid. Each dot represents 1 grid (2 analysed per sample, each prepared using lysate from separate biological replicates). Approximately 30 grid images used for analysis per sample. Statistical significance assessed by ordinary one-way ANOVA multi-comparisons (NS= P>0.05). Error bars= SEM.* ***C)*** *EM micrographs focusing on neuronal cell bodies within the fly brain. Upper panel: Nuclear envelope (green line) and nuclear structures (blue line) indicated. Bottom panel: Images without nuclear envelope and nuclear structures indicated. Scale bars: elavX;W1118 = 2 µm, elavX;HTTex1Q17-mNG/-mSc-I= 0.5 µm, elavX;HTTex1Q52-mNG/-mSc-I = 1 µm and elavX;HTTex1Q75-mNG/-mSc-I = 2 µm. (Performed by Mara Camelia Rusu).*

Next, to gain more comprehensive insight into the cellular localisation of mHTTex1-mNG/-mSc-I aggregates *in situ*, and therefore better understand how they may confer toxicity *in vivo*, whole brain tissue sections were analysed using EM (***Figure 19C***). First, tissue sections from 27-day old fly brains were stained using toluidine blue to confirm conservation of mid-brain morphology prior to EM analysis (***Supplementary Figure 5***). The EM micrographs obtained from elavX;W1118 and elavX;HTTex1Q17-mNG/-mSc-I brain sections showed regular nuclear packing (***indicated with blue line Figure 19C***), with EM dense nucleoli (grey circular structures) associated with chromatin [363] (black dots). In contrast, the EM micrographs obtained from elavX;HTTex1Q52-mNG/-mSc-I and elavX;HTTex1Q75-mNG/-mSc-I brain sections revealed a striking disruption of nuclear organisation. In elavX;HTTex1Q52-mNG/-mSc-I brain sections the nucleus contained large electron dense irregular structures, reminiscent of those previously published as mHTTex1 nuclear aggregates [278]. Similar nuclear structures were also present in elavX;HTTex1Q75-mNG/-mSc-I brain sections, however these structures appeared smaller and more numerous. The absence of such nuclear structures in control brain sections (elavX;W1118 and elavX;HTTex1Q17-mNG/-mSc-I), partnered with previously published data identifying similar structures as mHTTex1 aggregates [278], suggests the nuclear structures identified in elavX;HTTex1Q52-mNG/-mSc-I and elavX;HTTex1Q75-mNG/-mSc-I brain sections may be mHTTex1-mNG/-mSc-I aggregates. However, to ascertain whether these structures are in fact mHTTex1 aggregates or disorganised nuclear proteins, further antibody detection is required. Overall, the EM data indicate pathogenic mHTTex1-mNG/-mSc-I fusion proteins may co-aggregate in the nucleus of transgenic fly neurons. Alternatively, the co-production of mHTTex1-mNG/-mSc-I fusion proteins may significantly perturb nuclear organisation and structure.

3.3.7. FRET signal is a marker for in vivo mHTTex1-mNG/-mSc-I aggregation.

The prior HEK293 cell work (***see section 3.2.2***), in agreement with previously published literature [233,270,253,364–370] confirmed FRET measurements can be used to infer the co-aggregation of pathogenically expanded mHTTex1-mNG/-mSc-I fusion proteins *in vitro.* Hence following the observation of mHTTex1-mNG/-mSc-I aggregates in fly neurons, using biochemical methods and EM analyses (***Figure 18 and Figure 19***), the next aim of this work was to evaluate whether FRET can be used as a readout to monitor mHTTex1-mNG/-mSc-I aggregation *in vivo*.

With this objective, whole adult fly brains were first investigated using confocal microscopy. Fly brains were excited with a laser corresponding to the mNG excitation wavelength (490nm) and emission was detected in range corresponding to mSc-I (580-630nm), thereby enabling qualitative detection of FRET positive structures. In both elavX;HTTex1Q75-mNG/-mSc-I and elavX;HTTex1Q52-mNG/-mSc-I flies FRET positive puncta were observed throughout the midbrain (***Figure 20A***). FRET positive puncta were found to be most abundant in elavX;HTTex1Q75-mNG/-mSc-I samples, with less observed in elavX;HTTex1Q52-mNG/-mSc-I samples and none observed in elavX;HTTex1Q17-mNG/-mSc-I, indicating a polyQ dependant trend in FRET puncta detection. Moreover, no such puncta were observed in elavX;mNG-mSc-I and elavX;mNG/-mSc-I fly brains, validating that FRET puncta were due to pathogenic mHTTex1-mNG/-mSc-I fusion protein co-expression only. The polyQ dependant trend in FRET positive puncta formation correlated with the detection of SDS-stable HTTex1Q75-mNG/-mSc-I and HTTex1Q52-mNG/-mSc-I aggregates using dFRA (***Figure 18D and 18E***). Thus, showing that the FRET positive puncta observed in fly brains are the result of *in vivo* HTTex1Q75-mNG/-mSc-I and HTTex1Q52-mNG/-mSc-I co-aggregation.

Next, it was assessed whether FRET can be used to detect mHTTex1-mNG/-mSc-I co-aggregates in live fly neurons. To do this, a previously published FACS protocol which enabled the isolation of live single cells from whole fly brains [371] was optimised for detecting expression of mNG and mSc-I fluorophores. In short, 40 whole fly brains were dissected from 27-day old flies, enzymatically digested, and filtered to produce a single cell solution (***Figure 20B***). The single cell solution was analysed using DAPI, FSC and SSC gating to select live single cells (***Supplementary Figure 6A***). Then, the FRET gating method [345,346], which was previously used for FRET FACS of HEK293 cells (***Figure 12***), was adapted to detect FRET positive single cells derived from whole fly brains. To achieve this, live single cells derived from elavX;mNG and elavX;mSc-I fly brains were analysed to establish the gates corresponding to mNG and mSc-I fluorescence (***Supplementary Figure 6A***).

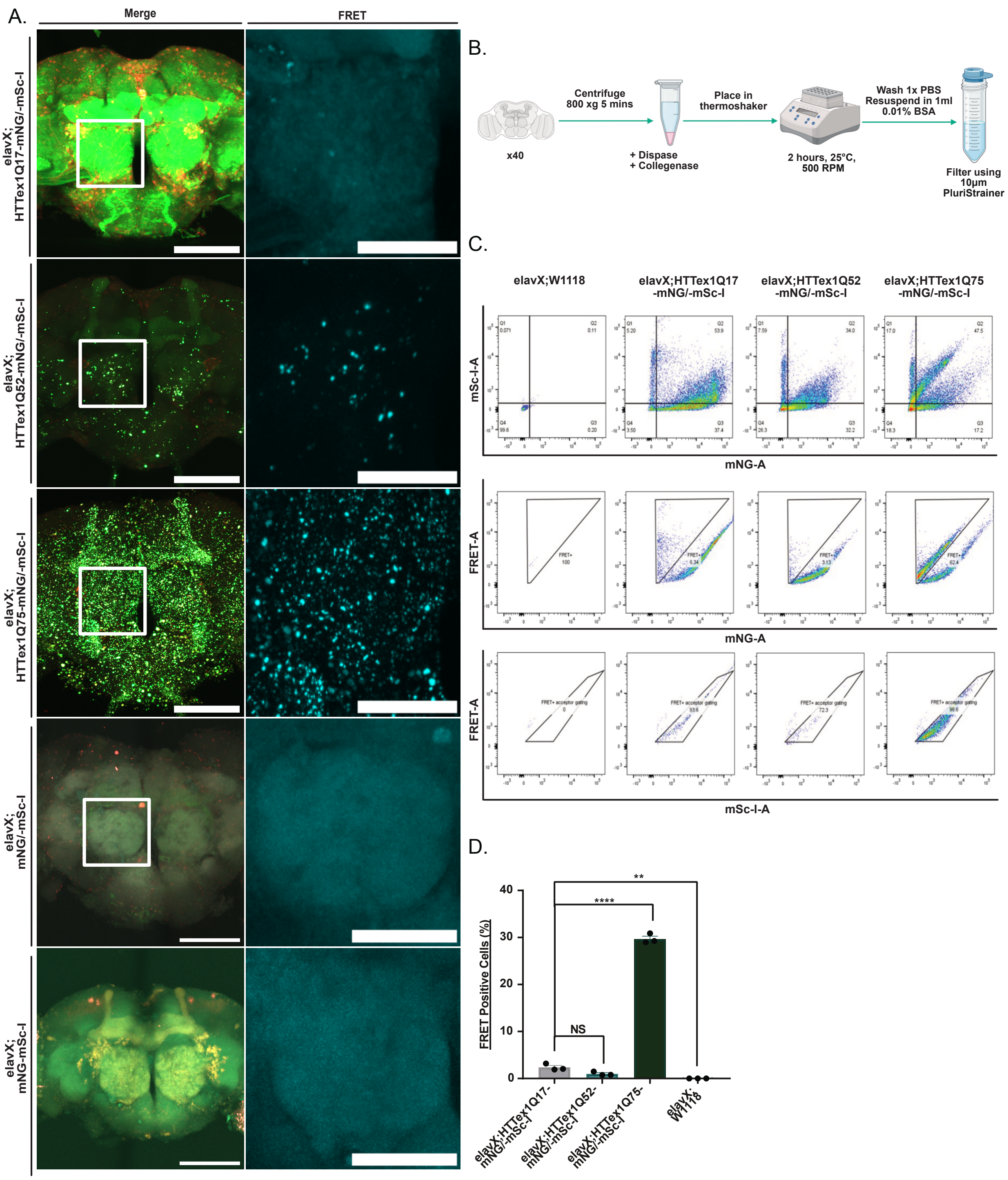

Figure 20. Neuronal puncta formed of HTTex1 aggregates can be detected in elavX;mHTTex1-mNG/-mSc-I fly brains using FRET

A)** Confocal images of the midbrains of transgenic elavX;HTTex1-mNG/-mSc-I flies (left panel). Zoomed in olfactory neuron, from the region of interest (ROI) (indicated with a white square), depicted in the right panel. Scale bar= 100µm. **B)** Schematic showing FACS workflow for generating single cell solutions from whole fly brains. Created using Biorender**.** **C)** FACS cytograms showing sequential double positive gating (mSc-I pulse area (mSc-I A) vs mNG pulse area (mNG-A)) , FRET donor-corrected gating (FRET pulse area (FRET A) vs mNG pulse area* *(mNG-A) and FRET acceptor-corrected gating (FRET-A vs mSc-I-A) in arbitrary units (a.u.) of 50,000 cells (n=50,000).* ***D) *Percentage of FRET positive cells in total cell population measured by FACS. Each dot represents 1 biological replicate (3 biological replicates per sample). Statistical significance assessed by ordinary one-way ANOVA multi-comparisons (NS=P>0.05, ***=P<0.001). Error bars=SEM*

Using these parameters, double positive cells, exhibiting both mNG and mSc-I fluorescence, were selected (***Supplementary Figure 6A***). Next, the double positive cells derived from elavX;mNG/-mSc-I and elavX;mNG-mSc-I fly brains were used to establish the FRET negative and FRET positive gates, to determine what proportion of the double positive cell population were also FRET positive (***Supplementary Figure 6A***). To correct for false positives arising from donor and acceptor fluorophore cross talk, the FRET signals of cells was plotted against their mNG, and mSc-I signals respectively (***Supplementary Figure 6A***). Cells derived from elavX;mNG/-mSc-I fly brains exhibited a negligible FRET positive population (1%), whereas approximately half of the elavX;mNG-mSc-I derived cells (48%) were FRET positive. Thus, validating the ability of FACS to accurately detect FRET in live cells derived from fly brains (***Supplementary Figure 6B***).

With this FRET FACS gating system, cells derived from elavX;HTTex1-mNG/-mSc-I fly brains were analysed (***Figure 20C***). Surprisingly, cells co-expressing HTTex1Q52-mNG/-mSc-I fusion proteins and those co-expressing HTTex1Q17-mNG/-mSc-I had a comparable mean FRET positive cell population to (1% and 2.4% respectively) (***Figure 20D***). This maybe be due to cells containing less abundant HTTex1Q52-mNG/-mSc-I aggregates which are not numerous enough to create a detectable FRET FACS signal. In contrast, cells co-expressing HTTex1Q75-mNG/-mSc-I displayed a significantly larger mean FRET positive cell population (30%) when compared to that of HTTex1Q17-mNG/-mSc-I controls (2.4%) (***Figure 20D***), a finding which echoed the previously obtained *in vitro* FACS and FRET efficiency results (***Figure 11D, Figure 12C and 12F***). Therefore, collectively these results indicate FRET-FACS measurements are well suited for the detection of HTTex1Q75-mNG/-mSc-I co-aggregates in live cells isolated from the brains of transgenic HD flies.

In summary, the WB, dFRA and EM data described above clearly evidenced that HTTex1Q52-mNG/-mSc-I and HTTex1Q75-mNG/-mSc-I fusion proteins co-aggregate *in vivo* and form

HTTex1 aggregates in the brains of HD flies. Moreover, the confocal microscopy data showed that the co-aggregation of HTTex1Q52-mNG/-mSc-I and HTTex1Q75-mNG/-mSc-I fusion proteins results in the formation of visible FRET positive structures in fly brains. Finally, the FRET-FACS results highlighted that the FRET signals of live cells derived from fly brains are indicative of the abundance of mHTTex1-mNG/-mSc-I aggregates. Hence, collectively these results establish that FRET signals can be used as a marker for the quantification of mHTTex1-mNG/-mSc-I aggregation.

3.3.8. Constitutive expression of pathogenic mHTTex1-mNG/mSc-I fusion proteins recapitulates HD phenotypes and significantly correlates with FRET-based detection of mHTTex1 aggregates

Previous research has established a link between mHTTex1 aggregate formation and symptom onset and progression of HD [358,359]. However, the fusion of fluorescent tags to mHTTex1 has been shown to hinder aggregation and thus impact HD pathogenesis [276]. Therefore, the next aim of this work was to investigate whether the presence of mHTTex1-mNG/-mSc-I aggregates is associated with a phenotypic decline in the elavX;HTTex1-mNG/-mSc-I flies.

To address this question, the effect of HTTex1-mNG/-mSc-I fusion protein co-expression in fly neurons on transgenic fly survival was assessed. Survival was measured by the counting of dead flies until the last fly in the experiment died. Based on the survival curves (***Supplementary Figure 7A***) the median lifespan, which represents the time point at which half the population died, was calculated (***Figure 21A***). The elavX;HTTex1Q17-mNG/-mSc-I and elavX;W1118 flies exhibited the same median lifespan of ~87 days, indicating the co-expression of HTTex1Q17-mNG/-mSc-I fusion proteins has no effect of survival. In contrast, the median lifespan of elavX;HTTex1Q52-mNG/-mSc-I and elavX;HTTex1Q75-mNG/-mSc-I flies was significantly reduced to ~73 days and ~59 days respectively when compared to elavX;HTTex1Q17-mNG/-mSc-I flies. Thus, indicating that only constitutive co-expression of HTTex1Q52-mNG/-mSc-I or HTTex1Q75-mNG/-mSc-I fusion proteins significantly affected survival.

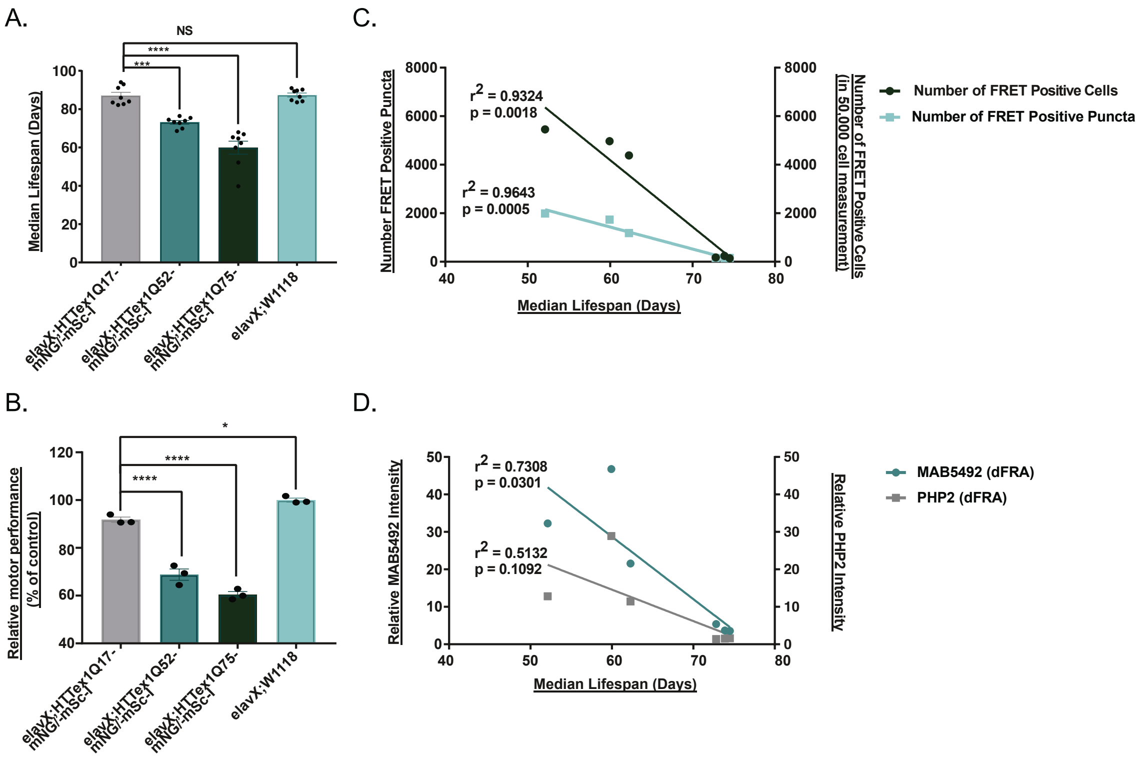

Figure 21. Constitutive co-expression of pathogenic mHTTex1-mNG/-mSc-I fusion proteins in vivo causes phenotypic decline which significantly correlates with FRET measurements

A)** Median lifespan calculated using IC50 values from lifespan curves for each biological replicate. Each dot represents 1 biological replicate (8 biological replicates per sample). Statistical significance assessed by ordinary one-way ANOVA multi-comparisons (= P<0.001, ****=P<0.0001). Error bars= SEM. **B)** Relative motor performance calculated as percentage of total area under the curves for each biological replicate relative to elavX;W1118. Each dot represents 1 biological replicate (3 biological replicates per sample). Statistical significance assessed by ordinary one-way ANOVA multi-comparisons (NS=P>0.05, *= P<0.05, ****=P<0.0001). Error bars=SEM. (Data collected by Frederick Wieshmann). **C)** Pearson's correlation analysis, correlating the median lifespan of elavX;HTTex1Q75-mNG/-mSc-I and elavX;HTTex1Q2-mNG/-mSc-I flies with the number of FRET positive puncta detected using confocal microscopy (Blue line) and number of FRET positive cells measured using FRET FACS (green line). Each point represents 1 biological replicate (3 analysed per group). Lines represent linear regression fit of data. **D)** Pearson's correlation analysis, correlating the median lifespan of elavX;HTTex1Q75-mNG/-mSc-I and elavX;HTTex1Q2-mNG/-mSc-I flies with the relative signal intensity from MAB5492 dFRA (blue line) and PHP2 dFRA (grey line). Each point represents 1 biological replicate (3 analysed per group). Lines represent linear regression fit of data.*

To ensure the observed changes in survival were solely due to HTTex1-mNG/-mSc-I expression, the survival of flies expressing mNG and mSc-I proteins individually (mNG and mSc-I), in combination (mNG/-mSc-I) or as a fusion (mNG-mSc-I) was subsequently measured. Constitutive expression of mNG, mSc-I, mNG/-mSc-I and mNG-mSc-I proteins resulted in similar median lifespans of the corresponding flies (~90, 93, 87 and 86 days respectively) (***Supplementary Figure 7B***). Therefore, evidencing that the pan-neuronal expression of fluorescent proteins alone conveys no significant toxic effect on survival. Hence, the observed differences in survival of HTTex1Q52-mNG/-mSc-I and HTTex1Q75-mNG/-mSc-I flies was the result of constitutive co-expression of the corresponding mHTTex1 protein fragments.

It is important to note that ~40% of the elavX;HTTex1Q75-mNG/-mSc-I flies survived as long as the wild type controls (elavX;HTTex1Q17-mNG/-mSc-I and elavX;W1118) (***Supplementary Figure 7A***) which was hypothesised to be due to problems with the HTTex1Q75-mNG/-mSc-I parental stock. To rectify this issue, single male HTTex1Q75-mNG/-mSc-I (genotype; +/+;HTTex1Q17-mNG/-mSc-I/HTTex1Q75-mNG/-mSc-I) were mated with single balancer (CyO/SP;TM6/MKRS) virgin female flies. Virgin female and male flies were selected from the F1 progeny which were CyO positive and TM6 positive with orange eyes. Additionally the progeny were negatively selected for Sp and MKRS (CyO/+;HTTex1Q75-mNG/-mSc-I/TM6). The selected flies were mated, therefore producing a balanced heterozygous HTTex1Q75-mNG/-mSc-I stock. The F1 progeny from this mating were taken forward as the basis for new parental stocks.

Next, the effect of HTTex1-mNG/-mSc-I expression on neuronal function was assessed using a negative geotaxis assay (also known as a climbing assay) [372.] The negative geotaxis assay assesses the movement of flies by observing their natural tendency to climb vertically as a means of escape. Climbing ability was measured by recording the number of flies which climbed to a height of 8cm in 15 seconds, each day until the flies could no longer climb. From this data the percentage of flies climbing each day (percentage climbing (%)) was calculated by dividing the number of flies climbed per day from the total number of flies counted, multiplied by 100. Similar to what was observed in the lifespan assay, there was no significant difference in the percentage of flies climbing over time between elavX;HTTex1Q17-mNG/-mSc-I and elavX;W1118 control flies (***Supplementary Figure 7C***). Both strains displayed a steady decline in climbing ability over time, which has been shown to be a normal age-related behaviour of flies [373]. Likewise the percentage of elavX;mNG-mSc-I and elavX;mNG/-mSc-I flies climbing over time was comparable to that of elavX;HTTex1Q17-mNG/-mSc-I and elavX;W1118 control flies. Therefore, showing fluorescence protein co-expression alone does not affect motor performance of flies (***Supplementary Figure 7C and 7D***). In contrast, both elavX;HTTex1Q52-mNG/-mSc-I and elavX;HTTex1Q75-mNG/-mSc-I flies showed a reduction in the percentage of flies climbing over time, indicating a polyQ dependent pattern in phenotypic decline (***Supplementary Figure 7C***).

The curves generated from climbing measurements were used to calculate the area under the curve (AUC), which gave an average measure of motor performance. The AUC values were then normalised to AUC for the elavX;W1118 control and multiplied by 100 to calculate the percentage relative motor performance (***Figure 21B***). Both elavX;HTTex1Q75-mNG/-mSc-I flies and elavX;HTTex1Q52-mNG/-mSc-I exhibited a statistically significant decrease in mean relative motor performance (60.4% and 68.8% respectively) when compared to elavX;HTTex1Q17-mNG/-mSc-I controls (91.8%). Interestingly, elavX;W1118 flies displayed a slight significant increase in mean relative motor performance (100%) when compared to elavX;HTTex1Q17-mNG/-mSc-I flies (91.8%) (***Figure 21B***). This may indicate that HTTex1Q17-mNG/-mSc-I fusion protein co-expression mildly decreases motor performance. Collectively these phenotypic data show that constitutive neuronal co-expression of pathogenic mHTTex1-mNG/-mSc-I fusion proteins induces neurotoxicity and dysfunction with phenotypic consequences, mirroring other HD models [374].

Following this observation, it was imperative to understand how the detection of mHTTex1 aggregation using FRET correlates with the phenotypic decline *in vivo*. To this end, Pearson's correlation analysis was performed comparing how phenotypic data trends with different measures of aggregation (***Figure 21C***). Both the number of FRET positive cells measured by FRET FACS and the number of FRET positive puncta counted from confocal microscopy data significantly correlated with median lifespan (P values 0.0018 and 0.0005 respectively). In contrast, the detection of large SDS stable mHTTex1 aggregates using dFRA did not correlate as significantly with the decline in median lifespan (***Figure 21D***). This result underscores FRET as a more sensitive method for mHTTex1 aggregate detection. Moreover, it suggests that mHTTex1 aggregates detected through FRET play a substantial role in the decline in survival observed in mHTTex1-mNG/-mSc-I co-expressing flies.

3.4. The proteomic impact of mHTTex1 aggregates in *D. melanogaster* brains

3.4.1. HTTex1-mNG/-mSc-I aggregates sequester key intercellular transport regulators

Up to this juncture, the results outlined above have detailed establishment of a novel *D. melanogaster* HD model. This data has demonstrated that the co- expression of pathogenic mHTTex1-mNG/-mSc-I fusion proteins resulted in formation of HTTex1 aggregates which can be detected using FRET and significantly correlated with phenotypic decline. However, the data presented thus far has been primarily descriptive and as such has not shed light on the potential mechanistic relationship between aggregation and HD pathogenesis. Previous studies have shown mHTTex1 aggregates can form IBs which sequester proteins, organelles and lipids in neurons leading to vast functional dysregulation (***see section 1.4.3***). Hence, to gain insight into possible biological processes perturbed by aggregates in HD, immunoprecipitation (IP) experiments were preformed to enrich for HTTex1Q75-mNG/-mSc-I aggregates. Immunoprecipitates were subsequently analysed using label-free mass spectrometry (MS) to determine what proteins are co-enriched with mHTTex1-mNG/-mSc-I co-aggregates.

In brief, head lysates from 27-day old elavX;HTTex1Q75-mNG/-mSc-I flies were incubated with PHP2 antibody coated beads to immunoprecipitate HTTex1Q75-mNG/-mSc-I aggregates. The beads and the associated HTTex1Q75-mNG/-mSc-I aggregates were flash frozen before on bead digestion and subsequent label free MS analysis (***Figure 22A***). As a control, head lysates from elavX;HTTex1Q17-mNG/-mSc-I flies were also subject to PHP2 immunoprecipitation and subsequent label-free MS analysis. To validate the IP approach, WB analysis was performed using the immunoprecipitated samples (***Figure 22B***).

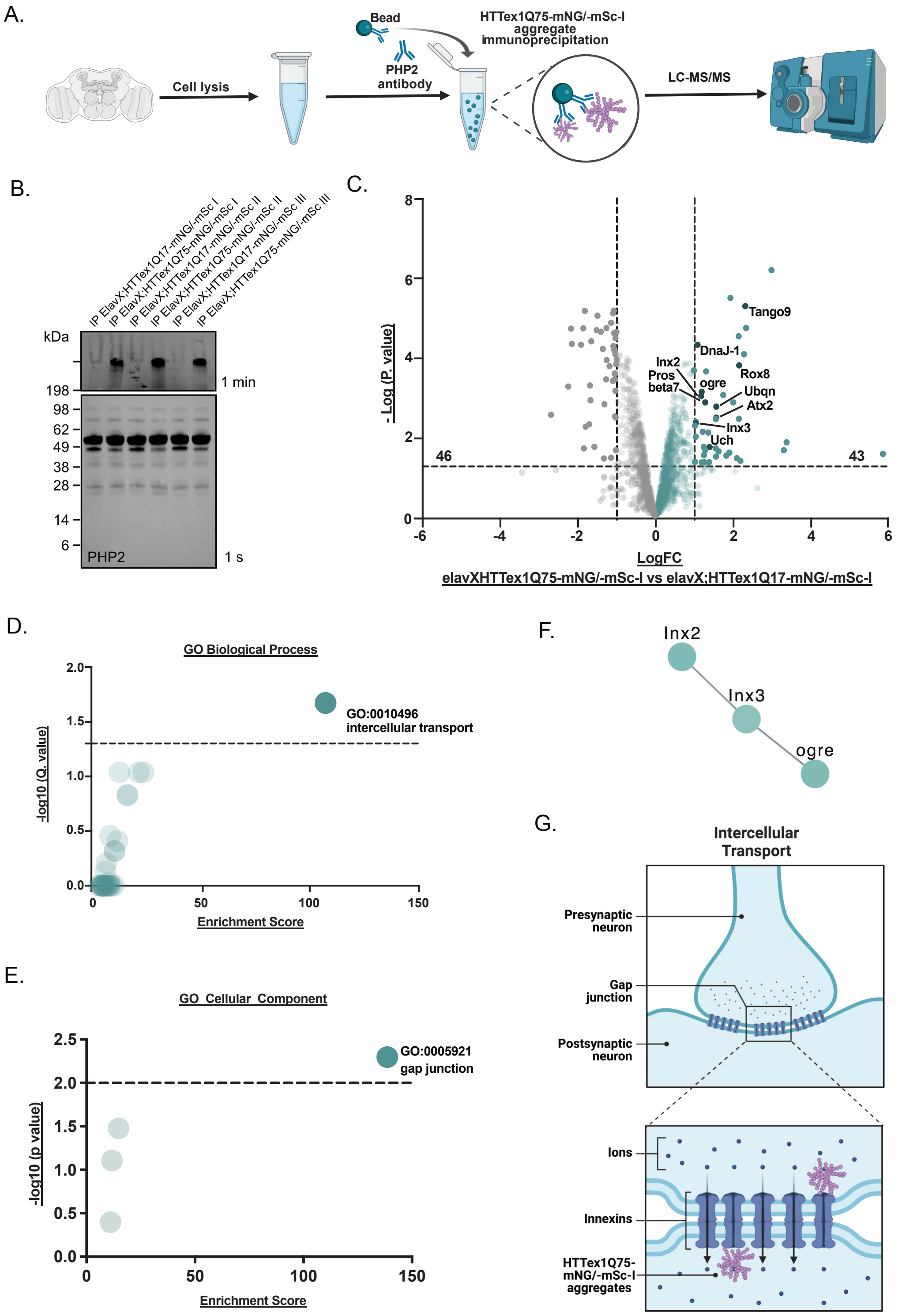

Figure 22. mHTTex1-mNG/-mSc-I aggregates sequester proteins involved in intercellular transport, splicing and proteostasis

A) *Schematic showing the experimental workflow of IP enrichment of HTTex1 aggregates from fly head lysates. Created using Biorender.* ***B)*** *Presence of HTTex1Q75-mNG/-mSc-I aggregates sequestered in SDS-PAGE gel pockets (upper panel) after IP was validated by WB using the PHP2 (anti-HTT) antibody. (Performed by Leonard Roth.)* ***C)*** *Volcano plot of 1607 proteins identified in IP MS. Proteins plotted via LogFC values calculated by* *comparing elavX;HTTex1Q75-mNG/-mSc-I vs elavX;HTTex1Q17-mNG/-mSc-I samples. Proteins enriched in HTTex1Q75-mNG/-mSc-I immunoprecipitates (green dots) and HTTex1Q17-mNG/-mSc-I immunoprecipitates (grey dots) respectively are plotted. Significance cut off: >1 or >-1 LFC and <0.05 P. value (>1.301 -log P. value) indicated by dotted lines on the x and y axis. Points of interest annotated with gene names.* ***D)*** *GO biological process and* ***E)*** *GO cellular component term enrichment analysis of upregulated protein hits. Plotted according to -Log (P. value). Significance cut-off: 0.05 P. value (>1.301 -log P. value) indicated on graph as dotted line. Performed using Metascape.* ***F)*** *Cluster of proteins significantly associated with HTTex1Q75-mNG/-mSc-I aggregates and involved in intercellular transport at the gap junction. Lines indicate STRING score. Created in Cytoscape.* ***G)*** *Schematic of hypothesised association of HTTex1Q75-mNG/-mSc-I aggregates with intercellular transport proteins at the gap junction between neurons. Created using Biorender.*

The immunoprecipitated fraction from elavX;HTTex1Q75-mNG/-mSc-I samples revealed a strong enrichment for insoluble HTTex1Q75-mNG/-mSc-I aggregates, which were sequestered in the gel pockets. While only a slight enrichment of the soluble, non-pathogenic HTTex1Q17-mNG/-mSc-I fusion proteins from fly head lysates was observed, indicated by an increase in band intensity at ~48 kDa (***Figure 22B***). In addition, no enrichment of insoluble HTTex1Q17-mNG/-mSc-I fusion protein was detected, indicated by an absence of signal in the gel pockets (***Figure 22B***). Therefore, supporting the notion that HTTex1 proteins with short polyQ tracts do not form large SDS-stable aggregates.

Subsequent quantitative MS was performed on the immunoprecipitated HTTex1Q75-mNG/-mSc-I aggregates and immunoprecipitated material from HTTex1Q17-mNG/-mSc-I samples. In short, samples were subject to on bead tryptic digestion, followed by label-free MS analysis to obtain label-free quantification (LFQ) values. The LFQ values were annotated with their respective gene names and Uniprot accession numbers using a MaxQuant pipeline (***see section 8.4.1***). In total, 1607 proteins were detected in both HTTex1Q17-mNG/-mSc-I and HTTex1Q75-mNG/-mSc-I immunoprecipitates (***Figure 22C***). Principle component analysis (PCA) highlighted the proteins detected within the elavX;HTTex1Q75-mNG/-mSc-I immunoprecipitates was distinctly separate from that of elavX;HTTex1Q17-mNG/-mSc-I immunoprecipitates, which indicated a strong polyQ-related clustering. Additionally, biological replicates of the respective samples clustered together, which confirmed a high similarity in sample identify (***Supplementary Figure 8A***).

Next, to find significant changes in protein levels, a T-test was performed. The significance threshold of greater than 1 log fold change (>1 LFC) and a P value of less than 0.05 (<0.05 P. value) was applied to uncover proteins which were significantly enriched in association with immunoprecipitated HTTex1Q75-mNG/-mSc-I aggregates compared to the immunoprecipitated background material from the head lysate of HTTex1Q17-mNG/-mSc-I co-producing flies. In doing so, 43 proteins were found to be significantly enriched only in association with HTTex1Q75-mNG/-mSc-I aggregates. In comparison, 46 proteins were significantly enriched only in HTTe1Q17-mNG/-mSc-I immunoprecipitates (***Figure 22C***).

To better understand whether the proteins enriched in the immunoprecipitates were involved in specific biological processes, a GO term enrichment analysis of the significantly enriched proteins was performed using Metascape [375]. In HTTex1Q17-mNG/-mSc-I immunoprecipitates, there was an enrichment of proteins which play a role in metabolic processes involving oxoacid (GO:0043436), carboxylic acid (GO:0019752), Organic acid (GO:006082),monocarboxylic acid (GO:0032787), small molecule (GO:0044281) and pyruvate (GO:0006090) metabolites (***Supplementary Figure 8C***). Therefore, implying that in that soluble, non-pathogenic HTTex1Q17 may associate with proteins involved in metabolic pathways. Whereas HTTex1Q75-mNG/-mSc-I aggregates were found to associate with proteins predominantly involved in intercellular transport (GO:0010496) (***Figure 22D***) at the gap junction (GO: 0005821) (***Figure 22E***). Therefore, suggesting mHTTex1 aggregates, through sequestering proteins involved in intercellular transport at the gap junction, may significantly perturb cell to cell communication through an aggregate specific gain-of-function.

Upon closer analysis of the HTTex1Q75-mNG/-mSc-I associated proteins, a cluster of invertebrate homologues for human connexins, Optic ganglion reduced (ogre), Innexin 2 (Inx2) and Innexin 3 (Inx3), (***Figure 22F***) were identified as the only proteins which were members of both the intercellular transport (GO:0010496) and gap junction (GO: 0005821) GO terms in the dataset. Ogre is a membrane bound Innexin subunit which forms a complex with Inx2 and Inx3 to establish gap junctions to allow the transport of cargo between cells [376]. Interestingly, research suggests gap junctions may play a role in the regulation of local neuronal activity and network dynamics in the striatum [377,378]. Therefore, enrichment of the membrane-bound Ogre, Inx2 and Inx3 proteins with HTTex1Q75-mNG/-mSc-I aggregates implies a potential interaction of these aggregates with gap junctions which may have neurotoxic effects within the striatum (***Figure 22G***).

Notably, previously known HTT-associated proteins were also enriched in association with HTTex1Q75-mNG/-mSc-I aggregates. These included, the polyQ protein ataxin-2 (Atx2) (***Figure 22C***), a key protein involved in the neurodegenerative disease spinocerebellar ataxia 2 (SCA2) [379], as well as key mediators of proteostasis such as proteasome subunit beta type-4 (Prosbeta7) a subunit of the proteome [380]. Furthermore, components of the UPS pathway, including ubiquitin carboxyl-terminal hydrolase (Uch) which processes ubiquitinated proteins [381], ubiquilin (ubqn), a protein with a ubiquitin-like protein domain and a ubiquitin-associated domain which physically associate with both the ubiquitination machinery and the proteosome [382], and DnaJ-1 (also known as hsp40), a molecular chaperone crucial for preventing protein aggregation [383] were enriched with HTTex1Q75-mNG/-mSc-I aggregates (***Figure 22C***). The identification of these proteins, confirms previous research showing mHTTex1 aggregates associate with the proteostasis machinery in cells, therefore disrupting downstream protein clearance processes [278,384].

Interestingly, novel HTTex1Q75-mNG/-mSc-I aggregate associated proteins were also identified. One such protein was Rox8 (***Figure 22C***), a *D. melanogaster* homologue of the known alternative splicing regulator cytotoxic granule associated RNA binding protein like 1 (TIAL1). Alternative splicing has been shown to be a key mechanism in HD patients which results in the formation of the *HTT1a* transcript [135,137] , therefore indicating Rox8 sequestration by HTTex1Q75-mNG/-mSc-I aggregates may have HD-relevant toxic effects. Moreover, the novel transport and Golgi organisation 9 protein (Tango9, or also known as LP09696p or SLC35F6), a protein predicted to be involved in protein secretion from the ER to the Golgi [385], was found to be the most significantly enriched in association with HTTex1Q75-mNG/-mSc-I aggregates (***Figure 22C***). Previous work has highlighted the interaction between the Golgi network and mHTTex1 aggregates [276]. Additionally, other studies have established wtHTT is required for ER-to-Golgi transport, with polyQ expansion drastically reducing cargo movement from the ER to the Golgi [386]. Therefore, the association of mHTTex1 aggregates and Tango9 may contribute to a reduction of ER-to-Golgi transport observed in HD models[387,388].

Collectively, the proteomics data obtained from fly immunoprecipitates showed mHTTex1-mNG/-mSc-I aggregates sequester key components of the proteome, ubiquitination pathways and the heat shock chaperone system. Additionally, mHTTex1-mNG/-mSc-I aggregates were found to predominantly associate with proteins involved in intercellular transport at the gap junction. Therefore, it can be inferred that mHTTex1-mNG/-mSc-I aggregates impact intercellular transport processes at the neuron- neuron junctions which may be partially responsible for the striatal neurotoxicity observed in HD brains [377,378].

3.4.2. The presence of mHTTex1-mNG/-mSc-I co-aggregates globally dysregulates RNA processing and ER-to-Golgi vesicle transport

The observation that HTTex1-mNG/-mSc-I co-aggregates associate with key intercellular transport proteins prompted investigation into how aggregate-mediated protein sequestration relates to global proteomic changes and subsequent pathogenesis observed in HD. From the biochemical and imaging data, it was apparent that HTTex1Q52-mNG/-mSc-I flies, despite harbouring a lower amount of mHTTex1-mNG/-mSc-I aggregates (***Figure 18 and Figure 20***), still exhibit a significant level of neurotoxicity *in vivo* (***Figure 21***). Therefore, it was hypothesised that the small amount of neuronal aggregates present within these flies may lead to significant proteomic changes, which may contribute to HD pathology.

With this objective in mind, quantitative proteomic analysis of HTTex1Q17-mNG/-mSc-I and HTTex1Q52-mNG/-mSc-I brain lysate samples was performed, to gain an overview of the global proteomic impact of mHTTex1-mNG/-mSc-I aggregates in fly brains. In brief, 10 whole brains per group across 3 biological replicates were dissected from 27-day old flies and lysed. The brain lysate was then denatured and analysed via SDS-PAGE. Coomassie blue staining of the SDS-PAGE gels allowed for excision of the total protein band, which was subsequently in-gel digested before quantitative label- free MS analysis (***Figure 23A***). Using a MaxQuant pipeline, gene names and Uniprot accession numbers were assigned to the identified peptides (***see section 8.4.2***). Within this dataset a total of 3590 proteins were identified, which is comparable to the number of proteins detected in other proteomic analyses of fly brains [389–392].

Subsequently, a PCA was performed on the resulting HTTex1Q17-mNG/-mSc-I and HTTex1Q52-mNG/-mSc-I datasets. As was observed for the IP MS dataset, PCA of the elavX;HTTex1Q52-mNG/-mSc-I and elavX;HTTex1Q17-mNG/-mSc-I brain lysate sample data showed a polyQ-related proteomic shift, indicating the global proteomes of the corresponding samples were distinct from one another (***Supplementary Figure 8B***). Therefore, demonstrating the proteome of the HTTex1Q52-mNG/-mSc-I HD flies was divergent from that of the non-pathogenic HTTex1Q17-mNG/-mSc-I strain. Furthermore, biological replicates of each strain clustered together, indicating reproducibility between sample preparations.

Next, to detect significant changes in protein levels, a T-test was performed. A significance threshold of greater than 1 log fold change (>1 LFC) and a P value of less than 0.05 (<0.05 P. value) was applied to identify proteins which were significantly changed in elavX;HTTex1Q52-mNG/-mSc-I fly brain lysates when compared to elavX;HTTex1Q17-mNG/-mSc-I controls. Subsequently, 132 proteins were found to be significantly changed of which 47 proteins were found to be increased in abundance and 85 proteins decreased in abundance in elavX;HTTex1Q52-mNG/-mSc-I fly brains when compared to elavX;HTTex1Q17-mNG/-mSc-I controls (***Figure 23B***).

Amongst the 85 significantly decreased proteins were key proteins involved in RNA splicing such as Neosin (Neos) and SMU1 (Smu1) (***Figure 23B***). Neos is orthologous for human nuclear receptor coactivator 5 (NCOA5). While the function of Neos is unknown, it contains an RNA binding motif (RRM) and is hypothesised to form part of the spliceosomal complex [393]. Additionally, the WD40 repeat-containing protein SMU1 is a splicing factor known in humans to be involved in pre-mRNA splicing. Specifically, SMU1 is a key component of the pre-catalytic spliceosome (also known as the B complex) where it stabilises interactions between the spliceosome domains [394,395]. Therefore, decrease of these splicing-related proteins would be detrimental to the cells ability to maintain canonical splicing and may contribute to the alternative splicing observed in HD [228,396].

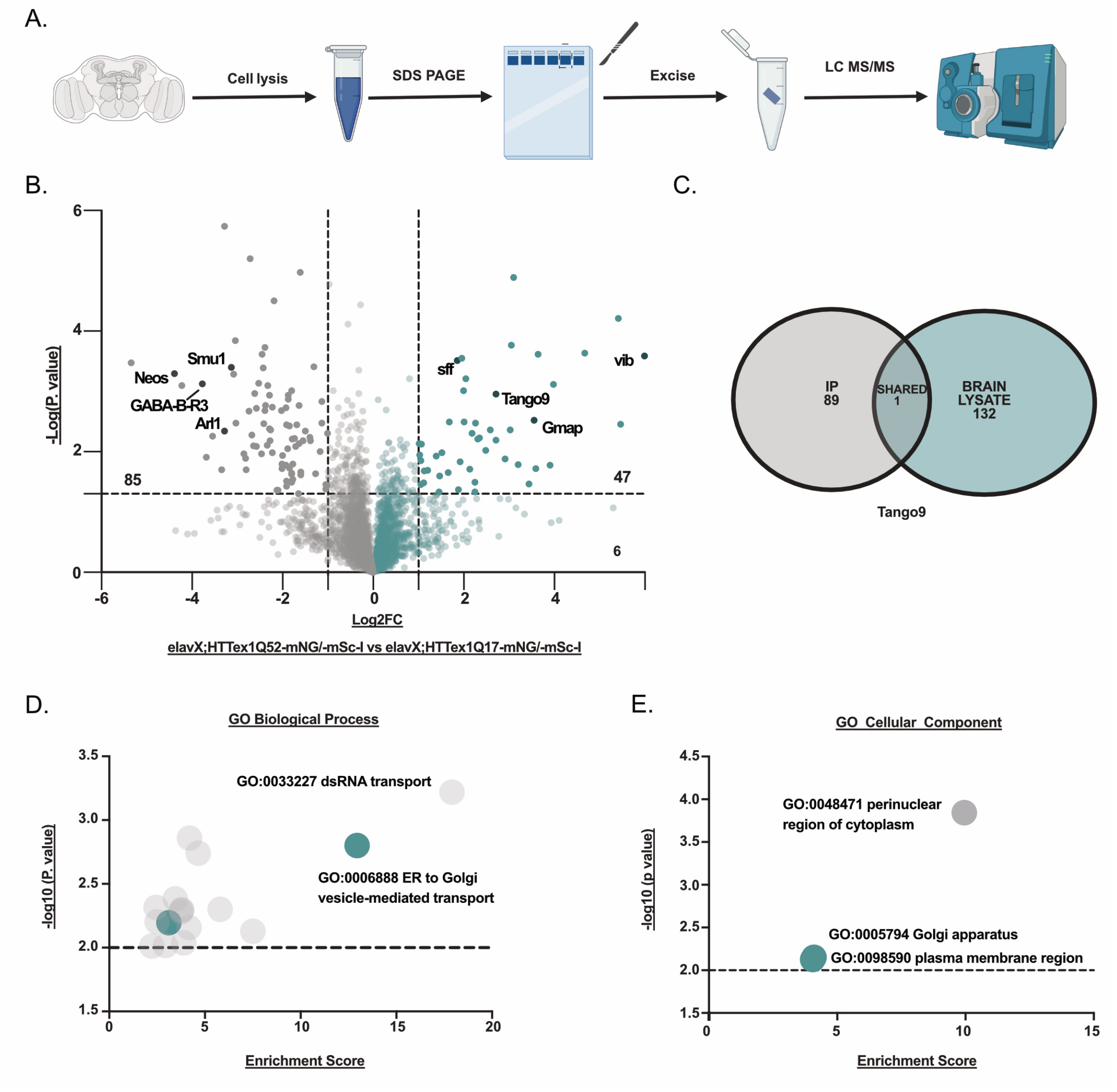

Figure 23. Pathogenic HTTex1Q52-mNG/-mSc-I expression results in global dysregulation of RNA splicing and ER-to-Golgi vesicle-mediated processes

A) *Schematic showing the experimental workflow of preparing fly brains for MS analysis.* ***B)*** *Volcano plot of 3590 proteins identified using MS. Proteins plotted via LogFC value calculated by comparing elavX;HTTex1Q52-mNG/-mSc-I vs elavX;HTTex1Q17-mNG/-mSc-I samples. Increased proteins (green dots) and decreased proteins (grey dots) in elavX;HTTex1Q52-mNG/-mSc-I fly brains are plotted. Significance cut off: >1 or >-1 LFC and <0.05 P. value (>1.301 -log P. value) indicated by dotted lines on the x and y axis. Points of interest annotated with gene names* ***C)*** *Venn diagram of the total number of significantly changed proteins identified in the IP proteomics dataset (89) and the brain lysate proteomics dataset (132). One protein (Tango9) is found in both.* ***D)*** *GO Biological Process and* ***E)*** *GO Cellular Component term enrichment analysis of decreased (grey circles) and increased (green circles) protein hits. Top terms plotted according to -Log (P. value). Significant cut-off: 0.05 P. value (>1.301 -log P. value) indicated on graph as dotted line. Performed using Metascape.*

Moreover, a significant decrease was observed of the gamma-amino butyric acid (GABA) receptor B subtype 3 (GABA-B-R3) (***Figure 23B***), a G-protein coupled receptor which regulates sleep and circadian rhythm through regulating GABA neurotransmitter transport [397,398]. In the context of HD, the GABAergic projection neurons of the striatum are predominantly affected by neurodegeneration [399]. Although many studies have implicated alterations in GABA-A receptor signalling in HD pathogenesis [400,401], to date there has been no mention of GABA-B receptor downregulation [400,401]. As GABA-B receptors are known inhibitory regulators of neurotransmitter release [402,403], reduction in GABA-B receptors like GABA-B-R3 may contribute to the alterations in GABA-mediated cortical inhibitory deficits in HD patients [404].

In addition, a significant decrease of the ADP-ribosylation factor-like protein (Arl1) was identified (***Figure 23B***). Arl1 is known to associate with the Ras-related protein (Rab-4A) subdomain of early endosomes where it recruits key proteins which modulate carrier vesicle formation [405]. Furthermore, Arl1 has been implicated as an important regulator of Golgi complex structure and vesicle trafficking recruiting effectors such as golgins and arfaptins to the trans-Golgi network (TGN) [406]. The significant decrease of Arl1 in elavX;HTTex1Q52-mNG/-mSc-I flies, accompanied by the aggregate sequestration of key intracellular transport proteins, may contribute to a dysregulation of TGN trafficking and downstream cellular processes.

On the other hand, the 47 proteins significantly increased in HTTe1Q52-mNG/-mSc-I fly heads were predominantly mediators of Golgi processes: Golgi microtubule-associated protein (Gmap), Tango9 and Vibrator (vib) (***Figure 23B***). Primarily located at the periphery of the cis- Golgi, Gmap (Orthologous to human TRIP11 or GMAP-210) tethers vesicles enabling their transport from the ER to the Golgi [407] . Thus, GMAP is essential for correct trafficking of transport vesicles within the early secretory pathway [408]. Intriguingly Tango9, which mediates protein secretion from the Golgi, was found as the only protein highly enriched both in association with mHTTex1-mNG/-mSc-I aggregates and in the global proteome of HD fly brains (***Figure 23C***). Therefore, suggesting the increase in Tango9 protein levels may be due to its association with mHTTex1 aggregates, leading to neuronal accumulation.

The most significantly increased protein globally in the presence of HTTex1Q52-mNG/-mSc-I aggregates was Vibrator isoform B (Vib), a phosphatidylinositol transfer protein which is orthologous to human phosphatidylinositol transfer protein beta (PITPNB). Phosphatidylinositol transfer proteins are responsible for catalysing the transfer of phospholipids between membranes [409] and are essential for COPI-mediated retrograde transport from the Golgi to the ER [410]. Interestingly, overexpression of Vib has been previously shown to both exacerbate HD-related neurodegenerative phenotypes and increase nuclear mHTTex1 aggregation toxicity in *D. melanogaster* and cell models [411]. Therefore, indicating that Vib may be a modulator of HD neurotoxicity. Further in-depth literature analysis revealed the significantly increased sugar free frosting protein (sff) (***Figure 23B***) also plays an active role in the Golgi apparatus. Orthologous to the Ser/Thr kinases SAD-A and SAD-B, sff is hypothesised to recruit vesicles to active zones of synapses. In an analogous function, sff has been shown to influence protein glycosylation in the Golgi cisternae [412].

In concordance, GO term enrichment analysis highlighted that co-expression of HTTex1Q52-mNG/-mSc-I fusion proteins associated with a decrease of proteins involved in dsRNA transport (GO:0033227) (***Figure 23D***) which were predominantly localised in the perinuclear region of the cytoplasm (GO:0048471) (***Figure 23E***). In parallel, the co-expression of HTTex1Q52-mNG/-mSc-I fusion proteins was related to a distinct increase of proteins involved in ER-to-Golgi vesicle-mediated transport (GO:0006888) (***Figure 23D***) and located primary at the Golgi apparatus (GO:0005794) or the plasma membrane (GO:0098590) (***Figure 23E***). String compartment scores were used to annotate clusters of significantly increased proteins which revealed a small cluster of Golgi localised proteins, including the proteins Gmap, vib, Arl1, Vti1a, g and Lerp all of which play key roles in ER-to-Golgi vesicle mediated transport (***Figure 24***).

In summary, the brain lysate proteomics data revealed the presence of HTTex1Q52-mNG/-mSc-I aggregates related to a global decrease in dsRNA transport, mediated by a decrease in spliceosomal proteins located at the perinuclear region of the cytoplasm.

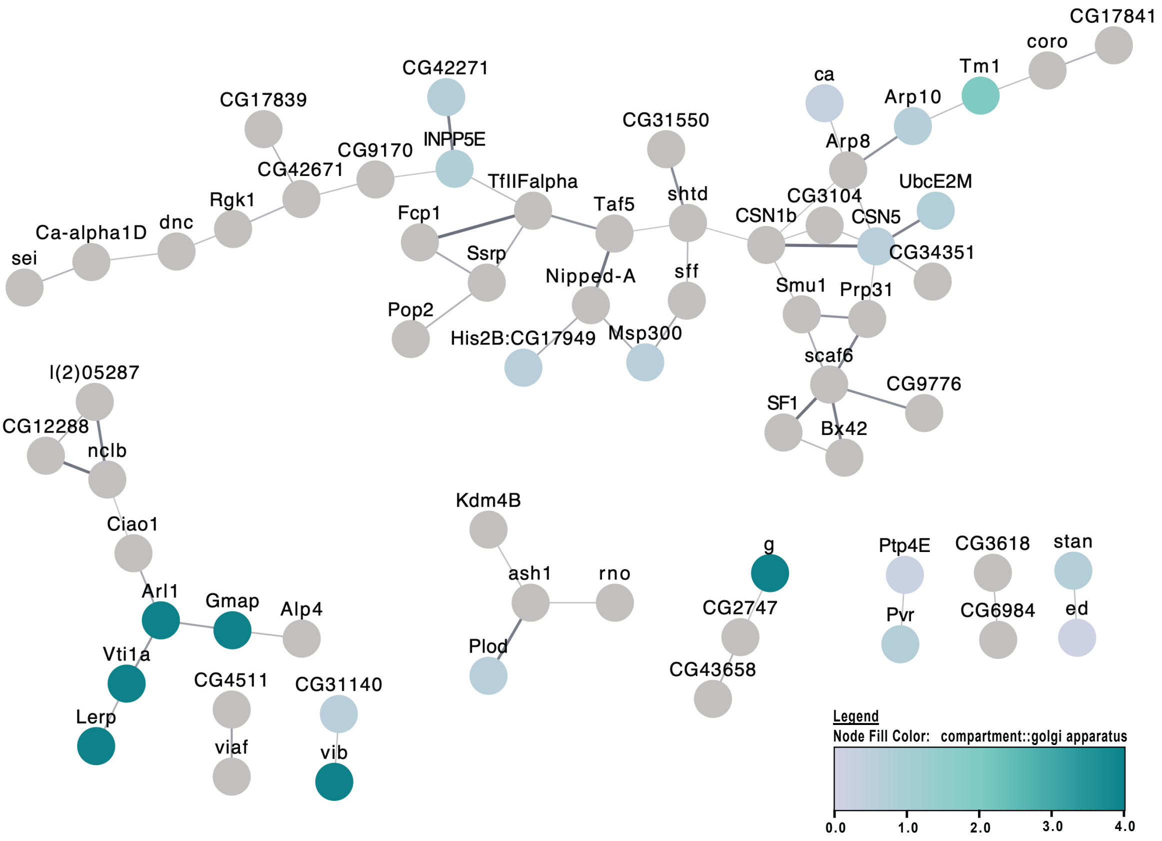

Figure 24. A cluster of Golgi associated proteins are upregulated in elavX;HTTex1Q52-mNG/-mSc-I transgenic flies

A) *STRING protein clusters of all significantly changed proteins detected in the whole brain lysate MS dataset (singlets excluded). Line thickness represents STRING database scores. Node fill represents the STRING compartment score for Golgi (see legend in bottom right of panel). Created in Cytoscape.*

Concomitantly, the presence of HTTex1Q52-mNG/-mSc-I aggregates was found to be associated with a global increase in ER-to-Golgi vesicle trafficking proteins primarily located at the Golgi apparatus and plasma membrane. When taken together, these data imply even the formation of low levels of pathogenic mHTTex1-mNG/-mSc-I aggregates is associated with vast proteomic dysregulation of neuronal intracellular trafficking. In turn, this may either protect neurons or contribute to the neuronal dysfunction and degeneration observed in HD.

3.5. Functional characterisation of mHTTex1 dysregulated proteins

3.5.1. Generating mHTTex1-mNG/-mSc-I RNAi *D. melanogaster* models

Both IP and global proteomics datasets highlighted the presence of mHTTex1-mNG/-mSc-I co-aggregates are associated with a dysregulation of transport proteins. On the one hand, association of mHTTex1-mNG/-mSc-I aggregates with intercellular transport proteins may directly influence neuron-to-neuron communication. On the other, the presence of mHTTex1-mNG/-mSc-I aggregates may indirectly change intracellular transport processes in neurons, specifically affecting the abundance of proteins involved in ER-to-Golgi vesicle transport processes. Intracellular and intercellular transport networks are highly interconnected and are vital for regulating the structural and functional integrity of neurons. Hence, dysregulation of intracellular transport, stemming from dysfunction in ER-to-Golgi vesicle transport, may disrupt the coordinated intercellular transport mediated by gap junctions. Thus, possibly resulting in the downstream neurotoxic cascade observed in HD. Following these observations, it was imperative to investigate what role the global increase of proteins involved in ER-to-Golgi vesicle-mediated processes plays, if any, in modulating mHTTex1-mNG/-mSc-I aggregate levels and subsequent HD-related neurotoxicity.

From the brain lysate proteomics dataset (***Figure 23***), 3 significantly changed proteins involved in ER-to-Golgi vesicle-mediated processes were selected to investigate further: Vib, GMAP and sff. Whilst Vib, GMAP and sff have been shown to regulate ER-to-Golgi vesicle mediated processes, they participate in distinct cellular roles (***Figure 25A***). Vib is key in vesicle membrane formation, GMAP facilitates tethering of vesicles to the Golgi and sff regulates organisation of Golgi processing and NMJ active zones [412–416]. These proteins were selected to gain a broad perspective on how several aspects of ER-to-Golgi vesicle-mediated processes are impacted in HD. As all these proteins were increased in the context of mHTTex1-mNG/-mSc-I aggregates, it was hypothesised that knockdown of said proteins may modulate HD-related phenotypes in flies. To investigate this hypothesis, new fly strains were created which both expressed RNAi, to facilitate knockdown of key ER-to-Golgi vesicle transport proteins, whilst also co-expressing the HTTex1-mNG/-mSc-I fusion proteins.

First, fly strains expressing RNAi hairpins against the respective target genes Vib, GMAP and sff were obtained from Vienna Biocenter (***Table 3***). The RNAi hairpin constructs in each of the fly strains was integrated on the 2nd chromosome [417] . Male flies from the RNAi strains were selected and mated with virgin female balancer flies (CyO/Sp;TM6/MKRS) to create stable RNAi fly lines (RNAi/Sp;+/MKRS). The balanced RNAi progeny were then mated with the HTTex1-mNG/-mSc-I fly strain (CyO/+; TM6/ HTTex1-mNG/-mSc-I). Using the phenotypic balancer markers, progeny flies negative for the markers Sp and TM6 and positive for markers CyO and MKRS were selected (CyO/RNAi;HTTex1-mNG/-mSc-I/MKRS). Hence, the resulting strains harboured hairpin RNAi constructs to mediate knockdown of either Vib, GMAP or sff in the background of HTTex1Q17-mNG/-mSc-I, HTTex1Q52-mNG/-mSc-I or HTTex1Q75-mNG/-mSc-I fusion protein co-expression (***Supplementary Table 4***). To enable co-expression of the RNAi hairpins and HTTex1-mNG/-mSc-I fusion proteins, the GAL4-UAS system was employed. The responder strains, containing both the HTTex1-mNG/-mSc-I transgenes and RNAi constructs were mated with the elavX driver strain. The resulting strains will henceforth be referred to as elavX;HTTex1-mNG/-mSc-I RNAi flies. In addition, the GMAP, sff and Vib RNAi flies which lacked the HTTex1-mNG/-mSc-I transgenes were mated with the elavX flies to act as HTTex1 negative control flies.

First, the efficacy of RNAi expression in elavX;HTTex1-mNG/-mSc-I RNAi flies was evaluated by quantifying Vib, Gmap, and sff transcript levels in 27-day old adult fly heads using qPCR. The RNAi-mediated knockdown of Gmap and sff transcripts in elavX;HTTex1-mNG/-mSc-I RNAi fly strains was confirmed by the absence of detectable transcripts (***Figure 25A and Figure 25B***). Unfortunately, RNAi-mediated Vib transcript knockdown could not be validated via qPCR in elavX;HTTex1-mNG/-mSc-I Vib fly strains (***Supplementary Figure 9E***), leading to their exclusion from further analysis. Subsequently, the co-expression of transcripts encoding for both mNG and mSc-I tagged HTTex1Q17, HTTex1Q52, and HTTex1Q75 fusions in elavX;HTTex1-mNG/-mSc-I RNAi flies was analysed using qPCR (***Supplementary Figure 9A-D***). In elavX;HTTex1-mNG/-mSc-I GMAP and elavX;HTTex1-mNG/-mSc-I sff flies, transcripts encoding for both mNG and mSc-I fusion proteins were detected (***Supplementary Figure 9A-D***). Notably, these transcripts were absent in elavX;W1118, elavX;GMAP, and elavX;sff control flies (***Supplementary Figure 9A-D***). Collectively, these results confirm the successful generation of elavX;HTTex1-mNG/-mSc-I GMAP RNAi and elavX;HTTex1-mNG/-mSc-I sff

RNAi flies by demonstrating the co-expression of RNAi hairpins and HTTex1-mNG/-mSc-I transcripts in fly neurons.

3.5.2. RNAi mediated knockdown of key Golgi proteins does not alter mHTTex1-mNG/-mSc-I fusion protein co-aggregation

Next, the impact of Gmap or sff knockdown on the co-aggregation of HTTex1-mNG/-mSc-I fusion proteins was assessed. Whole brains from 27-day old flies were analysed using confocal microscopy, and the quantification of FRET positive puncta within the mid-brain was performed (***Figure 25D***). No significant difference was observed in the number of FRET-positive puncta in elavX;mHTTex1-mNG/-mSc-I RNAi flies compared to elavX;mHTTex1-mNG/-mSc-I flies (***Figure 25D***). Further examination of the fly mid-brains revealed a consistent distribution of FRET-positive puncta between elavX;mHTTex1-mNG/-mSc-I RNAi and elavX;mHTTex1-mNG/-mSc-I flies (***Figure 25E, 25F, 25G***). Therefore, these findings indicate that knockdown of sff and Gmap does not impact the co-aggregation of either HTTex1Q52-mNG/-mSc-I or HTTex1Q75-mNG/-mSc-I fusion proteins in neurons.

3.5.3 RNAi mediated knockdown of sff drastically reduces lifespan and motor abilities of transgenic HD *D. melanogaster* strains

As stated previously, the level of mHTTex1 aggregates or inclusions has been previously correlated with HD toxicity [418] , however this toxicity may be initiated before or after aggregate formation. Therefore, it was hypothesised that, due to unaltered levels of aggregates in HTTex1-mNG/-mSc-I RNAi strains, sff and GMAP may not modulate processes upstream of mHTTex1 aggregate formation. Instead, these proteins may modulate processes downstream of mHTTex1 aggregation, which may lead to phenotypic changes in HD flies. To investigate this, it was assessed whether the knockdown of Gmap or sff was associated with any phenotypic changes.

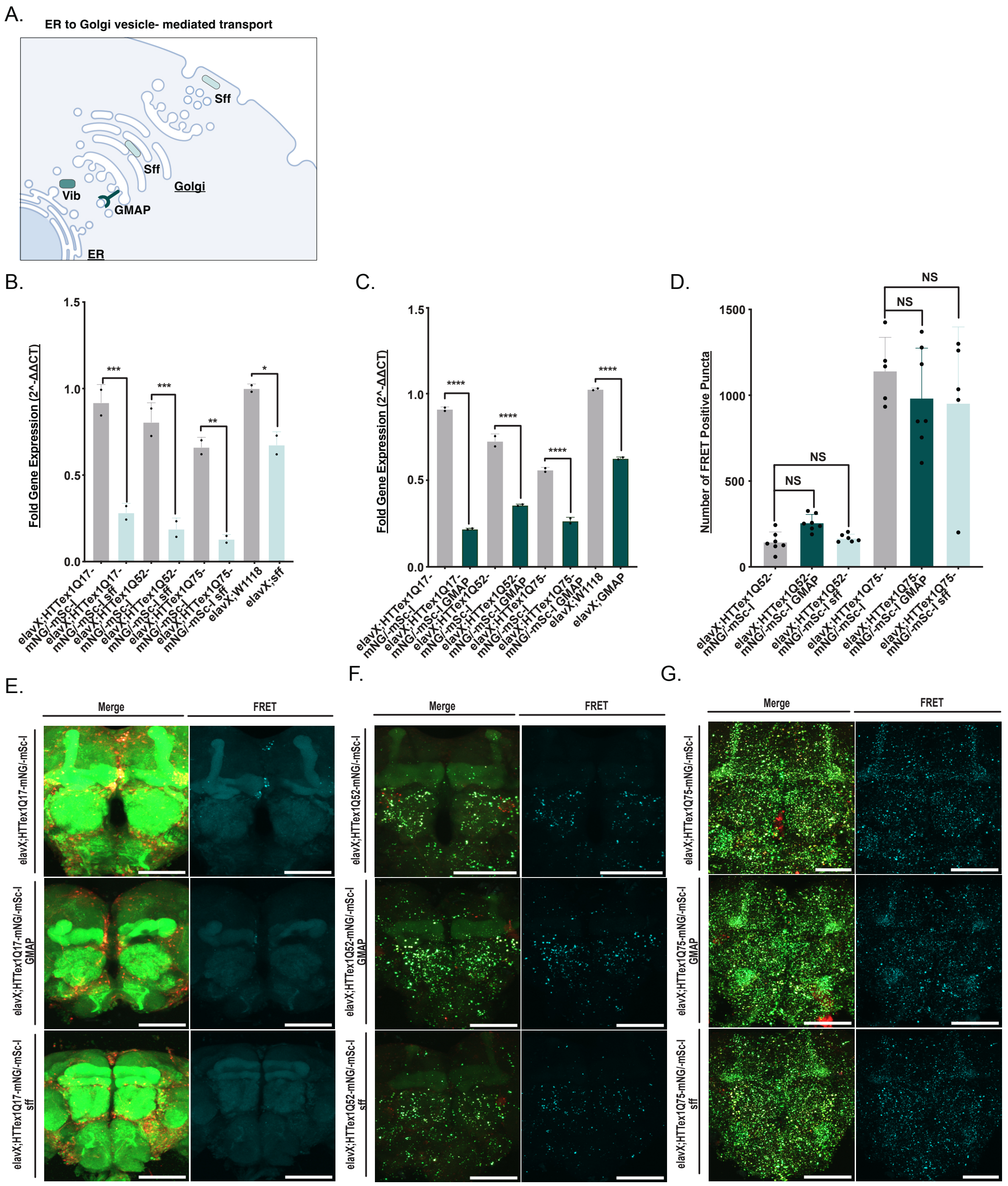

Figure 25. Knockdown of proteins involved in ER-to-Golgi vesicle mediated processes does not affect mHTTex1-mNG/-mSc-I neuronal puncta formation

A)** Schematic depicting where the proteins Vib, GMAP and sff perform their biological functions in the cell. **B)** qPCR analysis of sff and **C)** GMAP transcript expression. RNA from 27-day old fly heads from the indicated strains was analysed by qPCR to obtain Ct values. Fold gene expression calculated using the 2–ΔΔCt method [360] normalising to elavX;W1118 and actin (Act42). Each dot represents 1 biological replicate (2 analysed per sample). Each biological replicate value was the average of 2 technical replicates. Statistical significance assessed by* *ordinary one-way ANOVA multi-comparisons (*=P<0.05, **=P<0.01, ***=P<0.001, ****=P<0.0001). Error bars= SD.* ***D) *Quantification of FRET-positive puncta number from confocal microscopy images. Each dot represents an individual brain (6-7 analysed per strain). Statistical significance assessed by ordinary one-way ANOVA multi-comparisons (NS= P>0.05). Error bars= Standard deviation* ***E)****,* ***F)*** *and* ***G)*** *Confocal images of transgenic elavX;HTTex1Q17-mNG/-mSc-I fly brains (****E****), elavX;HTTex1Q52-mNG/-mSc-I (****F****) and elavX;HTTex1Q75-mNG/-mSc-I (****G****) fly brains. Scale bar= 100µm.*

First, it was evaluated whether knockdown of sff or Gmap in fly neurons had an influence on the survival of the flies. The elav;Gmap and elavX;sff strains exhibited no difference in median lifespan when compared to the elav;W1118 background control strain (~86, ~76 and ~88 days respectively) (***Figure 26A and 26B***). Therefore, showing that in a wild-type background, sff and Gmap knockdown does are significantly influence survival. The median lifespans of elavX;HTTex1Q17-mNG-mSc-I Gmap, elavX;HTTex1Q52-mNG/-mSc-I Gmap and HTTex1Q75-mNG/-mSc-I Gmap flies (~79, 63 and 48 days respectively) were comparable to that of the respective elavX;HTTex1-mNG/-mSc-I strains with no RNAi knockdown (elavX;HTTex1Q17-mNG/-mSc-I = ~83 days, elavX;HTTex1Q52-mNG/-mSc-I = ~67 days and elavX;HTTex1Q75-mNG/-mSc-I = ~55 days). Therefore, Gmap knockdown had no effect on survival (***Figure 26A and 26B***). In contrast, the median lifespans of elavX;HTTex1Q17-mNG/-mSc-I sff, elavX;HTTex1Q52-mNG/-mSc-I sff and elavX;HTTex1Q75-mNG/-mSc-I sff flies (~26, ~16 and 13 days respectively) were significantly reduced when compared to the respective elavX;mHTTex1-mNG/-mSc-I strains (elavX;HTTex1Q17-mNG/-mSc-I = ~83 days, elavX;HTTex1Q52-mNG/-mSc-I = ~67 days and elavX;HTTex1Q75-mNG/-mSc-I = ~55 days) (***Figure 26A and 26B***). Intriguingly, even in the non-pathogenic elavX;HTTex1Q17-mNG/-mSc-I flies sff knockdown drastically reduced the median lifespan. Thus, sff knockdown is detrimental to survival in flies co-expressing pathogenic as well as non-pathogenic HTTex1-mNG/-mSc-I fusion proteins.

Next, to evaluate whether knockdown of sff or Gmap in fly neurons resulted in motor neuron dysfunction the motor ability of elavX;HTTex1-mNG/-mSc-I RNAi flies was measured using the climbing assay. Similar to what was found in the lifespan assay, elavX;sff, elavX;Gmap and elavX;W1118 flies exhibited no significant differences in relative motor performance (~80%, ~97% and 100% respectively) (***Figure 26C and 26D***).

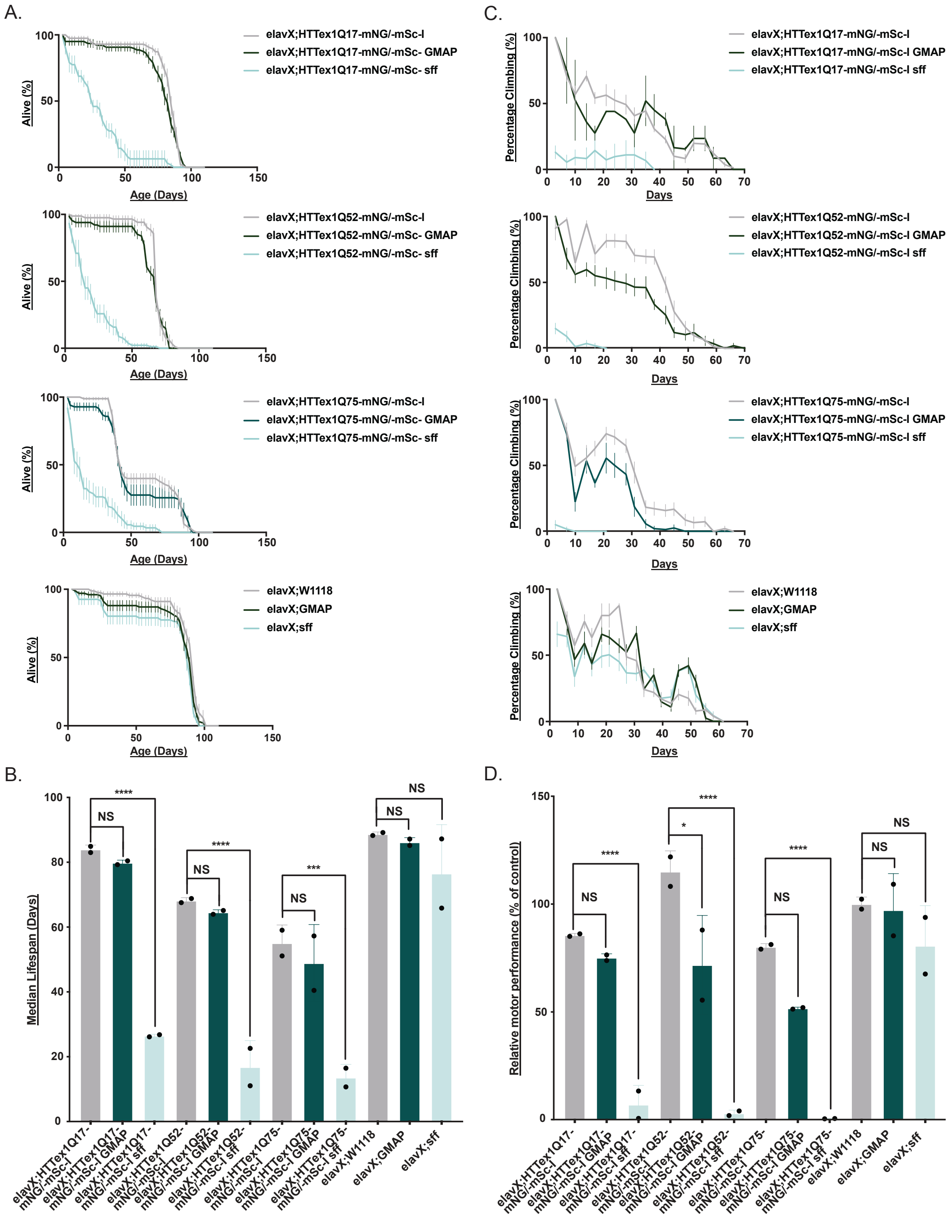

Figure 26. Knockdown of sff significantly reduces lifespan and motility of elavX;HTTex1-mNG/-mSc-I flies

A) *Lifespan plotted as percentage of alive flies from 2 biological replicates per strain (N≈ 50 flies per biological replicate) (left panel of graphs).* ***B)*** *Median lifespans calculated using IC50 values from lifespan curves for each biological replicate (right panel of graphs). Each dot represents one biological replicate. Statistical significance assessed by ordinary one way ANOVA multi-comparisons (NS=P>0.05,***= P<0.001, ****=P<0.0001). Error* *bars= SEM.* ***C)*** *Climbing ability plotted as percentage flies climbed of the total per day from 2 biological replicates (N≈ 50 flies per biological replicate) (left panel of graphs).* ***D)*** *Relative motor performance calculated as percentage of total area under the curves for each biological replicate relative to the respective elavX;HTTex1-mNG/-mSc-I strain (right panel of graphs). Each dot represents one biological replicate. Statistical significance assessed by ordinary one-way ANOVA multi-comparisons (NS= P>0.05, *=P<0.01, ****=P<0.0001). Error bars= SEM.*

Moreover, no significant difference in the relative performance of HTTex1-mNG/-mSc-I Gmap flies (elavX; HTTex1Q17-mNG/-mSc-I Gmap = ~75% , elavX; HTTex1Q52-mNG/-mSc-I Gmap = ~71% and elavX; HTTex1Q75-mNG/-mSc-I Gmap = ~79%) was observed when compared to the respective HTTex1-mNG/-mSc-I flies (elavX;HTTex1Q17-mNG/-mSc-I = ~85%, elavX;HTTex1Q52-mNG/-mSc-I = ~115% and elavX;HTTex1Q75-mNG/-mSc-I = ~79%) (***Figure 26C and 26D***). In contrast, the knockdown of sff was found to significantly reduce the relative climbing abilities of flies co-expressing non-pathogenic (elavX;HTTex1Q17-mNG/-mSc-I sff = ~7%) as well as pathogenic HTTex1-mNG/-mSc-I (elavX;HTTex1Q52-mNG/-mSc-I sff = ~2% and elavX;HTTex1Q52-mNG/-mSc-I sff = ~0.4%) fusion proteins.

Consequently, when taken together the lifespan and climbing assay data suggest that a knockdown of Gmap in HD transgenic flies does not significantly influence mHTTex1-mNG/-mSc-I neurotoxicity. Whereas the upregulation of sff in the presence of mHTTex1-mNG/-mSc-I aggregates may potentially be neuroprotective because its knockdown in HD transgenic flies dramatically increased neurotoxicity.

4. Discussion

In 1872 George Huntington published the first comprehensive description of a hereditary chorea now known as Huntington's disease (HD) [28]. At the time, the roots of this rare disease mystified the medical community. In writing about HD, Huntington himself admitted: "I know nothing of its pathology. I have drawn your attention to this form of chorea gentlemen, not that I considered it of any great practical importance to you, but merely as a medical curiosity, and as such it may have some interest." [28]. With this humble statement, Huntington indeed ignited a spark of interest into unravelling the mysteries of HD. Generations of researchers around the world have been inspired by Huntington's words, and have likewise strived to understand the causal underpinnings of HD. However, almost 200 years on from Huntington's seminal paper, how far have we come in understanding the pathology of HD?

HD is a debilitating neurodegenerative disease that devastates families and communities worldwide (***see section 1.1***). Following the breakthrough 1993 discovery of the causative mutation responsible for HD [39] great strides have been made in understanding how this inherited CAG repeat mutation in the *HTT* gene affects the protein (***see section 1.2***). However, understanding the complexities of the pathogenic mechanisms involved in HD has remained a challenge for researchers (***see section 1.4***). As such, there exists no disease modifying treatment or targeted therapy for HD (***see section 1.1.5***). Protein aggregates, consisting of mutant N-terminal HTT fragments including mHTTex1, have long been regarded as a hallmark feature of HD [255] , yet their link to HD pathology has been extensively contested (***see section 1.4.3***). Despite this, there has been an increasing body of evidence that points to mHTTex1 aggregates as potentially central to the pathogenesis of HD [253,419] . The precise mechanisms by which such aggregates may induce neuronal toxicity remains largely elusive.

In response to this gap in understanding, this project aimed to develop a novel HTTex1-mNG/-mSc-I fusion protein biosensor to enable FRET-based detection of aggregated mHTTex1 both *in vitro* and *in vivo*. First, this aggregation biosensor was used *in vitro*, to monitor co-expression of HTTex1-mNeongreen (HTTex1Q17-mNG, HTTex1Q52-mNG and

HTTex1Q75-mNG) and HTTex1-mScarlet-I (HTTex1Q17-mSc-I, HTTex1Q52-mSc-I and HTTex1Q75-mSc-I) fusion proteins. Large SDS-insoluble aggregates were observed in cells co-expressing pathogenic mHTTex1-mNG/-mSc-I fusion proteins (HTTex1Q52-mNG/-mSc-I and HTTex1Q75-mNG/-mSc-I) (***Figure 11B***). The polyQ-dependant appearance of mHTTex1-mNG/-mSc-I aggregates was accompanied by a similar polyQ-dependant increase in FRET (***Figure 11D***), suggesting that FRET could be used as a quantitative measure for mHTTex1-mNG/-mSc-I co-aggregation *in vitro*. Expanding on these findings, an *in vivo D. melanogaster* HD model was subsequently established, employing the FRET-based HTTex1 aggregation biosensor. Pan-neuronal expression of pathogenically expanded mHTTex1-mNG/-mSc-I fusion proteins *in vivo* resulted in reduced survival, impaired motor function, and the formation of SDS-stable aggregates (***Figure 18, 21A and 21B***), reproducing core HD characteristics [64]. Moreover, FRET was measured in live cells derived from flies co-expressing pathogenic mHTTex1-mNG/-mSc-I fusion proteins (***Figure 20C***), suggesting that FRET can be used to detect mHTTex1 aggregation *in vivo*. These FRET measurements were found to significantly correlate with the observed reduction in fly lifespan (***Figure 21C***), which cemented FRET as a novel *in vivo* method by which to detect and subsequently investigate mHTTex1 aggregates. Collectively, this work evidenced FRET as an effective biosensor for mHTTex1 aggregation both *in vitro* and *in vivo*, which is compatible with a diverse array of experimental techniques and is a valuable tool for future studies into the *in vivo* properties of mHTTex1 aggregates.

In addition to these experiments, the *in vivo D. melanogaster* HD model was investigated using label-free mass spectrometry (MS). IP experiments were used to enrich HTTex1Q75-mNG/-mSc-I aggregates from fly heads which were found to significantly associate with key intra and intercellular transport proteins (***Figure 22***). Subsequent MS analysis of fly head lysates derived from the heads of HTTex1Q52-mNG/-mSc-I co-expressing flies showed the presence of even a small amount of insoluble mHTTex1 aggregates related to a vast global dysregulation of proteins involved in a variety of intracellular processes, most significantly affecting proteins involved in ER-to-Golgi vesicle mediated transport (***Figure 23***). When taken together, these proteomic data provide insight into how insoluble mHTTex1 aggregates, are associated with a pronounced disruption of intra and intercellular transport in an *in vivo* context.

Finally, through RNAi mediated knockdown of key Golgi associated proteins, sugar free frosting (sff) was demonstrated to be vital for the survival and motility of HTTex1-mNG/-mSc-I co-expressing flies (***Figure 26)***. Therefore, indicating the potentially neuroprotective effect sff may exert in the brains of HD transgenic flies.

The following sections will delve into the interpretation of these findings. Initially, exploring the advantages and disadvantages associated with using FRET to measure mHTTex1 aggregation, with a specific focus on its application in the *in vivo D. melanogaster* HD model. Subsequently, elaborating on the proteins associated with mHTTex1 aggregates, as identified through mass spectrometry (MS), and discussing their potential implications for HD pathogenesis. Next, providing an in-depth analysis of the observed changes in the soluble proteome, shedding light on their potential significance in the context of HD. Lastly, this chapter will conclude by examining the role of ER-to-Golgi vesicle-mediated processes, particularly those involving sff, and their potential contribution to the neurotoxicity of the mHTTex1 protein.

4.1. FRET is a robust measure and marker of mHTTex1 aggregation

FRET-based aggregation detection has been previously shown to be a valuable tool in the study of neurodegenerative diseases [264,420–423]. With regards to HD research, a collection of studies have used FRET to study mHTTex1 aggregation [253,364–370] . A popular approach to monitoring mHTTex1 aggregation in these studies has been to use a time resolved FRET (TR-FRET) based immunoassay to quantify the mHTTex1 aggregate species present in complex biological samples [364,424] and cell extracts [368,369,425] . Similarly, cell-free assays have been shown to be accurate detectors of small, seeding-competent mHTTex1 aggregate species within complex bio samples [253,270]. While these methods are novel, innovate solutions for monitoring changes in mHTTex1 aggregation over time via FRET, they rely on the use of sample-derived lysates and therefore do not allow for the measurement or visualisation of mHTTex1 aggregation in a live system.

To offer an alternative approach for tracking mHTTex1 aggregation without the aforementioned constraints, a FRET-based HTTex1 aggregation biosensor was designed to be compatible with both *in vitro* and *in vivo* model systems (***Figure 9C***). This biosensor consists of two fluorescently tagged HTTex1 fusion proteins, one fused to the fluorescent protein mNeongreen (HTTex1-mNG) and one fused to the fluorescent protein mScarlet-I (HTTex1-mSc-I), both co-expressed within the same cell (HTTex1-mNG/-mSc-I). To compare the effect of pathogenic and non-pathogenic HTTex1 expression, fusion proteins containing either 17,52 or 75 glutamines (HTTex1Q17-mNG/-mSc-I, HTTex1Q52-mNG/-mSc-I and HTTex1Q75-mNG/-mSc-I) were assessed. Using a combination of biochemical, microscopy and FACS techniques (***Figure 11, 12, 18 and 20***), FRET was found to increase relative to the aggregation propensity of the HTTex1-mNG/-mSc-I fusion protein and as such could be used as a measure of mHTTex1 aggregation *in vitro* and *in vivo*.

In comparison with other methods of mHTTex1 aggregate detection, FRET-based HTTex1 aggregation biosensor offers several advantages. One advantage is that it enables sensitive, quantitative and non-invasive monitoring of HTTex1 aggregation. FRET can measure protein-protein interactions within 1 to 10 nanometres distance [338] because the intensity of FRET signal is directly proportionate to the distance between the donor and acceptor fluorophores [426]. Therefore, FRET provides a quantitative measure of molecular distances between proteins and thus protein interaction or aggregation. This is superior to other methods such a co-localisation, as these methods can only infer protein localisation and as such cannot provide information regarding molecular distances between proteins. Additionally, the measurement of FRET does not require the lysis of cells. As FRET can be measured fluorescently, it is compatible with live cell imaging thus providing an avenue to investigate protein interactions in the native context. In contrast, biochemical methods used to detect protein interactions and aggregation commonly rely on the use of antibodies and the lysis of cells under harsh detergent conditions which may alter protein properties.

Furthermore, the design of the FRET-based HTTex1 aggregation biosensor deliberately included several fusion protein features to generate an optimal, versatile method for mHTTex1 aggregate detection. Previously, FRET-based models of mHTTex1 aggregation have employed fluorophores such as YFP and CFP [427,428] . While these fluorophores are compatible with FRET-based detection, they commonly exhibit a high fluorescence bleed through and cross excitation due to their heavily overlapping excitation and emission spectra. Therefore, use of such fluorophores requires time consuming fluorescence correction. To solve these issues, a new family of fluorescent molecules has been synthesised, which exhibit superior fluorescence, faster maturation and photostability when compared to classical fluorophores [429,430]. Previous work has established these next generation fluorophores, including mNG and mSc-I, as excellent FRET donor and acceptor molecules which exhibit minimal fluorescence bleed-through and cross-excitation [429–432]. Therefore, by employing the mNG and mSc-I fluorophores fused to HTTex1, the FRET-based HTTex1 aggregation biosensor results in an easily detectable FRET signal.

The FRET-based HTTex1 aggregation biosensor design also considered how fusing of fluorescent proteins to HTTex1 would affect protein folding. Previous work has shown the N-terminus of HTTex1 to be critical for the formation of HTTex1 aggregates [144,433,434]. Therefore, addition of large tags to the N-terminus of HTTex1 may sterically hinder the folding and subsequent aggregation of mHTTex1. Thus, resulting in observations which do not accurately reflect the true aggregation properties and subsequent toxicity of mHTTex1. To avoid this, the FRET-based HTTex1 aggregation biosensor consists of fluorophores C-terminally fused to HTTex1 (***Figure 10***).

Moreover, the FRET-based HTTex1 aggregation biosensor vectors were designed to be highly versatile and user friendly. The pUAST-mNG/-mSc-I vector contains two enzyme restriction sites: one upstream of mNG and one upstream of mSc-I (***Figure 10***). Therefore, any two proteins of interest can be easily cloned into the pUAST-mNG/-mSc-I. In addition, the use of the pUAST-attB vector means the HTTex1-mNG/-mSc-I vectors are compatible with both *in vitro* and *in vivo* experiments. This flexibility can allow future researchers to study mHTTex1 aggregation in various experimental settings, enhancing the translational relevance of the findings.

Alongside the advantages, it is important to recognise that FRET based measurements of mHTTex1 aggregation have limitations. Firstly, FRET measurements significantly rely on the performance of the corresponding fluorophores. As fluorophores are sensitive to local changes like pH, ionic concentrations and temperature, FRET measurements can be skewed by subtle environmental changes [435]. Due to the sequestration of proteins, it is reasonable to assume mHTTex1 aggregates alter the cellular environment, therefore it is plausible that the mHTTex1 aggregate micro-environment may influence FRET measurements. To interrogate this possibility, it would be interesting to gain high resolution insight into the performance of fluorophores when soluble and aggregated through techniques such as fluorescence recovery after bleaching (FRAP).

Additionally, due to sensitivity of FRET to intramolecular distance, FRET signal can be reduced if the two fluorophores are not aligned. Therefore, if two proteins interact but the fluorophores are on opposite sides of the complex there may be no detectable FRET signal which generates false negative results [435]. Paradoxically, small protein interaction complexes generate a small FRET signal which is hard to distinguish from the background fluorescence [435,436]. Indeed, this was observed in the FRET-FACS analysis of elavX;HTTex1Q52-mNG/-mSc-I flies (***Figure 20C and 20D***). Due to the low abundance of HTTex1Q52-mNG/-mSc-I aggregates, the collective FRET signal *in vivo* was not strong enough to surpass the background fluorescent signal produced by soluble HTTex1Q52-mNG/-mSc-I fusion proteins. Therefore, as mHTTex1 is known to form large inclusions and small oligomers (***see section 1.3***), it is possible that the FRET measurements performed in this work were not detecting all sizes of mHTTex1 aggregates. Rather, the FRET signal represents a subsection of aggregates which are large enough to generate a strong FRET signal but not so large as to disrupt the distance between the two fluorophores. Hence, one future application of the FRET HTTex1 aggregation biosensor would be to structurally interrogate the FRET-positive mHTTex1-mNG/-mSc-I aggregates using correlative electron microscopy (CLEM) or fluorescence lifetime imaging microscopy (FLIM) to determine what aggregate species specifically cause the observed FRET.

Finally, while the HTTex1 aggregation biosensor employs C-terminally tagged fluorophores to minimise any impact of HTTex1 protein folding, the fusion of tags to HTTex1 regardless of location may impact aggregation. Recently, a study found the presence of single GPF tag significantly altered the structure and cellular properties of HTTex1 aggregates [278]. Moreover, research has found this effect is not limited to the presence of relatively large fluorescent proteins, but even the fusion of small epitope tags to HTTex1 can alter subcellular behaviour and toxicity [437]. Therefore, using this HTTex1 aggregation biosensor model, one must distinguish the effects of HTTex1 from the effect of the fluorophore. Additional optimisation of this model could incorporate HTTex1 controls without fluorescent tags to assess to what extent mNG and mSc-I labelling affects the polymerisation of HTTex1 proteins.

4.2. The *D. melanogaster* HD FRET model presents a novel avenue for *in vivo* mHTTex1 aggregation study

Exploiting the translational flexibility of our approach, the FRET-based HTTex1 aggregation biosensor was incorporated into *D. melanogaster,* thus generating a novel *in vivo* HD model organism (***Figure 13***). *D. melanogaster*, commonly known as the fruit fly, was chosen as a model organism as it is a well-established and widely used in scientific research, contributing significantly to our understanding of diverse biological topics, including genetic inheritance, development, innate immunity, and circadian rhythm [438–443]. Utilising flies in research provides a key advantage shared with other *in vivo* organisms — the ability to observe how genetic factors impact behaviour in a complex living system. Thus, allowing researchers to delve into the intricate complexities of biological systems, examining interactions among diverse cell types within tissues and organs. Yet, what distinguishes flies as a model organism is their accessibility and the simplicity with which fly experiments can be conducted. With a short developmental cycle of approximately 14 days from egg to adult fly and the ability of a single female fly to lay eggs upwards of 80 times a day [444], large experimental groups can be generated rapidly. Additionally, their modest size (around 3mm long) [445] and cost-effective diet of agar, yeast, and sugar make flies highly practical for extensive investigations while minimising laboratory space and expenses. Furthermore, owing to their significant genetic homology with humans, flies offer a valuable model for studying various aspects of human biology.

This is particularly evident in HD research, where a landmark 1998 study first demonstrated that polyQ expanded HTTex1 fragments in flies formed aggregates and induced neurodegeneration, mirroring the neuronal cell death seen in human HD brains [446]. This study established fly models of HD as a potent genetic system which can be used in investigations to better understand the role of mHTTex1 aggregates in HD pathology. Subsequent studies have since utilised fly models expressing fluorescently tagged HTTex1 fusion proteins [447–453]. Several of these investigations share a common methodology, employing a single GFP fluorophore tag to fuse with HTTex1 [447,448,450–453]. This approach facilitates the visualisation and quantification of mHTTex1 aggregate abundance. However, it lacks the capability to selectively isolate cells containing aggregates. Notably, only one study to date has used two distinct fluorescent tags for examining HTTex1 aggregation in flies, employing fluorescence co-localisation as an indicator for aggregation [449]. In addition, surprisingly few studies have used mHTTex1 fusion proteins to measure intermolecular FRET [365,367,427,428]. Of these few studies, all have used mHTTex1 fusion protein co-expression in cultured cells. Therefore, such cell-based assays are limited to an *in vitro* perspective on mHTTex1 aggregation, and thus cannot provide detailed information on the systemic role mHTTex1 aggregates play in HD. To date no studies have used FRET to study mHTTex1 aggregation in an *in vivo* model organism.

Hence, in contrast to other HD fly models, the FRET-based HTTex1 aggregation biosensor fly model holds a unique position. While, like other fluorescence-based HD fly models, it permits the investigation of mHTTex1 aggregates *in situ* within the native context of the brain, the utilisation of FRET in this model expands its potential. The use of FRET enables enrichment of live cells containing aggregates, which have the potential to be investigated with single cell resolution techniques to gain more comprehensive view of mHTTex1 aggregation *in vivo.*

Using this model, co-expression of pathogenic HTTex1-mNG/-mSc-I fusion proteins resulted the formation of SDS-stable aggregates which was associated with reduced survival and impaired motor function (***Figure 18D, 18E, 21A and 21B***). These findings support the well published notion that mHTT aggregates are associated with toxicity *in vivo* [253,277,315]. Subsequent confocal imaging highlighted mHTTex1-mNG/-mSc-I aggregates could be visualised in neurons using FRET (***Figure 20A***). Following this, FACS analysis highlighted the ability of FRET signals to enrich for live cells containing mHTTex1 aggregates (***Figure 20C and 20D***). These results collectively showed that FRET could not only be used to visualise mHTTex1 aggregates *in vivo*, but also be used as a selection marker for cells containing aggregates. Importantly, FRET correlated most significantly with the decrease in survival observed in flies expressing pathogenically expanded HTTex1-mNG/-mSc-I fusion proteins when compared to the detection of mHTTex1 aggregates using biochemical methods (***Figure 21C and 21D***). Thus, further supporting the notion that mHTTex1 aggregates are tightly linked to pathogenesis in HD and cementing FRET as a sensitive tool to detect mHTTex1 aggregates *in vivo.*

While the results obtained from the FRET HD fly model present promising insights, there remains opportunity for refinement. Initially, though FRET successfully detected mHTTex1 aggregates, the lack of specificity in identifying the type of aggregate poses a limitation. Given the diverse range of aggregate species coexisting within a cell, as previously discussed (***see section 1.3***), the current FRET methodology does not offer in-depth insights into the morphology and subcellular localisation of mHTTex1 aggregates. To address this limitation, electron microscopy (EM) was employed on whole fly brain sections. Notably, in the brains of elavX;HTTex1Q52-mNG/-mSc-I and elavX;HTTex1Q75-mNG/-mSc-I flies large structures were detected (***Figure 19***) which resembled previously reported mHTTex1 aggregates found in HD models and patients [64,238,277,290,454]. However, due to the absence of antibody or fluorescence detection, the identity of these structures remains speculatory. The ongoing debate in HD research regarding the neurotoxicity of specific mHTTex1 aggregate species necessitates a comprehensive understanding of the aggregate profile in the fly brain. Therefore, future iterations of the FRET HD fly model should explore the combination of FRET detection with structural imaging techniques, such as correlated light and electron microscopy (CLEM), to gain a nuanced perspective on the aggregate population within the fly brain.

Moreover, the experiments detailed in this study focused on a singular timepoint (27 days), providing only a snapshot into the timeline of HD pathogenesis. Given evidence suggesting that neurodegenerative processes in HD can initiate before visible markers like mHTTex1 aggregates emerge [455], exploring the relationship between early pathogenic changes and the presence of mHTTex1 aggregate species demands a temporal approach. Therefore, a more inclusive evaluation of the FRET HD fly model should involve assessments at various timepoints to capture the dynamic changes in mHTTex1 aggregates over the lifespan of an HD fly and their consequential impacts on HD phenotypes.

Furthermore, the FRET HD fly model created in this study, while insightful, does also have inherent limitations due to the use of flies as a model organism. Notably, the anatomical and physiological distinctions between fly and vertebrate nervous systems pose a significant challenge. With approximately 200,000 neurons [456], the fly brain has a reduced neuronal complexity in comparison with other disease model organisms like mice. As such, despite functional similarities between the fly central complex and the human basal ganglia implicated in HD pathology [457,458], the fly fails to fully recapitulate the intricate neuronal complexity of the human brain. Consequently, the application of the FRET HD fly model requires careful consideration as to whether its use aligns with the specific goals of the research. It is designed to unravel the fundamental biological processes underpinning mHTTex1 aggregation and toxicity in HD, rather than serve as a comprehensive model of human HD.

In conclusion, an assessment of the FRET HD fly model's efficacy must be grounded in the initial aim of this work: exploring the impact of mHTTex1 aggregates on the proteomic, cellular, and phenotypic *in vivo* landscape. By utilising FRET to detect aggregation and correlating this with phenotypic decline in flies, the FRET HD fly model effectively fulfils this aim. The model's impact can be expanded by leveraging the FRET signal to delve deeper into how the structure or localisation of mHTTex1 aggregates influences neurodegeneration over time in HD. While acknowledging that this work does not strive to replicate all intricacies of human HD in flies, the FRET HD fly model offers a truly novel means to investigate specific aspects of HD pathology, such as mHTTex1 aggregation, with the goal of translating these findings to other higher organisms.

4.3. HTTex1-mNG/-mSc-I aggregates associate significantly with intra and intercellular transport proteins

Following establishment of the FRET HD fly model, MS-based quantitative proteomics was employed to investigate the impact mHTTex1 aggregates have on the *in vivo* protein landscape. To achieve this the PHP2 immunoprecipitated material from elavX;HTTex1Q75-mNG/-mSc-I fly heads was compared to that of elavX;HTTex1Q17-mNG/-mSc-I flies (***Figure 22***). While the comparison between the immunoprecipitated fractions of pathogenic and non-pathogenic samples is valuable, additional studies could include proteomic assessment of the soluble proteins left in solution following mHTTex1-mNG/-mSc-I aggregate IP. Examination of such samples could provide additional insight into the broader soluble proteomic changes which occur in the presence of mHTTex1 aggregates in HD fly brains.

The use of PHP2 antibody enabled HTTex1Q75-mNG/-mSc-I aggregates formed *in vivo* to be specifically enriched from fly head lysates (***Figure 22B***). PHP2 recognises the proline rich domain (PRD) of HTT, which has been shown to be exposed on mHTTex1 fibrils [361] but is also present in soluble HTTex1 proteins. As such, the use of the PHP2 antibody for IP enabled preferential purification of mHTTex1 aggregates formed *in vivo* from fly head lysates. However, due to the presence of the PRD also in non-pathogenic HTTex1Q17-mNG/-mSc-I and soluble HTTex1Q75-mNG/-mSc-I fusion proteins, the co-purification of soluble mHTTex1 could not be completely prevented. In comparison, other proteomics investigations into mHTTex1 aggregates have relied on collecting the insoluble pellet fraction after lysate denaturation [278,459]. Such approaches produce insoluble samples which contain mHTTex1 aggregates in addition to other precipitated insoluble proteins, hence cannot provide specific detail as to the proteins associated with mHTTex1 aggregates. Therefore, due to the use of PHP2 the IP proteomics dataset can be seen as a comparatively more specific database of *in vivo* mHTTex1-mNG/-mSc-I aggregate-associated proteins. It is important to note, this dataset represents the proteins sequestered on the surface of HTTex1-mNG/-mSc-I aggregates. Future studies could therefore implement formic acid digestion of the immunoprecipitated mHTTex1-mNG/-mSc-I aggregates to reveal what proteins are co-polymerised with mHTTex1 aggregates and therefore are recruited early in the aggregation process [316,460]. Thus, deepening our insight into the protein mechanisms perturbed by mHTTex1 aggregation in HD.

In the IP proteomics dataset, a total of 1607 proteins were successfully identified in the immunoprecipitated samples, with 43 proteins exhibiting significant associations with mHTTex1-mNG/-mSc-I aggregates (***Figure 22C***). Notably, this subset of proteins included well-established components known from prior studies to associate with mHTTex1 aggregates, such as elements of the proteasome, chaperones, and ubiquitin-related proteins [461,462] which validated our analysis approach. In addition, previous research that has conclusively demonstrated a reduction in the function of the ubiquitin-proteasome system (UPS) in HD [463,464]. Therefore, the alignment between the IP proteomics data and previous research suggests that disruptions in the UPS may be mediated by aggregate sequestration of UPS proteins. This aggregate- mediated gain-of-function may impede the neuronal capacity to clear misfolded proteins, potentially intensifying the formation and persistence of mHTTex1 aggregates.

Furthermore, Rox8, the fly orthologue for TIAL1 a human protein already implicated in HD, was also found to be associated with mHTTex1 aggregates in our data (***Figure 22C***). The human TIAL1 is a stress granule associated protein which also plays a role in regulating RNA splicing [465,466] and is present in both soluble and insoluble factions of the HD patient prefrontal cortex [467,468]. Fascinatingly, TIAL1 possesses a glutamine rich ‘prion -related domain’ which has been shown to control the formation of prion-like aggregates which are recruited into stress granules [466]. As polyQ proteins are known to associate with other polyQ proteins, possibly through coiled coil interactions [469–473], the association of Rox8 and mHTTex1-mNG/-mSc-I aggregates in our proteomics data is in some regards not surprising. However, the association of Rox8 with mHTTex1-mNG/-mSc-I aggregates is intriguing, as aberrant alternative splicing has been observed in HD patients and models [136,227,396]. It is possible mHTTex1 aggregate-mediated association with Rox8 results in downstream disruption of alternative splicing, which may result in increased levels of HTTex1 transcripts and the expression of highly pathogenic HTTex1 protein [136]. Therefore, sequestration of *D. melanogaster* TIAL1 in mHTTex1 aggregates may potentially hint at stress granule involvement in the aberrant splicing pathology of HD. Alternatively, prion-like aggregates of TIAL1 may template the further aggregation of mHTTex1 protein, expediting the aggregation process.

Aligned with this theory of aggregate-mediated stress granule dysregulation, the stress granule polyQ protein Atxn2 which is associated with the hereditary polyQ disease spinocerebellar ataxia 2 (SCA2) was also identified as a HTTex1-mNG/-mSc-I aggregate-associated protein (***Figure 22C***). This supports previous work which has shown an association between Atxn2 and mHTTex1 [474,475]. Interestingly, knockdown Atxn2 has been shown to reduce mHTTex1 aggregate formation and toxicity *in vivo* [474]. Specifically, the removal of the C-terminal intrinsically disordered region of Atxn2, has been shown to significantly reduce both neurodegeneration and aggregate abundance HD *in vivo* models [475]. While the mechanisms behind the relationship between ATXN2 and mHTTex1 toxicity remain to be clarified, these findings provide a tantalising possibility that ATXN2 may be a key modifier of mHTTex1 aggregate-related toxicity.

In addition to uncovering well-known proteins associated with aggregates, this work also identified novel proteins with significant associations with mHTTex1-mNG/-mSc-I aggregates. Notably, the IP proteomics dataset revealed an enrichment of the membrane-bound Innexin proteins Ogre, Inx2 and Inx3, which may indicate potential interactions between mHTTex1-mNG/-mSc-I aggregates and gap junctions or membranes (***Figure 22C, 22F and 22G***). The Ogre-Inx2-Inx3 Innexins serve as invertebrate counterparts to human connexins, essential for forming gap junction channels that regulate small molecule flux between cells [476]. Gap junctions, recognised as the fastest means of cellular communication, are influenced by ionic concentration, pH, and phosphorylation without requiring receptors or chemical binding [476,477]. Specific cell populations in the brain such as glial cells employ gap junctions to buffer potassium ions among neurons to shield active neurons from glutamate excitotoxicity [478]. Therefore, any alteration in gap junctions can disrupt the maintenance of normal neuronal activity, potentially leading to glutamate excitotoxicity-induced neuronal death—a phenomenon implicated in HD due to heightened glutamate sensitivity in mice expressing HTTex1 [479]. Moreover, human connexins, particularly Cx43, exhibit abnormal distribution in the HD brain, with increased levels during disease development [480]. Therefore, supporting the notions that dysregulation of connexins may play a part in HD neurotoxicity.

It is important to note, that the co-enrichment of Ogre, Inx2 and Inx3 proteins with mHTTex1 aggregates observed may reflect either mHTTex1 aggregates directly associating with gap junction proteins at the plasma membrane (***Figure 22G***) or at any step during the synthesis, folding or transport pathway. On the one hand, previous work has established

HTTex1 preferentially binds curved phospholipid membranes [481], such as cell membranes and vesicles, via its N-terminal alpha helical domain [482]. Moreover, these membrane interactions of HTTex1 have been shown to strongly accelerate the fibrilization of HTTex1 proteins [481,483], thus resulting in downstream membrane disruption and cellular toxicity [484,485]. Therefore, the enrichment of proteins involved in cell adhesion and cell junction formation may support the notion that HTTex1 aggregates potentially propagate at cellular membranes. On the other hand, mHTTex1 aggregates have been shown to sequester endomembrane vesicles [486] and therefore might associate with gap junction proteins during their transport from the Golgi to the plasma membrane. Consequently, deeper analysis of the sub-cellular localisation of the Ogre, Inx2 and Inx3 in the presence and absence of mHTTex1 aggregates would be vital for bettering our understanding of the cellular processes most affected by mHTTex1 aggregation. Further investigations into the cell-specific functions of these Innexin proteins in the HD fly brain are required to understand wider role of gap junctions my play in HD pathogenesis.

Collectively, the presence of known proteins in the IP proteomics dataset serves as a robust validation of the MS approach used in this study, aligning with previous research. Additionally, this dataset also reveals that the intercellular transport Innexin proteins Ogre, Inx2 and Inx3 are novel mHTTex1 aggregate-associated proteins. While detailed investigation remains to be performed to address the molecular link between dysregulation of Innexin-mediated transport in HD, the findings of this project serve as an initial reference point for its potential role in mHTTex1 aggregate-related pathogenesis.

4.4. The presence of mHTTex1-mNG/-mSc-I aggregates affects RNA processing and intracellular transport

To complement the characterisation of the insoluble mHTTex1-mNG/-mSc-I aggregate associated proteins, the whole proteome of elavX;HTTex1Q52-mNG/-mSc-I fly heads was assessed (***Figure 23***). To this end, MS-based quantitative proteomics was performed on whole brain lysates from elavX;HTTex1Q52-mNG/-mSc-I flies and compared to that of elavX;HTTex1Q17-mNG/-mSc-I flies. This approach provides a broad view of the proteins changed in the presence of relatively low levels of mHTTex1-mNG/-mSc-I aggregates. Within this proteomics dataset at total of 3590 proteins were identified, 132 of which were significantly changed in elavX;HTTex1Q52-mNG/-mSc-I brains when compared to those of elavX;HTTex1Q17-mNG/-mSc-I flies (***Figure 23B***), indicating a profound difference in the proteosome in response to a modest quantity of HTTex1 aggregates.

Within the 132 significantly changed proteins, 85 were found to be decreased in the presence of HTTex1Q52-mNG/-mSc-I aggregates (***Figure 23B***). Primarily, this subset of decreased proteins included proteins involved in RNA splicing regulation (***Figure 23D***). The RNA binding protein Neosin (Neos) was found to be significantly lower in the presence of HTTex1Q52-mNG/-mSc-I aggregates. Neos is orthologous to human nuclear receptor coactivator 5 (NCOA5) and is speculated to be a component of the spliceosomal complex [393]. Likewise, a significant decrease in the levels of the spliceosomal protein SMU1 was observed. SMU1 is a key component of the pre-catalytic spliceosome (also known as the B complex) where it stabilises interactions between the spliceosome domains [394,395]. Interestingly, proteins involved in RNA splicing have been shown to significantly bind *HTT1a* RNA [487]. Rescue of HD phenotypes *in vivo* has been achieved through overexpressing splicing factors sequestered on *HTT1a* RNA [487], validating the importance of RNA splicing in mediating HD pathology. Additionally, aberrant splicing is an important pathological feature of HD with vast dysregulation in splicing observed in HD patients [398]. Dysregulation in RNA splicing can result in anomalous patterns of protein expression, with some proteins being overexpressed while others are under expressed. Such discrepancies can significantly influence downstream processes and may be responsible for the proteomic alterations observed in the proteome of HTTex1Q52-mNG/-mSc-I expressing flies.

When considered with the aforementioned HTTex1Q75-mNG/-mSc-I aggregate association with RNA splicing proteins, this result bears profound implications for the impact of mHTTex1 aggregates on the broader proteome and cellular functionality. Collectively, the data presented suggest the presence of mHTTex1 aggregates is intricately linked to the global decrease in RNA splicing proteins. However, to discern whether the proteomic changes of these RNA processes are a direct consequence of mHTTex1 aggregates or occur prior to aggregate formation, potentially due to the toxic effects of HTTex1 RNA itself [488–490] future studies must undertake time-resolved transcriptomic and proteomic investigations.

Such studies will be instrumental in gaining a more comprehensive understanding of how mHTTex1 aggregates impact RNA processes throughout the course of HD.

In addition, within the 136 significantly changed proteins, 47 were found to be increased in abundance in the presence of HTTex1Q52-mNG/-mSc-I aggregates (***Figure 23B***). These increased proteins were found to predominantly be involved in intracellular ER-to-Golgi vesicle-mediated trafficking (***Figure 23D***). ER-to-Golgi vesicle transport is the first step in the secretory pathway where proteins are packaged into vesicles destined for secretion into the extracellular space or to the Golgi for processing before being targeted to lysosomes and the plasma membrane [491]. Interestingly, wtHTT has been shown to be required for vesicle transport from the ER to the Golgi [492] . Therefore, the global increase of ER-to-Golgi vesicle transport proteins may have several implications for how the presence of pathogenic mHTTex1-mNG/-mSc-I aggregates relates to toxicity in HD.

First, the increase in ER-to-Golgi vesicle transport proteins could relate to a loss of wtHTT function. The expression of mHTT (140Q) has been shown to result in delay of ER-to-Golgi vesicle transport, whereas the expression of one copy of wtHTT was sufficient to ameliorate this phenotype in fibroblasts which implies HTT is required for ER-to-Golgi transport [492]. When extrapolated to *in vivo* neurons, the distance ER vesicles packed with cargo must travel to successfully be delivered to the Golgi are large. Hence, any impairment of ER-to-Golgi vesicle trafficking would have vast ramifications for protein production and secretion in HD. Consequently, the increase of proteins involved in ER-to-Golgi vesicle mediated transport, in general, may be a compensatory response to the reduced availability of wtHTT. To ascertain whether this is indeed the case in HD flies, further studies should monitor the levels of wtHTT in the presence and absence of pathogenic mHTTex1 protein.

Second, increase in ER-to-Golgi transport proteins suggests an increase in protein synthesis in the ER which must be trafficked to the Golgi for processing, therefore leading to a high functional demand. The association of HTTex1Q75-mNG/-mSc-I aggregates with key gap junction transport proteins, as identified in the IP proteomics dataset, implies a disruption in intercellular communication which may hinder the regular exchange of ions, amino acids and small molecules between neurons and other cells in the HD fly brain. Consequently, neurons harbouring mHTTex1-mNG/-mSc-I aggregates may have to compensate for this diminished intercellular transport capacity through increased protein production. In turn, to cope with this increase in protein and to circumvent the compromised intercellular protein transfer, an increase in ER-to-Golgi transport proteins may be required. Furthermore, the concurrent reduction in proteins involved in RNA splicing suggests the neuron may be attempting to curtail translation, potentially as a mechanism to control overall protein production. In support of this theory, research has shown increased translation is a pathological feature of HD due to an inactivation of the translation inhibitor eIF4E binding protein (4E-BP) in the striatum [493]. Administration of the translatory inhibitor 4EGI-1 ameliorated motor decline in HTTex1 mice models [493]. However, conflicting reports have also stated that mHTT expression represses protein synthesis through the stalling of ribosomes and reducing the expression of genes involved in ribosome biogenesis [494–496]. Therefore, the increase in ER-to-Golgi vesicle mediated transport proteins may be a response to an overall increase in protein synthesis in the HD fly, however further investigation into if translation is increased or decreased in our model is required to definitively state this.

Third, an increase of ER-to-Golgi vesicle mediated proteins can be an indication of cellular stress due to unfolded or misfolded proteins [497,498]. Due to the sequestration of key components of the UPR by HTTex1Q75-mNG/-mSc-I aggregates, the capability of the cell to re-fold or degrade both misfolded and potentially also non-misfolded proteins is reduced. As a result, misfolded proteins can accumulate in the ER, triggering an ER stress response pathway [499]. Additionally, overproduction of protein, such as in the overexpression system used in this work, can likewise instigate ER stress [499]. Interestingly, HD is associated with increased ER stress [500–502] , although the precise impact of this stress pathway on HD pathology remains incompletely understood. Studies indicate that overexpression of the ER stress-activated protein Sigma-1 receptor (S1R) can reduce HTT inclusions [502], suggesting a potential role for ER stress in the aggregate-related pathology observed in HD. Therefore, an increase in the abundance of vesicle-associated trafficking proteins may be an attempt by the mHTTex1-mNG/-mSc-I expressing cells to alleviate ER stress by trafficking protein out of the ER.

Finally, the increase in ER-to-Golgi vesicle mediated transport proteins may be simply due to IB sequestration, increasing the local concentration of the proteins trapped within the IBs. In support of this hypothesis, HTTex1-containing inclusions have been found to sequester proteins involved in ER-to-Golgi vesicle mediated transport [278]. Such studies have been corroborated by the well-documented sequestration of the ER, Golgi apparatus, endosomal membranes and endosomal vesicles by mHTT IBs [486]. Moreover, our own IP proteomics dataset revealed an enrichment for the ER-to-Golgi transport protein Tango9 with HTTex1 aggregates, which was also found to be enriched in the lysate proteomics dataset (***Figure 23C***). Therefore, there is convincing evidence that HTTex1 aggregates sequester endomembrane components which may lead to an increase in abundance of ER and Golgi proteins.

In summary, the collective evidence strongly suggests that the increase in ER-to-Golgi transport proteins observed in the brains of HTTex1Q75-mNG/-mSc-I and HTTex1Q52-mNG/-mSc-I co-expressing flies represents a potential compensatory response to the presence of pathogenic mHTTex1-mNG/-mSc-I aggregates. If this increase in protein abundance indeed serves as a compensatory mechanism, the logical implication follows that reducing the levels of proteins involved in this response could exacerbate mHTTex1-aggregate-mediated toxicity. The interplay between intracellular trafficking, RNA splicing, and ER stress introduces a multifaceted landscape that warrants deeper exploration to advance our understanding of HD pathology. Further studies should focus on whether the increase in ER-to-Golgi vesicle-mediated transport proteins is a direct result of mHTTex1 aggregates, or a stress response to overall proteostasis disruption. To this end, transcriptomic studies should be conducted to investigate whether the increase in the levels of these transport proteins is a result of increased gene expression or a result of mHTTex1 aggregate-mediated mechanisms.

4.5. sff may be key in HTTex1- related pathology

To interrogate the importance of vesicle-associated transport in HD pathology, three significantly increased proteins were selected from the whole brain lysate proteomics dataset: Vibrator (Vib), Golgi microtubule-associated protein (GMAP) and sugar free frosting (sff) (***Figure 23B and Figure 25A***). These proteins were selected as they all have been documented to be involved in ER-to-Golgi vesicle-mediated transport, however through divergent biological mechanisms. Vib is a phosphatidylinositol transfer protein, orthologous to human phosphatidylinositol transfer protein beta (PITPNB), and as such is required for the transfer of vital polyphosphoinositides between the ER and Golgi for vesicle synthesis [503]. Whereas GMAP acts downstream of vesicle formation at the ER. Orthologous to human GMAP210 (also known as TRIP11) [504], GMAP belongs to the Golgin protein family which are tethered to the cis-Golgi membrane and capture vesicles released from the ER [505–507]. While sff regulates downstream Golgi processing and active zone dynamics. Orthologous to the human serine/theonine kinase (BRSK2 or SAD-A), sff exerts dual functions both at the Golgi, where is has been shown to regulate N-linked glycosylation [412], and at the neuromuscular junction where it promotes vesicle clustering at the pre-synapse [416,508]. Therefore, analysis of these selected proteins was performed to provide a multifaceted view of how various aspects of ER-to-Golgi vesicle-mediated transport may contribute to HD pathogenesis.

It must be noted that proteins from the HTTex1Q52-mNG/-mSc-I aggregate-associated proteomics dataset were not taken forward for functional analysis *in vivo.* Within this dataset there are also interesting Golgi-related proteins such as Tango9 that would be fascinating to examine in the context of HD. Therefore, further work could focus on establishing RNAi knockdown FRET HD fly models for key aggregate-associated proteins to interrogate their role in HD pathogenesis. In doing so, this would deepen our understanding of the wider role HTTex1-mNG/-mSc-I aggregates play in HD.

Interestingly, pan-neuronal RNAi knockdown of GMAP had no effect on mHTTex1-mNG/-mSc-I fusion protein aggregation, lifespan or climbing in the FRET HD fly model (***Figure 25D, 25F, 25G and 26***). This may be due to the highly complex Golgin activity at the cis-Golgi. Research has shown GMAP210 knockout to be highly toxic in certain cell populations such as kidney cells, but other cells such as lung cells are unaffected [509]. Therefore, indicating that different cell types display varying degrees of vulnerability to GMAP knockdown. This may be in part due to the high degree of functional overlap between different Golgin protein variants. GMAP210 has been shown to share functional redundancy with GM130 another important cis-Golgi Golgin [507]. Additionally, loss-of-function experiments in flies have shown the cis-Golgins to individually be dispensable, whereas loss-of-function of multiple cis-Golgins is detrimental to viability [415]. Specifically, mutations in GMAP have been demonstrated to result in a compensatory cellular mechanism whereby another cis-Golgi Golgin (TMF) can acquire the ability to capture GMAP cargos [415]. Ensuring correct cargo trafficking between the ER and the Golgi is particularly important in neurons, as cargos must traverse large distances along neuronal axons between organelles [510]. Hence, this functional plasticity between different Golgin protein variants may be an adaptive cellular response to prevent any perturbations in Golgin activity, such as a GMAP knockdown, affecting vital endocytic function in vulnerable organs like the brain where correct ER-to-Golgi transfecting is required for neuronal activity and survival.

By utilising RNAi to reduce the abundance of the sff protein pan-neuronally, a striking increase in toxicity of both pathogenically expanded and wild-type HTTex1 was observed-marked by a significant decrease in both lifespan and motility of HTTex1-mNG/-mSc-I sff flies (***Figure 26***). Therefore, suggesting sff-mediated vesicle transport may be a required neuroprotective mechanism in HD. Intriguingly, the observed reduction in lifespan and impaired motility was not accompanied by any discernible alteration in the number of mHTTex1-mNG/-mSc-I fusion protein aggregates in the brains of sff knockdown flies (***Figure 25D, 25F and 25G***). Therefore, suggesting that increase of sff-related processes is necessary for survival and motor co-ordination when neuronal cells containing pathogenic mHTTex1 aggregates or high levels of non-pathogenic HTTex1 protein. Thus, prompting the question: How does a reduction in sff levels lead to increased HTTex1-mNG/-mSc-I fusion protein toxicity?

To answer this question, we must first establish in greater detail the role sff plays in neurons. The sff protein is a homologue of the SAD (Synapses of the Amphid Defective) kinase, called BRSK1/2 in humans [412]. One of the primary functions of SAD kinases in neurons is the regulation of axon growth, guidance, and branching, influencing the intricate wiring of neural circuits during development [511]. SAD kinases are required for the maintenance of neuronal polarity, a crucial aspect of neuronal morphology essential for proper function [511]. Through phosphorylation of Tau, the microtubule-associated protein, SAD kinases regulate microtubule dynamics during neuronal polarisation [512]. Importantly, SAD kinases are also key in modulating synaptic activity, through regulating presynaptic vesicle clustering at active zones and subsequent neurotransmitter release [513,514]. Thus, dysregulation of SAD kinase activity has been implicated in a variety of neurodegenerative diseases. For example, in Alzheimer's disease (AD), Tau has been found to be hyperphosphorylated by several kinases including SAD kinases [515,516]. Although not explicitly implicated in HD, the role of SAD kinases in phosphorylating microtubule-associated proteins such as Tau may be relevant to HD. For instance, wtHTT is known to be a hub for linking cargo transport and motor proteins, such as Tau, to co-ordinate microtubule trafficking [184]. Furthermore, Tau has been found in mHTT inclusions in HD patient brains [517–519], indicating HTT and Tau may be associated in HD. Therefore, it would be interesting to see whether sff modulates the phosphorylation of HTT as well as of Tau, and what collective impact sff phosphorylation has on vesicle transport along microtubules in HD.

Additionally, sff is recognised for its role in modulating Golgi vesicle interactions, subsequently influencing N-linked glycan expression in neurons [412]. N-linked glycans are complex sugar structures post-translationally attached to asparagine (N) resides in proteins. N-linked glycosylation starts in the ER for protein folding regulation before advancing to the cis-Golgi. In specific Golgi compartments, enzymes further modify the glycoprotein, with glycan types determined by the spatial organisation of the ER and Golgi. Although the role of sff remains to be fully established, previous studies have hypothesised sff modulates the compartmentalisation of glycan processing within the Golgi [412] . Mutations in sff have been shown to diminish its activity, resulting in alterations of the N-glycan profile in *D. melanogaster* and subsequent motility impairments [412]. Interestingly, sff is hypothesised to affect N-linked glycosylation by phosphorylating key proteins involved in vesicle interactions with Golgi stack-specific tethering factors, such as Golgins [412]. Consequently, reduced sff activity may lead to aberrant trafficking, resulting in the delivery of ER cargo to altered Golgi compartments, causing significant changes in N-linked glycans on glycoproteins.

The correct N-linked glycosylation is vital for correct protein folding, function, and localisation [520–522]. As such, alterations in N-linked glycosylation have been linked to several neurodegenerative diseases [523–525]. For example, increases in specific N-glycan structures have been identified in the cerebrospinal fluid and serum of Alzheimer's disease patients[526]. Additionally altered N-linked glycosylation has been implicated in Parkinson's disease [527,528] and multiple sclerosis [529]. In the context of HD, N-linked glycosylation has not been extensively studied, however increases in N-glycans have been noted in the brain tissue of HD transgenic mice and HD cell models [530,531]. Importantly, monitoring of glycan levels has emerged as a promising biomarker for tracking the progression of multiple neurodegenerative diseases [532].

While the toxicity of sff knockdown in HTTex1-mNG/-mSc-I co-expressing flies is tantalising, extrapolation of these results should be done with caution. Firstly, the GAL4 elav-driven HTTex1-mNG/-mSc-I fusion protein co-expression can be seen as an overexpression system due to the use of the exogenous UAS promoter. Hence, any alteration in Golgi processing through sff knockdown may disrupt the ability of the cell to cope with large amounts of misfolded and potentially non-misfolded protein. Therefore, the effects of sff knockdown may not be mHTTex1-mNG/-mSc-I specific but rather the result of protein overexpression. To definitively conclude the true role of sff in HD, the effect of sff knockdown in flies expressing non-huntingtin proteins must be assessed. Furthermore, due to the dual role of sff at both the Golgi and the pre-synapse, it is tricky to assess whether dysfunction of the processes at the Golgi or at the synapse are responsible for the observed increase in neurotoxicity observed in the HD flies. The Golgi apparatus and pre-synapse are inextricably linked, with the Golgi forming the vesicles which are sent to the active zone for transmission across the synapse [533–535]. Therefore, it is hard to analyse with the data presented here whether alterations at the Golgi or pre-synapse are behind to the enhanced toxicity of HTTex1-mNG/-mSc-I fusion proteins. Investigations into the pre-synapse structure and function in the FRET HD fly model are necessary to gain the full picture of sff's role in HD.

Ultimately, it is intriguing to speculate that the global increase of sff in HD is a response to increased ER stress resulting from aggregate-mediated sequestration of the proteostasis machinery. The increase of sff protein levels potentially augments N-glycosylation. Any reduction in sff levels may compromise the cell's ability to ensure correct N-linked glycosylation, with profound implications for protein localisation, functionality, and folding. Thus, causing toxicity even in the presence of non-pathogenically expanded HTTex1. Further in-depth research is required to identify sff's substrates and determine their significance in regulating Golgi dynamics and N-linked glycosylation. Additionally, it would be interesting to dissect whether the NMJ-related function of Sff contributes to HD, through characterisation of NMJ structure and function in our *in vivo* FRET HD fly model. Still, future work focused on understanding the role of glycosylation in HD, through the application of glycomics techniques [536,537], may provide promising data to aid biomarker development and treatment strategies.

5. Conclusion and Outlook

In closing, this project has contributed valuable insights into the mechanisms underlying mHTTex1 aggregate-related toxicity in HD. The work detailed herein has established a novel *D. melanogaster* HD model which enables the use of FRET techniques to track the effects of mHTTex1 aggregation *in vivo*. This model offers a promising platform for future research, particularly in the realms of single-cell proteomics, transcriptomics, and advanced electron microscopy (EM) approaches, capitalising on FRET as a marker of mHTTex1 aggregation. Moreover, combination of this innovative HD model with proteomics analysis has provided detailed insight into how insoluble mHTTex1 aggregates relate to global protein changes observed in HD. Functional *in vivo* validation of novel protein hits established the global increase of sff protein levels as potentially neuroprotective in the context of both pathogenic and non-pathogenic HTTex1 expression. The project outlined within this work serves as an initial point of reference for the role of sff and the wider implication of ER-to-Golgi vesicle-mediated transport in HD.

While considerable progress has been achieved in HD research over the centuries, understanding the depths of its pathology remain an ongoing endeavour. This sentiment is eloquently captured by George Huntington: “And here we must leave the interesting subject of the pathology of this disease, and trust that the science, which has accomplished such wonders, through the never-tiring devotion of its votaries, may yet “overturn and overturn, and overturn it,” until it is laid open to the light of day.” [28].

6. Materials

6.1. Chemicals and consumables

0.05% trypsin EDTA	Gibco
0.5, 1.5, 2 , 5 ml tubes	Eppindorf
15, 50 ml tubes	BD Falcon
20mm x 20mm coverslips	Epredia
384 well black/clear plates	Falcon
3M plate film	QIAGEN
4-12% bis Tris gels	Novex by Life Sciences
5ml polystyrene round bottom tubes with cell strainer cap	Falcon
99 well PCR plate (without skirt)	Sarstedt
Amphicillin	Biomol
Amytracker 480	Ebba Biotech
Applied Biosystems™ MicroAmp™ Optical 384-Well Reaction Plate	Thermo Fisher Scientific
Bacto-Peptone	Roth
Bacto-yeast	Roth
Beer yeast	Gewürzmühle Brecht
Bovine serum albumin (BSA)	Roth
Calcium chloride (CaCl3)	Roth
Cell culture plates 6 well, 24 well	Sarstedt
Chloroacetaminde (CAA)	Sigma
cOmplete™ protease inhibitor cocktail, EDTA free	Roche
Coomassie brillian blue G-250	Serva
Corn flour	Mühle Schlingermann
CoverGrip™ sealant	Biotium
DAKO fluorescence mounting media	Dako
Deoxyribonucleotides (dNTPs)	Thermo Scientific

DEPC-treated water	Ambion
Dimethylsulfoxide	Roth
Dithiothreitol (DTT)	Sigma
DMEM 4.5g/L Glucose	Gibco
DMEM 4.5g/L Glucose phenol-free	Gibco
DNA gel loading dye (6X)	In house AG Wanker stock
Dualfilter T.I.P.S	Eppindorf
Dulbecco's Phosphate-Buffered Saline (DPBS)	Gibco
Dynabeads™ Protein G for Immunoprecipitation	Invitrogen by Thermo Fisher Scientific
ep T.I.P.S	Eppindorf
Ethanol (pure 100%)	Roth
Ethidium bromide (10mg/ml)	Sigma-Aldrich
Ethylenediaminetetra acetic acid (EDTA)	Merk
Fetal bovine serum (FBS)	Life technologies
Fly vials 26 and 49 mm diameter	K-TK
Forceps	Carl Roth GmbH
Glycerol	Honeywell
Glycogen, RNA grade	Thermo Fisher Scientific
HEPES	Sigma
Hoechst 33342 (Trihydrochloride)	Invitrogen
Isoproanol	Roth
Kanamycin	Sigma
LE agarose	Biozym
Lipofectamine 2000	Life technologies
Magnesium chloride (MgCl)	Roth
Malzin	Ulmer Spatz
Membrane filter 0.2 µm	Whatman® Cytiva
Mesh plano 200	Plano
Methanol	Sigma
Methyl 4-hydroxybenzonate (Nipagin)	AppliChem
Microplate 384 well clear	Greiner bio one

Microscopy slides	Thermo Scientific
Mifepristone (RU486)	Sigma
Nonidet (NP40)	Roche
Normal goat serum (NGS)	Jackson ImmunoResearch
NuPAGE LDS sample buffer (4X)	Novex by Life Sciences
NuPAGE MES SDS running buffer (20X)	Invitrogen
NuPAGE MES SDS tranfer buffer (20X)	Novex by Life Sciences
Opti-MEM (1X) + Glutamax™	Gibco
p-t-Octylphenyl-polyoxethylen (Triton X-100)	Sigma-Aldrich
Paraformaldehyde (PFA) (16%)	Sigma-Aldrich
PBS	In house AG Wanker stock
Penicillin/Streptomycin (Pen/Strep)	Life Technologies
Pierce Protease and Phosphatase Inhibitor Mini Tablets	Thermo Scientific
pluriStrainer® 10 µm	pluriSelect
Polyethylenimine (PEI)	Polysciences
Ponceau-S solution	Sigma-Aldrich
Precellys CK14 tubes	Bertin Technologies
Propionic acid	Roth
RNase-free water	QIAGEN
Serological pipettes (2, 5, 10, 25ml)	Greiner bio one
Skimmed milk powder	Sigma-Aldrich
Sodium chloride (NaCl)	Roth
Soy flour	Bauck GmbH
Staining block, clear glass with cavity	Fisher Scientific
Sucrose	Janssen Pharmaceuticals
Sugar syrup	Grafschafter Krautfabrick
T75 flasks	Sarstedt
Transfer membrane Amersham™ Protran® 0.45 µm	Amersham Cytiva
Triethylammonium bicarbonate (TEAB) 1M	Thermo Scientific

TRIS Base (hydroxymethylaminomethane)	Merk
TWEEN 20	Sigma-Aldrich
VECTASHIELD® Antifade Mounting Media	Vector Laboratories
Whatman® gel blot paper	GE healthcare lifesciences

Any chemical not included in this list which were required for the preparation of buffers were purchased from Roth.

6.2. Enzymes, proteins, and markers

Benzonase Nuclease	Merck Millipore
Collagenase I	Invitrogen
Dispase	Sigma- Aldrich
Gateway BP clonase Enzyme Mix	Thermo Scientific
Gateway LR Clonase Enzyme Mix	Thermo Scientific
GeneRuler 1kb DNA Ladder	Life Technologies
Gibson Assembly Mix	New England Biolabs
PWO SuperYield DNA Polymerase	Roche
Restriction Enzymes	New England Biolabs
SeeBlue™ Plus2 Pre-stained Protein Standard	Invitrogen

6.3 Kits

BCA Protein Assay Reagents	Pierce
Dneasy® Blood and Tissue Kit	QIAGEN
High-Capacity cDNA Reverse Transcription Kit	Thermo Fisher Scientific
InviSorb® Fragment CleanUp	INVITEK
NucleoBond Xtra Midi EF, Midi Kit	Machery-Nagel
NuPAGE Novex® Bis-Tris gel system	Invitrogen
PWO polymerase kit	Sigma Aldrich
QIAprep Spin Miniprep Kit	QIAGEN
RNeasy® Mini Kit	QIAGEN
SYBR Green PCR Master Mix	Applied Biosystems by Thermo Fisher Scientific
WesternBright Quantum Chemiluminescent HRP substrate	Biozym

6.4. Buffers

Blocking buffer	3% Skimmed milk powder in PBS-T
Brain lysis buffer (BLB)	10mM Tris-HCL pH 7.4, 0.8M NaCl, 1mM EDTA, 10% Sucrose, 1x cOmplete™ Protease Inhibitor Cocktail tablet

Cell lysis buffer	50mM HEPES pH 7.4, 150mM NaCl, 1.5mM MgCl2, 0.1% NP-40, 1mM EDTA, 1x cOmplete™ Protease Inhibitor Cocktail tablet, 2units/ml benzonase
Coomassie staining solution	30% Ethanol, 10% Acetic acid, 0.05% Coomassie brilliant blue G-250
DNA gel loading dye (6X)	25mg Bromophenol blue, 25mg Xylencyanol FF, 15mg Ficoll 400, 30ml 99% Glycerin, Bidest added to make total volume 100ml
HL3 (1L)	4.09g NaCl, 0.37 KCl, 4.07g MgCl2, 0.84g NaHCO3, 1.19g HEPES, 1.89g Trehalose, 39.36g Sucrose pH 7.2
LB- (Luria Bertani) agar	1% Bacto Peptone, 0.5% yeast-extract, 1% NaCl, 2% Agar, Antibiotic
LB- (Luria Bertani) medium	1% Bacto Peptone, 0.5% yeast-extract, 1% NaCl, Antibiotic
Lysis buffer (for whole brain lysate MS)	1xPBS, 10% SDS, 1x Sample buffer and 1 Pierce Protease and Phosphatase Inhibitor Mini Tablet
Minimal BLB	Tris-HCl pH 7.4 (4°C) 10 nM
PBS (10X)	1.37 mM NaCl, 27 mM KCl, 100 mM Na2HPO4, 17.6 mM KH2PO4, pH 7.4
PBS-T	1x PBS, 0.05 % Tween-20
Sample buffer (5X) (for whole brain lysate MS studies)	15ml 2M Tris/HCL pH 6.8, 10g SDS, 50g Glycerin, 25ml β-Mercaptoethanol, 5ml BFB

SOC medium	2 % Tryptone, 0.5 % yeast-extract, 10 mM NaCl, 2.5 mM KCl, 10 mM MgCl2, 10 mM MgSO4, 20 mM Glucose
Special fly medium (6L)	48 g Agar, 480 g beer yeast, 120 g Bacto-peptone, 120 g Bacto-yeast, 420 ml Sugar syrup, 3 g MgSO4, 3 g CaCl3, 6 g Nipagin, 60 ml EtOH, 36 ml Propionic acid
Standard fly medium (6L)	25 g Agar, 45 g beer yeast, 50 g soy flour, 400 g corn flour, 75 ml Sugar syrup, 300 ml Malzin, 8 g Nipagin, 25 ml EtOH, 32 ml Propionic acid
TAE (20X) (1L)	Tris/base 242g, acetic acid 57.1ml, 100ml EDTA (0.5M pH 8)
TE buffer	1 mM EDTA, 10 mM Tris, pH 8.0
Wash buffer (for EM studies)	1ml glycine, 1ml 1xPBS, 1ml 10% BSA, 7ml Bidest

6.5. Oligonucleotides

Table 1: Oligonucleotides

Primer Name	Sequence (5’-3’)	Notes
446. mScarlet-I attb fw	GGGGACAAGTTTGTACAAAAAAGCAGGCTTGatggtgagcaagggcgag	
447. mScarlet-I attb rev	AGACCACTTTGTACAAGAAAGCTGGGTTTAGCCCGTAGAATCGAGACC	
448. mNeongreen attb fw	GGGGACAAGTTTGTACAAAAAAGCAGGCTTGATGGTGTCCAAGGGCGAAG	
449. mNeongreen attb rev	AGACCACTTTGTACAAGAAAGCTGGGTTTAGCCCAGGTCTTCTTCAGAG	
Act42A (FBgn0000043) qPCR fw	CTTTAGTGGTCGACAACGGATCCG	
Act42A (FBgn0000043) qPCR rev	CCTTTTGTCCCATTCCTACCATTACGCC	
aTub84B (FBgn0003884) qPCR fw	TATCCATGTTGGTCAGGCTGGTGTCC	
aTub84B (FBgn0003884) qPCR rev	CGTGCTTGCCAGCTCCAGTCTC	
Genotyping mNG fw	AACCAAGTAAATCAACTGC-	
Genotyping mNG rev	ATCTCTGTAGGTAGTTTGTC	
Genotyping mSc-I fw	AGGAGTGTCAAACCGCTTAg	
Genotyping mSc-I rev	TAGAATCGAGACCGAGGAGAG	
Genotyping pUAST - fw	AACCAAGTAAATCAACTGC-	
Genotyping pUAST - rev	ATCTCTGTAGGTAGTTTGTC	
GMAP qPCR fw	GCGTACACATCGGCCAGCATTC	
GMAP qPCR rev	ACTGCTCCAGGGCACACTGC	

MDM1_mNeonGreen CO_fw	AGAACTGAACTTCAAAGAGTG	Provided by Marta Domínguez
MDM2_mNeonGreen CO_rev	GTAGCCGTCGTTGGGATT	Provided by Marta Domínguez
mNG qPCR rev	CGGGGCCATCAGCAGGGAAG	
mNG qPCR fw	AGGTGCACCGGACCATGCAG	
mSc-I qPCR rev	CGCCGTCCTCGGGGTACAAC	
mSc-I qPCR fw	AGCTCCGCGGCACCAACTTC	
mScarlet_seq1	GCAGTGATCAAGGAGTTCAT	Provided by Philipp Trepte.
mScarlet_seq2	TTGGTCACCTTCAGCTTGG	Provided by Philipp Trepte.
mScarlet_seq3	CCCCGTAATGCAGAAGAAGA	Provided by Philipp Trepte.
pUAST - fw	AACCAAGTAAATCAACTGC	Provided by Anne Ast
pUAST - rev	ATCTCTGTAGGTAGTTTGTC	Provided by Anne Ast
Q17 PmeI fw	caagtttGTACAAAAAAGCAGGCGTTTCCATGGCGACCCTGGAAAAGCTGATGAAGGCC	
Q17 PmeI rev	GGACACCATACCAGAACCAGAACCGTTTGGTGGTCGGTGCAGCGGCTCCTCagc	
Q17 ZraI fw	AAGAAGAGAACTCTGAATAGGGAATTGGACATGGCGACCCTGGAAAAGCTGATGAAGGCC	
Q17 ZraI rev	caccatACTTCCACTTCCACTGACTGGTCGGTGCAGCGGCTCCTC	
Q55 PmeI fw	caagtttGTACAAAAAAGCAGGCGTTTCCATGGCGACCctggaaaagctgatgaaggcc	
Q55 PmeI rev	GGACACCATACCAGAACCAGAACCGTTTGGTCTTGGTCGGTGCAGCGGCTCCTC	
Q55 ZraI fw	AAGAAGAGAACTCTGAATAGGGAATTGGACATGGCGACCctggaaaagctgatgaaggcc	

Q55 ZraI rev	cttgctcaccatACTTCCACTTCCACTGACTCTTGGTCGGTGCAGCGGCTCCTC
Q75 PmeI fw	acaagtttGTACAAAAAAGCAGGCGTTTCCATGGCGACCCTGGAAAAGCTGATGAAGGCC
Q75 PmeI rev	GGACACCATACCAGAACCAGAACCGTTTGGTGGTCGGTGCAGCGGCTCCTC
Q75 ZraI fw	AAGAAGAGAACTCTGAATAGGGAATTGGACATGGCGACCCTGGAAAAGCTGATGAAGGCC
Q75 ZraI rev	cttgctcaccatACTTCCACTTCCACTGACTGGTCGGTGCAGCGGCTCCT
sff qPCR fw	GTGCGTTGCCCTTCGACGAC -
sff qPCR rev	CCGGTTGATTTCAGCCAGCGTG
vib qPCR fw	AGATTTTCCCCTGCTGGGTGGC
vib qPCR rev	ATGAGCCCTTGGGTGCCAATAGTC

Table 1: Oligonucleotides.

Abbreviations: fw= forward primer, rev= reverse primer. All oligonucleotides with HPLC purification grade and were synthesised by BioTeZ Berlin-Buch GmbH (10 nM). Oligonucleotides were dissolved in TE-Buffer or ultra-pure water.

6.6. Expression vectors

pDONR221	A Gateway® vector containing attP sites. Used for cloning attB flanked PCR products to generate entry clones. Contains the ccdB gene for negative selection and the kanamycin resistance gene for selection in E.coli (Invitrogen).
pMK-RQ	The vector used by GeneArt (Thermo Fischer Scientific) where the designed sequence is inserted between SfiI restriction enzyme sites. The vector contains kanamycin for selection in E.coli
pUAST-attB-rfA	Expression vector for expression in transgenic flies under the GAL4 inducible UAS promoter. Contains attB site for site- specific integration in the fly genome by _C31 integrase (provided by Prof. Sigrist, FU Berlin). Contains an ampicillin resistance gene for selection in E.coli

All final destination fly vectors created in this project are listed in ***Supplementary Table 1***.

6.7. Antibodies

Table 2: Antibodies

Name	Species	Provider	Working dilution
MAB5492	Mouse	Sigma-Aldrich	1 to 1000
PHP2	Mouse	Merk	1 to 1000 (for WB), 1:25 for EM)
mCherry	Rabbit	Abcam	1 to 1000
c-Myc	Mouse	Sigma-Aldrich	1 to 2500
α-tubulin	Rabbit	Sigma-Aldrich	1 to 2000
cyclophillin B	Rabbit	Abcam	1 to 1000
Anti-Mouse IgG-HRP	Goat	Sigma-Aldrich	1 to 2000
Anti-Rabbit IgG-HRP	Goat	Sigma-Aldrich	1 to 2000
18 nm Colloidal Gold AffiniPure™ Goat Anti-Mouse IgG (H+L)	Goat	Jackson ImmunoResearch	1 to 20

Table 2: Antibodies.

All antibody dilutions were optimised for detection of proteins from fly head lysates.

6.8. Experimental models

Table 3: Experimental models

Species	Name	Source
Fly	elavX-GAL4	AG Wanker fly stocks
Fly	GSelav-GAL4	AG Wanker fly stocks
Fly	W1118	AG Wanker fly stocks
Fly	Balancer (CyO/Sp;MKRS,Sb/TM6,Tb)	Generated by F. Schindler (Max Delbrueck Center for Molecular Medicine, Berlin, Germany)
Fly	HTTex1Q17-mNG/-mSc-I	Own production

Fly	HTTex1Q52-mNG/-mSc-I	Own production
Fly	HTTex1Q75-mNG/-mSc-I	Own production
Fly	mNG	Own production
Fly	mSc-I	Own production
Fly	mNG/-mSc-I	Own production
Fly	mNG-mSc-I	Own production
Fly	HTTex1Q17-mNG/-mSc-I vib	Own production
Fly	HTTex1Q52-mNG/-mSc-I vib	Own production
Fly	HTTex1Q75-mNG/-mSc-I vib	Own production
Fly	Vib	Own production
Fly	HTTex1Q17-mNG/-mSc-I GMAP	Own production
Fly	HTTex1Q52-mNG/-mSc-I GMAP	Own production
Fly	HTTex1Q75-mNG/-mSc-I GMAP	Own production
Fly	GMAP	Own production
Fly	HTTex1Q17-mNG/-mSc-I sff	Own production
Fly	HTTex1Q52-mNG/-mSc-I sff	Own production
Fly	HTTex1Q75-mNG/-mSc-I sff	Own production
Fly	sff	Own production
Fly	Vib (SHRNA-330680)	Vienna Drosophila Resource Center (VDRC)
Fly	GMAP (KK-108063)	Vienna Drosophila Resource Center (VDRC)
Fly	sff (KK-100717)	Vienna Drosophila Resource Center (VDRC)
Cell line	HEK293T cells	DSMZ
E.coli	Mach1 T1	Invitrogen

Table 2: Experimental models.

All strains are stored in the AG Wanker live fly stock.

6.9. Laboratory equipment

16M Ceta CMOS camera	Ceta
BD FACSAria™ III Sorter	BD Biosciences
CO_2 incubators	Binder

EASY-nLC™ 1200	Thermo Fisher Scientific
Electrophoresis power supply	Aversham Biosciences
EMSIS 11M Morada CCD camera	EMSIS
EMSIS 11M Quemesa CCD camera	EMSIS
Eppendorf 5427R Centrifuge	Eppendorf
FEI Morgagni 80 kV TEM	FEI
GloQube Plus Glow discharge system	Quorum Technologies
Heidolph DUOMAX 1030 Rocker	Heidolph
Horizontal gel electrophoresis system	Whatman
iBright CL 1500	Invitrogen
Incubators	Binder
Innova44 incubator shaker	New Brunswick Scientific
Leica MZ6 Stereo Microscope	Leica Microsystems
Leica SP8 Confocal Microscope	Leica Microsystems
Nanodrop 8000	Thermo Fisher Scientific
Orbitrap Exploris™ 480 MS	Thermo Fisher Scientific
Orbitrap Fusion Lumos Tribrid MS	Thermo Fisher Scientific
Orbitrap Fusion MS	Thermo Fisher Scientific
Pipettes (p2, p10, p20, p100, p200, p1000)	Gilson
Power Blotter Station	Invitrogen
PowerEase® 300W	Life technologies
Precellys Evolution Touch Homogenizer	Bertin Instruments
Reichert Ultracut S ultramicrotome	Diatome
SevenEasy™ pH meter	Mettler Toledo
Tecan Infinite® M1000 Plate Reader	Tecan
Thermo Fischer Talos L120C 120 kV Transmission Electron Microscope	Thermo Fisher Scientific

Thermomixer comfort	Eppendorf
UltiMate™ 3000 RSLCnano System	Thermo Fisher Scientific
Ultra 45° diamond knife	Diatome
Vaccum pump	VWR
ViiA7 Real-time PCR system	Thermo Fisher Scientific
Vortex-Genie® 2	Scientific Industries
Water bath	Julabo
XCell SureLock™ Mini-Cell	Invitrogen
Zeiss Axioplan2 light microscope	Zeiss
Zeiss EM910 80 kV Transmission Electron Microscope	Zeiss

7. Software

Affinity Designer	Affinity
Biorender Scientific Image and Illustration Software	Biorender
Cytoscape 3.9.1	Cytoscape
Fiji	ImageJ
FloJo v10.8.1	BD Biosciences
GraphPad Prism 7	GraphPad
MaxQuant version 1.6.2.6	MaxQuant
MaxQuant version 2.0.3.0	MaxQuant
Perseus	MaxQuant
QuantStudio™ Real-time PCR Software	Thermo Fisher Scientific
Serial Cloner 2.5	Serial

8. Methods

8.1. Molecular biology

8.1.1. Cloning of HTTex1-mNG/-mSc-I vectors

To generate plasmids encoding mNG and mSc-I tagged HTTex1Q17, HTTex1Q52 or HTTex1Q75, a backbone coding sequence was produced by gene synthesis using Thermo Fisher GeneArt. The coding sequence contained a UAS sequence followed by a PmeI restriction digest site, the mNG coding sequence and a stop codon. This was followed by a second UAS sequence, a ZraI restriction digest site, the mSc-I coding sequence and a stop codon (***see Supplementary Figure 1A***). The coding sequence was flanked by attL sites and was provided as integrated into pMK-RQ entry vector (Thermo Fisher GeneArt). L/R recombination was performed to shuttle the mNG/mSc-I coding sequence into the destination vector pUAST-attB-rfA plasmid (provided by Prof. S. Sigrist, Freie University, Berlin). The correct identity of the resulting pUAST-mNG/-mSc-I plasmid was confirmed using Sanger sequencing with the following primers:

mScarlet_seq1	5'-GCAGTGATCAAGGAGTTCAT-3'
mScarlet_seq2	5'-TTGGTCACCTTCAGCTTGG-3'
mScarlet_seq3	5'-CCCCGTAATGCAGAAGAAGA-3'
MDM1_mNeonGreenCO_FW	5'-AGAACTGAACTTCAAAGAGTG-3'
MDM2_mNeonGreenCO_RV	5'-GTAGCCGTCGTTGGGATT-3'

To insert the HTTex1 coding sequences into the pUAST-mNG/-mSc-I plasmid, cDNAs were PCR amplified from pDONR221 HTTex1Q75-V5 (provided by Anne Ast), pDONR221 HTTex1Q17-V5 (provided by Anne Ast) and pDONR221 HTTex1Q55 (created using Thermo Fisher GeneArt) plasmids. One HTTTex1 cDNA sequence was PCR amplified from the corresponding plasmids using the respective primer pairs:

Q17 Pmel fw	5'-caagtttGTACAAAAAAGCAGGCGTTTCCATGGCGACCCTGGAAAAGCTGATGAAGGCC-3'
Q17 Pmel rev	5'-GGACACCATACCAGAACCAGAACCGTTTGGTGGTCGGTGCAGCGGCTCCTCagc-3'
Q55 Pmel fw	5'-caagtttGTACAAAAAAGCAGGCGTTTCCATGGCGACCctggaaaagctgatgaaggcc-3'
Q55 Pmel rev	5'-GGACACCATACCAGAACCAGAACCGTTTGGTCTTGGTCGGTGCAGCGGCTCCTC-3'
Q75 Pmel fw	5'-acaagtttGTACAAAAAAGCAGGCGTTTCCATGGCGACCCTGGAAAAGCTGATGAAGGCC-3'
Q75 Pmel rev	5'-GGACACCATACCAGAACCAGAACCGTTTGGTGGTCGGTGCAGCGGCTCCTC-3'

These primer pairs were designed to introduce flanking homology arms upstream and downstream of the HTTex1 coding sequence, which were complementary to the ends of the pUAST-mNG/-mSc-I vector when linearised with the PmeI restriction enzyme. The HTTex1 PCR fragments were then inserted into the PmeI digested pUAST-mNG/-mSc-I plasmid using Gibson assembly. The resulting pUAST-HTTex1-mNG plasmids contained HTTex1Q17, HTTex1Q52 and HTTex1Q75 coding sequences upstream of the mNG coding sequence. The correct identity of the pUAST-HTTex1-mNG plasmids was confirmed using Sanger sequencing using the primers used for PCR amplification.

To insert a second HTTex1 coding sequence into the pUAST-HTTex1-mNG plasmids, cDNAs were subsequently PCR amplified from pDONR221 HTTex1Q75-V5 (provided by Anne Ast), pDONR221 HTTex1Q17-V5 (provided by Anne Ast) and pDONR221 HTTex1Q55 (created using Thermo Fisher GeneArt) plasmids using the respective primer pairs:

Q17 ZraI fw	5'-AAGAAGAGAACTCTGAATAGGGAATTGGACATGGCGACCCTGGAAAAGCTGATGAAGGCC-3'
Q17 ZraI rev	5'-caccatACTTCCACTTCCACTGACTGGTCGGTGCAGCGGCTCCTC-3'
Q55 ZraI fw	5'AAGAAGAGAACTCTGAATAGGGAATTGGACATGGCGACCctggaaaagctgatgaaggcc-3'
Q55 ZraI rev	5'-cttgctcaccatACTTCCACTTCCACTGACTCTTGGTCGGTGCAGCGGCTCCTC-3'
Q75 ZraI fw	5'-AAGAAGAGAACTCTGAATAGGGAATTGGACATGGCGACCCTGGAAAAGCTGATGAAGGCC-3'
Q75 ZraI rev	5'-cttgctcaccatACTTCCACTTCCACTGACTGGTCGGTGCAGCGGCTCCT-3'

These primer pairs were designed to introduce flanking homology arms upstream and downstream of the HTTex1 coding sequence, which were complementary to the ends of the pUAST-HTTex1-mNG vectors when linearised with the ZraI restriction enzyme. The HTTex1 PCR fragments were then inserted into the ZraI digested pUAST-HTTex1-mNG plasmid using Gibson assembly. The resulting pUAST-HTTex1-mNG/-mSc-I plasmids contained one copy of the HTTex1Q17, HTTex1Q52 and HTTex1Q75 coding sequences upstream of the mNG coding sequence followed by a second copy upstream of the mSc-I coding sequence. The correct identity of the pUAST-HTTex1-mNG/-mSc-I plasmids was confirmed using Sanger sequencing using the same primers used for PCR amplification.

8.1.2. Cloning of mNG/-mSc-I, mNG-mSc-I, mNG and mSc-I control vectors

The pUAST-mNG/-mSc-I plasmid generated as stated above, was used as a FRET negative control plasmid. To generate a FRET positive control plasmid, a coding sequence was designed which contained a UAS sequence followed by the mNG coding sequence, the mSc-I coding sequence and a stop codon. The coding sequence was flanked by attL sites. and was provided as integrated into the pMK-RQ entry vector (Thermo Fisher GeneArt). L/R recombination was performed to shuttle the mNG-mSc-I coding sequence into the destination vector pUAST-attB-rfA plasmid (provided by Prof. S. Sigrist, Freie University, Berlin). The correct identity of the resulting pUAST-mNG-mSc-I plasmid was confirmed using Sanger sequencing with the following primers:

pUAST - fw	5'-AACCAAGTAAATCAACTGC-3'
pUAST - rev	5'-ATCTCTGTAGGTAGTTTGTC-3'

To generate single fluorophore control plasmids mNG and mSc-I cDNA sequences were PCR amplified from the pUAST-mNG/-mSc-I plasmid using the following primers:

446. mScarlet-I attb fw	5'-GGGGACAAGTTTGTACAAAAAAGCAGGCTTGatggtgagcaagggcgag-3'
447. mScarlet-I attb rev	5'-AGACCACTTTGTACAAGAAAGCTGGGTTTAGCCCGTAGAATCGAGACC-3'
448. mNeongreen attb fw	5'-GGGGACAAGTTTGTACAAAAAAGCAGGCTTGATGGTGTCCAAGGGCGAAG-3'
449. mNeongreen attb rev	5'-AGACCACTTTGTACAAGAAAGCTGGGTTTAGCCCAGGTCTTCTTCAGAG-3'

These primer pairs were designed to introduce attB recombination sites flanking the mNG and mSc-I coding sequence. To create an entry clone, the PCR fragments were integrated into the pDONR221 plasmid through B/P recombination. The mNG and mSc-I coding sequences were then shuttled to the pUAST-attB-rfA plasmid via L/R recombination to generate the pUAST-mNG and pUAST-mSc-I destination vectors. The correct identity of the plasmids was verified by Sanger sequencing using the following primers:

pUAST - fw	5'-AACCAAGTAAATCAACTGC-3'
pUAST - rev	5'-ATCTCTGTAGGTAGTTTGTC-3'

8.2. Protein Biochemistry

8.2.1. SDS PAGE and western blotting (WB)

Lysates were mixed with 1x LDS sample buffer (Novex by Life Sciences) and 50mM DTT and boiled at 95°C for 5 min. Samples were loaded onto Novex NuPAGE 4-12% Bis-Tris gradient gels (Novex by Life Sciences). 30 μg of cell lysate and 20 μg of fly head lysate was loaded per well.

Gels were exposed to 200 V 0.37 A for 35 min using 1X NuPAGE running buffer (Novex by Life Sciences). Gels were blotted onto nitrocellulose membranes (Amersham™) with 1x NuPAGE transfer buffer (Novex by Life Sciences) using the semi-dry powerblotter (Invitrogen) at 20 V 1 A for 1 h. Membranes were blocked with 3% milk for 1 h followed by primary antibody incubation with the respective antibodies indicated for the experiment.

Corresponding peroxidase conjugated secondary antibodies (Sigma-Aldrich) were used in conjunction with WesternBright Chemiluminescence Substrate (Biozym) to enable immunodetection. The working dilution of all antibodies used can be found in ***Table 2***. Membranes were imaged using the iBright CL 1500 (Invitrogen).

8.2.2. Filter retardation analysis (FRA)

Lysates were analysed by FRA according to the previously published protocol [344]. For FRA analysis of cell lysates, 80 μg of protein was loaded per well. For FRA analysis of fly head lysates, 70 μg of protein was loaded per well. Blots were quantified by calculating the intensity of the dots using the gel analyser tool in Fiji. Relative intensity was then calculated by normalising to HTTex1Q17-mNG/-mSc-I sample intensity. Plots were created using GraphPad Prism 7.

8.2.3. Immunoprecipitation (IP) of HTTex1 aggregates from fly head lysates

Dynabeads™ protein G for immunoprecipitation (Invitrogen by Thermo Fisher Scientific) were washed twice with PBS and incubated with 12 µl PHP2 antibody (Merk) for 30 min rotating at room temperature. Beads were washed 2x with PBS, by applying the tubes to a magnet and removing the supernatant, to remove excess antibody. 400 μg of protein derived from fly head lysates in brain lysis buffer (BLB) were incubated with the beads overnight rotating at 4°C. The flowthrough was discarded, and beads were washed 1x with BLB and 1x with minimal BLB. After the last washing step, beads were resuspended in minimal BLB. The resuspension was split into two separate Eppendorf tubes, both supernatants were removed leaving the beads. One tube of beads was resuspended in NuPAGE LDS sample buffer with 50mM DTT and boiled at 95°C for 5 min before SDS-PAGE and western blotting. For MS analysis, the other beads were snap frozen in liquid N2 were used (performed by Leonard Roth).

8.3. Flow cytometry

8.3.1. Fluorescence activated cell-sorting (FACS)

Single cell solutions were analysed on the BD FACSAria™ III Sorter (BD Biosciences). To detect FRET, both the B-695/40 filter and 655LP filter of the 488 nm laser were exchanged for the 610/20 and 600LP filters. Exactly 50,000 cells were analysed per measurement. Data was analysed using FloJo v10.8.1.

8.4. Mass spectrometry (MS)

8.4.1. IP LC MS

8.4.1.1. Sample preparation

Frozen beads from IP experiments (3 biological replicates per strain) were submitted to researchers at the proteomics core facility at the MDC, who performed label-free quantitative LC-MS experiments and analysis (performed by Dr. Oliver Popp). Tryptic on-bead digestion was conducted according to a previously published protocol [538] and then de-salted on stage-tips [539].

8.4.1.2. Measurement

LC-MS measurements were performed on an orbitrap Exploris 480 mass spectrometer coupled to an EASY-nLC 1200 system applying a 110 min gradient and operating the MS in data-dependent mode.

8.4.1.3. Data analysis

For analysis, MaxQuant version 2.0.3.0 [540] was used employing MaxLFQ-based [541] quantitation and using the match-between runs algorithm. Carbamidomethylation was set as a fixed and oxidized methionine as variable modification. For the Andromeda search, a Uniprot Drosophila database (2022) plus common contaminants was used in combination with the recombinant HTT sequences. Downstream analysis was done in R using two-sample moderated t-statistics with the limma package [542].

Gene ontology (GO) term enrichment was performed using Metascape [375] using the parameters P value < 0.01, minimal overlap 3 and minimum enrichment 1.5. All graphs were plotted using Graphpad Prism 7. Clustering was performed using Cytoscape 3.9.1 and the STRING protein query plug in [543]. For clustering, the MCL clustering algorithm in Cytoscape was used with a granularity of 4.

8.4.2. Whole brain lysate LC-MS

8.4.2.1. Sample preparation

Sample preparation for whole brain lysate MS was performed according to a protocol provided by David Toppe (AG Sigrist, Freie University, Berlin). Whole fly brains were dissected in ice-cold HL3 (10 per replicate, 3 biological replicates per strain) and transferred to 50 µl HL3 in 1.5 ml tubes. After dissection, tubes were centrifuged at 4°C, 13.000 rpm for 5 min. Supernatant was removed and brain pellets stored at -80°C until further processing.

Brain pellets were resuspended in 20 µl lysis buffer (1xPBS, 10% SDS, 1x sample buffer and 1 precise protease and phosphatase inhibitor mini tablet) and lysed at 4°C rotating overnight. Complete lysis was confirmed by centrifugating tubes at 13,000 rpm for 5 min and observing no visible pellet. 1 µl 100 nM DTT (100mM DTT dissolved in 50mM TEAB) was added to 20 µl lysate and samples were incubated for 30 min at 55°C, 300 rpm on heating block. To this, 2.1 µl of chloroacetamide (CAA) (400nM CAA dissolved in TEAB) was added and samples were covered to prevent light exposure and incubated for 30 min at room temperature, 300 rpm on heating block. Samples were boiled at 95°C for 5 min and loaded onto Novex NuPAGE 4-12% Bis-Tris gradient gels. Gels were exposed to 200 V until the samples completely ran out of the gel pockets (2-3 min). The gel was then stained with Coomassie G-

250 stain (Serva) according to manufacturer recommendations. Each lane was cut from the gel and divided into 3 pieces for subsequent LC-MS analysis (3 gel pieces submitted per biological replicate).

Gel pieces were submitted to Heike Stephanowitz (AG Liu, FMP, Berlin) who performed label-free quantitative LC-MS experiments. Gel pieces reduced with 5 mM DTT at 56 °C for 30 min and alkylated with 40 mM CAA at room temperature for 30 min in the dark. Protein digestion was performed using trypsin at an enzyme-to-protein ratio of 1:100 (w/w) at 37°C overnight.

8.4.2.2. Measurement

LC-MS analysis was performed using an UltiMate 3000 RSLC nano LC system coupled on-line to an Orbitrap Fusion or LUMOS mass spectrometer (Thermo Fisher Scientific). Reversed-phase separation was performed using a 50 cm analytical column (in-house packed with Poroshell 120 EC-C18, 2.7µm, Agilent Technologies) with a 120 min gradient. MS1 scans were performed in the orbitrap using 120000 resolution; MS2 scans were acquired in the ion trap with an AGC target of 10000 and maximum injection time of 35 ms, charge state 2-4 enable for MS2.

8.4.2.3. Data analysis

Data analysis including label free quantification was performed with MaxQuant (version 1.6.2.6) using the following parameters: MS ion mass tolerance: 4.5 ppm; MS2 ion mass tolerance: 0.5 Da; variable modification: Met oxidation, Acetyl (protein N-term); fixed modification: Cys carbamidomethyl; protease: trypsin (R,K); allowed number of missed-cleavaged: 2, database: SwissProt database of drome (Drosophila+melanogaster); label-free quantification and match between runs were enabled. Results were reported at 1% FDR at the protein level.

The calculated LFQ intensities were then analysed using a Perseus pipeline [544] (performed by Megan Bonsor). In brief, contaminants were removed, and data was Log2 transformed. Valid values were filtered, and imputation was performed, where missing values were replaced from the normal distribution. A t-test was performed (HTTex1Q52-mNG/-mSc-I and HTTex1Q17-mNG/-mSc-I) to obtain LFC and P values.

Gene ontology (GO) term enrichment was performed using Metascape [375] using the parameters P value < 0.01, minimal overlap 3 and minimum enrichment 1.5. All graphs were plotted using Graphpad Prism 7. Clustering was performed using Cytoscape 3.9.1 and the STRING protein query plug in [543]. For clustering, MCL clustering algorithm in Cytoscape was used with a granularity of 4.

8.5. HEK293 cell biology

8.5.1. Cell maintenance and seeding

HEK293 cells were maintained between 10% and 90% confluency in a 37°C, 5% CO2 tissue culture incubator, and were passaged twice a week. Cells were grown in DMEM 4.5g/L glucose (L Glutamine, 50ml FBS, 5ml Pen/Strep).

8.5.2. pCMV-GAL4 and pUAST-HTTex1-mNG/-mSc-I co-transfection

HEK293 cells at 70-90% confluency were transfected with 2.5 µg pCMV-GAL4, 1.5 µg pUAST-HTTex1-mNG/-mSc-I and 1 µg pcDNA. DNA was diluted in Opti-MEM (Gibco), and Lipofectamine 2000 (Life Technologies) according to the manufacturer’s recommendations. The diluted DNA was added to the diluted Lipofectamine in a 1:1 ratio and incubated for 5 min at room temperature. The resulting DNA-lipid complex was incubated with cells for 48 h at 37°C before further analysis.

8.5.3. Lysate preparation for WB and FRA

Cells were seeded and transfected with Lipofectamine 2000 according to manufacturer’s recommendations (Life Technologies). After 48 h cells were washed with PBS and lysis buffer applied (20mM Hepes pH7.5, 150mM NaCl, 2mM EDTA, 0.5% NP40, 5mM MgCl2, protease inhibitor and benzonase nuclease). Cells in lysate buffer were dislodged and transferred to a 15 ml tube (Falcon) which was incubated for 30 min on ice. After incubation, cells were centrifuged, and the supernatant taken forward as lysate for biochemical analysis.

8.5.4. Fixation and staining for confocal microscopy

100,000 cells were seeded onto coverslips in 24 well plates and taken forward for confocal analysis 48 h post transfection. Cells were fixed with 4% PFA for 15 min at room temperature. Cells were then washed twice with PBS-T before staining with Hoechst solution (1: 5000) (Invitrogen). Coverslips were washed once with PBS and once with water before mounting using Dako fluorescence mounting media (Dako). Slides were stored at 4°C. Images were taken on the Leica SP8 DLS confocal microscope at the ALM facility (MDC Berlin).

8.5.5. Preparation for FACS

100,000 cells were seeded per well of a 6 well plate and cultured in DMEM 4.5 g/L glucose phenol-free (L-glutamine, 50ml FBS, 5ml Pen/Strep) (Gibco cat no 41965-062) and taken forward for analysis 48 h post transfection. Cells were trypsinised (0.05% trypsin EDTA, Gibco), washed three times with PBS and pelleted after each washing step. Cells were resuspended in ice cold PBS and 1% FBS and applied to a cell strainer tube (Falcon) to obtain a single cell solution which was kept on ice until FACS measurement. Cells were analysed using the BD FACSAria™ III Sorter (BD Biosciences).

8.5.6. Plate-reader FRET measurements

45,000 cells were seeded into 96-well plates (Greiner bio-one: 655986, black, clear bottom) in DMEM 4.5 g/L glucose phenol-free (L-glutamine, 50ml FBS, 5ml Pen/Strep). 200 ng/μl of DNA samples were incubated with 150 μl of OptiMEM (Gibco) and polyethylenimine (PEI) (Polysciences) master mix (1.1 μl PEI to 1ml OptiMEM) for 20 min at room temperature. 50 μl of the DNA-OptiMEM-PEI mix was added per well. Measurements taken 48 h post transfection. Fluorescence per well was measured using the TECAN M1000 plate reader (Tecan) at 37°C for 10 ms. mNG fluorescence was measured at excitation (Ex): 495 nm and emission (Em): 525 nm, mSc-I fluorescence was measured at Ex: 569 nm Em: 594 nm and FRET was measured at Ex:495 nm Em:594 nm.

Raw fluorescent values were processed by subtracting background fluorescence of pUAST-attB-rfA transfected cells in all channels. FRET channel fluorescence was corrected for donor bleed through (cD) and acceptor cross excitation (cA) using mNG transfected cells and mSc-I transfected cells respectively to obtain sensitised emission values. Sensitised emission was normalised to the mSc-I only transfected cells, therefore normalising to the acceptor. Percentage FRET efficiency (E) was calculated as E = (DA-cDxDD-cAxAA)/AA with DD = donor channel signal and AA = acceptor channel signal.

8.6. *D. melanogaster* biology

8.6.1. Generating transgenic flies and maintenance

ElavGS and ElavX lines were obtained from Bloomington Drosophila Stock Center. The w1118 strain was provided by Dr. Robert Zinzen (MDC, Berlin). The HTTex1-mNG/-mSc-I strains were generated by co-injection of the phiC31 integrase and the pUAST-HTTex1-mNG/-mSc-I DNAs into embryos with an integration site at 68E on chromosome 3 (ZH-68E yw; M{3xP3-RFP.attP'}ZH-68E) by Rainbow Transgenic Flies Inc. The transgenic strains were then crossed with the balancer stain (CyO/Sp;TM6/MKRS) and maintained as stable strains (CyO/+;HTTex1-mNG/-mSc-I/TM6). All strains were kept on standard yeast-agar medium in incubators at 25°C and 65% humidity with a 12 h light-dark cycle. For experiments using the elavGS driver strain, transgene expression was induced by maintaining flies on standard medium containing 400µM RU486 (Mifepristone, Sigma).

8.6.2. Generating RNAi flies

Vib (SKU SHRNA-330680), GMAP (SKU KK-108063) and sff (SKU KK-100717) RNAi flies were obtained from Vienna Drosophila Resource Center (VDRC) which harboured RNAi constructs integrated on chromosome 2. The RNAi flies were crossed with the balancer strain (CyO/Sp;TM6/MKRS) and maintained as stable strains (RNAi/Sp;MKRS/+). Balanced RNAi male flies (RNAi/Sp;MKRS/+) were crossed with balanced HTTex1-mNG/-mSc-I (CyO/+;HTTex1-mNG/-mSc-I/TM6) virgin female flies. Virgin female and male flies from the F1 progeny which contained the RNAi construct on chromosome 2 and the HTTex1-mNG/-mSc-I cDNA on chromosome 3 (CyO/RNAi;HTTex1-mNG/-mSc-I/MKRS) were selected, crossed. The resulting progeny were maintained as a stable RNAi;HTTex1-mNG/-mSc-I stock.

8.6.3. Fly husbandry

~100 driver virgin flies (elavX or elavGS) were mated with ~20 male responder strains (HTTex1-mNG/-mSc-I). Flies were maintained on standard yeast-agar medium in incubators at 25°C and 65% humidity with a 12 h light-dark cycle. For experiments, only female flies from the F1 progeny were selected and taken forward for analysis

8.6.4. Fly head collection for DNA, RNA, and protein isolation

30-40 flies were anaesthetized using CO2 and transferred into 1.5 mL Eppendorf tubes. Tubes were promptly transferred to liquid N_2 for flash freezing and were either stored at -80°C or taken forward immediately for processing. To detach fly heads from the bodies, tubes were removed from N_2 with forceps, shaken and placed back into the N_2 which was repeated three times. The fly heads were then filtered from the other fly material by transferring the tube contents to N_2 cooled sieves. The fly heads were then stored at -80°C or immediately used for DNA, RNA, or protein isolation.

8.6.5. DNA isolation and genotyping

Genomic DNA was extracted from fly heads using the DNeasy® Blood & Tissue Kit (Qiagen). The concentration of DNA was assessed using the Nanodrop 8000 (Thermo Fisher Scientific). DNA was PCR amplified using the PWO DNA polymerase kit (Roche) according to the manufacturer's recommendations. For pUAST-mNG, pUAST-mSc-I, pUAST-mNG/-mSc-I and pUAST-mNG-mSc-I the following primers were used:

Genotyping pUAST - fw	5'-AACCAAGTAAATCAACTGC-3'
Genotyping pUAST - rev	5'-ATCTCTGTAGGTAGTTTGTC-3'

For pUAST-HTTex1Q17-mNG/-mSc-I, pUAST-HTTex1Q52-mNG/-mSc-I and pUAST-HTTex1Q75-mNG-mSc-I the following primers were used to amplify HTTex1-mNG and HTTex1-mSc-I cDNA separately:

Genotyping mNG fw	5'-AACCAAGTAAATCAACTGC-3'
Genotyping mNG rev	5'-ATCTCTGTAGGTAGTTTGTC-3'
Genotyping mSc-I fw	5'-AGGAGTGTCAAACCGCTTAg-3'
Genotyping mSc-I rev	5'-TAGAATCGAGACCGAGGAGAG-3'

PCR products were analysed by agarose gel electrophoresis and Sanger sequencing.

8.6.6. RNA isolation

RNA was isolated from fly heads using the RNeasy® Mini Kit (Qiagen) as per manufacturers recommendation. Following RNA isolation, RNA was re-eluted using isopropanol and ethanol to remove contaminants. To do this, 40 µl of RNA was mixed with 460 µl DEPC-treated water (Ambion), 50 µl 3M NaAc, pH 5.5, 10 µg glycogen and 500 µl room temperature isopropanol. Samples were mixed well and incubated at -80°C for 30 min. Re-eluted RNA was pelleted by centrifugation for 10 min at 12,000-13,000 rpm 4°C. The pellet was washed twice with ice cold 70% ethanol then air dried before resuspension in 40 µl DEPC-treated water. RNA concentration was assessed using the Nanodrop 8000 (Thermo Fisher Scientific).

8.6.7. Real-time PCR (qPCR)

For analysis of HTTex1-mNG/-mSc-I transcript expression, 100 ng/µl RNA was converted to cDNA using the High-Capacity cDNA Reverse Transcription Kit from Thermo Fisher Scientific as per the manufacturer’s recommendations. 2 µl of 10 ng/µl cDNA was mixed with 6 µl SYBR Green PCR Master Mix (Applied Biosystems by Thermo Fisher Scientific), 2 µl 2 µM forward primer and 2 µl 2 µM reverse primer. The following primers were used for qPCR analysis at an annealing temperature of 64.3°C:

sff qPCR fw	5'-GTGCGTTGCCCTTCGACGAC-3'
sff qPCR rev	5'-CCGGTTGATTTCAGCCAGCGTG-3'
vib qPCR fw	5'-AGATTTTCCCCTGCTGGGTGGC-3'
vib qPCR rev	5'-ATGAGCCCTTGGGTGCCAATAGTC-3'
GMAP qPCR fw	5'-GCGTACACATCGGCCAGCATTC-3'
GMAP qPCR rev	5'-ACTGCTCCAGGGCACACTGC-3'
mSc-I qPCR fw	5'-AGCTCCGCGGCACCAACTTC-3'
mSc-I qPCR rev	5'-CGCCGTCCTCGGGGTACAAC-3'
mNG qPCR fw	5'-AGGTGCACCGGACCATGCAG-3'
mNG qPCR rev	5'-CGGGGCCATCAGCAGGGAAG-3'
Act42A (FBgn0000043) qPCR fw	5'-CTTTAGTGGTCGACAACGGATCCG-3'
Act42A (FBgn0000043) qPCR rev	5'-CCTTTTGTCCCATTCCTACCATTACGCC-3'
aTub84B (FBgn0003884) qPCR fw	5'-TATCCATGTTGGTCAGGCTGGTGTCC-3'
aTub84B (FBgn0003884) qPCR rev	5'-CGTGCTTGCCAGCTCCAGTCTC-3'

Samples were analysed using a ViiA7 Real-Time PCR System (Applied Biosystems by Thermo Scientific) to obtain raw threshold cycle (CT) values. To analyse transcript expression, fold change values were calculated using the delta delta CT (2–ΔΔCt) method [360], normalising to aTub84B transcripts and the W1118 control flies.

8.6.8. Lysate preparation for WB and FRA

Fly heads were transferred to Precellys CK14 tubes (Bertin Technologies) and 400 µl BLB added. Tubes were shaken in the Precellys Evolution Touch Homogenizer (Bertin Technologies) three times for 10 sec at 6,000 rpm. Between each round of shaking samples were incubated for 5 min on ice. Homogenate was transferred from the Precellys CK14 tubes to 1.5 ml Eppendorf tubes and centrifuged for 10 min at 1,000 rpm to clear debris from the lysate. The supernatant was transferred to a new tube and total protein concentration was determined with a Pierce BCA assay (Pierce) using BSA as a standard.

8.6.9. Lifespan assay

Flies were maintained at 25°C and 65% humidity with a 12 h light-dark cycle, with 10 flies per vial. Flies were transferred onto new food every 3 days and dead flies were counted every 2-3 days. Each biological replicate consisted of ~50 flies. The percentage of live flies per day was plotted, and the age at which 50% of the flies were dead was taken as the median lifespan. The median lifespan was calculated by fitting the survival curves to the log(inhibitor) vs. normalised response (variable slope) equation using GraphPad Prism 7.

8.7.0. Climbing assay

The motility of flies was assessed by exploiting the negative geotaxis behaviour of flies. For one measurement, 10 flies were placed into transparent plastic tubes and tapped to the bottom. The number of flies which climbed to a height of 8 cm in 15 sec was counted. Flies were placed back onto normal food and maintained at 25°C and 65% humidity with a 12 h light-dark cycle. Climbing measurements were taken every 3 days. Each biological replicate consisted of ~50 flies.

8.7.1. Brain dissection and mounting for confocal microscopy

15-20 flies per strain were anaesthetized using CO2 and transferred into 2mL Eppendorf tubes. For fixation, flies were incubated with 1.8ml of 4% paraformaldehyde (PFA) in 0.5% PBS-T for 3 h on a rocker. Flies were then washed 4 times with 0.5% PBS-T, 15 min on the rocker per wash. Flies were kept in PBS at 4°C for a maximum of 1 week prior to dissection.

Fly brains were dissected from fixed whole flies in ice cold HL3. Using forceps, the chitin layer, the trachea and the ommatidia were removed exposing the brain. Brains were then incubated with 1:1000 DAPI for 30 min on a rocker. Brains were washed once with PBS before being covered in VECTASHIELD® Antifade Mounting Media (Vector). Brains were then mounted onto slides and images were taken using the 20x oil immersion objective on the Leica SP8 DLS confocal microscope at the ALM facility (Advanced Light Microscopy, MDC, Berlin).

8.7.2. Preparation of fly brains for FACS

Fly brains were dissociated into a single cell solution using an altered version of a previous protocol used by Davie et al [371]. In brief, 40 fly brains per strain were dissected in ice cold DPBS within 2 h and transferred to a 1.5 ml Eppendorf tube. Tubes were then centrifuged at 4°C 800xg for 5 min to pellet the brains. The supernatant was removed and 50 µl of Dispase (3 mg/mL, Sigma-Aldrich_D4818-2mg) and 75 µl Collagenase I (100 mg/mL, Invitrogen_17100-017) was added to the pellet. To dissociate the brains into cells, tubes were then incubated at 25°C in a Thermoshaker (Thermo-Fischer Scientific) for 2 h at 25°C, 500 rpm. The reaction mixture was pipetted up and down every 15 min to re-enforce the enzymatic reaction. After the 2 h incubation the tubes were centrifuged at 4°C 800xg for 5 min to pellet the cells. Cells were then washed once with ice cold DPBS and resuspended in DPBS 0.01% BSA. The cell solution was then filtered through a 10 µM pluriStrainer (pluriSelect). The resulting single cell solution was transferred to FACS tubes, to which 1:1000 DAPI was added 15 min before analysis. The cells were then analysed using the BD FACSAria™ III Sorter (BD Biosciences).

8.8. Electron microscopy (EM)

8.8.1. Immuno-negative staining electron microscopy (iNS) using fly lysates

200 mesh grid plano grids (Plano) were glow discharged for 30 s at 15 mA using negative polarity mode in the GloQube Plus Glow discharge system (Quorum Technologies). To the grids, 5 µl of 0.1 µg/µl lysate (0.5 µg total amount) was pipetted and incubated for 1 min. Grids were then washed 3x with wash buffer (1ml glycine, 1ml 1xPBS, 1ml 10% BSA, 7ml Bidest). To detect HTTex1 aggregates, grids were then incubated with a 1:25 dilution of the PHP2 antibody (Merk) for 15 min and washed 3x with wash buffer. Grids were then incubated with a 1:20 dilution of anti-mouse gold labelled secondary antibody (Jackson ImmunoResearch) and washed 3x with H_2O. To have a contrast staining, grids were then incubated with uranyl acetate (2% w/v) for approximately 1.5 min. Grids were imaged using the Zeiss EM910 80 kV transmission electron microscope (TEM) equipped with the EMSIS 11M Quemesa CCD camera (EMSIS) or using the Thermo Fischer Talos L120C 120 kV TEM equipped with the 16M Ceta CMOS camera.

8.8.2. Transmission electron microscopy (TEM) of whole brain tissue

8.8.2.1. Fixation and embedding

Whole fly brains were fixed by immersion in a solution of 2% formaldehyde (FA) and 2% glutaraldehyde (GA) (Sigma-Aldrich G5882-10ml) in HL3 buffer on ice for 1 h. The fixative was then changed to 2% FA, 2% GA in 0.1 M HEPES pH 7.2 and fixed for a further hour at room temperature. After thorough washing, the tissue was incubated in 1% tannic acid in 0.1 M HEPES pH 7.1 for 1 h at room temperature. The tissue was washed with 0.1M HEPES pH 7.1, followed by treatment with 1% osmium tetroxide in 0.1M HEPES pH 7.2 for 90 min on ice in the dark. After washing with MilliQ water, the tissue was stained *en bloc* with 2% uranyl acetate for 1 h in the dark at 4°C. Following the removal of the uranyl acetate solution, the tissue was washed with MilliQ water and dehydrated in a series of ethanol solutions as follows: 10 min in 30% ethanol, 10 min in 50% ethanol, 30 min in 70% ethanol, 3x 20 min in 100% ethanol. After dehydration, the tissue was incubated in propylene oxide for 30 min. Infiltration in epoxy resin (Polybed812, Polysciences) was performed by incubating the tissue for 30 min in 30% resin mixed with propylene oxide, followed by a further 30 min in 70% resin mixed with propylene oxide. Infiltration with 100% epoxy resin was carried out overnight at room temperature.

8.8.2.2. Sectioning and imaging

Resin blocks were sectioned using the Reichert Ultracut S ultramicrotome and an Ultra 45° diamond knife (Diatome). To target specific areas of the brain tissue, 250 nm thick sections were stained with 0.05% Toluidine blue in 0.05 M Na_2HPO_4 pH9 and imaged using the Zeiss Axioplan2 light microscope. For TEM, 70 nm sections were picked up on in-house Formvar/Carbon coated grids and post-stained with uranyl acetate and lead citrate using the Leica EM AC20 grid stainer. Grids were imaged on three transmission electron microscopes: the Zeiss EM910 80 kV TEM with the EMSIS 11M Quemesa CCD camera; the FEI Morgagni 80 kV TEM equipped with the EMSIS 11M Morada CCD camera and the Thermo Fischer Talos L120C 120 kV TEM equipped with the 16M Ceta CMOS camera.

8.9. Statistical Analysis

Statistical parameters including the statistical test performed and statistical significance are reported in the figures and figure legends. Data is judged to be statistically significant when $p < 0.05$ by the indicated statistical test. In figures, asterisks denote statistical significance as calculated by the indicated statistical test (*, $p < 0.05$; **, $p < 0.01$; ***, $p < 0.001$). Statistical analysis was performed in GraphPad Prism 7.

8.9.1. Correlation Analysis

To calculate the correlation between lifespan and the biochemical detection of HTTex1 aggregates, the median lifespan of 3 biological replicates of HTTex1Q52-mNG/-mSc-I and HTTex1Q75-mNG/-mSc-I flies was plotted alongside the calculated PHP2 and MAB5492 FRA intensities. FRA intensities were calculated using Fiji and normalised to HTTex1Q17-mNG/-mSc-I samples for 3 biological replicates to give relative intensity values.

To calculate the correlation between lifespan and the FRET-based detection of HTTex1 aggregates, the median lifespan of 3 biological replicates of HTTex1Q52-mNG/-mSc-I and HTTex1Q75-mNG/-mSc-I flies was plotted alongside the number of FRET positive cells and number of FRET positive puncta. The number of FRET positive cells was calculated from FRET FACS analysis for 3 biological replicates. The number of FRET positive puncta was calculated from confocal microscopy images of the fly mid brains. Using Fiji, the FRET channel image was converted to a grey scale 8-bit image and the auto-threshold parameter Intermodes was used [545] to distinguish puncta from the background. The “analyse particles” function in Fiji was used to count the puncta in 3 biological replicates.

Values were plotted, a trendline calculated from linear regression analysis and a Pearson correlation was performed in GraphPad Prism 7. R represents the Pearson correlation coefficient and P represents the P value calculated from the Pearson correlation analysis.

9. Supplementary figures

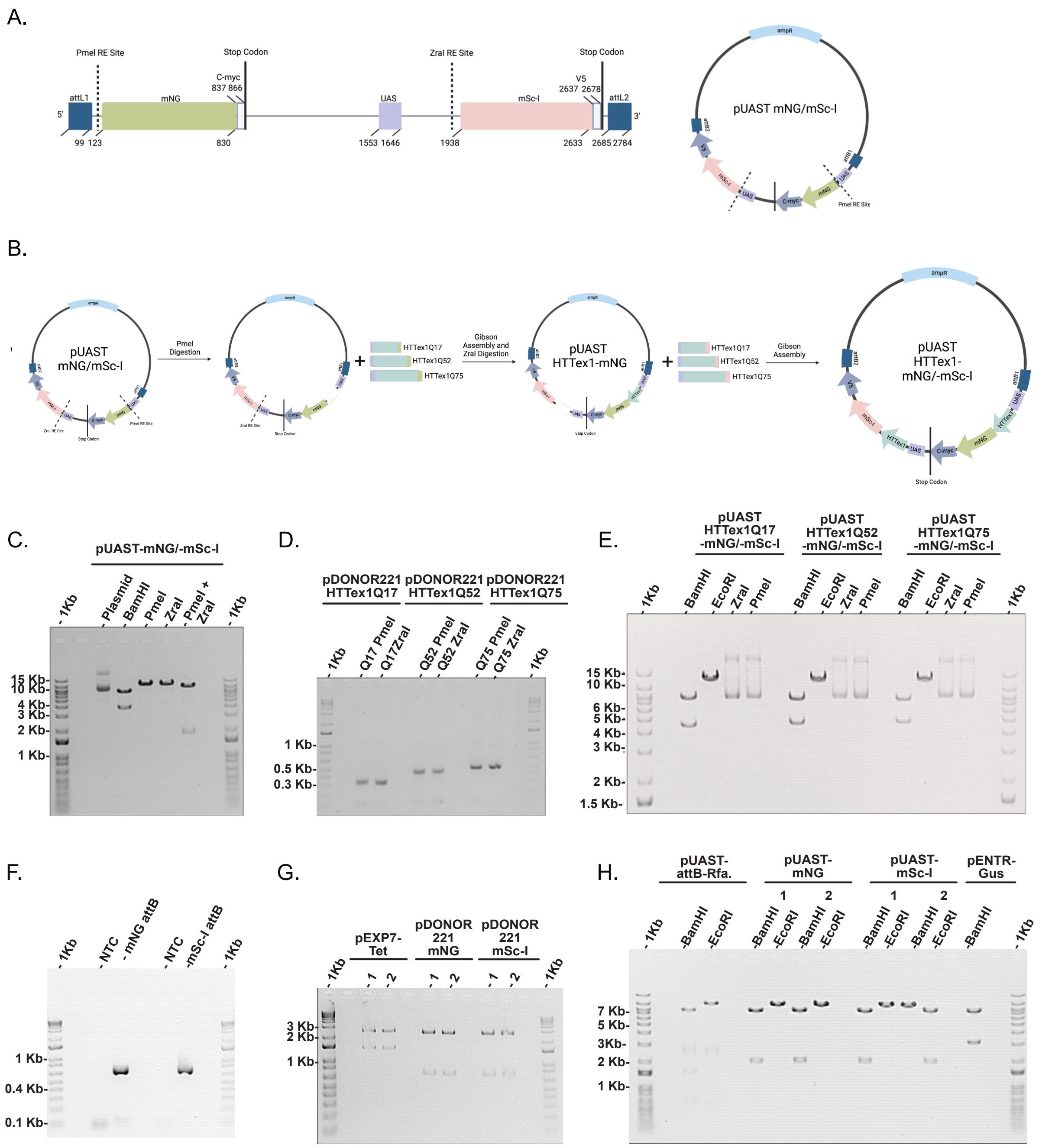

Supplementary Figure 1. Generation of the pUAST-HTTex1-mNG/-mSc-I plasmids and cloning validation

A) *Schematic showing the mNG/-mSc-I insert (generated by GeneArt Thermofisher) (left). The insert was L/R recombined with the pUAST-attB-rFA. The resulting pUAST-mNG/-mSc-I plasmid is illustrated (right). Created using Biorender.* ***B)*** *Schematic of the cloning strategy used to produce pUAST-HTTex1-mNG/-mSc-I plasmids.* ***C)*** *Agarose gel image of pUAST-mNG/-mSc-I plasmid restriction digestion analysis. Expected products: BamHI=7.3 and 3.7 kb, PmeI=11.1 kb, ZraI=11.1 kb and PmeI/ZraI double digest= 9.3 and 1.8 kb.* ***D)*** *Agarose gel image of PCR amplified fragments from HTTex1Q17, HTTex1Q55 and HTTex1Q75 pDonor221 plasmids with homologous ends to PmeI or ZraI insertion sites. Expected products: Q17 PmeI/ZraI=0.31 kb, Q55*

ZraI=0.42 kb and Q75 PmeI/ZraI=0.48 kb ***E)*** *Agarose gel image of pUAST-HTTex1-mNG/-mSc-I plasmid restriction digestion analysis. No digestion by PmeI or ZraI was detected. Expected products: HTTex1Q17-mNG/-mSc-I EcoRI=11.6 kb, BamHI=7.3 and 4.3 kb; HTTex1Q52-mNG/-mSc-I EcoRI=11.8 kb, BamHI= 7.3 and 4.5 kb; HTTex1Q75-mNG/-mSc-I EcoRI= 12 BamHI= 7.3 and 4.6 kb.* ***F)*** *Agarose gel image of PCR amplified mNG and mSc-I attB flanked fragments. Expected products: mNG=0.74 kb, mSc-I=0.74 kb. NTC= no template control.* ***G)*** *Agarose gel image of pDONOR 221 mNG and pDONOR221 mSc-I plasmid BsrGI restriction digestion analysis. Expected products: pDONOR 221 mNG= 2.514 kb and 0.720 kb, pDONOR 221 mSc-I=2.514 and 0.708 kb. pEXP7-Tet ran as positive control insert which runs at 1.4 kb.* ***H)*** *Agarose gel image of pUAST attB.Rfa, pUAST mNG and pUAST mSc-I plasmids digested ecoRI and BamHI. Expected products: pUAST attB.Rfa EcoRI= 9.723 kb and 0.496 kb, BamHI= 7.356 kb, 1.522 kb, 0.702 kb and 0.637 kb, pUAST mNG EcoRI= 9.317 kb, BamHI= 7.35 kb and 1.959 kb, pUAST mSc-I EcoRI= 9.314 kb, BamHI=7.358 kb, and 1.956 kb. pENTR-Gus ran as positive control insert which runs at approximately 3Kb.*

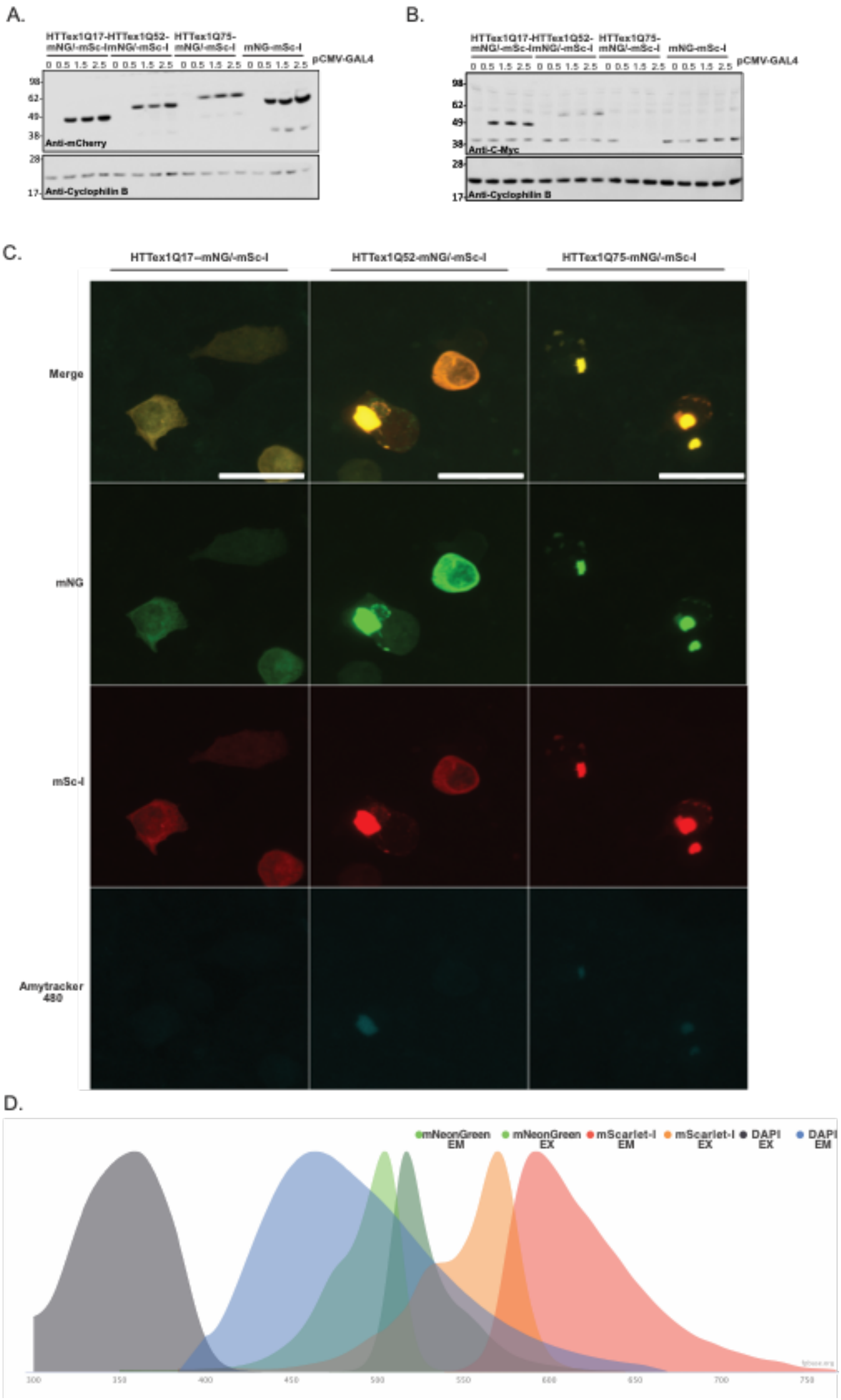

Supplementary Figure 2. mHTTex1-mNG/-mSc-I fusion protein co-expression results in amyloidogenic aggregates

WB analysis of the HTTex1-mNG/-mSc-I fusion protein in HEK293 cells co-transfected with 0, 0.5, 1.5 and 2.5µg of pCMV-GAL4 plasmid and 1.5 µg of pUAST-HTTex1-mNG/-mSc-I plasmids. ***A)*** *Anti-mCherry and* ***B)*** *Anti-cMyc antibodies used for immunodetection. Anti-cyclophilin B antibody was used as a loading control for immunodetection.* ***C)*** *HEK293 cells co-transfected with 7.5 µg of pCMV-GAL4 and 4.5 µg of pUAST-HTTex1-mNG/-mSc-I plasmids, stained with 1:100 dilution of Amytracker 480. Scale bars= 25 µm.* ***D)***

Excitation and emission spectra of Amytracker 480 (blue line) (depicted as DAPI as per the manufacturers recommendations), mNG (green lines) and mSc-I (red lines). Created using FPbase.

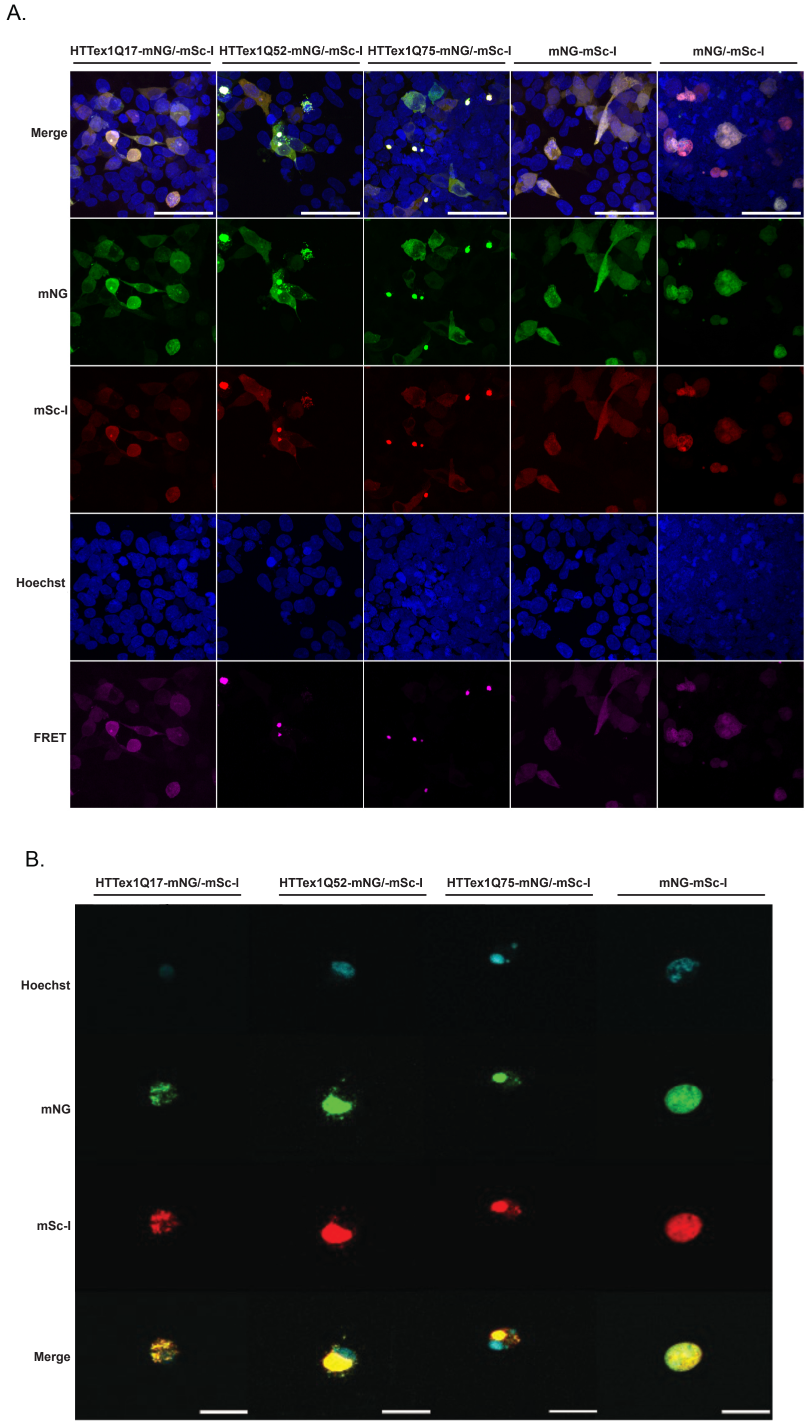

Supplementary Figure 3. FACS sorted FRET positive mHTTex1-mNG/-mSc-I co-expressing HEK293 cells have large inclusions

__A)__ Confocal images of HEK293 cells using FRET settings to qualitatively detect FRET positive structures. Scale bar represents 25 µm. __B)__ Confocal images of transfected HEK293 cells after FACS sorting of FRET positive population. Scale bars represent 25 µm.

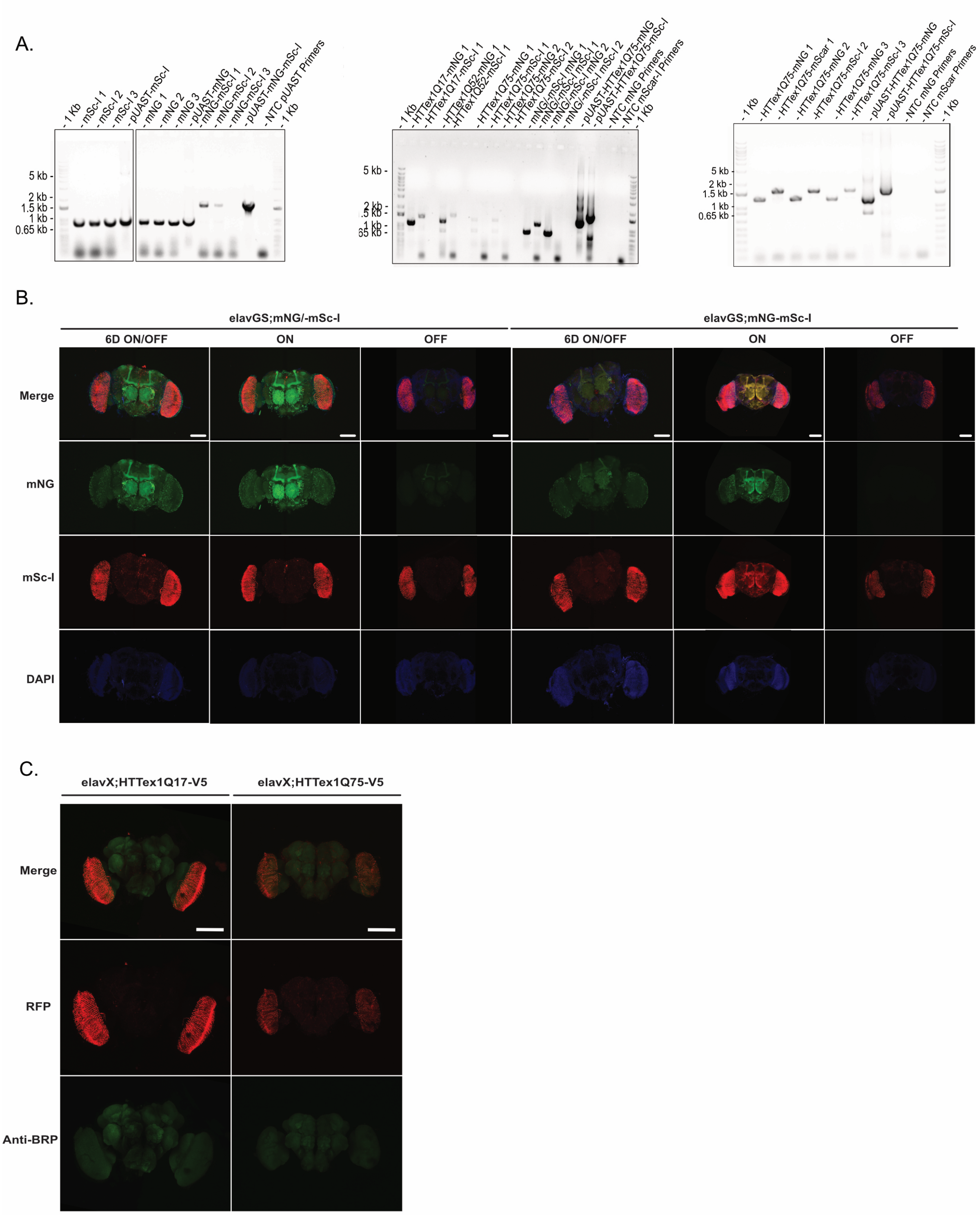

Supplementary Figure 4. Genotyping of transgenic HTTex1-mNG/-mSc-I fly strains

__A)__ Agarose gel image of PCR amplified fragments from transgenic fly genomic DNA using primers for the mNG and mSc-I sequences (indicated by inclusion of mNG or mSc-I in the labelling) which was sent for sanger sequencing. Numbers 1, 2, 3 indicate separate clones. __B)__ Confocal images of transgenic elavGS; mNG/-mSc-I and elavGS;mNG-mSc-I fly brains. Scale bar= 100 µm. __C)__ Confocal images of other transgenic fly brains which do not express mNG or mSc-I fluorescent proteins. Scale bar=100 µm.

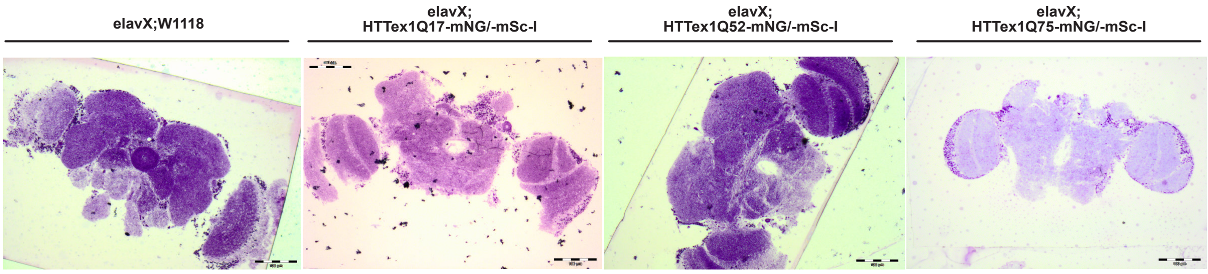

Supplementary Figure 5. Toluidine blue stained elavX;HTTex1-mNG/-mSc-I fly brain sections

Toluidine blue staining of sections of the fly brain (Performed by Mara Rusu). Scale bar= 100 µm

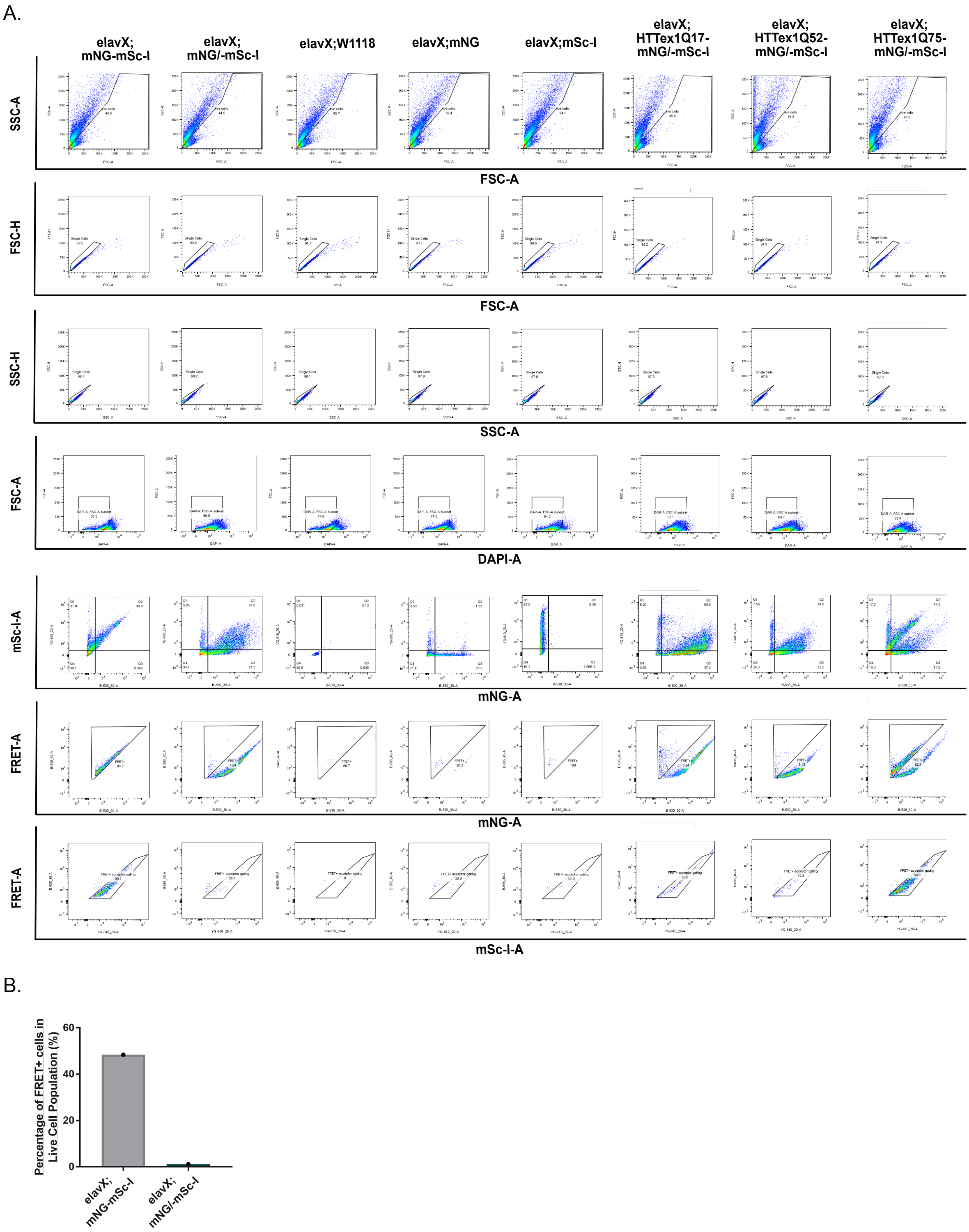

Supplementary Figure 6. FRET FACS gating strategy for FRET positive live cells derived from fly brains

A) *FACS cytograms showing single fluorophore control-based (mNG and mSc-I) FACS gating method for fly single cells. Sequential debris exclusion (side scatter area (SSC-A) vs forward scatter area (FSC-A)), doublet exclusion (forward scatter height (FSC-H) vs FSC-A and side scatter height (SSC-H) vs SSC-A)), live/dead selection (FSCA vs DAPI area (DAPI-A)), double positive gating (mSc-I pulse area (mSc-I A) vs mNG pulse area (mNG-A)) , FRET donor-corrected gating (FRET pulse area (FRET A) vs mNG pulse area (mNG-A) and FRET* *acceptor-corrected gating (FRET-A vs mSc-I-A). Arbitrary units (a.u.) of exactly 50,000 cells (n= 50,000) plotted.* ***B)*** *Percentage of FRET positive cells present in the live cell population of the FRET positive control sample (elavX;mNG-mSc-I) and the FRET negative control sample (elavX;mNG/-mSc-I) as determined by FRET FACS. 1 biological replicate analysed per sample.*

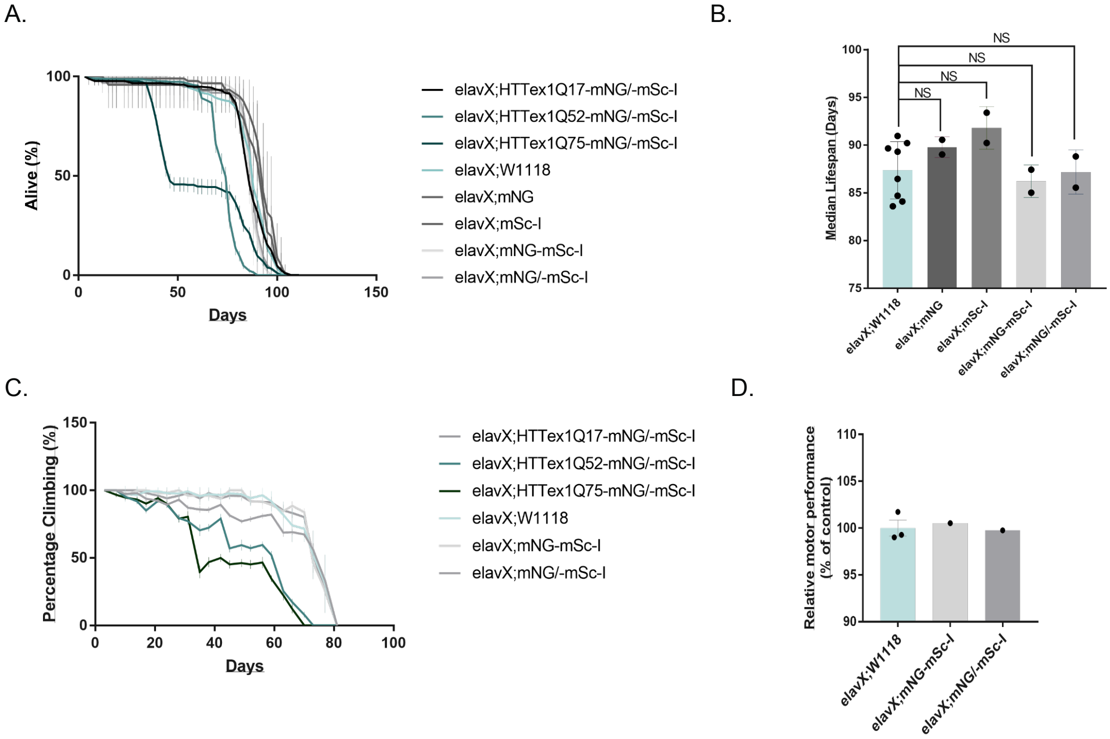

Supplementary Figure 7. Co-expression of pathogenic HTTex1-mNG/-mSc-I fusion proteins decreases lifespan and climbing

A) *Lifespan plotted as percentage of alive flies from 8 biological replicates per strain (N≈ 50 flies per biological replicate). Error bars= SEM.* ***B)*** *Median lifespan values for control fly strains calculated from IC50 values from curves depicted in A. Each dot represents 1 biological replicate (8 biological replicates analysed for elavX;W1118, 2 for all other strains). ~50 flies analysed per biological replicate. Statistical significance assessed by ordinary one-way ANOVA multi-comparisons (NS= P>0.05). Error bars= SEM.* ***C)*** *Climbing ability plotted as percentage flies climbed of the total per day from 3 biological replicates (N≈ 50 flies per biological replicate) Error bars= SEM (performed by Frederick Wieshmann).* ***D)*** *Relative motor performance calculated from area under the curve values obtained from curves depicted in C, relative to elavX;W1118. Each dot represents a biological replicate (3 biological replicates analysed for elavX;W1118, 1 for all other strains). ~ 50 flies analysed per biological replicate.*

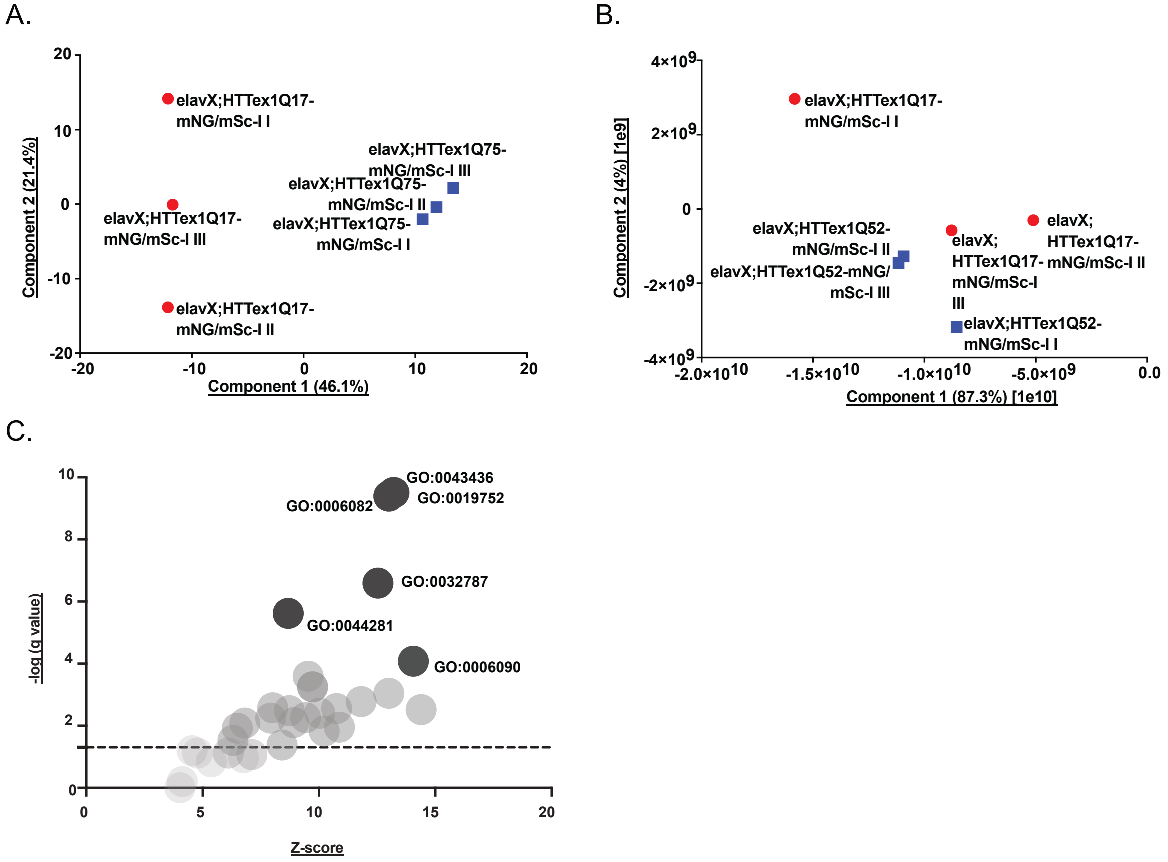

Supplementary Figure 8. PCA analysis of MS datasets and HTTex1Q17-mNG/-mSc-I IP GO enrichment

A) *Principal Component Analysis (PCA) plot depicting the distribution of IP MS samples in a reduced-dimensional space. Data obtained from elavX;HTTex1Q17-mNG/-mSc-I IP material (red circles) and elavX;HTTex1Q75-mNG/-mSc-I IP material (blue squares) depicted. Roman numerals represent the corresponding biological replicates (3 analysed per group). Axes represent principal component 2 (y axis) and component 1 (x axis), which represent the percentage of variance 21.4% and 46.1%, respectively.* ***B)*** *Principal Component Analysis (PCA) plot depicting the distribution of whole brain lysate MS samples in a reduced-dimensional space. Data obtained from elavX;HTTex1Q17-mNG/-mSc-I brain lysates (red circles) and elavX;HTTex1Q52-mNG/-mSc-I brain lysates (blue squares) depicted. Roman numerals represent the corresponding biological replicate (3 analysed per group). Axes represent principal component 2 (y axis) and component 1 (x axis), which represent the percentage of variance 4% and 87.3%, respectively.* ***C)*** *GO biological process term enrichment analysis of proteins enriched with HTTex1Q17-mNG/-mSc-I immunoprecipitates (grey circles). Top 6 terms plotted: GO:0043436=Oxoacid metabolic processes, GO:0019752= Carboxylic acid metabolic processes, GO:006082= Organic acid metabolic processes, GO:0032787= Monocarboxylic acid metabolic processes, GO:0044281=Small molecule metabolic processes and GO:0006090=Pyruvate metabolic processes. Significance cut-off: 0.05 P. value (>1.301 -log P. value) indicated on graph as dotted line. Performed using Metascape.*

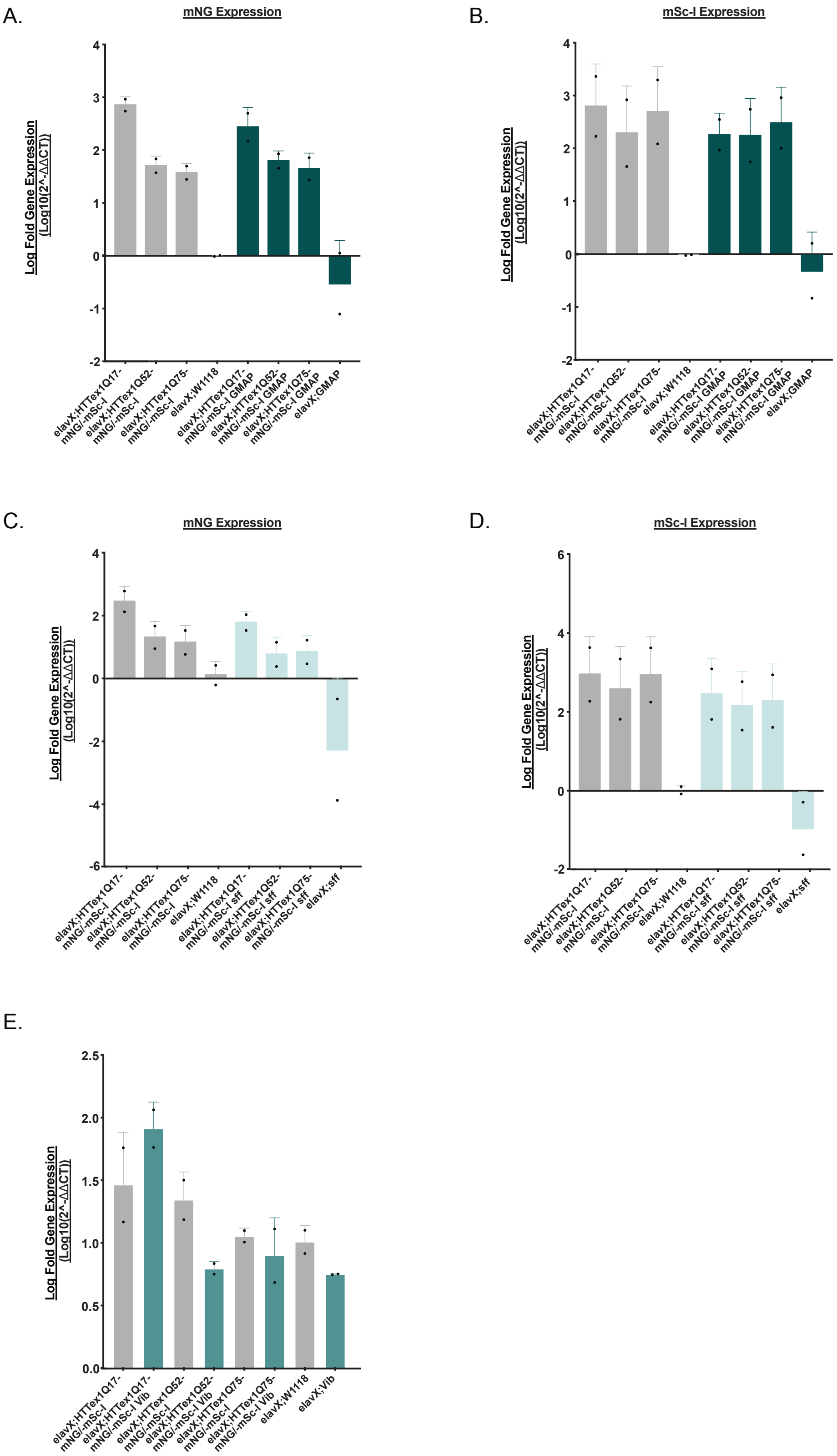

Supplementary Figure 9. qPCR validation of elavX;HTTex1-mNG/-mSc-I RNAi fly strains

RNA from fly heads from the indicated strains was analysed via qPCR to obtain Ct values. Fold gene expression calculated using the 2–ΔΔCt method [360]*. Data were normalised to elavX;W1118 and Actin (Act42) transcripts.*

Each dot represents 1 biological replicate (2 analysed per sample). Each biological replicate value was the average of 2 technical replicates. Statistical significance assessed by ordinary one-way ANOVA multi-comparisons (=P<0.05, **=P<0.01, ***=P<0.001, ****=P<0.0001). Error bars= SD.* ***A)*** *qPCR analysis of HTTex1-mNG transcript expression in elavX;HTTex1 GMAP flies****.*** ***B)*** *qPCR analysis of HTTex1-mSc-I transcript expression in elavX;HTTex1 GMAP flies****.*** ***C)*** *qPCR analysis of HTTex1-mNG transcript expression in elavX;HTTex1 sff flies.* ***D)*** *qPCR analysis of HTTex1-mSc-I transcript expression in elavX;HTTex1 sff flies.* ***E)*** *qPCR analysis of Vib transcript expression in elavX;HTTex1 Vib flies* ***.***

<u>Supplementary Table 1. pUAST plasmids</u>

<u>Plasmid Name</u>	<u>Details</u>	<u>Description</u>
pUAST-attB-rFA	pUAST-Amp-UAS>attB.ccdb>attB	Construct which is optimised for use with *D. melanogaster*. Contains attB site to enable integration into fly genome
pUAST-mNG/-mSc-I	pUAST-Amp-UAS>(RE) PmeI /mNeongreen/cMyc.UAS>(RE) ZraI /mScarlet-I/V5	Backbone for all HTTex1 insertions. Results in the individual expression of mNG and mSc-I which functions as a FRET negative control.
pUAST-HTTex1Q17-mNG/-mSc-I	pUAST-Amp-UAS>HTTex1Q17/mNeongreen/cMyc. UAS>HTTex1Q17/mScarlet-I/V5	Results in expression of both HTTex1Q17-mNG and HTTex1Q17-mSc-I
pUAST-HTTex1Q52-mNG/-mSc-I	pUAST-Amp-UAS>HTTex1Q75/mNeongreen/cMyc. UAS>HTTex1Q75/mScarlet-	Results in expression of both HTTex1Q52-mNG and HTTex1Q52-mSc-I
pUAST-HTTex1Q75-mNG/-mSc-I	pUAST-Amp-UAS>HTTex1Q75/mNeongreen/cMyc. UAS>HTTex1Q75/mScarlet-I/V5	Results in expression of both HTTex1Q75-mNG and HTTex1Q75-mSc-I
pUAST-mNG-mSc-I	pUAST-Amp-UAS>mNeongreen/mScarlet-I/V5.	Results in the expression of mNG fused to mSc-I which acts as a FRET positive control
pUAST -mNG	pUAST-Amp-UAS>mNeongreen/c-myc	Results in the expression of mNG only
pUAST -mSc-I	pUAST-Amp-UAS>mScarlet-I/V5	Results in the expression of mSc-I only

pCMV-GAL4	Amp-CMV-T7>GAL4/Myc	Results in the expression of GAL4 which is required for UAS regulated transgene expression

Supplementary Table 2. Transgenic fly strains

Strain Name	Details	Expressed Proteins
HTTex1Q17-mNG/-mSc-I	CyO/+;TM6/HTTex1Q17-mNG/-mSc-I	HTTex1Q17-mNG HTTex1Q17-mSc-I
HTTex1Q52-mNG/-mSc-I	CyO/+;TM6/HTTex1Q52-mNG/-mSc-I	HTTex1Q52-mNG HTTex1Q52-mSc-I
HTTex1Q75-mNG/-mSc-I	CyO/+;TM6/HTTex1Q75-mNG/-mSc-I	HTTex1Q75-mNG HTTex1Q75-mSc-I
mNG/-mSc-I	CyO/+;TM6/ mNG/-mSc-I	mNG mSc-I
mNG-mSc-I	CyO/+;TM6/mNG-mSc-I	mNG-mSc-I
mNG	CyO/+;TM6/mNG	Results in the expression of mNG fused to mSc-I which acts as a FRET positive control
mSc-I	CyO/+;TM6/mSc-I	Results in the expression of mNG only
W1118	Wildtype control fly	-
elavX	Gal4 pan-neuronal driver	GAL4

Supplementary Table 3. Expected size of transgenes after PCR amplification

Transgene	Size (kb)
HTTex1Q17-mNG/-mSc-I-C-myc	1.05
HTTex1Q17-mNG/-mSc-I-V5	1.40
HTTex1Q52-mNG/-mSc-I-C-myc	1.18
HTTex1Q52-mNG/-mSc-I-V5	1.51
HTTex1Q75-mNG/-mSc-I-C-myc	1.24
HTTex1Q75-mNG/-mSc-I-V5	1.57
mNG-C-myc	0.74
mSc-I-V5	0.74
mNG-mSc-I-V5	1.73
mNG-C-myc/mSc-I-V5	2.85

Supplementary Table 4. Transgenic RNAi and HTTex1-mNG/-mSc-I expressing strains

Strain Name	Details	Expressed Proteins
HTTex1Q17-mNG/-mSc-I Vib	CyO/Vib RNAi; HTTex1Q17-mNG/-mSc-I/TM6	HTTex1Q17-mNG/-mSc-I
HTTex1Q17-mNG/-mSc-I GMAP	CyO/GMAP RNAi; HTTex1Q17-mNG/-mSc-I/TM6	HTTex1Q17-mNG/-mSc-I
HTTex1Q17-mNG/-mSc-I sff	CyO/sff RNAi; HTTex1Q17-mNG/-mSc-I/TM6	HTTex1Q17-mNG/-mSc-I

HTTex1Q52-mNG/-mSc-I Vib	CyO/Vib RNAi; HTTex1Q52-mNG/-mSc-I/TM6	HTTex1Q52-mNG/-mSc-I
HTTex1Q52-mNG/-mSc-I GMAP	CyO/GMAP RNAi; HTTex1Q52-mNG/-mSc-I/TM6	HTTex1Q52-mNG/-mSc-I
HTTex1Q52-mNG/-mSc-I sff	CyO/sff RNAi; HTTex1Q52-mNG/-mSc-I/TM6	HTTex1Q52-mNG/-mSc-I
HTTex1Q75-mNG/-mSc-I Vib	CyO/Vib RNAi; HTTex1Q75-mNG/-mSc-I/TM6	HTTex1Q75-mNG/-mSc-I
HTTex1Q75-mNG/-mSc-I GMAP	CyO/GMAP RNAi; HTTex1Q75-mNG/-mSc-I/TM6	HTTex1Q75-mNG/-mSc-I
HTTex1Q75-mNG/-mSc-I sff	CyO/sff RNAi; HTTex1Q75-mNG/-mSc-I/TM6	HTTex1Q75-mNG/-mSc-I
Vib	Vib RNAi/Sp;MKRS/+	-
GMAP	GMAP RNAi/Sp;MKRS/+	-
sff	sff RNAi/Sp;MKRS/+	-

10. Statement of contributions

This project was funded by the MDC Graduate School and Prof. Erich Wanker. Prof. Erich Wanker, Dr. Anne Ast and myself all contributed to the project idea and planning. For biochemical experiments: Frederick Weismann performed dFRA experiments with elavX head lysates and Leonard Roth performed IP experiments with elavX head lysates for IP MS, under my supervision. For fly phenotyping: Frederick Weismann performed the climbing assay under my supervision. For MS sample handling: IP MS LFQ values were obtained by Dr. Oliver Popp and whole brain lysate MS LFQ values were obtained by Heike Stephanowitz. For EM data: Dr. Mara Rusu performed whole brain sample preparation, imaging for whole brain and iEM experiments and quantification of iEM data.

11. List of figures

12. List of tables

13. References

1. Arani MG, Fakharian E, Sarbandi F. Ancient Legacy of Cranial Surgery. *Arch Trauma Res*. 2012;1(2):72. doi:10.5812/ATR.6556
2. Faria M. Neolithic trepanation decoded- A unifying hypothesis: Has the mystery as to why primitive surgeons performed cranial surgery been solved? *Surg Neurol Int*. 2015;6(1). doi:10.4103/2152-7806.156634
3. Van Middendorp JJ, Sanchez GM, Burridge AL. The Edwin Smith papyrus: a clinical reappraisal of the oldest known document on spinal injuries. *Eur Spine J*. 2010;19(11):1815-1823. doi:10.1007/S00586-010-1523-6
4. Aphrodisiensis A, Asclepius Ad H). Alcmaeon of Croton: His Life, Work, and Fragments. *Proc R Soc Med*. 1932;25(7):1041. doi:10.1177/003591573202500759
5. Kidd GJ, Ohno N, Trapp BD. Biology of Schwann cells. *Handb Clin Neurol*. 2013;115:55-79. doi:10.1016/B978-0-444-52902-2.00005-9
6. Mazurak M, Kusa J. Jan Evangelista Purkinje: A Passion for Discovery. *Tex Heart Inst J*. 2018;45(1):23-26. doi:10.14503/THIJ-17-6351
7. López-Muñoz F, Boya J, Alamo C. Neuron theory, the cornerstone of neuroscience, on the centenary of the Nobel Prize award to Santiago Ramón y Cajal. *Brain Res Bull*. 2006;70(4-6):391-405. doi:10.1016/J.BRAINRESBULL.2006.07.010
8. Scheuerlein H, Henschke F, Köckerling F. Wilhelm von Waldeyer-Hartz-A Great Forefather: His Contributions to Anatomy with Particular Attention to “His” Fascia. *Front Surg*. 2017;4. doi:10.3389/FSURG.2017.00074
9. Herculano-Houzel S. The human brain in numbers: a linearly scaled-up primate brain. *Front Hum Neurosci*. 2009;3(NOV). doi:10.3389/NEURO.09.031.2009
10. Herculano-Houzel S. The remarkable, yet not extraordinary, human brain as a scaled-up primate brain and its associated cost. *Proc Natl Acad Sci U S A*. 2012;109 Suppl 1(Suppl 1):10661-10668. doi:10.1073/PNAS.1201895109
11. Herculano-Houzel S, Catania K, Manger PR, Kaas JH. Mammalian Brains Are Made of These: A Dataset of the Numbers and Densities of Neuronal and Nonneuronal Cells in the Brain of Glires, Primates, Scandentia, Eulipotyphlans, Afrotherians and Artiodactyls, and Their Relationship with Body Mass. *Brain Behav Evol*. 2015;86(3-4):145-163. doi:10.1159/000437413
12. Beaulieu-Laroche L, Brown NJ, Hansen M, et al. Allometric rules for mammalian cortical layer 5 neuron biophysics. *Nature*. 2021;600(7888):274-278. doi:10.1038/S41586-021-04072-3
13. Lamptey RNL, Chaulagain B, Trivedi R, Gothwal A, Layek B, Singh J. A Review of the Common Neurodegenerative Disorders: Current Therapeutic Approaches and the Potential Role of Nanotherapeutics. *Int J Mol Sci*. 2022;23(3). doi:10.3390/IJMS23031851
14. Dugger BN, Dickson DW. Pathology of Neurodegenerative Diseases. *Cold Spring Harb Perspect Biol*. 2017;9(7). doi:10.1101/CSHPERSPECT.A028035
15. Giordano A, De Panfilis L, Perin M, et al. Advance Care Planning in Neurodegenerative Disorders: A Scoping Review. *Int J Environ Res Public Health*. 2022;19(2). doi:10.3390/IJERPH19020803
16. Aza A, Gómez-Vela M, Badia M, et al. Listening to families with a person with neurodegenerative disease talk about their quality of life: integrating quantitative

and qualitative approaches. *Health Qual Life Outcomes*. 2022;20(1). doi:10.1186/S12955-022-01977-Z

17. Strafella C, Caputo V, Galota MR, et al. Application of Precision Medicine in Neurodegenerative Diseases. *Front Neurol*. 2018;9(AUG). doi:10.3389/FNEUR.2018.00701
18. Bates GP, Dorsey R, Gusella JF, et al. Huntington disease. *Nat Rev Dis Primers*. 2015;1. doi:10.1038/NRDP.2015.5
19. McColgan P, Tabrizi SJ. Huntington's disease: a clinical review. *Eur J Neurol*. 2018;25(1):24-34. doi:10.1111/ene.13413
20. Paulson HL, Albin RL. Huntington's Disease: Clinical Features and Routes to Therapy. *Neurobiology of Huntington's Disease: Applications to Drug Discovery*. Published online 2011.
21. Gusella JF, Wexler NS, Conneally PM, et al. A polymorphic DNA marker genetically linked to Huntington's disease. *Nature*. 1983;306(5940):234-238. doi:10.1038/306234A0
22. Wexler NS, Lorimer J, Porter J, et al. Venezuelan kindreds reveal that genetic and environmental factors modulate Huntington's disease age of onset. *Proc Natl Acad Sci U S A*. 2004;101(10):3498-3503. doi:10.1073/PNAS.0308679101
23. Williams JK, Erwin C, Juhl AR, et al. In their own words: Reports of stigma and genetic discrimination by people at risk for huntington disease in the international RESPOND-HD study. *American Journal of Medical Genetics, Part B: Neuropsychiatric Genetics*. 2010;153(6):1150-1159. doi:10.1002/ajmg.b.31080
24. Erwin C, Williams JK, Juhl AR, et al. Perception, experience, and response to genetic discrimination in Huntington disease: the international RESPOND-HD study. *Am J Med Genet B Neuropsychiatr Genet*. 2010;153B(5):1081-1093. doi:10.1002/AJMG.B.31079
25. Vale TC, Cardoso F. Chorea: A Journey through History. *Tremor Other Hyperkinet Mov (N Y)*. 2015;5(0):5. doi:10.7916/D8WM1C98
26. Haas LF. St Vitus (286-302). *J Neurol Neurosurg Psychiatry*. 1991;54(5):387. doi:10.1136/JNNP.54.5.387
27. HECKER. JFC. *The Black Death, and The Dancing Mania*. (BABINGTON. BG, ed.). CASSELL & COMPANY, Limited; 1888. Accessed November 20, 2023. https://www.gutenberg.org/files/1739/1739-h/1739-h.htm
28. Huntington G. On chorea. George Huntington, M.D. *J Neuropsychiatry Clin Neurosci*. 2003;15(1):109-112. doi:10.1176/jnp.15.1.109
29. Mendel's principles of heredity, by W. Bateson : Bateson, William, 1861-1926. University Press, Cambridge. Published 1909. Accessed November 20, 2023. https://archive.org/details/mendelsprinciple00bate/page/228/mode/2up
30. Wexler A. Stigma, history, and Huntington's disease. *Lancet*. 2010;376(9734):18-19. doi:10.1016/S0140-6736(10)60957-9
31. Davenport CB. Huntington's Chorea in Relation to Heredity and Eugenics. *Proc Natl Acad Sci U S A*. 1915;1(5):283-285. doi:10.1073/PNAS.1.5.283
32. Vessie PR. ON THE TRANSMISSION OF HUNTINGTON'S CHOREA FOR 300 YEARS—THE BURES FAMILY GROUP. *J Nerv Ment Dis*. 1932;76(6):553-573. doi:10.1097/00005053-193212000-00001
33. *HUNTINGTON'S CHOREA AND EAST ANGLIA*. Vol. 42, N. Oxford University Press; 1934. Accessed November 20, 2023. https://www.jstor.org/stable/45208438

34. Hans MB, Gilmore TH. Huntington’s chorea and genealogical credibility. *J Nerv Ment Dis*. 1969;148(1):5-13. doi:10.1097/00005053-196901000-00002
35. Wexler A. Eugenics, heredity, and huntington’s disease: A brief historical perspective. *J Huntingtons Dis*. 2012;1(2):139-141. doi:10.3233/JHD-129007
36. Ridley RM, Frith CD, Crow TJ, Conneally PM. Anticipation in Huntington’s disease is inherited through the male line but may originate in the female. *J Med Genet*. 1988;25(9):589-595. doi:10.1136/JMG.25.9.589
37. Went LN, Vegter-van der Vlis M, Bruyn GW. Parental transmission in Huntington’s disease. *Lancet*. 1984;1(8386):1100-1102. doi:10.1016/S0140-6736(84)92510-8
38. Reik W. Genomic imprinting: a possible mechanism for the parental origin effect in Huntington’s chorea. *J Med Genet*. 1988;25(12):805-808. doi:10.1136/JMG.25.12.805
39. MacDonald ME, Ambrose CM, Duyao MP, et al. A novel gene containing a trinucleotide repeat that is expanded and unstable on Huntington’s disease chromosomes. The Huntington’s Disease Collaborative Research Group. *Cell*. 1993;72(6):971-983. doi:10.1016/0092-8674(93)90585-E
40. Walker FO. Huntington’s disease. *Lancet*. 2007;369(9557):218-228. doi:10.1016/S0140-6736(07)60111-1
41. Bozza A, Malagù S, Calzolari E, Novelletto A, Pavoni M, del Senno L. Expansion of a (CAG)n repeat region in a sporadic case of HD. *Acta Neurol Scand*. 1995;92(2):132-134. doi:10.1111/J.1600-0404.1995.TB01026.X
42. Batino LKJ, Hiyadan J, Liquete D, Flores M. Sporadic Huntington’s disease in the Philippines: A case report. *Neurodegener Dis Manag*. 2021;11(6):445-449. doi:10.2217/nmt-2021-0023
43. Myers RH, Macdonald ME, Koroshetz WJ, et al. De novo expansion of a (CAG)n repeat in sporadic Huntington’s disease. *Nat Genet*. 1993;5(2):168-173. doi:10.1038/NG1093-168
44. Andrew SE, Goldberg YP, Kremer B, et al. The relationship between trinucleotide (CAG) repeat length and clinical features of Huntington’s disease. *Nat Genet*. 1993;4(4):398-403. doi:10.1038/NG0893-398
45. Duyao M, Ambrose C, Myers R, et al. Trinucleotide repeat length instability and age of onset in Huntington’s disease. *Nat Genet*. 1993;4(4):387-392. doi:10.1038/NG0893-387
46. Stine OC, Pleasant N, Franz ML, Abbott MH, Folstein SE, Ross CA. Correlation between the onset age of Huntington’s disease and length of the trinucleotide repeat in IT-15. *Hum Mol Genet*. 1993;2(10):1547-1549. doi:10.1093/HMG/2.10.1547
47. Semaka A, Kay C, Doty C, et al. CAG size-specific risk estimates for intermediate allele repeat instability in Huntington disease. *J Med Genet*. 2013;50(10):696-703. doi:10.1136/jmedgenet-2013-101796
48. Gusella JF, MacDonald ME. Huntington’s disease: the case for genetic modifiers. *Genome Med*. 2009;1(8). doi:10.1186/GM80
49. Li JL, Hayden MR, Warby SC, et al. Genome-wide significance for a modifier of age at neurological onset in Huntington’s disease at 6q23-24: The HD MAPS study. *BMC Med Genet*. 2006;7. doi:10.1186/1471-2350-7-71
50. Donaldson J, Powell S, Rickards N, Holmans P, Jones L. What is the Pathogenic CAG Expansion Length in Huntington’s Disease? *J Huntingtons Dis*. 2021;10(1):175-202. doi:10.3233/JHD-200445

51. De Rooij KE, De Koning Gans PAM, Roos RAC, Van Ommen GJB, Den Dunnen JT. Somatic expansion of the (CAG)n repeat in Huntington disease brains. *Hum Genet*. 1995;95(3):270-274. doi:10.1007/BF00225192
52. Lee JM, Wheeler VC, Chao MJ, et al. Identification of Genetic Factors that Modify Clinical Onset of Huntington’s Disease. *Cell*. 2015;162(3):516-526. doi:10.1016/j.cell.2015.07.003
53. Moss DJH, Tabrizi SJ, Mead S, et al. Identification of genetic variants associated with Huntington’s disease progression: a genome-wide association study. *Lancet Neurol*. 2017;16(9):701-711. doi:10.1016/S1474-4422(17)30161-8
54. Novati A, Nguyen HP, Schulze-Hentrich J. Environmental stimulation in Huntington disease patients and animal models. *Neurobiol Dis*. 2022;171. doi:10.1016/J.NBD.2022.105725
55. Medina A, Mahjoub Y, Shaver L, Pringsheim T. Prevalence, and Incidence of Huntington’s Disease: An Updated Systematic Review and Meta-Analysis. *Movement Disorders*. 2022;37(12):2327-2335. doi:10.1002/mds.29228
56. Kounidas G, Cruickshank H, Kastora S, Sihlabela S, Miedzybrodzka Z. The known burden of Huntington disease in the North of Scotland: prevalence of manifest and identified pre-symptomatic gene expansion carriers in the molecular era. *J Neurol*. 2021;268(11):4170-4177. doi:10.1007/s00415-021-10505-w
57. Evolution as a process / edited by Julian Huxley, A.C. Hardy, E.B. Ford. | Wellcome Collection. Accessed November 20, 2023. https://wellcomecollection.org/works/vf9q9akq
58. Andhale R, Shrivastava D. Huntington’s Disease: A Clinical Review. *Cureus*. 2022;14(8). doi:10.7759/cureus.28484
59. Khavinson V, Popovich I, Mikhailova O. Towards realization of longer life. *Acta Biomed*. 2020;91(3):1-9. doi:10.23750/ABM.V91I3.10079
60. Ferguson MW, Kennedy CJ, Palpagama TH, Waldvogel HJ, Faull RLM, Kwakowsky A. Current and Possible Future Therapeutic Options for Huntington’s Disease. *J Cent Nerv Syst Dis*. 2022;14. doi:10.1177/11795735221092517
61. Sampaio C, Levey J, Klitzman R. Predictive testing and clinical trials in Huntington’s disease: An ethical analysis. *Movement Disorders*. 2018;33(2):243-247. doi:10.1002/mds.27247
62. Baine FK, Kay C, Ketelaar ME, et al. Huntington disease in the South African population occurs on diverse and ethnically distinct genetic haplotypes. *Eur J Hum Genet*. 2013;21(10):1120-1127. doi:10.1038/EJHG.2013.2
63. Futter MJ, Heckmann JM, Greenberg LJ. Predictive testing for Huntington disease in a developing country. *Clin Genet*. 2009;75(1):92-97. doi:10.1111/J.1399-0004.2008.01044.X
64. Roos RAC. Huntington’s disease: a clinical review. *Orphanet J Rare Dis*. 2010;5(1). doi:10.1186/1750-1172-5-40
65. Duff K, Paulsen JS, Beglinger LJ, Langbehn DR, Stout JC. Psychiatric Symptoms in Huntington’s Disease before Diagnosis: The Predict-HD Study. *Biol Psychiatry*. 2007;62(12):1341-1346. doi:10.1016/j.biopsych.2006.11.034
66. Paulsen JS. Cognitive impairment in Huntington disease: Diagnosis and treatment. *Curr Neurol Neurosci Rep*. 2011;11(5):474-483. doi:10.1007/s11910-011-0215-x

67. Molano-Eslava JC, Iragorri-Cucalón A, Ucrós-Rodríguez G, et al. Obsessive-Compulsive Disorder Symptoms in Huntington's Disease: A Case Report. *Rev Colomb Psiquiatr*. 2008;37(4):644-654. doi:10.1901/JABA.2008.37-644
68. Jaini A, Yomtoob J, Yeh C, Bega D. Understanding HD psychosis: An analysis from the ENROLL-HD database. *Tremor and Other Hyperkinetic Movements*. 2020;10(1):1-8. doi:10.5334/tohm.395
69. Goodman AOG, Barker RA. How vital is sleep in Huntington's disease? *J Neurol*. 2010;257(6):882-897. doi:10.1007/S00415-010-5517-4
70. Herzog-Krzywoszanska R, Krzywoszanski L. Sleep disorders in Huntington's disease. *Front Psychiatry*. 2019;10(APR). doi:10.3389/fpsyt.2019.00221
71. Epping EA, Paulsen JS. Depression in the early stages of Huntington disease. *Neurodegener Dis Manag*. 2011;1(5):407-414. doi:10.2217/nmt.11.45
72. Van Duijn E, Reedeker N, Giltay EJ, Roos RAC, Van Der Mast RC. Correlates of apathy in Huntington's disease. *J Neuropsychiatry Clin Neurosci*. 2010;22(3):287-294. doi:10.1176/JNP.2010.22.3.287
73. Van Duijn E, Kingma EM, Van Der Mast RC. Psychopathology in verified Huntington's disease gene carriers. *Journal of Neuropsychiatry and Clinical Neurosciences*. 2007;19(4):441-448. doi:10.1176/jnp.2007.19.4.441
74. Kingma EM, van Duijn E, Timman R, van der Mast RC, Roos RAC. Behavioural problems in Huntington's disease using the Problem Behaviours Assessment. *Gen Hosp Psychiatry*. 2008;30(2):155-161. doi:10.1016/J.GENHOSPPSYCH.2007.11.005
75. Julien CL, Thompson JC, Wild S, et al. Psychiatric disorders in preclinical Huntington's disease. *J Neurol Neurosurg Psychiatry*. 2007;78(9):939-943. doi:10.1136/jnnp.2006.103309
76. Paulsen JS, Hoth KF, Nehl C, Stierman L. Critical periods of suicide risk in Huntington's disease. *Am J Psychiatry*. 2005;162(4):725-731. doi:10.1176/APPI.AJP.162.4.725
77. Wetzel HH, Gehl CR, Dellefave-Castillo L, Schiffman JF, Shannon KM, Paulsen JS. Suicidal ideation in Huntington disease: the role of comorbidity. *Psychiatry Res*. 2011;188(3):372-376. doi:10.1016/J.PSYCHRES.2011.05.006
78. Sørensen SA, Fenger K. Causes of death in patients with Huntington's disease and in unaffected first degree relatives. *J Med Genet*. 1992;29(12):911-914. doi:10.1136/jmg.29.12.911
79. Solomon AC, Stout JC, Johnson SA, et al. Verbal episodic memory declines prior to diagnosis in Huntington's disease. *Neuropsychologia*. 2007;45(8):1767-1776. doi:10.1016/J.NEUROPSYCHOLOGIA.2006.12.015
80. Solomon AC, Stout JC, Weaver M, et al. Ten-year rate of longitudinal change in neurocognitive and motor function in prediagnosis Huntington disease. *Mov Disord*. 2008;23(13):1830-1836. doi:10.1002/MDS.22097
81. Paulsen JS, Zhao H, Stout JC, et al. Clinical markers of early disease in persons near onset of Huntington's disease. *Neurology*. 2001;57(4):658-662. doi:10.1212/WNL.57.4.658
82. Paulsen JS. Early detection of Huntington's disease. *Future Neurol*. 2010;5(1):85-104. doi:10.2217/fnl.09.78
83. Corey-Bloom J, Williams ME, Beltran-Najera I, et al. Central Cognitive Processing Speed Is an Early Marker of Huntington's Disease Onset. *Mov Disord Clin Pract*. 2020;8(1):100-105. doi:10.1002/MDC3.13121

84. Beste C, Saft C, Andrich J, Müller T, Gold R, Falkenstein M. Time processing in Huntington’s disease: a group-control study. *PLoS One*. 2007;2(12). doi:10.1371/JOURNAL.PONE.0001263
85. Peavy GM, Jacobson MW, Goldstein JL, et al. Cognitive and functional decline in Huntington’s disease: dementia criteria revisited. *Mov Disord*. 2010;25(9):1163-1169. doi:10.1002/MDS.22953
86. Kirkwood SC, Su JL, Conneally PM, Foroud T. Progression of symptoms in the early and middle stages of Huntington disease. *Arch Neurol*. 2001;58(2):273-278. doi:10.1001/archneur.58.2.273
87. Jacobs M, Hart EP, van Zwet EW, et al. Progression of motor subtypes in Huntington’s disease: a 6-year follow-up study. *J Neurol*. 2016;263(10):2080-2085. doi:10.1007/s00415-016-8233-x
88. Reetz K, Werner CJ, Schiefer J. Clinical diagnosis and management in early Huntington’s disease: a review. *Degener Neurol Neuromuscul Dis*. 2015;5:37. doi:10.2147/DNND.S49135
89. Djoussé L, Knowlton B, Cupples LA, Marder K, Shoulson I, Myers RH. Weight loss in early stage of Huntington’s disease. *Neurology*. 2002;59(9):1325-1330. doi:10.1212/01.WNL.0000031791.10922.CF
90. Hunt VP, Walker FO. Dysphagia in Huntington’s disease. *J Neurosci Nurs*. 1989;21(2):92-95. doi:10.1097/01376517-198904000-00005
91. Gilbert GJ. Weight loss in Huntington disease increases with higher CAG repeat number. *Neurology*. 2009;73(7):572. doi:10.1212/WNL.0B013E3181AF0CF4
92. Skene DJ, Middleton B, Fraser CK, et al. Metabolic profiling of presymptomatic Huntington’s disease sheep reveals novel biomarkers. *Sci Rep*. 2017;7. doi:10.1038/srep43030
93. Skirton H, Williams JK, Jackson Barnette J, Paulsen JS. Huntington disease: Families’ experiences of healthcare services. *J Adv Nurs*. 2010;66(3):500-510. doi:10.1111/j.1365-2648.2009.05217.x
94. De Tommaso M, Nuzzi A, Dellomonaco AR, et al. Dysphagia in Huntington’s disease: Correlation with clinical features. *Eur Neurol*. 2015;74(1-2):49-53. doi:10.1159/000435833
95. Rodrigues FB, Abreu D, Damásio J, et al. Survival, Mortality, Causes and Places of Death in a European Huntington’s Disease Prospective Cohort. *Mov Disord Clin Pract*. 2017;4(5):737-742. doi:10.1002/MDC3.12502
96. Varela LE, Arias MM, Martorell-Poveda MA, Giraldo C V., Estrada-Acuña RA. Beyond the clinical context: the process of losing oneself living with Huntington’s disease. *Orphanet J Rare Dis*. 2022;17(1). doi:10.1186/S13023-022-02330-9
97. Leidl BF, Fox-Davis D, Walker FO, Gabbard J, Marterre B. Layers of Loss: A Scoping Review and Taxonomy of HD Caregivers’ Spiritual Suffering, Grief/Loss and Coping Strategies. *J Pain Symptom Manage*. 2023;65(1):e29-e50. doi:10.1016/j.jpainsymman.2022.09.010
98. Jona CMH, Labuschagne I, Mercieca EC, et al. Families Affected by Huntington’s Disease Report Difficulties in Communication, Emotional Involvement, and Problem Solving. *J Huntingtons Dis*. 2017;6(3):169-177. doi:10.3233/JHD-170250
99. Gibson JS, Springer K. Social Withdrawal in Huntington’s Disease: A Scoping Review. *J Huntingtons Dis*. 2022;11(1):17-24. doi:10.3233/JHD-210519

100. Tabrizi SJ, Reilmann R, Roos RAC, et al. Potential endpoints for clinical trials in premanifest and early Huntington's disease in the TRACK-HD study: analysis of 24 month observational data. *Lancet Neurol*. 2012;11(1):42-53. doi:10.1016/S1474-4422(11)70263-0
101. Paulsen JS, Langbehn DR, Stout JC, et al. Detection of Huntington's disease decades before diagnosis: the Predict-HD study. *J Neurol Neurosurg Psychiatry*. 2008;79(8):874-880. doi:10.1136/JNNP.2007.128728
102. Ross CA, Aylward EH, Wild EJ, et al. Huntington disease: natural history, biomarkers and prospects for therapeutics. *Nat Rev Neurol*. 2014;10(4):204-216. doi:10.1038/NRNEUROL.2014.24
103. Kinnunen KM, Schwarz AJ, Turner EC, et al. Volumetric MRI-Based Biomarkers in Huntington's Disease: An Evidentiary Review. *Front Neurol*. 2021;12. doi:10.3389/FNEUR.2021.712555
104. Rüb U, Seidel K, Heinsen H, Vonsattel JP, den Dunnen WF, Korf HW. Huntington's disease (HD): the neuropathology of a multisystem neurodegenerative disorder of the human brain. *Brain Pathol*. 2016;26(6):726-740. doi:10.1111/BPA.12426
105. Bamford IJ, Bamford NS. The Striatum's Role in Executing Rational and Irrational Economic Behaviors. *Neuroscientist*. 2019;25(5):475-490. doi:10.1177/1073858418824256
106. Ehrlich ME. Huntington's disease and the striatal medium spiny neuron: cell-autonomous and non-cell-autonomous mechanisms of disease. *Neurotherapeutics*. 2012;9(2):270-284. doi:10.1007/S13311-012-0112-2
107. Deng YP, Albin RL, Penney JB, Young AB, Anderson KD, Reiner A. Differential loss of striatal projection systems in Huntington's disease: A quantitative immunohistochemical study. *J Chem Neuroanat*. 2004;27(3):143-164. doi:10.1016/j.jchemneu.2004.02.005
108. Rosas HD, Hevelone ND, Zaleta AK, Greve DN, Salat DH, Fischl B. Regional cortical thinning in preclinical Huntington disease and its relationship to cognition. *Neurology*. 2005;65(5):745-747. doi:10.1212/01.WNL.0000174432.87383.87
109. Tabrizi SJ, Langbehn DR, Leavitt BR, et al. Biological and clinical manifestations of Huntington's disease in the longitudinal TRACK-HD study: cross-sectional analysis of baseline data. *Lancet Neurol*. 2009;8(9):791-801. doi:10.1016/S1474-4422(09)70170-X
110. Paulsen JS, Nopoulos PC, Aylward E, et al. Striatal and white matter predictors of estimated diagnosis for Huntington disease. *Brain Res Bull*. 2010;82(3-4):201-207. doi:10.1016/J.BRAINRESBULL.2010.04.003
111. Domínguez D JF, Egan GF, Gray MA, et al. Multi-modal neuroimaging in premanifest and early Huntington's disease: 18 month longitudinal data from the IMAGE-HD study. *PLoS One*. 2013;8(9). doi:10.1371/JOURNAL.PONE.0074131
112. Rosas HD, Koroshetz WJ, Chen YI, et al. Evidence for more widespread cerebral pathology in early HD: an MRI-based morphometric analysis. *Neurology*. 2003;60(10):1615-1620. doi:10.1212/01.WNL.0000065888.88988.6E
113. De La Monte SM, Vonsattel JP, Richardson EP. Morphometric demonstration of atrophic changes in the cerebral cortex, white matter, and neostriatum in Huntington's disease. *J Neuropathol Exp Neurol*. 1988;47(5):516-525. doi:10.1097/00005072-198809000-00003

114. Heinsen H, Strik M, Bauer M, et al. Cortical and striatal neurone number in Huntington’s disease. *Acta Neuropathol*. 1994;88(4):320-333. doi:10.1007/BF00310376
115. Hayden MR, Leavitt BR, Yasothan U, Kirkpatrick P. Tetrabenazine. *Nat Rev Drug Discov*. 2009;8(1):17-18. doi:10.1038/NRD2784
116. Zheng G, Dwoskin LP, Crooks PA. Vesicular monoamine transporter 2: role as a novel target for drug development. *AAPS J*. 2006;8(4). doi:10.1208/AAPSJ080478
117. Coppen EM, Roos RAC. Current Pharmacological Approaches to Reduce Chorea in Huntington’s Disease. *Drugs*. 2017;77(1):29-46. doi:10.1007/S40265-016-0670-4
118. Duff K, Beglinger LJ, O’Rourke ME, Nopoulos P, Paulson HL, Paulsen JS. Risperidone and the treatment of psychiatric, motor, and cognitive symptoms in Huntington’s disease. *Ann Clin Psychiatry*. 2008;20(1):1-3. doi:10.1080/10401230701844802
119. Squitieri F, Cannella M, Porcellini A, Brusa L, Simonelli M, Ruggieri S. Short-term effects of olanzapine in Huntington disease. *Neuropsychiatry Neuropsychol Behav Neurol*. 2001;14(1):69-72.
120. Gibson JS, Claassen DO. State-of-the-art pharmacological approaches to reduce chorea in Huntington’s disease. *Expert Opin Pharmacother*. 2021;22(8):1015-1024. doi:10.1080/14656566.2021.1876666
121. Busse ME, Khalil H, Quinn L, Rosser AE. Physical therapy intervention for people with Huntington disease. *Phys Ther*. 2008;88(7):820-831. doi:10.2522/ptj.20070346
122. Mirek E, Filip M, Banaszkiewicz K, et al. The effects of physiotherapy with PNF concept on gait and balance of patients with Huntington’s disease – pilot study. *Neurol Neurochir Pol*. 2015;49(6):354-357. doi:10.1016/j.pjnns.2015.09.002
123. Hamilton A, Ferm U, Heemskerk AW, et al. Management of speech, language and communication difficulties in Huntington’s disease. *Neurodegen Dis Manage*. 2012;2(1):67-77. Accessed November 20, 2023. https://ehdn.org/wp-content/uploads/2016/08/Management_of_speech_language_and_communication_difficulties_in_HD.pdf
124. Żukiewicz-Sobczak W, Król R, Wróblewska P, Piątek J, Gibas-Dorna M. Huntington Disease - principles and practice of nutritional management. *Neurol Neurochir Pol*. 2014;48(6):442-448. doi:10.1016/J.PJNNS.2014.10.006
125. Zarotti N, Dale M, Eccles F, Simpson J. Psychological Interventions for People with Huntington’s Disease: A Call to Arms. *J Huntingtons Dis*. 2020;9(3):231-243. doi:10.3233/JHD-200418
126. Rook ME, Southwell AL. Antisense Oligonucleotide Therapy: From Design to the Huntington Disease Clinic. *BioDrugs*. 2022;36(2):105-119. doi:10.1007/s40259-022-00519-9
127. Butland SL, Devon RS, Huang Y, et al. CAG-encoded polyglutamine length polymorphism in the human genome. *BMC Genomics*. 2007;8. doi:10.1186/1471-2164-8-126
128. Tabrizi SJ, Leavitt BR, Landwehrmeyer GB, et al. Targeting Huntingtin Expression in Patients with Huntington’s Disease. *New England Journal of Medicine*. 2019;380(24):2307-2316. doi:10.1056/nejmoa1900907
129. Kay C, Skotte NH, Southwell AL, Hayden MR. Personalized gene silencing therapeutics for Huntington disease. *Clin Genet*. 2014;86(1):29-36. doi:10.1111/CGE.12385

130. Kay C, Collins JA, Skotte NH, et al. Huntingtin Haplotypes Provide Prioritized Target Panels for Allele-specific Silencing in Huntington Disease Patients of European Ancestry. *Mol Ther*. 2015;23(11):1759-1771. doi:10.1038/MT.2015.128
131. Ruzo A, Ismailoglu I, Popowski M, et al. Discovery of novel isoforms of huntingtin reveals a new hominid-specific exon. *PLoS One*. 2015;10(5). doi:10.1371/JOURNAL.PONE.0127687
132. Romo L, Ashar-Patel A, Pfister E, Aronin N. Alterations in mRNA 3' UTR Isoform Abundance Accompany Gene Expression Changes in Human Huntington's Disease Brains. *Cell Rep*. 2017;20(13):3057-3070. doi:10.1016/J.CELREP.2017.09.009
133. Lin B, Rommens JM, Graham RK, et al. Differential 3' polyadenylation of the Huntington disease gene results in two mRNA species with variable tissue expression. *Hum Mol Genet*. 1993;2(10):1541-1545. doi:10.1093/HMG/2.10.1541
134. Saudou F, Humbert S. The Biology of Huntingtin. *Neuron*. 2016;89(5):910-926. doi:10.1016/j.neuron.2016.02.003
135. Neueder A, Landles C, Ghosh R, et al. The pathogenic exon 1 HTT protein is produced by incomplete splicing in Huntington's disease patients. *Sci Rep*. 2017;7(1). doi:10.1038/S41598-017-01510-Z
136. Sathasivam K, Neueder A, Gipson TA, et al. Aberrant splicing of HTT generates the pathogenic exon 1 protein in Huntington disease. *Proc Natl Acad Sci U S A*. 2013;110(6):2366-2370. doi:10.1073/PNAS.1221891110/-/DCSUPPLEMENTAL/PNAS.201221891SI.PDF
137. Fienko S, Landles C, Sathasivam K, et al. Alternative processing of human HTT mRNA with implications for Huntington's disease therapeutics. *Brain*. 2022;145(12):4409-4424. doi:10.1093/BRAIN/AWAC241
138. Schilling G, Klevytska A, Tebbenkamp ATN, et al. Characterization of huntingtin pathologic fragments in human Huntington disease, transgenic mice, and cell models. *J Neuropathol Exp Neurol*. 2007;66(4):313-320. doi:10.1097/NEN.0B013E318040B2C8
139. DiFiglia M, Sapp E, Chase KO, et al. Aggregation of huntingtin in neuronal intranuclear inclusions and dystrophic neurites in brain. *Science (1979)*. 1997;277(5334):1990-1993. doi:10.1126/science.277.5334.1990
140. Tartari M, Gissi C, Lo Sardo V, et al. Phylogenetic comparison of huntingtin homologues reveals the appearance of a primitive polyQ in sea urchin. *Mol Biol Evol*. 2008;25(2):330-338. doi:10.1093/molbev/msm258
141. Guo Q, Huang B, Cheng J, et al. The cryo-electron microscopy structure of huntingtin. *Nature*. 2018;555(7694):117-120. doi:10.1038/NATURE25502
142. Harding RJ, Deme JC, Hevler JF, et al. Huntingtin structure is orchestrated by HAP40 and shows a polyglutamine expansion-specific interaction with exon 1. *Commun Biol*. 2021;4(1). doi:10.1038/s42003-021-02895-4
143. Arndt JR, Chaibva M, Legleiter J. The emerging role of the first 17 amino acids of huntingtin in Huntington's disease. *Biomol Concepts*. 2015;6(1):33-46. doi:10.1515/BMC-2015-0001
144. Sivanandam VN, Jayaraman M, Hoop CL, Kodali R, Wetzel R, Van Der Wel PCA. The aggregation-enhancing huntingtin N-terminus is helical in amyloid fibrils. *J Am Chem Soc*. 2011;133(12):4558-4566. doi:10.1021/JA110715F
145. Mishra R, Jayaraman M, Roland BP, et al. Inhibiting the nucleation of amyloid structure in a huntingtin fragment by targeting α-helix-rich oligomeric intermediates. *J Mol Biol*. 2012;415(5):900-917. doi:10.1016/j.jmb.2011.12.011

146. Nagarajan A, Jawahery S, Matysiak S. The effects of flanking sequences in the interaction of polyglutamine peptides with a membrane bilayer. *J Phys Chem B*. 2014;118(24):6368-6379. doi:10.1021/JP407900C
147. Zheng Z, Li A, Holmes BB, Marasa JC, Diamond MI. An N-terminal nuclear export signal regulates trafficking and aggregation of Huntingtin (Htt) protein exon 1. *J Biol Chem*. 2013;288(9):6063-6071. doi:10.1074/JBC.M112.413575
148. Klein FAC, Pastore A, Masino L, et al. Pathogenic and non-pathogenic polyglutamine tracts have similar structural properties: towards a length-dependent toxicity gradient. *J Mol Biol*. 2007;371(1):235-244. doi:10.1016/J.JMB.2007.05.028
149. Robertson AL, Horne J, Ellisdon AM, Thomas B, Scanlon MJ, Bottomley SP. The structural impact of a polyglutamine tract is location-dependent. *Biophys J*. 2008;95(12):5922-5930. doi:10.1529/BIOPHYSJ.108.138487
150. Kim MW, Chelliah Y, Kim SW, Otwinowski Z, Bezprozvanny I. Secondary structure of Huntingtin amino-terminal region. *Structure*. 2009;17(9):1205-1212. doi:10.1016/J.STR.2009.08.002
151. Nagai Y, Inui T, Popiel HA, et al. A toxic monomeric conformer of the polyglutamine protein. *Nat Struct Mol Biol*. 2007;14(4):332-340. doi:10.1038/NSMB1215
152. Kim M. Beta conformation of polyglutamine track revealed by a crystal structure of Huntingtin N-terminal region with insertion of three histidine residues. *Prion*. 2013;7(3):221-228. doi:10.4161/PRI.23807
153. Kang H, Vázquez FX, Zhang L, et al. Emerging β-Sheet Rich Conformations in Supercompact Huntingtin Exon-1 Mutant Structures. *J Am Chem Soc*. 2017;139(26):8820-8827. doi:10.1021/JACS.7B00838
154. Hoop CL, Lin HK, Kar K, et al. Polyglutamine amyloid core boundaries and flanking domain dynamics in huntingtin fragment fibrils determined by solid-state nuclear magnetic resonance. *Biochemistry*. 2014;53(42):6653-6666. doi:10.1021/BI501010Q
155. Bhattacharyya A, Thakur AK, Chellgren VM, et al. Oligoproline effects on polyglutamine conformation and aggregation. *J Mol Biol*. 2006;355(3):524-535. doi:10.1016/J.JMB.2005.10.053
156. Gerbich TM, Gladfelter AS. Moving beyond disease to function: Physiological roles for polyglutamine-rich sequences in cell decisions. *Curr Opin Cell Biol*. 2021;69:120-126. doi:10.1016/J.CEB.2021.01.003
157. Jung T, Shin B, Tamo G, et al. The Polyglutamine Expansion at the N-Terminal of Huntingtin Protein Modulates the Dynamic Configuration and Phosphorylation of the C-Terminal HEAT Domain. *Structure*. 2020;28(9):1035-1050.e8. doi:10.1016/j.str.2020.06.008
158. Falk AS, Bravo-Arredondo JM, Varkey J, Pacheco S, Langen R, Siemer AB. Structural Model of the Proline-Rich Domain of Huntingtin Exon-1 Fibrils. *Biophys J*. 2020;119(10):2019-2028. doi:10.1016/J.BPJ.2020.10.010
159. Darnell GD, Derryberry J, Kurutz JW, Meredith SC. Mechanism of cis-inhibition of polyQ fibrillation by polyP: PPII oligomers and the hydrophobic effect. *Biophys J*. 2009;97(8):2295-2305. doi:10.1016/j.bpj.2009.07.062
160. Pigazzini ML, Lawrenz M, Margineanu A, Kaminski Schierle GS, Kirstein J. An Expanded Polyproline Domain Maintains Mutant Huntingtin Soluble in vivo and During Aging. *Front Mol Neurosci*. 2021;14. doi:10.3389/fnmol.2021.721749

161. Harjes P, Wanker EE. The hunt for huntingtin function: interaction partners tell many different stories. *Trends Biochem Sci*. 2003;28(8):425-433. doi:10.1016/S0968-0004(03)00168-3
162. Faber PW, Barnes GT, Srinidhi J, Chen J, Gusella JF, MacDonald ME. Huntingtin interacts with a family of WW domain proteins. *Hum Mol Genet*. 1998;7(9):1463-1474. doi:10.1093/HMG/7.9.1463
163. Gao YG, Yan XZ, Song AX, et al. Structural insights into the specific binding of huntingtin proline-rich region with the SH3 and WW domains. *Structure*. 2006;14(12):1755-1765. doi:10.1016/J.STR.2006.09.014
164. Andrade MA, Bork P. HEAT repeats in the Huntington's disease protein. *Nat Genet*. 1995;11(2):115-116. doi:10.1038/ng1095-115
165. Xia J, Lee DH, Taylor J, Vandelft M, Truant R. Huntingtin contains a highly conserved nuclear export signal. *Hum Mol Genet*. 2003;12(12):1393-1403. doi:10.1093/HMG/DDG156
166. Seong IS, Woda JM, Song JJ, et al. Huntingtin facilitates polycomb repressive complex 2. *Hum Mol Genet*. 2009;19(4):573-583. doi:10.1093/hmg/ddp524
167. Palidwor GA, Shcherbinin S, Huska MR, et al. Detection of alpha-rod protein repeats using a neural network and application to huntingtin. *PLoS Comput Biol*. 2009;5(3). doi:10.1371/JOURNAL.PCBI.1000304
168. Duyao MP, Auerbach AB, Ryan A, et al. Inactivation of the mouse huntington's disease gene homolog Hdh. *Science (1979)*. 1995;269(5222):407-410. doi:10.1126/science.7618107
169. Nasir J, Floresco SB, O'Kusky JR, et al. Targeted disruption of the Huntington's disease gene results in embryonic lethality and behavioral and morphological changes in heterozygotes. *Cell*. 1995;81(5):811-823. doi:10.1016/0092-8674(95)90542-1
170. Reiner A, Dragatsis I, Zeitlin S, Goldowitz D. Wild-type huntingtin plays a role in brain development and neuronal survival. *Mol Neurobiol*. 2003;28(3):259-275. doi:10.1385/MN:28:3:259
171. El-Daher M, Hangen E, Bruyère J, et al. Huntingtin proteolysis releases non-polyQ fragments that cause toxicity through dynamin 1 dysregulation. *EMBO J*. 2015;34(17):2255-2271. doi:10.15252/EMBJ.201490808/SUPPL_FILE/EMBJ201490808.REVIEWER_COMMENTS.PDF
172. Mende-Mueller LM, Toneff T, Hwang SR, Chesselet MF, Hook VYH. Tissue-specific proteolysis of Huntingtin (htt) in human brain: evidence of enhanced levels of N- and C-terminal htt fragments in Huntington's disease striatum. *J Neurosci*. 2001;21(6):1830-1837. doi:10.1523/JNEUROSCI.21-06-01830.2001
173. Landles C, Sathasivam K, Weiss A, et al. Proteolysis of mutant huntingtin produces an exon 1 fragment that accumulates as an aggregated protein in neuronal nuclei in huntington disease. *Journal of Biological Chemistry*. 2010;285(12):8808-8823. doi:10.1074/jbc.M109.075028
174. Ehrnhoefer DE, Sutton L, Hayden MR. Small changes, big impact: posttranslational modifications and function of huntingtin in Huntington disease. *Neuroscientist*. 2011;17(5):475-492. doi:10.1177/1073858410390378
175. Lontay B, Kiss A, Virág L, Tar K. How do post-translational modifications influence the pathomechanistic landscape of Huntington's disease? A comprehensive review. *Int J Mol Sci*. 2020;21(12):1-34. doi:10.3390/ijms21124282

176. Aiken CT, Steffan JS, Guerrero CM, et al. Phosphorylation of threonine 3: implications for Huntingtin aggregation and neurotoxicity. *J Biol Chem*. 2009;284(43):29427-29436. doi:10.1074/JBC.M109.013193
177. Atwal RS, Desmond CR, Caron N, et al. Kinase inhibitors modulate huntingtin cell localization and toxicity. *Nat Chem Biol*. 2011;7(7):453-460. doi:10.1038/NCHEMBIO.582
178. Chaibva M, Jawahery S, Pilkington AW, et al. Acetylation within the First 17 Residues of Huntingtin Exon 1 Alters Aggregation and Lipid Binding. *Biophys J*. 2016;111(2):349-362. doi:10.1016/j.bpj.2016.06.018
179. O'Rourke JG, Gareau JR, Ochaba J, et al. SUMO-2 and PIAS1 modulate insoluble mutant huntingtin protein accumulation. *Cell Rep*. 2013;4(2):362-375. doi:10.1016/J.CELREP.2013.06.034
180. Podvin S, Rosenthal SB, Poon W, Wei E, Fisch KM, Hook V. Mutant Huntingtin Protein Interaction Map Implicates Dysregulation of Multiple Cellular Pathways in Neurodegeneration of Huntington's Disease. *J Huntingtons Dis*. 2022;11(3):243-267. doi:10.3233/JHD-220538
181. Ochaba J, Lukacsovich T, Csikos G, et al. Potential function for the Huntingtin protein as a scaffold for selective autophagy. *Proc Natl Acad Sci U S A*. 2014;111(47):16889-16894. doi:10.1073/PNAS.1420103111
182. Rui YN, Xu Z, Patel B, et al. Huntingtin functions as a scaffold for selective macroautophagy. *Nat Cell Biol*. 2015;17(3):262-275. doi:10.1038/NCB3101
183. Caviston JP, Holzbaur ELF. Huntingtin as an essential integrator of intracellular vesicular trafficking. *Trends Cell Biol*. 2009;19(4):147-155. doi:10.1016/J.TCB.2009.01.005
184. Zuccato C, Ciammola A, Rigamonti D, et al. Loss of huntingtin-mediated BDNF gene transcription in Huntington's disease. *Science (1979)*. 2001;293(5529):493-498. doi:10.1126/science.1059581
185. Zhang Y, Leavitt BR, Van Raamsdonk JM, et al. Huntingtin inhibits caspase-3 activation. *EMBO J*. 2006;25(24):5896-5906. doi:10.1038/SJ.EMBOJ.7601445
186. Stavoe AKH, Holzbaur ELF. Autophagy in Neurons. *Annu Rev Cell Dev Biol*. 2019;35:477-500. doi:10.1146/ANNUREV-CELLBIO-100818-125242
187. Knutson BA. Insights into the domain and repeat architecture of target of rapamycin. *J Struct Biol*. 2010;170(2):354-363. doi:10.1016/J.JSB.2010.01.002
188. Zachari M, Ganley IG. The mammalian ULK1 complex and autophagy initiation. *Essays Biochem*. 2017;61(6):585-596. doi:10.1042/EBC20170021
189. Kim J, Kundu M, Viollet B, Guan KL. AMPK and mTOR regulate autophagy through direct phosphorylation of Ulk1. *Nat Cell Biol*. 2011;13(2):132-141. doi:10.1038/NCB2152
190. Rui YN, Xu Z, Patel B, Cuervo AM, Zhang S. HTT/Huntingtin in selective autophagy and Huntington disease: A foe or a friend within? *Autophagy*. 2015;11(5):858-860. doi:10.1080/15548627.2015.1039219
191. Caviston JP, Ross JL, Antony SM, Tokito M, Holzbaur ELF. Huntingtin facilitates dynein/dynactin-mediated vesicle transport. *Proc Natl Acad Sci U S A*. 2007;104(24):10045-10050. doi:10.1073/pnas.0610628104
192. Engelender S, Sharp AH, Colomer V, et al. Huntingtin-associated protein 1 (HAP1) interacts with the p150Glued subunit of dynactin. *Hum Mol Genet*. 1997;6(13):2205-2212. doi:10.1093/HMG/6.13.2205

193. McGuire JR, Rong J, Li SH, Li XJ. Interaction of Huntingtin-associated protein-1 with kinesin light chain: Implications in intracellular trafficking in neurons. *Journal of Biological Chemistry*. 2006;281(6):3552-3559. doi:10.1074/jbc.M509806200
194. Velier J, Kim M, Schwarz C, et al. Wild-type and mutant huntingtins function in vesicle trafficking in the secretory and endocytic pathways. *Exp Neurol*. 1998;152(1):34-40. doi:10.1006/exnr.1998.6832
195. DiFiglia M, Sapp E, Chase K, et al. Huntingtin is a cytoplasmic protein associated with vesicles in human and rat brain neurons. *Neuron*. 1995;14(5):1075-1081. doi:10.1016/0896-6273(95)90346-1
196. Li H, Wyman T, Yu ZX, Li SH, Li XJ. Abnormal association of mutant huntingtin with synaptic vesicles inhibits glutamate release. *Hum Mol Genet*. 2003;12(16):2021-2030. doi:10.1093/HMG/DDG218
197. Zala D, Hinckelmann MV, Saudou F. Huntingtin's function in axonal transport is conserved in Drosophila melanogaster. *PLoS One*. 2013;8(3). doi:10.1371/JOURNAL.PONE.0060162
198. Caviston JP, Zajac AL, Tokito M, Holzbaur ELF. Huntingtin coordinates the dynein-mediated dynamic positioning of endosomes and lysosomes. *Mol Biol Cell*. 2011;22(4):478-492. doi:10.1091/MBC.E10-03-0233
199. Baquet ZC, Gorski JA, Jones KR. Early striatal dendrite deficits followed by neuron loss with advanced age in the absence of anterograde cortical brain-derived neurotrophic factor. *J Neurosci*. 2004;24(17):4250-4258. doi:10.1523/JNEUROSCI.3920-03.2004
200. Zala D, Hinckelmann MV, Yu H, et al. Vesicular glycolysis provides on-board energy for fast axonal transport. *Cell*. 2013;152(3):479-491. doi:10.1016/j.cell.2012.12.029
201. Atanesyan L, Günther V, Dichtl B, Georgiev O, Schaffner W. Polyglutamine tracts as modulators of transcriptional activation from yeast to mammals. *Biol Chem*. 2012;393(1-2):63-70. doi:10.1515/BC-2011-252
202. Steffan JS, Kazantsev A, Spasic-Boskovic O, et al. The Huntington's disease protein interacts with p53 and CREB-binding protein and represses transcription. *Proc Natl Acad Sci U S A*. 2000;97(12):6763-6768. doi:10.1073/pnas.100110097
203. Takano H, Gusella JF. The predominantly HEAT-like motif structure of huntingtin and its association and coincident nuclear entry with dorsal, an NF-kB/Rel/dorsal family transcription factor. *BMC Neurosci*. 2002;3. doi:10.1186/1471-2202-3-15
204. Yohrling IV GJ, Farrell LA, Hollenberg AN, Cha JHJ. Mutant huntingtin increases nuclear corepressor function and enhances ligand-dependent nuclear hormone receptor activation. *Molecular and Cellular Neuroscience*. 2003;23(1):28-38. doi:10.1016/S1044-7431(03)00032-0
205. Kegel KB, Meloni AR, Yi Y, et al. Huntingtin is present in the nucleus, interacts with the transcriptional corepressor C-terminal binding protein, and represses transcription. *Journal of Biological Chemistry*. 2002;277(9):7466-7476. doi:10.1074/jbc.M103946200
206. Dunah AW, Jeong H, Griffin A, et al. Sp1 and TAFII130 transcriptional activity disrupted in early Huntington's disease. *Science*. 2002;296(5576):2238-2243. doi:10.1126/SCIENCE.1072613
207. Zuccato C, Tartari M, Crotti A, et al. Huntingtin interacts with REST/NRSF to modulate the transcription of NRSE-controlled neuronal genes. *Nat Genet*. 2003;35(1):76-83. doi:10.1038/ng1219

208. Rigamonti D, Sipione S, Goffredo D, Zuccato C, Fossale E, Cattaneo E. Huntingtin's Neuroprotective Activity Occurs via Inhibition of Procaspase-9 Processing. *Journal of Biological Chemistry*. 2001;276(18):14545-14548. doi:10.1074/jbc.C100044200
209. Leavitt BR, Van Raamsdonk JM, Shehadeh J, et al. Wild-type huntingtin protects neurons from excitotoxicity. *J Neurochem*. 2006;96(4):1121-1129. doi:10.1111/J.1471-4159.2005.03605.X
210. O'Kusky JR, Nasir J, Cicchetti F, Parent A, Hayden MR. Neuronal degeneration in the basal ganglia and loss of pallido-subthalamic synapses in mice with targeted disruption of the Huntington's disease gene. *Brain Res*. 1999;818(2):468-479. doi:10.1016/S0006-8993(98)01312-2
211. Zhang Y, Li M, Drozda M, et al. Depletion of wild-type huntingtin in mouse models of neurologic diseases. *J Neurochem*. 2003;87(1):101-106. doi:10.1046/j.1471-4159.2003.01980.x
212. O'Regan GC, Farag SH, Ostroff GR, Tabrizi SJ, Andre R. Wild-type huntingtin regulates human macrophage function. *Sci Rep*. 2020;10(1). doi:10.1038/S41598-020-74042-8
213. Li B, Altelaar M, van Breukelen B. Identification of Protein Complexes by Integrating Protein Abundance and Interaction Features Using a Deep Learning Strategy. *Int J Mol Sci*. 2023;24(9). doi:10.3390/ijms24097884
214. Ming Q, Gonzalez-Perez D, Luca VC. Molecular engineering strategies for visualizing low-affinity protein complexes. *Exp Biol Med (Maywood)*. 2019;244(17):1559-1567. doi:10.1177/1535370219855401
215. Galaway F, Wright GJ. Rapid and sensitive large-scale screening of low affinity extracellular receptor protein interactions by using reaction induced inhibition of Gaussia luciferase. *Sci Rep*. 2020;10(1). doi:10.1038/S41598-020-67468-7
216. van der Bent ML, Evers MM, Vallès A. Emerging Therapies for Huntington's Disease - Focus on N-Terminal Huntingtin and Huntingtin Exon 1. *Biologics*. 2022;16:141-160. doi:10.2147/BTT.S270657
217. Goldberg YP, Nicholson DW, Rasper DM, et al. Cleavage of huntingtin by apopain, a proapoptotic cysteine protease, is modulated by the polyglutamine tract. *Nat Genet*. 1996;13(4):442-449. doi:10.1038/NG0896-442
218. Wellington CL, Ellerby LM, Hackam AS, et al. Caspase cleavage of gene products associated with triplet expansion disorders generates truncated fragments containing the polyglutamine tract. *Journal of Biological Chemistry*. 1998;273(15):9158-9167. doi:10.1074/jbc.273.15.9158
219. Wellington CL, Singaraja R, Ellerby L, et al. Inhibiting caspase cleavage of huntingtin reduces toxicity and aggregate formation in neuronal and nonneuronal cells. *J Biol Chem*. 2000;275(26):19831-19838. doi:10.1074/JBC.M001475200
220. Martin DDO, Schmidt ME, Nguyen YT, Lazic N, Hayden MR. Identification of a novel caspase cleavage site in huntingtin that regulates mutant huntingtin clearance. *FASEB Journal*. 2019;33(3):3190-3197. doi:10.1096/fj.201701510RRR
221. Gafni J, Ellerby LM. Calpain activation in Huntington's disease. *J Neurosci*. 2002;22(12):4842-4849. doi:10.1523/JNEUROSCI.22-12-04842.2002
222. Sun B, Fan W, Balciunas A, et al. Polyglutamine repeat length-dependent proteolysis of huntingtin. *Neurobiol Dis*. 2002;11(1):111-122. doi:10.1006/nbdi.2002.0539
223. Lunkes A, Lindenberg KS, Ben-Haem L, et al. Proteases acting on mutant huntingtin generate cleaved products that differentially build up cytoplasmic and nuclear inclusions. *Mol Cell*. 2002;10(2):259-269. doi:10.1016/S1097-2765(02)00602-0

224. El-Daher M, Hangen E, Bruyère J, et al. Huntingtin proteolysis releases non-polyQ fragments that cause toxicity through dynamin 1 dysregulation. *EMBO J*. 2015;34(17):2255-2271. doi:10.15252/embj.201490808
225. Heinz A, Nabariya DK, Krauss S. Huntingtin and Its Role in Mechanisms of RNA-Mediated Toxicity. *Toxins (Basel)*. 2021;13(7). doi:10.3390/TOXINS13070487
226. Neueder A, Dumas AA, Benjamin AC, Bates GP. Regulatory mechanisms of incomplete huntingtin mRNA splicing. *Nat Commun*. 2018;9(1). doi:10.1038/S41467-018-06281-3
227. Lin L, Park JW, Ramachandran S, et al. Transcriptome sequencing reveals aberrant alternative splicing in Huntington's disease. *Hum Mol Genet*. 2016;25(16):3454-3466. doi:10.1093/HMG/DDW187
228. Elorza A, Márquez Y, Cabrera JR, et al. Huntington's disease-specific mis-splicing unveils key effector genes and altered splicing factors. *Brain*. 2021;144(7):2009-2023. doi:10.1093/BRAIN/AWAB087
229. Hoffner G, Djian P. Polyglutamine Aggregation in Huntington Disease: Does Structure Determine Toxicity? *Mol Neurobiol*. 2015;52(3):1297-1314. doi:10.1007/S12035-014-8932-1
230. Gu X, Richman J, Langfelder P, et al. Uninterrupted CAG repeat drives striatum-selective transcriptionopathy and nuclear pathogenesis in human Huntingtin BAC mice. *Neuron*. 2022;110(7):1173-1192.e7. doi:10.1016/J.NEURON.2022.01.006
231. Mangiarini L, Sathasivam K, Seller M, et al. Exon 1 of the HD gene with an expanded CAG repeat is sufficient to cause a progressive neurological phenotype in transgenic mice. *Cell*. 1996;87(3):493-506. doi:10.1016/S0092-8674(00)81369-0
232. Barbaro BA, Lukacsovich T, Agrawal N, et al. Comparative study of naturally occurring huntingtin fragments in Drosophila points to exon 1 as the most pathogenic species in Huntington's disease. *Hum Mol Genet*. 2015;24(4):913-925. doi:10.1093/HMG/DDU504
233. Warner JB, Ruff KM, Tan PS, Lemke EA, Pappu R V., Lashuel HA. Monomeric Huntingtin Exon 1 Has Similar Overall Structural Features for Wild-Type and Pathological Polyglutamine Lengths. *J Am Chem Soc*. 2017;139(41):14456-14469. doi:10.1021/JACS.7B06659
234. Gopalakrishnan C, Jethi S, Kalsi N, Purohit R. Biophysical Aspect of Huntingtin Protein During polyQ: An In Silico Insight. *Cell Biochem Biophys*. 2016;74(2):129-139. doi:10.1007/S12013-016-0728-7
235. Davies SW, Turmaine M, Cozens BA, et al. Formation of neuronal intranuclear inclusions underlies the neurological dysfunction in mice transgenic for the HD mutation. *Cell*. 1997;90(3):537-548. doi:10.1016/S0092-8674(00)80513-9
236. Becher MW, Kotzuk JA, Sharp AH, et al. Intranuclear neuronal inclusions in Huntington's disease and dentatorubral and pallidoluysian atrophy: correlation between the density of inclusions and IT15 CAG triplet repeat length. *Neurobiol Dis*. 1998;4(6):387-397. doi:10.1006/NBDI.1998.0168
237. Gutekunst CA, Li SH, Yi H, et al. Nuclear and neuropil aggregates in Huntington's disease: relationship to neuropathology. *J Neurosci*. 1999;19(7):2522-2534. doi:10.1523/JNEUROSCI.19-07-02522.1999
238. Scherzinger E, Sittler A, Schweiger K, et al. Self-assembly of polyglutamine-containing huntingtin fragments into amyloid-like fibrils: implications for Huntington's disease pathology. *Proc Natl Acad Sci U S A*. 1999;96(8):4604-4609. doi:10.1073/PNAS.96.8.4604

239. Hoop CL, Lin HK, Kar K, et al. Huntingtin exon 1 fibrils feature an interdigitated β-hairpin-based polyglutamine core. *Proc Natl Acad Sci U S A*. 2016;113(6):1546-1551. doi:10.1073/PNAS.1521933113
240. Kar K, Hoop CL, Drombosky KW, et al. Β-Hairpin-Mediated Nucleation of Polyglutamine Amyloid Formation. *J Mol Biol*. 2013;425(7):1183-1197. doi:10.1016/j.jmb.2013.01.016
241. Ceccon A, Tugarinov V, Torricella F, Clore GM. Quantitative NMR analysis of the kinetics of prenucleation oligomerization and aggregation of pathogenic huntingtin exon-1 protein. *Proc Natl Acad Sci U S A*. 2022;119(29). doi:10.1073/pnas.2207690119
242. Nazarov S, Chiki A, Boudeffa D, Lashuel HA. Structural Basis of Huntingtin Fibril Polymorphism Revealed by Cryogenic Electron Microscopy of Exon 1 HTT Fibrils. *J Am Chem Soc*. 2022;144(24):10723-10735. doi:10.1021/JACS.2C00509
243. Kar K, Jayaraman M, Sahoo B, Kodali R, Wetzel R. Critical nucleus size for disease-related polyglutamine aggregation is repeat-length dependent. *Nat Struct Mol Biol*. 2011;18(3):328-336. doi:10.1038/nsmb.1992
244. van der Wel PCA. Insights into protein misfolding and aggregation enabled by solid-state NMR spectroscopy. *Solid State Nucl Magn Reson*. 2017;88:1-14. doi:10.1016/j.ssnmr.2017.10.001
245. Dehay B, Bertolotti A. Critical role of the proline-rich region in Huntingtin for aggregation and cytotoxicity in yeast. *J Biol Chem*. 2006;281(47):35608-35615. doi:10.1074/JBC.M605558200
246. Boatz JC, Piretra T, Lasorsa A, Matlahov I, Conway JF, van der Wel PCA. Protofilament Structure and Supramolecular Polymorphism of Aggregated Mutant Huntingtin Exon 1. *J Mol Biol*. 2020;432(16):4722-4744. doi:10.1016/j.jmb.2020.06.021
247. Drombosky KW, Rode S, Kodali R, Jacob TC, Palladino MJ, Wetzel R. Mutational analysis implicates the amyloid fibril as the toxic entity in Huntington’s disease. *Neurobiol Dis*. 2018;120:126-138. doi:10.1016/j.nbd.2018.08.019
248. Helabad MB, Matlahov I, Daldrop JO, Jain G, van der Wel PCA, Miettinen MS. Integrative determination of the atomic structure of mutant huntingtin exon 1 fibrils from Huntington’s disease. *bioRxiv*. Published online July 21, 2023. doi:10.1101/2023.07.21.549993
249. Bugg CW, Isas JM, Fischer T, Patterson PH, Langen R. Structural features and domain organization of huntingtin fibrils. *J Biol Chem*. 2012;287(38):31739-31746. doi:10.1074/JBC.M112.353839
250. Isas JM, Langen R, Siemer AB. Solid-State Nuclear Magnetic Resonance on the Static and Dynamic Domains of Huntingtin Exon-1 Fibrils. *Biochemistry*. 2015;54(25):3942-3949. doi:10.1021/ACS.BIOCHEM.5B00281
251. Wagner AS, Politi AZ, Ast A, et al. Self-assembly of Mutant Huntingtin Exon-1 Fragments into Large Complex Fibrillar Structures Involves Nucleated Branching. *J Mol Biol*. 2018;430(12):1725-1744. doi:10.1016/J.JMB.2018.03.017
252. Knowles TPJ, Waudby CA, Devlin GL, et al. An analytical solution to the kinetics of breakable filament assembly. *Science*. 2009;326(5959):1533-1537. doi:10.1126/SCIENCE.1178250
253. Ast A, Buntru A, Schindler F, et al. mHTT Seeding Activity: A Marker of Disease Progression and Neurotoxicity in Models of Huntington’s Disease. *Mol Cell*. 2018;71(5):675-688.e6. doi:10.1016/J.MOLCEL.2018.07.032

254. Hervás R, Murzin AG, Si K. Implications of the Orb2 Amyloid Structure in Huntington's Disease. *Int J Mol Sci*. 2020;21(18):1-7. doi:10.3390/IJMS21186910
255. DiFiglia M, Sapp E, Chase KO, et al. Aggregation of huntingtin in neuronal intranuclear inclusions and dystrophic neurites in brain. *Science*. 1997;277(5334):1990-1993. doi:10.1126/SCIENCE.277.5334.1990
256. Hoffner G, Djian P. Monomeric, oligomeric and polymeric proteins in huntington disease and other diseases of polyglutamine expansion. *Brain Sci*. 2014;4(1):91-122. doi:10.3390/BRAINSCI4010091
257. Sahl SJ, Weiss LE, Duim WC, Frydman J, Moerner WE. Cellular inclusion bodies of mutant huntingtin exon 1 obscure small fibrillar aggregate species. *Sci Rep*. 2012;2. doi:10.1038/srep00895
258. Sahoo B, Arduini I, Drombosky KW, et al. Folding Landscape of Mutant Huntingtin Exon1: Diffusible Multimers, Oligomers and Fibrils, and No Detectable Monomer. *PLoS One*. 2016;11(6). doi:10.1371/JOURNAL.PONE.0155747
259. Jayaraman M, Kodali R, Sahoo B, et al. Slow amyloid nucleation via α-helix-rich oligomeric intermediates in short polyglutamine-containing huntingtin fragments. *J Mol Biol*. 2012;415(5):881-899. doi:10.1016/j.jmb.2011.12.010
260. Marcellin D, Abramowski D, Young D, et al. Fragments of HdhQ150 Mutant Huntingtin Form a Soluble Oligomer Pool That Declines with Aggregate Deposition upon Aging. *PLoS One*. 2012;7(9). doi:10.1371/journal.pone.0044457
261. Olshina MA, Angley LM, Ramdzan YM, et al. Tracking mutant huntingtin aggregation kinetics in cells reveals three major populations that include an invariant oligomer pool. *Journal of Biological Chemistry*. 2010;285(28):21807-21816. doi:10.1074/jbc.M109.084434
262. Legleiter J, Mitchell E, Lotz GP, et al. Mutant huntingtin fragments form oligomers in a polyglutamine length-dependent manner in Vitro and in Vivo. *Journal of Biological Chemistry*. 2010;285(19):14777-14790. doi:10.1074/jbc.M109.093708
263. Iuchi S, Hoffner G, Verbeke P, Djian P, Green H. Oligomeric and polymeric aggregates formed by proteins containing expanded polyglutamine. *Proc Natl Acad Sci U S A*. 2003;100(5):2409-2414. doi:10.1073/pnas.0437660100
264. Takahashi T, Kikuchi S, Katada S, Nagai Y, Nishizawa M, Onodera O. Soluble polyglutamine oligomers formed prior to inclusion body formation are cytotoxic. *Hum Mol Genet*. 2008;17(3):345-356. doi:10.1093/HMG/DDM311
265. Weiss A, Klein C, Woodman B, et al. Sensitive biochemical aggregate detection reveals aggregation onset before symptom development in cellular and murine models of Huntington's disease. *J Neurochem*. 2008;104(3):846-858. doi:10.1111/J.1471-4159.2007.05032.X
266. Poirier MA, Li H, Macosko J, Cai S, Amzel M, Ross CA. Huntingtin spheroids and protofibrils as precursors in polyglutamine fibrilization. *Journal of Biological Chemistry*. 2002;277(43):41032-41037. doi:10.1074/jbc.M205809200
267. Nekooki-Machida Y, Kurosawa M, Nukina N, Ito K, Oda T, Tanaka M. Distinct conformations of in vitro and in vivo amyloids of huntingtin-exon1 show different cytotoxicity. *Proc Natl Acad Sci U S A*. 2009;106(24):9679-9684. doi:10.1073/PNAS.0812083106
268. Lin HK, Boatz JC, Krabbendam IE, et al. Fibril polymorphism affects immobilized non-amyloid flanking domains of huntingtin exon1 rather than its polyglutamine core. *Nat Commun*. 2017;8. doi:10.1038/NCOMMS15462

269. Mario Isas J, Pandey NK, Xu H, et al. Huntingtin fibrils with different toxicity, structure, and seeding potential can be interconverted. *Nat Commun*. 2021;12(1). doi:10.1038/s41467-021-24411-2
270. Schindler F, Praedel N, Neuendorf N, et al. Small, Seeding-Competent Huntingtin Fibrils Are Prominent Aggregate Species in Brains of zQ175 Huntington's Disease Knock-in Mice. *Front Neurosci*. 2021;15. doi:10.3389/FNINS.2021.682172
271. Sathasivam K, Lane A, Legleiter J, et al. Identical oligomeric and fibrillar structures captured from the brains of R6/2 and knock-in mouse models of Huntington's disease. *Hum Mol Genet*. 2010;19(1):65-78. doi:10.1093/HMG/DDP467
272. Lee CYD, Wang N, Shen K, et al. Disease-related Huntingtin seeding activities in cerebrospinal fluids of Huntington's disease patients. *Sci Rep*. 2020;10(1). doi:10.1038/S41598-020-77164-1
273. Kazantsev A, Preisinger E, Dranovsky A, Goldgaber D, Housman D. Insoluble detergent-resistant aggregates form between pathological and nonpathological lengths of polyglutamine in mammalian cells. *Proc Natl Acad Sci U S A*. 1999;96(20):11404-11409. doi:10.1073/pnas.96.20.11404
274. Qin ZH, Wang Y, Sapp E, et al. Huntingtin Bodies Sequester Vesicle-Associated Proteins by a Polyproline-Dependent Interaction. *Journal of Neuroscience*. 2004;24(1):269-281. doi:10.1523/JNEUROSCI.1409-03.2004
275. Peskett TR, Rau F, O'Driscoll J, Patani R, Lowe AR, Saibil HR. A Liquid to Solid Phase Transition Underlying Pathological Huntingtin Exon1 Aggregation. *Mol Cell*. 2018;70(4):588-601.e6. doi:10.1016/J.MOLCEL.2018.04.007
276. Riguet N, Mahul-Mellier AL, Maharjan N, et al. Nuclear and cytoplasmic huntingtin inclusions exhibit distinct biochemical composition, interactome and ultrastructural properties. *Nat Commun*. 2021;12(1). doi:10.1038/S41467-021-26684-Z
277. Sieradzan KA, Mechan AO, Jones L, Wanker EE, Nukina N, Mann DMA. Huntington's disease intranuclear inclusions contain truncated, ubiquitinated huntingtin protein. *Exp Neurol*. 1999;156(1):92-99. doi:10.1006/exnr.1998.7005
278. Suhr ST, Senut MC, Whitelegge JP, Faull KF, Cuizon DB, Gage FH. Identities of sequestered proteins in aggregates from cells with induced polyglutamine expression. *Journal of Cell Biology*. 2001;153(2):283-294. doi:10.1083/jcb.153.2.283
279. Iwata A, Christianson JC, Bucci M, et al. Increased susceptibility of cytoplasmic over nuclear polyglutamine aggregates to autophagic degradation. *Proc Natl Acad Sci U S A*. 2005;102(37):13135-13140. doi:10.1073/PNAS.0505801102
280. Choo YS, Johnson GVW, MacDonald M, Detloff PJ, Lesort M. Mutant huntingtin directly increases susceptibility of mitochondria to the calcium-induced permeability transition and cytochrome c release. *Hum Mol Genet*. 2004;13(14):1407-1420. doi:10.1093/HMG/DDH162
281. Bäuerlein FJB, Saha I, Mishra A, et al. In Situ Architecture and Cellular Interactions of PolyQ Inclusions. *Cell*. 2017;171(1):179-187.e10. doi:10.1016/J.CELL.2017.08.009
282. Waelter S, Boeddrich A, Lurz R, et al. Accumulation of mutant huntingtin fragments in aggresome-like inclusion bodies as a result of insufficient protein degradation. *Mol Biol Cell*. 2001;12(5):1393-1407. doi:10.1091/mbc.12.5.1393
283. Gasset-Rosa F, Chillon-Marinas C, Goginashvili A, et al. Polyglutamine-Expanded Huntingtin Exacerbates Age-Related Disruption of Nuclear Integrity and Nucleocytoplasmic Transport. *Neuron*. 2017;94(1):48-57.e4. doi:10.1016/j.neuron.2017.03.027

284. Hickman RA, Faust PL, Marder K, Yamamoto A, Vonsattel JP. The distribution and density of Huntingtin inclusions across the Huntington disease neocortex: regional correlations with Huntingtin repeat expansion independent of pathologic grade. *Acta Neuropathol Commun*. 2022;10(1). doi:10.1186/S40478-022-01364-1

285. Maat-Schieman MLC, Dorsman JC, Smoor MA, et al. Distribution of inclusions in neuronal nuclei and dystrophic neurites in Huntington disease brain. *J Neuropathol Exp Neurol*. 1999;58(2):129-137. doi:10.1097/00005072-199902000-00003

286. Leitman J, Ulrich Hartl F, Lederkremer GZ. Soluble forms of polyQ-expanded huntingtin rather than large aggregates cause endoplasmic reticulum stress. *Nat Commun*. 2013;4. doi:10.1038/NCOMMS3753

287. Fan HC, Ho LI, Chi CS, et al. Polyglutamine (PolyQ) diseases: Genetics to treatments. *Cell Transplant*. 2014;23(4-5):441-458. doi:10.3727/096368914X678454

288. Lieberman AP, Shakkottai VG, Albin RL. Polyglutamine Repeats in Neurodegenerative Diseases. *Annual Review of Pathology: Mechanisms of Disease*. 2019;14:1-27. doi:10.1146/annurev-pathmechdis-012418-012857

289. Stoyas CA, La Spada AR. The CAG-polyglutamine repeat diseases: a clinical, molecular, genetic, and pathophysiologic nosology. *Handb Clin Neurol*. 2018;147:143-170. doi:10.1016/B978-0-444-63233-3.00011-7

290. Holmes SE, Hearn EO, Ross CA, Margolis RL. SCA12: an unusual mutation leads to an unusual spinocerebellar ataxia. *Brain Res Bull*. 2001;56(3-4):397-403. doi:10.1016/S0361-9230(01)00596-2

291. Ganaraja VH, Holla V V., Stezin A, et al. Clinical, Radiological, and Genetic Profile of Spinocerebellar Ataxia 12: A Hospital-Based Cohort Analysis. *Tremor and Other Hyperkinetic Movements*. 2022;12(1). doi:10.5334/tohm.686

292. Hsu RJ, Hsiao KM, Lin MJ, et al. Long Tract of untranslated CAG repeats is deleterious in transgenic mice. *PLoS One*. 2011;6(1). doi:10.1371/journal.pone.0016417

293. Wang LC, Chen KY, Pan H, et al. Muscleblind participates in RNA toxicity of expanded CAG and CUG repeats in Caenorhabditis elegans. *Cell Mol Life Sci*. 2011;68(7):1255-1267. doi:10.1007/S00018-010-0522-4

294. Nalavade R, Griesche N, Ryan DP, Hildebrand S, Krauß S. Mechanisms of RNA-induced toxicity in CAG repeat disorders. *Cell Death Dis*. 2013;4(8). doi:10.1038/cddis.2013.276

295. De Mezer M, Wojciechowska M, Napierala M, Sobczak K, Krzyzosiak WJ. Mutant CAG repeats of Huntingtin transcript fold into hairpins, form nuclear foci and are targets for RNA interference. *Nucleic Acids Res*. 2011;39(9):3852-3863. doi:10.1093/NAR/GKQ1323

296. Chung DW, Rudnicki DD, Yu L, Margolis RL. A natural antisense transcript at the Huntington's disease repeat locus regulates HTT expression. *Hum Mol Genet*. 2011;20(17):3467-3477. doi:10.1093/HMG/DDR263

297. He Y, Vogelstein B, Velculescu VE, Papadopoulos N, Kinzler KW. The antisense transcriptomes of human cells. *Science*. 2008;322(5909):1855-1857. doi:10.1126/SCIENCE.1163853

298. Ratovitski T, Chighladze E, Arbez N, et al. Huntingtin protein interactions altered by polyglutamine expansion as determined by quantitative proteomic analysis. *Cell Cycle*. 2012;11(10):2006-2021. doi:10.4161/CC.20423

299. Raychaudhuri S, Dey S, Bhattacharyya NP, Mukhopadhyay D. The role of intrinsically unstructured proteins in neurodegenerative diseases. *PLoS One*. 2009;4(5). doi:10.1371/journal.pone.0005566
300. Song W, Chen J, Petrilli A, et al. Mutant huntingtin binds the mitochondrial fission GTPase dynamin-related protein-1 and increases its enzymatic activity. *Nat Med*. 2011;17(3):377-383. doi:10.1038/NM.2313
301. Li XJ, Li SH, Sharp AH, et al. A huntingtin-associated protein enriched in brain with implications for pathology. *Nature*. 1995;378(6555):398-402. doi:10.1038/378398A0
302. Subramaniam S, Sixt KM, Barrow R, Snyder SH. Rhes, a striatal specific protein, mediates mutant-huntingtin cytotoxicity. *Science*. 2009;324(5932):1327-1330. doi:10.1126/SCIENCE.1172871
303. Wanker EE, Ast A, Schindler F, Trepte P, Schnoegl S. The pathobiology of perturbed mutant huntingtin protein-protein interactions in Huntington’s disease. *J Neurochem*. 2019;151(4):507-519. doi:10.1111/JNC.14853
304. Ratovitski T, O’Meally RN, Jiang M, et al. Post-Translational Modifications (PTMs), Identified on Endogenous Huntingtin, Cluster within Proteolytic Domains between HEAT Repeats. *J Proteome Res*. 2017;16(8):2692-2708. doi:10.1021/ACS.JPROTEOME.6B00991
305. Yanai A, Huang K, Kang R, et al. Palmitoylation of huntingtin by HIP14 is essential for its trafficking and function. *Nat Neurosci*. 2006;9(6):824-831. doi:10.1038/NN1702
306. Wang CE, Tydlacka S, Orr AL, et al. Accumulation of N-terminal mutant huntingtin in mouse and monkey models implicated as a pathogenic mechanism in Huntington’s disease. *Hum Mol Genet*. 2008;17(17):2738-2751. doi:10.1093/HMG/DDN175
307. Graham RK, Deng Y, Slow EJ, et al. Cleavage at the Caspase-6 Site Is Required for Neuronal Dysfunction and Degeneration Due to Mutant Huntingtin. *Cell*. 2006;125(6):1179-1191. doi:10.1016/j.cell.2006.04.026
308. Miller JP, Holcomb J, Al-Ramahi I, et al. Matrix metalloproteinases are modifiers of huntingtin proteolysis and toxicity in Huntington’s disease. *Neuron*. 2010;67(2):199-212. doi:10.1016/j.neuron.2010.06.021
309. Gafni J, Hermel E, Young JE, Wellington CL, Hayden MR, Ellerby LM. Inhibition of calpain cleavage of huntingtin reduces toxicity: accumulation of calpain/caspase fragments in the nucleus. *J Biol Chem*. 2004;279(19):20211-20220. doi:10.1074/JBC.M401267200
310. Zu T, Gibbens B, Doty NS, et al. Non-ATG-initiated translation directed by microsatellite expansions. *Proc Natl Acad Sci U S A*. 2011;108(1):260-265. doi:10.1073/PNAS.1013343108
311. Bañez-Coronel M, Ayhan F, Tarabochia AD, et al. RAN Translation in Huntington Disease. *Neuron*. 2015;88(4):667-677. doi:10.1016/J.NEURON.2015.10.038
312. Cox DC, Cooper TA. Non-canonical RAN Translation of CGG Repeats Has Canonical Requirements. *Mol Cell*. 2016;62(2):155-156. doi:10.1016/J.MOLCEL.2016.04.004
313. Yang S, Yang H, Huang L, et al. Lack of RAN-mediated toxicity in Huntington’s disease knock-in mice. *Proc Natl Acad Sci U S A*. 2020;117(8):4411-4417. doi:10.1073/PNAS.1919197117
314. Jimenez-Sanchez M, Licitra F, Underwood BR, Rubinsztein DC. Huntington’s Disease: Mechanisms of Pathogenesis and Therapeutic Strategies. *Cold Spring Harb Perspect Med*. 2017;7(7):1-22. doi:10.1101/CSHPERSPECT.A024240

315. Ordway JM, Tallaksen-Greene S, Gutekunst CA, et al. Ectopically expressed CAG repeats cause intranuclear inclusions and a progressive late onset neurological phenotype in the mouse. *Cell*. 1997;91(6):753-763. doi:10.1016/S0092-8674(00)80464-X
316. Hosp F, Gutiérrez-Ángel S, Schaefer MH, et al. Spatiotemporal Proteomic Profiling of Huntington’s Disease Inclusions Reveals Widespread Loss of Protein Function. *Cell Rep*. 2017;21(8):2291-2303. doi:10.1016/J.CELREP.2017.10.097
317. Liu KY, Shyu YC, Barbaro BA, et al. Disruption of the nuclear membrane by perinuclear inclusions of mutant huntingtin causes cell-cycle re-entry and striatal cell death in mouse and cell models of Huntington’s disease. *Hum Mol Genet*. 2015;24(6):1602-1616. doi:10.1093/HMG/DDU574
318. Ueda M, Li S, Itoh M, et al. Expanded polyglutamine embedded in the endoplasmic reticulum causes membrane distortion and coincides with Bax insertion. *Biochem Biophys Res Commun*. 2016;474(2):259-263. doi:10.1016/j.bbrc.2016.04.034
319. Yano H, Baranov S V., Baranova O V., et al. Inhibition of mitochondrial protein import by mutant huntingtin. *Nat Neurosci*. 2014;17(6):822-831. doi:10.1038/NN.3721
320. Ross CA, Poirier MA. What is the role of protein aggregation in neurodegeneration? *Nat Rev Mol Cell Biol*. 2005;6(11):891-898. doi:10.1038/nrm1742
321. Kuemmerle S, Gutekunst CA, Klein AM, et al. Huntingtin aggregates may not predict neuronal death in Huntington’s disease. *Ann Neurol*. 1999;46(6):842-849. doi:10.1002/1531-8249(199912)46:6<842::AID-ANA6>3.0.CO;2-O
322. Slow EJ, Graham RK, Osmand AP, et al. Absence of behavioral abnormalities and neurodegeneration in vivo despite widespread neuronal huntingtin inclusions. *Proc Natl Acad Sci U S A*. 2005;102(32):11402-11407. doi:10.1073/PNAS.0503634102
323. Arrasate M, Mitra S, Schweitzer ES, Segal MR, Finkbeiner S. Inclusion body formation reduces levels of mutant huntingtin and the risk of neuronal death. *Nature*. 2004;431(7010):805-810. doi:10.1038/nature02998
324. Wellington CL, Ellerby LM, Gutekunst CA, et al. Caspase cleavage of mutant huntingtin precedes neurodegeneration in Huntington’s disease. *Journal of Neuroscience*. 2002;22(18):7862-7872. doi:10.1523/jneurosci.22-18-07862.2002
325. Saudou F, Finkbeiner S, Devys D, Greenberg ME. Huntingtin acts in the nucleus to induce apoptosis but death does not correlate with the formation of intranuclear inclusions. *Cell*. 1998;95(1):55-66. doi:10.1016/S0092-8674(00)81782-1
326. Khoshnan A, Ko J, Patterson PH. Effects of intracellular expression of anti-huntingtin antibodies of various specificities on mutant huntingtin aggregation and toxicity. *Proc Natl Acad Sci U S A*. 2002;99(2):1002-1007. doi:10.1073/PNAS.022631799
327. Kopito RR. Aggresomes, inclusion bodies and protein aggregation. *Trends Cell Biol*. 2000;10(12):524-530. doi:10.1016/S0962-8924(00)01852-3
328. Schaffar G, Breuer P, Boteva R, et al. Cellular toxicity of polyglutamine expansion proteins: Mechanism of transcription factor deactivation. *Mol Cell*. 2004;15(1):95-105. doi:10.1016/j.molcel.2004.06.029
329. Sugars KL, Rubinsztein DC. Transcriptional abnormalities in Huntington disease. *Trends Genet*. 2003;19(5):233-238. doi:10.1016/S0168-9525(03)00074-X
330. Tian J, Yan YP, Zhou R, Lou HF, Rong Y, Zhang BR. Soluble N-terminal fragment of mutant Huntingtin protein impairs mitochondrial axonal transport in cultured hippocampal neurons. *Neurosci Bull*. 2014;30(1):74-80. doi:10.1007/s12264-013-1393-0

331. Trushina E, Dyer RB, Badger JD, et al. Mutant Huntingtin Impairs Axonal Trafficking in Mammalian Neurons In Vivo and In Vitro. *Mol Cell Biol*. 2004;24(18):8195-8209. doi:10.1128/mcb.24.18.8195-8209.2004
332. Gropp MHM, Klaips CL, Hartl FU. Formation of toxic oligomers of polyQ-expanded Huntingtin by prion-mediated cross-seeding. *Mol Cell*. 2022;82(22):4290-4306.e11. doi:10.1016/J.MOLCEL.2022.09.031
333. Chan HYE, Warrick JM, Andriola I, Merry D, Bonini NM. Aggregated polyglutamine peptides delivered to nuclei are toxic to mammalian cells. *Hum Mol Genet*. 2002;11(23):2905-2917. doi:10.1093/HMG/11.23.2905
334. Hnath B, Chen J, Reynolds J, et al. Big versus small: The impact of aggregate size in disease. *Protein Sci*. 2023;32(7). doi:10.1002/PRO.4686
335. Den Engelsman J, Garidel P, Smulders R, et al. Strategies for the assessment of protein aggregates in pharmaceutical biotech product development. *Pharm Res*. 2011;28(4):920-933. doi:10.1007/S11095-010-0297-1
336. Wang H, Lim PJ, Karbowski M, Monteiro MJ. Effects of overexpression of huntingtin proteins on mitochondrial integrity. *Hum Mol Genet*. 2009;18(4):737-752. doi:10.1093/HMG/DDN404
337. Aktar F, Burudpakdee C, Polanco M, et al. The huntingtin inclusion is a dynamic phase-separated compartment. *Life Sci Alliance*. 2019;2(5). doi:10.26508/LSA.201900489
338. Sekar RB, Periasamy A. Fluorescence resonance energy transfer (FRET) microscopy imaging of live cell protein localizations. *J Cell Biol*. 2003;160(5):629-633. doi:10.1083/JCB.200210140
339. Bajar BT, Wang ES, Zhang S, Lin MZ, Chu J. A Guide to Fluorescent Protein FRET Pairs. *Sensors (Basel)*. 2016;16(9). doi:10.3390/S16091488
340. McCullock TW, MacLean DM, Kammermeier PJ. Comparing the performance of mScarlet-I, mRuby3, and mCherry as FRET acceptors for mNeonGreen. *PLoS One*. 2020;15(2). doi:10.1371/journal.pone.0219886
341. Hochreiter B, Garcia AP, Schmid JA. Fluorescent proteins as genetically encoded FRET biosensors in life sciences. *Sensors (Basel)*. 2015;15(10):26281-26314. doi:10.3390/S151026281
342. Brand AH, Perrimon N. Targeted gene expression as a means of altering cell fates and generating dominant phenotypes. *Development*. 1993;118(2):401-415. doi:10.1242/dev.118.2.401
343. Scherzinger E, Lurz R, Turmaine M, et al. Huntingtin-encoded polyglutamine expansions form amyloid-like protein aggregates in vitro and in vivo. *Cell*. 1997;90(3):549-558. doi:10.1016/S0092-8674(00)80514-0
344. Ast A, Schindler F, Buntru A, Schnoegl S, Wanker EE. A Filter Retardation Assay Facilitates the Detection and Quantification of Heat-Stable, Amyloidogenic Mutant Huntingtin Aggregates in Complex Biosamples. *Methods Mol Biol*. 2018;1780:31-40. doi:10.1007/978-1-4939-7825-0_3
345. Magnusson K, Simon R, Sjölander D, Sigurdson CJ, Hammarström P, Nilsson KPR. Multimodal fluorescence microscopy of prion strain specific PrP deposits stained by thiophene-based amyloid ligands. *Prion*. 2014;8(4):319-329. doi:10.4161/PRI.29239
346. Klingstedt T, Nilsson KPR. Luminescent conjugated poly- and oligo-thiophenes: optical ligands for spectral assignment of a plethora of protein aggregates. *Biochem Soc Trans*. 2012;40(4):704-710. doi:10.1042/BST20120009

347. Banning C, Votteler J, Hoffmann D, et al. A flow cytometry-based FRET assay to identify and analyse protein-protein interactions in living cells. *PLoS One*. 2010;5(2). doi:10.1371/JOURNAL.PONE.0009344
348. McKinnon KM. Flow Cytometry: An Overview. *Curr Protoc Immunol*. 2018;120:5.1.1-5.1.11. doi:10.1002/CPIM.40
349. Ramdzan YM, Wood R, Hatters DM. Pulse shape analysis (PulSA) to track protein translocalization in cells by flow cytometry: applications for polyglutamine aggregation. *Methods Mol Biol*. 2013;1017:85-93. doi:10.1007/978-1-62703-438-8_6
350. Ramdzan YM, Polling S, Chia CPZ, et al. Tracking protein aggregation and mislocalization in cells with flow cytometry. *Nat Methods*. 2012;9(5):467-470. doi:10.1038/NMETH.1930
351. Venken KJT, Bellen HJ. Transgenesis upgrades for Drosophila melanogaster. *Development*. 2007;134(20):3571-3584. doi:10.1242/DEV.005686
352. Caygill EE, Brand AH. The GAL4 system: A versatile system for the manipulation and analysis of gene expression. *Methods in Molecular Biology*. 2016;1478:33-52. doi:10.1007/978-1-4939-6371-3_2/FIGURES/5
353. Osterwalder T, Yoon KS, White BH, Keshishian H. A conditional tissue-specific transgene expression system using inducible GAL4. *Proc Natl Acad Sci U S A*. 2001;98(22):12596-12601. doi:10.1073/pnas.221303298
354. Berger C, Renner S, Lüer K, Technau GM. The commonly used marker ELAV is transiently expressed in neuroblasts and glial cells in the Drosophila embryonic CNS. *Dev Dyn*. 2007;236(12):3562-3568. doi:10.1002/DVDY.21372
355. Poirier L, Shane A, Zheng J, Seroude L. Characterization of the Drosophila gene-switch system in aging studies: a cautionary tale. *Aging Cell*. 2008;7(5):758-770. doi:10.1111/J.1474-9726.2008.00421.X
356. Scialo F, Sriram A, Stefanatos R, Sanz A. Practical Recommendations for the Use of the GeneSwitch Gal4 System to Knock-Down Genes in Drosophila melanogaster. *PLoS One*. 2016;11(8). doi:10.1371/JOURNAL.PONE.0161817
357. Robles-Murguia M, Hunt LC, Finkelstein D, Fan Y, Demontis F. Tissue-specific alteration of gene expression and function by RU486 and the GeneSwitch system. *NPJ Aging Mech Dis*. 2019;5(1). doi:10.1038/S41514-019-0036-8
358. Landles C, Milton RE, Ali N, et al. Subcellular Localization And Formation Of Huntingtin Aggregates Correlates With Symptom Onset And Progression In A Huntington'S Disease Model. *Brain Commun*. 2020;2(2). doi:10.1093/BRAINCOMMS/FCAA066
359. Arrasate M, Finkbeiner S. Protein aggregates in Huntington's disease. *Exp Neurol*. 2012;238(1):1-11. doi:10.1016/j.expneurol.2011.12.013
360. Livak KJ, Schmittgen TD. Analysis of relative gene expression data using real-time quantitative PCR and the 2(-Delta Delta C(T)) Method. *Methods*. 2001;25(4):402-408. doi:10.1006/METH.2001.1262
361. Ko J, Isas JM, Sabbaugh A, et al. Identification of distinct conformations associated with monomers and fibril assemblies of mutant huntingtin. *Hum Mol Genet*. 2018;27(13):2330-2343. doi:10.1093/HMG/DDY141
362. Kolla R, Gopinath P, Ricci J, Reif A, Rostami I, Lashuel HA. A New Chemoenzymatic Semisynthetic Approach Provides Insight into the Role of Phosphorylation beyond Exon1 of Huntingtin and Reveals N-Terminal Fragment Length-Dependent Distinct

Mechanisms of Aggregation. *J Am Chem Soc*. 2021;143(26):9798-9812. doi:10.1021/JACS.1C03108

363. Bozler J, Nguyen HQ, Rogers GC, Bosco G. Condensins exert force on chromatin-nuclear envelope tethers to mediate nucleoplasmic reticulum formation in Drosophila melanogaster. *G3 (Bethesda)*. 2014;5(3):341-352. doi:10.1534/G3.114.015685
364. Cui X, Liang Q, Liang Y, Lu M, Ding Y, Lu B. TR-FRET assays of Huntingtin protein fragments reveal temperature and polyQ length-dependent conformational changes. *Sci Rep*. 2014;4. doi:10.1038/SREP05601
365. Lo CH, Pandey NK, Lim CKW, et al. Discovery of Small Molecule Inhibitors of Huntingtin Exon 1 Aggregation by FRET-Based High-Throughput Screening in Living Cells. *ACS Chem Neurosci*. 2020;11(15):2286-2295. doi:10.1021/ACSCHEMNEURO.0C00226
366. Raeburn CB, Ormsby AR, Cox D, et al. A biosensor of protein foldedness identifies increased "holdase" activity of chaperones in the nucleus following increased cytosolic protein aggregation. *J Biol Chem*. 2022;298(8). doi:10.1016/J.JBC.2022.102158
367. Wan Q, Mouton SN, Veenhoff LM, Boersma AJ. A FRET-based method for monitoring structural transitions in protein self-organization. *Cell reports methods*. 2022;2(3). doi:10.1016/J.CRMETH.2022.100184
368. Wilbertz JH, Frappier J, Muller S, et al. Time-resolved FRET screening identifies small molecular modifiers of mutant Huntingtin conformational inflexibility in patient-derived cells. *SLAS Discov*. 2022;27(4):219-228. doi:10.1016/J.SLASD.2021.10.005
369. Fodale V, Kegulian NC, Verani M, et al. Polyglutamine- and temperature-dependent conformational rigidity in mutant huntingtin revealed by immunoassays and circular dichroism spectroscopy. *PLoS One*. 2014;9(12). doi:10.1371/JOURNAL.PONE.0112262
370. Röthlein C, Miettinen MS, Borwankar T, et al. Architecture of polyglutamine-containing fibrils from time-resolved fluorescence decay. *J Biol Chem*. 2014;289(39):26817-26828. doi:10.1074/JBC.M114.581991
371. Davie K, Janssens J, Koldere D, et al. A Single-Cell Transcriptome Atlas of the Aging Drosophila Brain. *Cell*. 2018;174(4):982-998.e20. doi:10.1016/J.CELL.2018.05.057
372. Madabattula ST, Strautman JC, Bysice AM, et al. Quantitative Analysis of Climbing Defects in a Drosophila Model of Neurodegenerative Disorders. *J Vis Exp*. 2015;2015(100). doi:10.3791/52741
373. Thiem J, Viskadourou M, Gaitanidis A, et al. Biological aging of two innate behaviors of Drosophila melanogaster: escape climbing versus courtship learning and memory. *bioRxiv*. Published online October 13, 2023:2023.10.10.561752. doi:10.1101/2023.10.10.561752
374. Ramaswamy S, McBride JL, Kordower JH. Animal models of Huntington's disease. *ILAR J*. 2007;48(4):356-373. doi:10.1093/ilar.48.4.356
375. Zhou Y, Zhou B, Pache L, et al. Metascape provides a biologist-oriented resource for the analysis of systems-level datasets. *Nat Commun*. 2019;10(1). doi:10.1038/S41467-019-09234-6
376. Güiza J, Barría I, Sáez JC, Vega JL. Innexins: Expression, Regulation, and Functions. *Front Physiol*. 2018;9(OCT). doi:10.3389/FPHYS.2018.01414
377. Ren Y, Liu Y, Luo M. Gap Junctions Between Striatal D1 Neurons and Cholinergic Interneurons. *Front Cell Neurosci*. 2021;15. doi:10.3389/FNCEL.2021.674399

378. Hjorth J, Blackwell KT, Kotaleski JH. Gap junctions between striatal fast-spiking interneurons regulate spiking activity and synchronization as a function of cortical activity. *J Neurosci*. 2009;29(16):5276-5286. doi:10.1523/JNEUROSCI.6031-08.2009
379. Gispert S, Twells R, Orozco G, et al. Chromosomal assignment of the second locus for autosomal dominant cerebellar ataxia (SCA2) to chromosome 12q23-24.1. *Nat Genet*. 1993;4(3):295-299. doi:10.1038/ng0793-295
380. Coux O, Tanaka K, Goldberg AL. Structure and functions of the 20S and 26S proteasomes. *Annu Rev Biochem*. 1996;65:801-847. doi:10.1146/ANNUREV.BI.65.070196.004101
381. Bishop P, Rocca D, Henley JM. Ubiquitin C-terminal hydrolase L1 (UCH-L1): structure, distribution and roles in brain function and dysfunction. *Biochem J*. 2016;473(16):2453-2462. doi:10.1042/BCJ20160082
382. Jantrapirom S, Lo Piccolo L, Yoshida H, Yamaguchi M. A new Drosophila model of Ubiquilin knockdown shows the effect of impaired proteostasis on locomotive and learning abilities. *Exp Cell Res*. 2018;362(2):461-471. doi:10.1016/j.yexcr.2017.12.010
383. Hartl FU, Bracher A, Hayer-Hartl M. Molecular chaperones in protein folding and proteostasis. *Nature*. 2011;475(7356):324-332. doi:10.1038/NATURE10317
384. Yang H, Hu HY. Sequestration of cellular interacting partners by protein aggregates: implication in a loss-of-function pathology. *FEBS J*. 2016;283(20):3705-3717. doi:10.1111/FEBS.13722
385. Bard F, Casano L, Mallabiabarrena A, et al. Functional genomics reveals genes involved in protein secretion and Golgi organization. *Nature*. 2006;439(7076):604-607. doi:10.1038/NATURE04377
386. Brandstaetter H, Kruppa AJ, Buss F. Huntingtin is required for ER-to-Golgi transport and for secretory vesicle fusion at the plasma membrane. *DMM Disease Models and Mechanisms*. 2014;7(12):1335-1340. doi:10.1242/dmm.017368
387. Maity S, Komal P, Kumar V, Saxena A, Tungekar A, Chandrasekar V. Impact of ER Stress and ER-Mitochondrial Crosstalk in Huntington’s Disease. *Int J Mol Sci*. 2022;23(2). doi:10.3390/ijms23020780
388. Paul BD. Signaling Overlap between the Golgi Stress Response and Cysteine Metabolism in Huntington’s Disease. *Antioxidants (Basel)*. 2021;10(9). doi:10.3390/ANTIOX10091468
389. Li J, Han S, Li H, et al. Cell-Surface Proteomic Profiling in the Fly Brain Uncovers Wiring Regulators. *Cell*. 2020;180(2):373-386.e15. doi:10.1016/J.CELL.2019.12.029
390. Velentzas AD, Katarachia SA, Sagioglou NE, et al. Proteomic mapping of Drosophila transgenic elav.L-GAL4/+ brain as a tool to illuminate neuropathology mechanisms. *Scientific Reports 2020 10:1*. 2020;10(1):1-14. doi:10.1038/s41598-020-62510-0
391. Kuznetsova KG, Ivanov M V., Pyatnitskiy MA, et al. Brain Proteome of Drosophila melanogaster Is Enriched with Nuclear Proteins. *Biochemistry (Mosc)*. 2019;84(1):71-78. doi:10.1134/S0006297919010097
392. Scholes HM, Cryar A, Kerr F, et al. Dynamic changes in the brain protein interaction network correlates with progression of Aβ42 pathology in Drosophila. *Scientific Reports 2020 10:1*. 2020;10(1):1-13. doi:10.1038/s41598-020-74748-9
393. Herold N, Will CL, Wolf E, Kastner B, Urlaub H, Lührmann R. Conservation of the Protein Composition and Electron Microscopy Structure of Drosophila melanogaster and Human Spliceosomal Complexes . *Mol Cell Biol*. 2009;29(1):281-301. doi:10.1128/mcb.01415-08

394. Bertram K, Agafonov DE, Dybkov O, et al. Cryo-EM Structure of a Pre-catalytic Human Spliceosome Primed for Activation. *Cell*. 2017;170(4):701-713.e11. doi:10.1016/J.CELL.2017.07.011
395. Zhan X, Yan C, Zhang X, Lei J, Shi Y. Structures of the human pre-catalytic spliceosome and its precursor spliceosome. *Cell Res*. 2018;28(12):1129-1140. doi:10.1038/S41422-018-0094-7
396. Tano V, Utami KH, Yusof NABM, et al. Widespread dysregulation of mRNA splicing implicates RNA processing in the development and progression of Huntington's disease. *EBioMedicine*. 2023;94. doi:10.1016/J.EBIOM.2023.104720
397. Haynes PR, Christmann BL, Griffith LC. A single pair of neurons links sleep to memory consolidation in Drosophila melanogaster. *Elife*. 2015;4. doi:10.7554/ELIFE.03868
398. Driscoll M, Buchert SN, Coleman V, McLaughlin M, Nguyen A, Sitaraman D. Compartment specific regulation of sleep by mushroom body requires GABA and dopaminergic signaling. *Sci Rep*. 2021;11(1). doi:10.1038/S41598-021-99531-2
399. Rikani AA, Choudhry Z, Choudhry AM, et al. The mechanism of degeeeration of striatal neuronal subtypes in Huntington disease. *Ann Neurosci*. 2014;21(3):112-114. doi:10.5214/ans.0972.7531.210308
400. Garret M, Du Z, Chazalon M, Cho YH, Baufreton J. Alteration of GABAergic neurotransmission in Huntington's disease. *CNS Neurosci Ther*. 2018;24(4):292-300. doi:10.1111/CNS.12826
401. Hsu YT, Chang YG, Chern Y. Insights into GABAAergic system alteration in Huntington's disease. *Open Biol*. 2018;8(12). doi:10.1098/RSOB.180165
402. Terunuma M. Diversity of structure and function of GABAB receptors: a complexity of GABAB-mediated signaling. *Proc Jpn Acad Ser B Phys Biol Sci*. 2018;94(10):390-411. doi:10.2183/PJAB.94.026
403. Kohl MM, Paulsen O. The roles of GABAB receptors in cortical network activity. *Adv Pharmacol*. 2010;58(C):205-229. doi:10.1016/S1054-3589(10)58009-8
404. Philpott AL, Cummins TDR, Bailey NW, Churchyard A, Fitzgerald PB, Georgiou-Karistianis N. Cortical inhibitory deficits in premanifest and early Huntington's disease. *Behavioural brain research*. 2016;296:311-317. doi:10.1016/J.BBR.2015.09.030
405. D'Souza RS, Semus R, Billings EA, Meyer CB, Conger K, Casanova JE. Rab4 orchestrates a small GTPase cascade for recruitment of adaptor proteins to early endosomes. *Curr Biol*. 2014;24(11):1187-1198. doi:10.1016/J.CUB.2014.04.003
406. Yu CJ, Lee FJS. Multiple activities of Arl1 GTPase in the trans-Golgi network. *J Cell Sci*. 2017;130(10):1691-1699. doi:10.1242/JCS.201319
407. Park SY, Muschalik N, Chadwick J, Munro S. In vivo characterization of Drosophila golgins reveals redundancy and plasticity of vesicle capture at the Golgi apparatus. *Current Biology*. 2022;32(21):4549-4564.e6. doi:10.1016/j.cub.2022.08.054
408. Lowe M. The Physiological Functions of the Golgin Vesicle Tethering Proteins. *Front Cell Dev Biol*. 2019;7(JUN). doi:10.3389/FCELL.2019.00094
409. Selitrennik M, Lev S. The role of phosphatidylinositol-transfer proteins at membrane contact sites. *Biochem Soc Trans*. 2016;44(2):419-424. doi:10.1042/BST20150182
410. Carvou N, Holic R, Li M, Futter C, Skippen A, Cockcroft S. Phosphatidylinositol- and phosphatidylcholine-transfer activity of PITPbeta is essential for COPI-mediated retrograde transport from the Golgi to the endoplasmic reticulum. *J Cell Sci*. 2010;123(Pt 8):1262-1273. doi:10.1242/JCS.061986

411. Branco J, Al-ramahi I, Ukani L, et al. Comparative analysis of genetic modifiers in Drosophila points to common and distinct mechanisms of pathogenesis among polyglutamine diseases. *Hum Mol Genet*. 2008;17(3):376-390. doi:10.1093/HMG/DDM315
412. Baas S, Sharrow M, Kotu V, et al. Sugar-free frosting, a homolog of SAD kinase, drives neural-specific glycan expression in the Drosophila embryo. *Development*. 2011;138(3):553-563. doi:10.1242/DEV.055376
413. Giansanti MG, Belloni G, Gatti M. Rab11 is required for membrane trafficking and actomyosin ring constriction in meiotic cytokinesis of Drosophila males. *Mol Biol Cell*. 2007;18(12):5034-5047. doi:10.1091/MBC.E07-05-0415
414. De Vries KJ, Westerman J, Bastiaens PIH, Jovin TM, Wirtz KWA, Snoek GT. Fluorescently labeled phosphatidylinositol transfer protein isoforms (alpha and beta), microinjected into fetal bovine heart endothelial cells, are targeted to distinct intracellular sites. *Exp Cell Res*. 1996;227(1):33-39. doi:10.1006/EXCR.1996.0246
415. Park SY, Muschalik N, Chadwick J, Munro S. In vivo characterization of Drosophila golgins reveals redundancy and plasticity of vesicle capture at the Golgi apparatus. *Curr Biol*. 2022;32(21):4549-4564.e6. doi:10.1016/J.CUB.2022.08.054
416. Crump JG, Zhen M, Jin Y, Bargmann CI. The SAD-1 kinase regulates presynaptic vesicle clustering and axon termination. *Neuron*. 2001;29(1):115-129. doi:10.1016/S0896-6273(01)00184-2
417. Green EW, Fedele G, Giorgini F, Kyriacou CP. A Drosophila RNAi collection is subject to dominant phenotypic effects. *Nat Methods*. 2014;11(3):222-223. doi:10.1038/NMETH.2856
418. Bates G. Huntingtin aggregation and toxicity in Huntington’s disease. *Lancet*. 2003;361(9369):1642-1644. doi:10.1016/S0140-6736(03)13304-1
419. Xi W, Wang X, Laue TM, Denis CL. Multiple discrete soluble aggregates influence polyglutamine toxicity in a Huntington’s disease model system. *Sci Rep*. 2016;6. doi:10.1038/SREP34916
420. Holmes BB, Furman JL, Mahan TE, et al. Proteopathic tau seeding predicts tauopathy in vivo. *Proc Natl Acad Sci U S A*. 2014;111(41):E4376-E4385. doi:10.1073/PNAS.1411649111
421. Xu L, Tian S, Peng X, et al. Clusterin inhibits Aβ42 aggregation through a “strawberry model” as detected by FRET-FCS. *J Neurochem*. 2021;158(2):444-454. doi:10.1111/JNC.15344
422. Furman JL, Diamond MI. FRET and Flow Cytometry Assays to Measure Proteopathic Seeding Activity in Biological Samples. *Methods Mol Biol*. 2017;1523:349-359. doi:10.1007/978-1-4939-6598-4_23
423. Pollitt SK, Pallos J, Shao J, et al. A rapid cellular FRET assay of polyglutamine aggregation identifies a novel inhibitor. *Neuron*. 2003;40(4):685-694. doi:10.1016/S0896-6273(03)00697-4
424. Baldo B, Paganetti P, Grueninger S, et al. TR-FRET-based duplex immunoassay reveals an inverse correlation of soluble and aggregated mutant huntingtin in huntington’s disease. *Chem Biol*. 2012;19(2):264-275. doi:10.1016/J.CHEMBIOL.2011.12.020
425. Singer E, Hunanyan L, Melkonyan MM, Weber JJ, Danielyan L, Nguyen HP. The Novel Alpha-2 Adrenoceptor Inhibitor Beditin Reduces Cytotoxicity and Huntingtin Aggregates in Cell Models of Huntington’s Disease. *Pharmaceuticals (Basel)*. 2021;14(3). doi:10.3390/PH14030257

426. dos Remedios CG, Miki M, Barden JA. Fluorescence resonance energy transfer measurements of distances in actin and myosin. A critical evaluation. *J Muscle Res Cell Motil*. 1987;8(2):97-117. doi:10.1007/BF01753986
427. Desai UA, Pallos J, Ma AAK, et al. Biologically active molecules that reduce polyglutamine aggregation and toxicity. *Hum Mol Genet*. 2006;15(13):2114-2124. doi:10.1093/HMG/DDL135
428. Kim S, Nollen EAA, Kitagawa K, Bindokas VP, Morimoto RI. Polyglutamine protein aggregates are dynamic. *Nat Cell Biol*. 2002;4(10):826-830. doi:10.1038/NCB863
429. Shaner NC, Lambert GG, Chammas A, et al. A bright monomeric green fluorescent protein derived from Branchiostoma lanceolatum. *Nat Methods*. 2013;10(5):407-409. doi:10.1038/NMETH.2413
430. Bindels DS, Haarbosch L, Van Weeren L, et al. mScarlet: a bright monomeric red fluorescent protein for cellular imaging. *Nat Methods*. 2017;14(1):53-56. doi:10.1038/NMETH.4074
431. Mertens LMY, den Blaauwen T. Optimising expression of the large dynamic range FRET pair mNeonGreen and superfolder mTurquoise2ox for use in the Escherichia coli cytoplasm. *Sci Rep*. 2022;12(1). doi:10.1038/S41598-022-22918-2
432. Miyagi T, Yamanaka Y, Harada Y, et al. An improved macromolecular crowding sensor CRONOS for detection of crowding changes in membrane-less organelles under stressed conditions. *Biochem Biophys Res Commun*. 2021;583:29-34. doi:10.1016/J.BBRC.2021.10.055
433. Crick SL, Ruff KM, Garai K, Frieden C, Pappu R V. Unmasking the roles of N- and C-terminal flanking sequences from exon 1 of huntingtin as modulators of polyglutamine aggregation. *Proc Natl Acad Sci U S A*. 2013;110(50):20075-20080. doi:10.1073/PNAS.1320626110/-/DCSUPPLEMENTAL/SAPP.PDF
434. DeGuire SM, Ruggeri FS, Fares MB, et al. N-terminal Huntingtin (Htt) phosphorylation is a molecular switch regulating Htt aggregation, helical conformation, internalization, and nuclear targeting. *J Biol Chem*. 2018;293(48):18540-18558. doi:10.1074/JBC.RA118.004621
435. Leavesley SJ, Rich TC. Overcoming limitations of FRET measurements. *Cytometry A*. 2016;89(4):325-327. doi:10.1002/CYTO.A.22851
436. Piston DW, Kremers GJ. Fluorescent protein FRET: the good, the bad and the ugly. *Trends Biochem Sci*. 2007;32(9):407-414. doi:10.1016/J.TIBS.2007.08.003
437. Chongtham A, Bornemann DJ, Barbaro BA, et al. Effects of flanking sequences and cellular context on subcellular behavior and pathology of mutant HTT. *Hum Mol Genet*. 2020;29(4):674-688. doi:10.1093/HMG/DDAA001
438. Morgan TH. SEX LIMITED INHERITANCE IN DROSOPHILA. *Science*. 1910;32(812):120-122. doi:10.1126/SCIENCE.32.812.120
439. Nüsslein-volhard C, Wieschaus E. Mutations affecting segment number and polarity in Drosophila. *Nature*. 1980;287(5785):795-801. doi:10.1038/287795A0
440. Lemaitre B, Nicolas E, Michaut L, Reichhart JM, Hoffmann JA. The dorsoventral regulatory gene cassette spätzle/Toll/cactus controls the potent antifungal response in Drosophila adults. *Cell*. 1996;86(6):973-983. doi:10.1016/S0092-8674(00)80172-5
441. Bargiello TA, Young MW. Molecular genetics of a biological clock in Drosophila. *Proc Natl Acad Sci U S A*. 1984;81(7):2142-2146. doi:10.1073/PNAS.81.7.2142
442. Bargiello TA, Jackson FR, Young MW. Restoration of circadian behavioural rhythms by gene transfer in Drosophila. *Nature*. 1984;312(5996):752-754. doi:10.1038/312752A0

443. Reddy P, Zehring WA, Wheeler DA, et al. Molecular analysis of the period locus in Drosophila melanogaster and identification of a transcript involved in biological rhythms. *Cell*. 1984;38(3):701-710. doi:10.1016/0092-8674(84)90265-4

444. Oliveira-Ferreira C, Gaspar M, Vasconcelos ML. Neuronal substrates of egg-laying behaviour at the abdominal ganglion of Drosophila melanogaster. *Sci Rep*. 2023;13(1). doi:10.1038/S41598-023-48109-1

445. Fernández-Moreno MA, Farr CL, Kaguni LS, Garesse R. Drosophila melanogaster as a model system to study mitochondrial biology. *Methods Mol Biol*. 2007;372:33-49. doi:10.1007/978-1-59745-365-3_3

446. Jackson GR, Salecker I, Dong X, et al. Polyglutamine-expanded human huntingtin transgenes induce degeneration of Drosophila photoreceptor neurons. *Neuron*. 1998;21(3):633-642. doi:10.1016/S0896-6273(00)80573-5

447. Zhang S, Binari R, Zhou R, Perrimon N. A genomewide RNA interference screen for modifiers of aggregates formation by mutant Huntingtin in Drosophila. *Genetics*. 2010;184(4):1165-1179. doi:10.1534/GENETICS.109.112516

448. Roth JR, Moraes RCM de, Xu BP, Crawley SR, Khan MA, Melkani GC. Rapamycin reduces neuronal mutant huntingtin aggregation and ameliorates locomotor performance in Drosophila. *Front Aging Neurosci*. 2023;15. doi:10.3389/FNAGI.2023.1223911

449. Donnelly KM, Delorenzo OR, Zaya ADA, et al. Phagocytic glia are obligatory intermediates in transmission of mutant huntingtin aggregates across neuronal synapses. *Elife*. 2020;9:1. doi:10.7554/ELIFE.58499

450. Rocha JJ, Jayaram SA, Stevens TJ, et al. Functional unknomics: Systematic screening of conserved genes of unknown function. *PLoS Biol*. 2023;21(8). doi:10.1371/JOURNAL.PBIO.3002222

451. Menzies FM, Garcia-Arencibia M, Imarisio S, et al. Calpain inhibition mediates autophagy-dependent protection against polyglutamine toxicity. *Cell Death Differ*. 2015;22(3):433-444. doi:10.1038/CDD.2014.151

452. Melkani GC, Trujillo AS, Ramos R, Bodmer R, Bernstein SI, Ocorr K. Huntington's disease induced cardiac amyloidosis is reversed by modulating protein folding and oxidative stress pathways in the Drosophila heart. *PLoS Genet*. 2013;9(12). doi:10.1371/JOURNAL.PGEN.1004024

453. Swinter K, Salah D, Rathnayake R, Gunawardena S. PolyQ-Expansion Causes Mitochondria Fragmentation Independent of Huntingtin and Is Distinct from Traumatic Brain Injury (TBI)/Mechanical Stress-Mediated Fragmentation Which Results from Cell Death. *Cells*. 2023;12(19). doi:10.3390/CELLS12192406

454. Jansen AHP, van Hal M, op den Kelder IC, et al. Frequency of nuclear mutant huntingtin inclusion formation in neurons and glia is cell-type-specific. *Glia*. 2017;65(1):50-61. doi:10.1002/GLIA.23050

455. Bennett EJ, Bence NF, Jayakumar R, Kopito RR. Global impairment of the ubiquitin-proteasome system by nuclear or cytoplasmic protein aggregates precedes inclusion body formation. *Mol Cell*. 2005;17(3):351-365. doi:10.1016/J.MOLCEL.2004.12.021

456. Raji JI, Potter CJ. The number of neurons in Drosophila and mosquito brains. *PLoS One*. 2021;16(5). doi:10.1371/JOURNAL.PONE.0250381

457. Strausfeld NJ, Hirth F. Deep homology of arthropod central complex and vertebrate basal ganglia. *Science*. 2013;340(6129):157-161. doi:10.1126/SCIENCE.1231828

458. Wolff T, Rubin GM. Neuroarchitecture of the Drosophila central complex: A catalog of nodulus and asymmetrical body neurons and a revision of the protocerebral bridge catalog. *J Comp Neurol*. 2018;526(16):2585-2611. doi:10.1002/CNE.24512
459. Kim YE, Hosp F, Frottin F, et al. Soluble Oligomers of PolyQ-Expanded Huntingtin Target a Multiplicity of Key Cellular Factors. *Mol Cell*. 2016;63(6):951-964. doi:10.1016/J.MOLCEL.2016.07.022
460. Hazeki N, Tukamoto T, Goto J, Kanazawa I. Formic acid dissolves aggregates of an N-terminal huntingtin fragment containing an expanded polyglutamine tract: applying to quantification of protein components of the aggregates. *Biochem Biophys Res Commun*. 2000;277(2):386-393. doi:10.1006/BBRC.2000.3682
461. Seidel K, Siswanto S, Fredrich M, et al. Polyglutamine aggregation in Huntington's disease and spinocerebellar ataxia type 3: similar mechanisms in aggregate formation. *Neuropathol Appl Neurobiol*. 2016;42(2):153-166. doi:10.1111/NAN.12253
462. Yu A, Shibata Y, Shah B, Calamini B, Lo DC, Morimoto RI. Protein aggregation can inhibit clathrin-mediated endocytosis by chaperone competition. *Proc Natl Acad Sci U S A*. 2014;111(15). doi:10.1073/PNAS.1321811111/-/DCSUPPLEMENTAL/PNAS.201321811SI.PDF
463. Ortega Z, Lucas JJ. Ubiquitin-proteasome system involvement in Huntington's disease. *Front Mol Neurosci*. 2014;7(SEP). doi:10.3389/FNMOL.2014.00077
464. Mitra S, Tsvetkov AS, Finkbeiner S. Single neuron ubiquitin-proteasome dynamics accompanying inclusion body formation in huntington disease. *J Biol Chem*. 2009;284(7):4398-4403. doi:10.1074/JBC.M806269200
465. Le Guiner C, Lejeune F, Galiana D, et al. TIA-1 and TIAR activate splicing of alternative exons with weak 5' splice sites followed by a U-rich stretch on their own pre-mRNAs. *J Biol Chem*. 2001;276(44):40638-40646. doi:10.1074/JBC.M105642200
466. Gilks N, Kedersha N, Ayodele M, et al. Stress granule assembly is mediated by prion-like aggregation of TIA-1. *Mol Biol Cell*. 2004;15(12):5383-5398. doi:10.1091/MBC.E04-08-0715
467. Sanchez II, Nguyen TB, England WE, et al. Huntington's disease mice and human brain tissue exhibit increased G3BP1 granules and TDP43 mislocalization. *J Clin Invest*. 2021;131(12). doi:10.1172/JCI140723
468. Krach F, Stemick J, Boerstler T, et al. An alternative splicing modulator decreases mutant HTT and improves the molecular fingerprint in Huntington's disease patient neurons. *Nat Commun*. 2022;13(1). doi:10.1038/S41467-022-34419-X
469. Duennwald ML, Jagadish S, Giorgini F, Muchowski PJ, Lindquist S. A network of protein interactions determines polyglutamine toxicity. *Proc Natl Acad Sci U S A*. 2006;103(29):11051-11056. doi:10.1073/PNAS.0604548103
470. Schaefer MH, Wanker EE, Andrade-Navarro MA. Evolution and function of CAG/polyglutamine repeats in protein-protein interaction networks. *Nucleic Acids Res*. 2012;40(10):4273-4287. doi:10.1093/NAR/GKS011
471. Hong JY, Wang JY, Yue HW, et al. Coaggregation of polyglutamine (polyQ) proteins is mediated by polyQ-tract interactions and impairs cellular proteostasis. *Acta Biochim Biophys Sin (Shanghai)*. 2023;55(5):736-748. doi:10.3724/ABBS.2023081
472. Mier P, Andrade-Navarro MA. Between Interactions and Aggregates: The PolyQ Balance. *Genome Biol Evol*. 2021;13(11). doi:10.1093/GBE/EVAB246

473. Fiumara F, Fioriti L, Kandel ER, Hendrickson WA. Essential role of coiled coils for aggregation and activity of Q/N-rich prions and PolyQ proteins. *Cell*. 2010;143(7):1121-1135. doi:10.1016/J.CELL.2010.11.042
474. Xu F, Kula-Eversole E, Iwanaszko M, Lim C, Allada R. Ataxin2 functions via CrebA to mediate Huntingtin toxicity in circadian clock neurons. *PLoS Genet*. 2019;15(10). doi:10.1371/JOURNAL.PGEN.1008356
475. Huelsmeier J, Walker E, Bakthavachalu B, Ramaswami M. A C-terminal ataxin-2 disordered region promotes Huntingtin protein aggregation and neurodegeneration in Drosophila models of Huntington's disease. *G3 (Bethesda)*. 2021;11(12). doi:10.1093/G3JOURNAL/JKAB355
476. Hervé JC. Membrane channels formed by gap junction proteins. *Biochim Biophys Acta Biomembr*. 2018;1860(1):1-4. doi:10.1016/J.BBAMEM.2017.10.021
477. Hervé JC, Derangeon M. Gap-junction-mediated cell-to-cell communication. *Cell Tissue Res*. 2013;352(1):21-31. doi:10.1007/S00441-012-1485-6
478. Lu C, Meng Z, He Y, et al. Involvement of gap junctions in astrocyte impairment induced by manganese exposure. *Brain Res Bull*. 2018;140:107-113. doi:10.1016/J.BRAINRESBULL.2018.04.009
479. Estrada-Sánchez AM, Montiel T, Segovia J, Massieu L. Glutamate toxicity in the striatum of the R6/2 Huntington's disease transgenic mice is age-dependent and correlates with decreased levels of glutamate transporters. *Neurobiol Dis*. 2009;34(1):78-86. doi:10.1016/J.NBD.2008.12.017
480. Vis JC, Nicholson LFB, Faull RLM, Evans WH, Severs NJ, Green CR. Connexin expression in Huntington's diseased human brain. *Cell Biol Int*. 1998;22(11-12):837-847. doi:10.1006/CBIR.1998.0388
481. Chaibva M, Burke KA, Legleiter J. Curvature enhances binding and aggregation of huntingtin at lipid membranes. *Biochemistry*. 2014;53(14):2355-2365. doi:10.1021/BI401619Q
482. Tao M, Pandey NK, Barnes R, Han S, Langen R. Structure of Membrane-Bound Huntingtin Exon 1 Reveals Membrane Interaction and Aggregation Mechanisms. *Structure*. 2019;27(10):1570-1580.e4. doi:10.1016/J.STR.2019.08.003
483. Marquette A, Aisenbrey C, Bechinger B. Membrane Interactions Accelerate the Self-Aggregation of Huntingtin Exon 1 Fragments in a Polyglutamine Length-Dependent Manner. *Int J Mol Sci*. 2021;22(13). doi:10.3390/IJMS22136725
484. Pieri L, Madiona K, Bousset L, Melki R. Fibrillar α-synuclein and huntingtin exon 1 assemblies are toxic to the cells. *Biophys J*. 2012;102(12):2894-2905. doi:10.1016/J.BPJ.2012.04.050
485. Monsellier E, Bousset L, Melki R. α-Synuclein and huntingtin exon 1 amyloid fibrils bind laterally to the cellular membrane. *Sci Rep*. 2016;6. doi:10.1038/SREP19180
486. Qin ZH, Wang Y, Sapp E, et al. Huntingtin bodies sequester vesicle-associated proteins by a polyproline-dependent interaction. *J Neurosci*. 2004;24(1):269-281. doi:10.1523/JNEUROSCI.1409-03.2004
487. Schilling J, Broemer M, Atanassov I, et al. Deregulated Splicing Is a Major Mechanism of RNA-Induced Toxicity in Huntington's Disease. *J Mol Biol*. 2019;431(9):1869-1877. doi:10.1016/J.JMB.2019.01.034
488. Martí E. RNA toxicity induced by expanded CAG repeats in Huntington's disease. *Brain Pathol*. 2016;26(6):779-786. doi:10.1111/BPA.12427

489. Galka-Marciniak P, Urbanek MO, Krzyzosiak WJ. Triplet repeats in transcripts: structural insights into RNA toxicity. *Biol Chem*. 2012;393(11):1299-1315. doi:10.1515/HSZ-2012-0218
490. Gipson TA, Neueder A, Wexler NS, Bates GP, Housman D. Aberrantly spliced HTT, a new player in Huntington’s disease pathogenesis. *RNA Biol*. 2013;10(11):1647-1652. doi:10.4161/rna.26706
491. Gomez-Navarro N, Miller E. Protein sorting at the ER-Golgi interface. *J Cell Biol*. 2016;215(6):769-778. doi:10.1083/JCB.201610031
492. Brandstaetter H, Kruppa AJ, Buss F. Huntingtin is required for ER-to-Golgi transport and for secretory vesicle fusion at the plasma membrane. *Dis Model Mech*. 2014;7(12):1335-1340. doi:10.1242/DMM.017368
493. Creus-Muncunill J, Badillos-Rodríguez R, Garcia-Forn M, et al. Increased translation as a novel pathogenic mechanism in Huntington’s disease. *Brain*. 2019;142(10):3158-3175. doi:10.1093/BRAIN/AWZ230
494. Tauber E, Miller-Fleming L, Mason RP, et al. Functional gene expression profiling in yeast implicates translational dysfunction in mutant huntingtin toxicity. *J Biol Chem*. 2011;286(1):410-419. doi:10.1074/JBC.M110.101527
495. Joag H, Ghatpande V, Desai M, et al. A role of cellular translation regulation associated with toxic Huntingtin protein. *Cell Mol Life Sci*. 2020;77(18):3657-3670. doi:10.1007/S00018-019-03392-Y
496. Eshraghi M, Karunadharma PP, Blin J, et al. Mutant Huntingtin stalls ribosomes and represses protein synthesis in a cellular model of Huntington disease. *Nat Commun*. 2021;12(1). doi:10.1038/S41467-021-21637-Y
497. Lin JH, Walter P, Yen TSB. Endoplasmic reticulum stress in disease pathogenesis. *Annual Review of Pathology: Mechanisms of Disease*. 2008;3:399-425. doi:10.1146/annurev.pathmechdis.3.121806.151434
498. Schröder M, Kaufman RJ. ER stress and the unfolded protein response. *Mutat Res*. 2005;569(1-2):29-63. doi:10.1016/J.MRFMMM.2004.06.056
499. Almanza A, Carlesso A, Chintha C, et al. Endoplasmic reticulum stress signalling - from basic mechanisms to clinical applications. *FEBS J*. 2019;286(2):241-278. doi:10.1111/FEBS.14608
500. Shacham T, Sharma N, Lederkremer GZ. Protein Misfolding and ER Stress in Huntington’s Disease. *Front Mol Biosci*. 2019;6(APR). doi:10.3389/FMOLB.2019.00020
501. Duennwald ML, Lindquist S. Impaired ERAD and ER stress are early and specific events in polyglutamine toxicity. *Genes Dev*. 2008;22(23):3308-3319. doi:10.1101/GAD.1673408
502. Miki Y, Tanji K, Mori F, Wakabayashi K. Sigma-1 receptor is involved in degradation of intranuclear inclusions in a cellular model of Huntington’s disease. *Neurobiol Dis*. 2015;74:25-31. doi:10.1016/J.NBD.2014.11.005
503. Cockcroft S, Lev S. Mammalian PITPs at the Golgi and ER-Golgi Membrane Contact Sites. *Contact*. 2020;3. doi:10.1177/2515256420964170/ASSET/IMAGES/LARGE/10.1177_2515256420964170-FIG4.JPEG
504. Friggi-Grelin F, Rabouille C, Therond P. The cis-Golgi Drosophila GMAP has a role in anterograde transport and Golgi organization in vivo, similar to its mammalian ortholog in tissue culture cells. *Eur J Cell Biol*. 2006;85(11):1155-1166. doi:10.1016/J.EJCB.2006.07.001

505. Witkos TM, Lowe M. Recognition and tethering of transport vesicles at the Golgi apparatus. *Curr Opin Cell Biol*. 2017;47:16-23. doi:10.1016/J.CEB.2017.02.003
506. Cardenas J, Rivero S, Goud B, Bornens M, Rios RM. Golgi localisation of GMAP210 requires two distinct cis-membrane binding mechanisms. *BMC Biol*. 2009;7:56. doi:10.1186/1741-7007-7-56
507. Roboti P, Sato K, Lowe M. The golgin GMAP-210 is required for efficient membrane trafficking in the early secretory pathway. *J Cell Sci*. 2015;128(8):1595-1606. doi:10.1242/JCS.166710
508. Kim JSM, Hung W, Zhen M. The long and the short of SAD-1 kinase. *Commun Integr Biol*. 2010;3(3):251-255. doi:10.4161/CIB.3.3.11455
509. Smits P, Bolton AD, Funari V, et al. Lethal skeletal dysplasia in mice and humans lacking the golgin GMAP-210. *N Engl J Med*. 2010;362(3):206-216. doi:10.1056/NEJMOA0900158
510. Wang B, Stanford KR, Kundu M. ER-to-Golgi Trafficking and Its Implication in Neurological Diseases. *Cells*. 2020;9(2). doi:10.3390/CELLS9020408
511. Lilley BN, Pan YA, Sanes JR. SAD kinases sculpt axonal arbors of sensory neurons through long- and short-term responses to neurotrophin signals. *Neuron*. 2013;79(1):39-53. doi:10.1016/J.NEURON.2013.05.017
512. Barnes AP, Lilley BN, Pan YA, et al. LKB1 and SAD kinases define a pathway required for the polarization of cortical neurons. *Cell*. 2007;129(3):549-563. doi:10.1016/J.CELL.2007.03.025
513. Lilley BN, Krishnaswamy A, Wang Z, Kishi M, Frank E, Sanes JR. SAD kinases control the maturation of nerve terminals in the mammalian peripheral and central nervous systems. *Proc Natl Acad Sci U S A*. 2014;111(3):1138-1143. doi:10.1073/PNAS.1321990111
514. Inoue E, Mochida S, Takagi H, et al. SAD: a presynaptic kinase associated with synaptic vesicles and the active zone cytomatrix that regulates neurotransmitter release. *Neuron*. 2006;50(2):261-275. doi:10.1016/J.NEURON.2006.03.018
515. Kishi M, Pan YA, Crump JG, Sanes JR. Mammalian SAD kinases are required for neuronal polarization. *Science*. 2005;307(5711):929-932. doi:10.1126/SCIENCE.1107403
516. Schneider A, Mandelkow E. Tau-based treatment strategies in neurodegenerative diseases. *Neurotherapeutics*. 2008;5(3):443-457. doi:10.1016/J.NURT.2008.05.006
517. Jellinger KA. Alzheimer-type lesions in Huntington's disease. *J Neural Transm (Vienna)*. 1998;105(8-9):787-799. doi:10.1007/S007020050095
518. Reyes MG, Gibbons S. Dementia of the Alzheimer's type and Huntington's disease. *Neurology*. 1985;35(2):273-277. doi:10.1212/WNL.35.2.273
519. Vuono R, Winder-Rhodes S, De Silva R, et al. The role of tau in the pathological process and clinical expression of Huntington's disease. *Brain*. 2015;138(Pt 7):1907-1918. doi:10.1093/BRAIN/AWV107
520. Mitra N, Sinha S, Ramya TNC, Surolia A. N-linked oligosaccharides as outfitters for glycoprotein folding, form and function. *Trends Biochem Sci*. 2006;31(3):156-163. doi:10.1016/J.TIBS.2006.01.003
521. Parodi AJ. Role of N-oligosaccharide endoplasmic reticulum processing reactions in glycoprotein folding and degradation. *Biochem J*. 2000;348 Pt 1(Pt 1):1-13. doi:10.1042/0264-6021:3480001

522. Shental-Bechor D, Levy Y. Effect of glycosylation on protein folding: A close look at thermodynamic stabilization. *Proc Natl Acad Sci U S A*. 2008;105(24):8256-8261. doi:10.1073/pnas.0801340105
523. Conroy LR, Hawkinson TR, Young LEA, Gentry MS, Sun RC. Emerging roles of N-linked glycosylation in brain physiology and disorders. *Trends Endocrinol Metab*. 2021;32(12):980-993. doi:10.1016/J.TEM.2021.09.006
524. Pradeep P, Kang H, Lee B. Glycosylation and behavioral symptoms in neurological disorders. *Transl Psychiatry*. 2023;13(1). doi:10.1038/S41398-023-02446-X
525. Yang J, Li H, Zhao Y. Dessert or Poison? The Roles of Glycosylation in Alzheimer's, Parkinson's, Huntington's Disease, and Amyotrophic Lateral Sclerosis. *Chembiochem*. 2023;24(16). doi:10.1002/CBIC.202300017
526. Cho BG, Veillon L, Mechref Y. N-Glycan Profile of Cerebrospinal Fluids from Alzheimer's Disease Patients Using Liquid Chromatography with Mass Spectrometry. *J Proteome Res*. 2019;18(10):3770-3779. doi:10.1021/ACS.JPROTEOME.9B00504
527. Videira PAQ, Castro-Caldas M. Linking Glycation and Glycosylation With Inflammation and Mitochondrial Dysfunction in Parkinson's Disease. *Front Neurosci*. 2018;12(JUN). doi:10.3389/FNINS.2018.00381
528. Xu M, Jin H, Wu Z, et al. Mass Spectrometry-Based Analysis of Serum N-Glycosylation Changes in Patients with Parkinson's Disease. *ACS Chem Neurosci*. 2022;13(12):1719-1726. doi:10.1021/acschemneuro.2c00264
529. Cvetko A, Kifer D, Gornik O, et al. Glycosylation alterations in multiple sclerosis show increased proinflammatory potential. *Biomedicines*. 2020;8(10):1-14. doi:10.3390/biomedicines8100410
530. Hung WY, Mold DE, Tourian A. Huntington's-chorea fibroblasts. Cellular protein glycosylation. *Biochem J*. 1980;190(3):711-719. doi:10.1042/BJ1900711
531. Gizaw ST, Koda T, Amano M, et al. A comprehensive glycome profiling of Huntington's disease transgenic mice. *Biochim Biophys Acta Gen Subj*. 2015;1850(9):1704-1718. doi:10.1016/j.bbagen.2015.04.006
532. An HJ, Kronewitter SR, de Leoz MLA, Lebrilla CB. Glycomics and disease markers. *Curr Opin Chem Biol*. 2009;13(5-6):601-607. doi:10.1016/J.CBPA.2009.08.015
533. Kalyuzhny E, Petzoldt AG. Presynaptic Precursor Vesicles—Cargo, Biogenesis, and Kinesin-Based Transport across Species. *Cells 2023, Vol 12, Page 2248*. 2023;12(18):2248. doi:10.3390/CELLS12182248
534. Maas C, Torres VI, Altrock WD, et al. Formation of Golgi-derived active zone precursor vesicles. *J Neurosci*. 2012;32(32):11095-11108. doi:10.1523/JNEUROSCI.0195-12.2012
535. Götz TWB, Puchkov D, Lysiuk V, et al. Rab2 regulates presynaptic precursor vesicle biogenesis at the trans-Golgi. *J Cell Biol*. 2021;220(5). doi:10.1083/JCB.202006040
536. Paton B, Suarez M, Herrero P, Canela N. Glycosylation Biomarkers Associated with Age-Related Diseases and Current Methods for Glycan Analysis. *Int J Mol Sci*. 2021;22(11). doi:10.3390/IJMS22115788
537. Kobeissy F, Kobaisi A, Peng W, et al. Glycomic and Glycoproteomic Techniques in Neurodegenerative Disorders and Neurotrauma: Towards Personalized Markers. *Cells*. 2022;11(3). doi:10.3390/cells11030581
538. Hübner R, Steinhauser M, Lehle C. A dual-stage two-phase model of selective attention. *Psychol Rev*. 2010;117(3):759-784. doi:10.1037/A0019471

539. Rappsilber J, Mann M, Ishihama Y. Protocol for micro-purification, enrichment, pre-fractionation and storage of peptides for proteomics using StageTips. *Nat Protoc*. 2007;2(8):1896-1906. doi:10.1038/NPROT.2007.261

540. Cox J, Mann M. MaxQuant enables high peptide identification rates, individualized p.p.b.-range mass accuracies and proteome-wide protein quantification. *Nat Biotechnol*. 2008;26(12):1367-1372. doi:10.1038/NBT.1511

541. Cox J, Hein MY, Luber CA, Paron I, Nagaraj N, Mann M. Accurate proteome-wide label-free quantification by delayed normalization and maximal peptide ratio extraction, termed MaxLFQ. *Mol Cell Proteomics*. 2014;13(9):2513-2526. doi:10.1074/MCP.M113.031591

542. Ritchie ME, Phipson B, Wu D, et al. limma powers differential expression analyses for RNA-sequencing and microarray studies. *Nucleic Acids Res*. 2015;43(7):e47. doi:10.1093/NAR/GKV007

543. Szklarczyk D, Gable AL, Lyon D, et al. STRING v11: protein-protein association networks with increased coverage, supporting functional discovery in genome-wide experimental datasets. *Nucleic Acids Res*. 2019;47(D1):D607-D613. doi:10.1093/NAR/GKY1131

544. Tyanova S, Temu T, Sinitcyn P, et al. The Perseus computational platform for comprehensive analysis of (prote)omics data. *Nat Methods*. 2016;13(9):731-740. doi:10.1038/NMETH.3901

545. Prewitt JMS, Mendelsohn ML. The analysis of cell images. *Ann N Y Acad Sci*. 1966;128(3):1035-1053. doi:10.1111/J.1749-6632.1965.TB11715.X

14. Acknowledgements

I would like to take the opportunity to acknowledge all the individuals who have supported this work.

First, I would like to acknowledge my academic advisors. I would like to say thank you to Prof. Dr. Erich Wanker for selecting me to join his group for my PhD studies and for his continued guidance over the course of my studies. I greatly respect his advice, expertise, and passion for science. I would also like to extend thanks to my Dr. Anne Ast, who supervised my work in the lab and opened my eyes to the world of fly research. This work would not have been possible without her patience, guidance, and training. I would also like to thank my thesis advisory committee (TAC) members Prof. Dr. Stephan Sigrist and Dr. Robert Zinzen for their continued support and insightful suggestions throughout my PhD studies. I would like to also extend thanks to my PhD reviewers for dedicating the time to read and assess this work.

Next, I would like to acknowledge members of the Wanker Lab who have been involved in my PhD journey. To Leo and Roxane thank you for being my lunch companions, support network and friends. To Orchid, thanks for being a top-class mate. I will always remember our great American adventure and our chats on the sunny step. And thankyou to the best fly chef around Emily for always brightening my day, both inside and outside the lab. Thank you, Leo, Roxane, Orchid, and Emily for celebrating with me when things went well, and drowning your sorrows with me when things went wrong. To Martina and Nancy, thank you for always letting me bother you with silly questions and orders. Without you showing me the ropes, I would have been completely lost. To Lydia, thank you for putting up with me for this long and helping me learn the ways of the flies. To Sigrid, thank you for letting me pester you with all my bureaucratic struggles and helping me navigate the challenging world of German paperwork throughout my studies. Thank you to everyone at the Wanker Lab who has helped me grow and learn over the years.

A huge thankyou goes to my Mum. You have always encouraged me to be to be independent, work hard and take every opportunity offered to me. You always made us your number one priority, often at the sacrifice of yourself. Thank you for making me the person I am today and pushing me to me to pursue the opportunities you never had. Here’s to me joining many more rainy mountain top walks with you, Ralph, Poppy, and Arnie!

Finally, I would like to thank my amazing partner Dan:

Annwyl Dan,

Dwi'n sgwennu hwn yn Gymraeg i ddrysu unrhyw un arall sy'n trio darllen hwn. Dros yr 8 mlynedd diwethaf rydym wedi profi uchafbwyntiau anhygoel a rhai isafbwyntiau sydd wedi newid bywydau. Rydyn ni wedi symud gwledydd, wedi cael ein lle cyntaf gyda'n gilydd, wedi dechrau swyddi newydd ac wedi cael ci. Ond cawsom hefyd ddychryn iechyd dwys, colli anwyliaid, pandemig unwaith mewn oes a brwydro gyda materion bywyd cyffredinol. Ond clasurol fi, roedd yn rhaid i mi wneud pethau hyd yn oed yn fwy anodd a gwneud PhD. Pan oeddwn i'n gweithio'n hwyr, roeddech chi bob amser yn gwneud yn siŵr bod y fflat yn braf

ac yn glyd pan gyrhaeddais adref. Pan oeddwn yn gweithio ar y penwythnos, daethoch gyda mi a chael eich brathu gan y pryfed. Pan na fyddai fy meddwl yn ymlacio, fe wnaethoch chi fy ngorfodi i ymlacio. Pan oeddwn i eisiau pacio'r cyfan i mewn, fe wnaethoch chi fy ngwthio ymlaen o hyd. Hebddoch chi ni fyddai'r person ydw i heddiw, ac ni fyddai dim o'r gwaith hwn wedi bod yn bosibl.

Nid oes unrhyw ffordd y gallaf ddiolch ichi am yr amynedd a'r cariad rydych chi wedi'u dangos i mi dros yr ychydig flynyddoedd diwethaf. Rwy'n dy garu di yn fwy nag y byddwch byth yn ei wybod, dim ond gobeithio y gallaf ddangos i chi faint rydych chi'n ei olygu i mi. Ti yw fy neheulaw, byddwn ar goll yn y bywyd hwn hebddoch.

Nawr bod hyn o'r diwedd drosodd, gallwn edrych ymlaen at y dyfodol. Dyma i'r bennod nesaf, ni allaf aros i adeiladu gweddill fy mywyd gyda chi.

Yr eiddoch am byth,
Megan.

And thankyou reader. Wherever and whenever you are, I appreciate you reading this far. I hope this work inspires you to try something a little out of your comfort zone and truly immerse yourself in whatever you do.